I ELASTIC SCATTERING OF ^{13}C ON ^{12}C

II RADIATIVE ALPHA CAPTURE STUDIES

Lincoln Andrew Bennett

A thesis submitted for the

degree of Doctor of Philosophy

at The Australian National University,

Canberra.

February 1976

PREFACE

This thesis reports investigations made in two areas of nuclear physics. The work was carried out over a 3½ year period from August 1972 to February 1976.

The first chapter is on the elastic scattering of ^{13}C on ^{12}C at E_{LAB} = 12 MeV. The experiment was suggested by Dr D. Branford after Dr P.J.A. Buttle had made some calculations which implied that neutron transfer should be evident in the scattering. A new piece of apparatus was designed and constructed by myself (p.8) which facilitated this experiment. The data were collected by myself and Dr D.C. Weisser, and latterly with the assistance of Professor J.O. Newton. All data analysis was performed by the author with suggestions from the two previously mentioned people.

A computer program which ran on the A.N.U. UNIVAC 1108 computer was written by myself. This performed theoretical calculations of the elastic scattering cross section based on the neutron transfer theory due primarily to W. von Oertzen. Many other subsidiary programs were written to run on the UNIVAC 1108 and the department's IBM 1800 computer to assist in analysis and interpretation of the results. Several 'house' programs, written mainly by Dr T. Ophel were used in the initial data reduction.

The second part of this work concerns the radiative capture of alpha particles by targets in the range A=40 to A=62. In this case, data collection was shared for three of the reactions by members of the 'alpha capture group', viz. Drs Weisser, Shikazono, Hickey and myself. The data for one of the reactions was collected entirely by the author. All data analysis was performed by the author using programs already available for use on the IBM 1800, and programs such as angular distribution fitting routines were written and run on the UNIVAC 1108.

Calculations of alpha capture cross sections were carried out by Dr Moto Shikazono using programs he had written and based on a recently published theory by Shikazono and Terasawa.

No part of this thesis has been submitted for a degree at any other University.

L.A. Bennett.

L.A. Bennett.

ACKNOWLEDGEMENTS

There are many people in the Research School of Physical Sciences who have given invaluable knowledge and experience to me in the last 3½ years. I would like to thank principally my two supervisors. Dr D.C. Weisser for continued assistance throughout the time, and especially for his enthusiasm in keeping the EN Tandem running when all of physics seemed to conspire in halting it. Professor J.O. Newton has provided countless constructive comments during my scholarship as well as assisting in some of the data collection. Both people have been instrumental in pointing out improvements in the early drafts of this thesis; any mistakes which remain are entirely my own.

Dr F.C. Barker was kind enough to give me the benefit of his extensive knowledge of the optical model, without which some of the theoretical calculations would have been impossible.

Many other people have contributed in bringing this thesis to reality. Some of their ideas will be in these pages. The source will have been forgotten, but the idea or fact unconciously utilised in the learning process, so that in time what has been learned and what appears to be nascent in the mind become indistinguishable. I hope they will understand that the passage of time prevents me from acknowledging individual sources, but nevertheless be assured of my gratitude to them.

Finally, I would like to thank Professor J.O. Newton, not only for personal encouragement and assistance in this work but also for the opportunity of working in the department.

L.A. Bennett

ABSTRACT

The first chapter of this thesis describes an experiment on the elastic scattering of ^{13}C on ^{12}C at 12 MeV LAB energy. It has been found that the elastic transfer of a neutron between identical bound states in ^{13}C causes a modulation of the elastic differential cross section. The degree of modulation depends principally on the spectroscopic factor, S^2, of the ^{12}C core plus $p_{1/2}$ neutron component in the ^{13}C wave function since the probability of a bound neutron jumping to a passing ^{12}C core depends on how much ^{13}C 'looks' like a ^{12}C core plus extra neutron. As expected, a theory can be constructed in which the exchange probability is proportional to S^2. If the energy of the colliding nuclei is low enough, then Coulomb forces should be the major interaction. Since these are well known forces, only one unknown quantity remains, S^2. This is treated as a parameter in fitting the theory to experiment, and in the present case, a value of $S^2 = 0.59 \pm 0.12$ was obtained.

In the second part of this thesis, the nuclei ^{44}Ti, ^{58}Ni, ^{64}Zn and ^{66}Zn were studied in the region of the continuum through alpha capture on the appropriate target. Gamma ray emission was measured to the ground and first excited states of these nuclei. The capture of alpha particles by zero spin targets leads to aligned excited states and consequently a direction is established in space relative to which angular distributions can be measured. It was found that gamma ray angular distributions of ground state transitions showed characteristics of interference between 1^- and 2^+ levels. The cross section ratio for exciting these levels was $\sigma(2^+)/\sigma(1^-) \sim 15\%$. Excitation functions were measured over a range of excitation energy of roughly 10-20 MeV in energy steps ranging from 50 keV (^{44}Ti) to 250 keV (^{66}Zn). Fluctuations were seen in both γ_0 and γ_1 channels which were interpreted as Ericson fluctuations which were damped by energy loss in the target. Mean level widths were extracted on this basis, having a value of the order of a few keV. It is well known that (α,γ) cross sections do not show the classical Lorentzian G.D.R. absorption shape due to Coulomb penetration effects and favoured emission of neutrons and protons from the compound nucleus. However, (α,γ) cross sections can be converted to $\sigma_{\gamma G}$ (total absorption cross section) by dividing by essentially $T_{\alpha_0}/\sum_c T_c$ where the T_c are transmission coefficients. When this is done the shape of $\sigma_{\gamma G}$ is obtained, and it is interesting to look for evidence of isospin splitting in the $N \neq Z$ nuclei as well as the degree of isospin mixing in $N=Z$ nuclei. The

theory of Shikazono and Terasawa, which incorporates isospin mixing in the usual Hauser-Fesbach branching ratio, was used, and estimates of $\Gamma_\gamma/\Gamma_\gamma{}^{SR}\varepsilon^2$ made, where $\Gamma_\gamma/\Gamma_\gamma{}^{SR}$ is the fraction of the appropriate sum rule exhausted by the cross section and ε^2 the mixing of $T^<$ and $T^>$ levels. In all cases, the E1 cross section could be fitted assuming that the reaction proceeded through a compound process. It was shown that direct and semi direct processes were negligible in comparison.

About ten angular distributions were measured for each reaction, and the E2 cross section extracted by fitting these with the expression

$$|f(\theta)|^2 = |a^{1/2}\sin\theta + b^{1/2}e^{i\theta_{12}}\sin 2\theta|^2$$

$\sigma(1^-)$ and $\sigma(2^+)$ are absolute cross sections for 1^- and 2^+ levels and θ_{12} a phase angle between incoming $\ell=1$ and $\ell=2$ alpha partial waves. The total cross sections are given by

$$\sigma(1^-) = \frac{8\pi}{3}a$$

$$\sigma(2^+) = \frac{8\pi}{15}b$$

$\Delta T=0$, E2 radiation is permitted by isospin selection rules, and therefore isospin mixing of $T^<$ and $T^>$ states is not considered in the calculation of the E2 cross section. It was found that the ^{44}Ti and ^{58}Ni E2 cross sections could be accounted for by the mechanisms proposed (i.e. compound, direct, semi-direct) but for the two remaining cases, the measured E2 cross section was generally of the order of 10 times greater than the calculated one.

TABLE OF CONTENTS

RADIATIVE ALPHA CAPTURE STUDIES

CHAPTER 2

CHAPTER 3

CHAPTER 1

The $^{12}C(^{13}C,^{12}C)^{13}C$ Reaction

1.1.1. Introduction

The first chapter of this thesis is devoted to the $^{12}C(^{13}C,^{12}C)^{13}C$ transfer reaction at 12 MeV LAB energy. Motivation for this experiment was initially provided by D. Branford at the suggestion of P.J.A. Buttle (Bu 73). The latter performed calculations demonstrating that the elastic transfer of a neutron from ^{13}C to ^{12}C should manifest itself in observable perturbation of the Rutherford differential cross section.

1.1.2. The collision of carbon nuclei

The theoretical advantage of small, as against large, C.M.* energies relative to the Coulomb barrier is the exclusion of coordinate space describing nuclear interiors by the dominant Coulomb repulsion. For example, consider the case of two carbon nuclei approaching each other with a relative energy of 6 MeV. In an idealised classical picture, each nucleus behaves as a uniformly charged rigid sphere. Their minimum separation is given by:

$$d = Z_1 Z_2 e^2 / E_{cm} \quad \text{---} \qquad 1.1.$$

which is 8.64 fm. If the nuclear radius is taken as $R = r_o A^{1/3}$, then for a value of the radius parameter r_o = 1.44 fm., R = 3.3 fm. In this idealised situation, the surfaces of the two ions would be separated by 2 fm. at their minimum separation.

Following the success of the optical model in interpreting p,n,α,t and d scattering, it was subsequently applied to heavy ion scattering. The idea of a heavy ion moving through the complex potential of the optical model is less satisfactory than in the case of nucleons. However, at sub-Coulomb barrier energies, little overlap of the ions is expected, and knowledge of interior potentials is largely circumvented. This is expected to be true in the present case where only the tails of the nuclear wave functions will overlap. It is only the surface region of the potential which will influence the interaction.

By transforming spatial coordinates, two body collisions may be reduced to a single 'quasi' particle which is moving in the internuclear potential. The wave function of this particle satisfies a Schrödinger equation involving the internuclear coordinates and potential. This wave function can be written as a linear combination of radial and angular

---

* Centre of mass

Fig.1.1. Reflection coefficients n_ℓ calculated for ^{12}C on ^{12}C at E_{cm} = 6 MeV. The parameters of the nuclear potential are:

V_o = 100 r_o = 1.19 a_o = 0.48
W = 2.7 r_{oi} = 1.26 a_{oi} = 0.26

(Units are in MeV, fm)

$n_\ell = \exp(-2\,\mathrm{Im}(\delta_\ell))$

(Note the offset ordinate).

functions,

$$\Psi(\underline{R}) = \sum_{\ell=0}^{\infty} C_\ell u_\ell(R) P_\ell(\cos\theta)/R \quad \text{---} \qquad 1.2.$$

C_ℓ are constants, R is the internuclear coordinate, and $P_\ell(\cos\theta)$ an ℓ^{th} order Legendre Polynomial. $u_\ell(R)$ satisfies the radial wave equation:

$$u_\ell''(R) - (\ell(\ell+1)/R^2)u_\ell(R) + k^2 u_\ell(R) = 0 \quad \text{---} \qquad 1.3.$$

where $k^2 = 2\mu(E-V)/\hbar^2$, μ is the reduced mass of the collision partners, and V the potential.

At low energies (E_{cm} < Coulomb barrier), the partial waves $u_\ell(R)$ are strongly reflected by the potential barrier. In Fig.1.1, reflection coefficients for the scattering of ^{12}C on ^{12}C at 6 MeV C.M. energy are shown. These were calculated using a Woods-Saxon complex nuclear potential:

$$V_N = -V_o/(1 + \exp((R-R_o)/a_o)) - iW/(1+\exp((R-R_i)/a_i)) \quad \text{---} \qquad 1.4.$$

The first term is a parametric form of the real part of the potential, and the second term is that for the imaginary part. The particular parameter values were those for the scattering of ^{10}B on ^{12}C at E_{LAB} = 18 MeV taken from Voos et.al. (Vo 69).

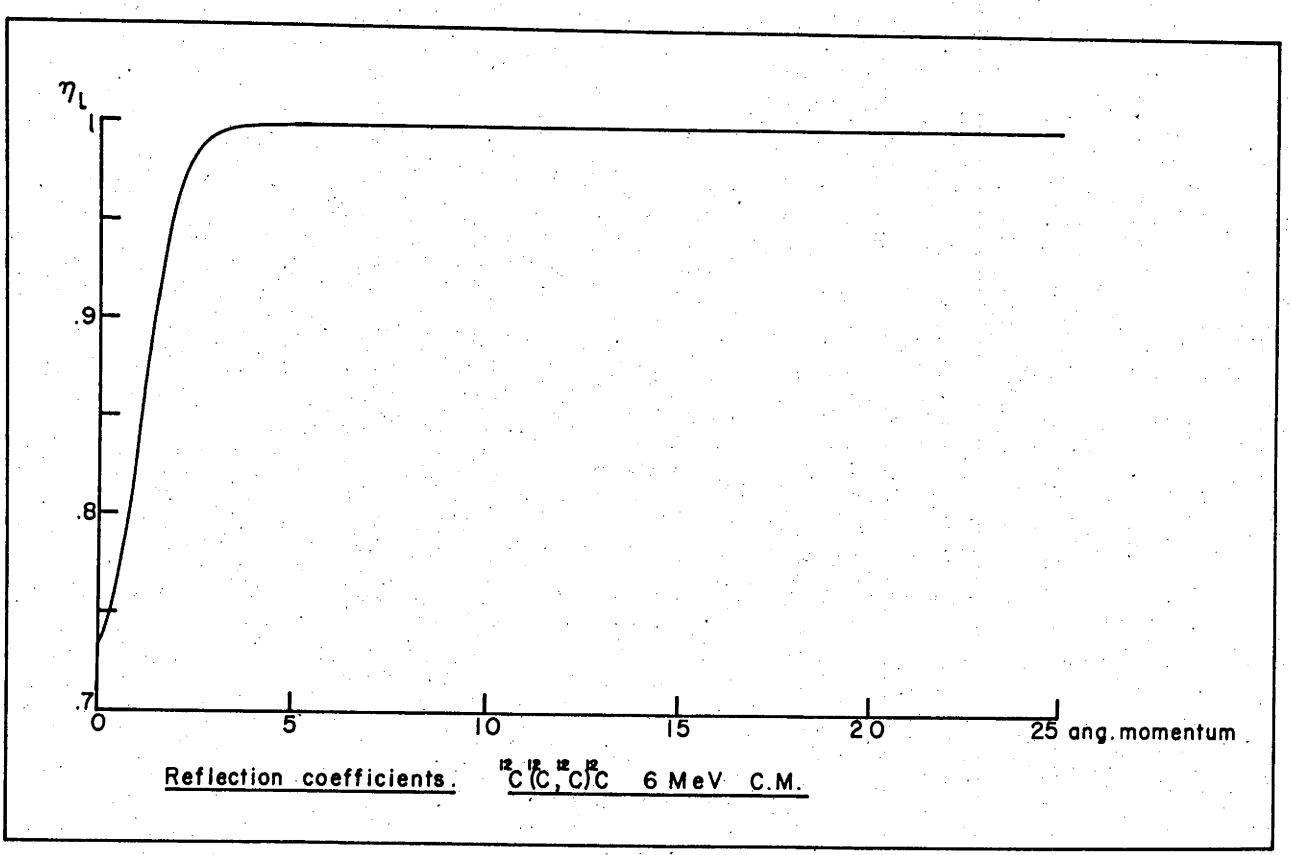

It is apparent from Fig.1.1 that only the first few ℓ values penetrate the potential barrier. This evidence supports quantitatively the qualitative arguments made earlier about the small overlap of nuclear wave functions.

1.1.3. The Interference phenomenon

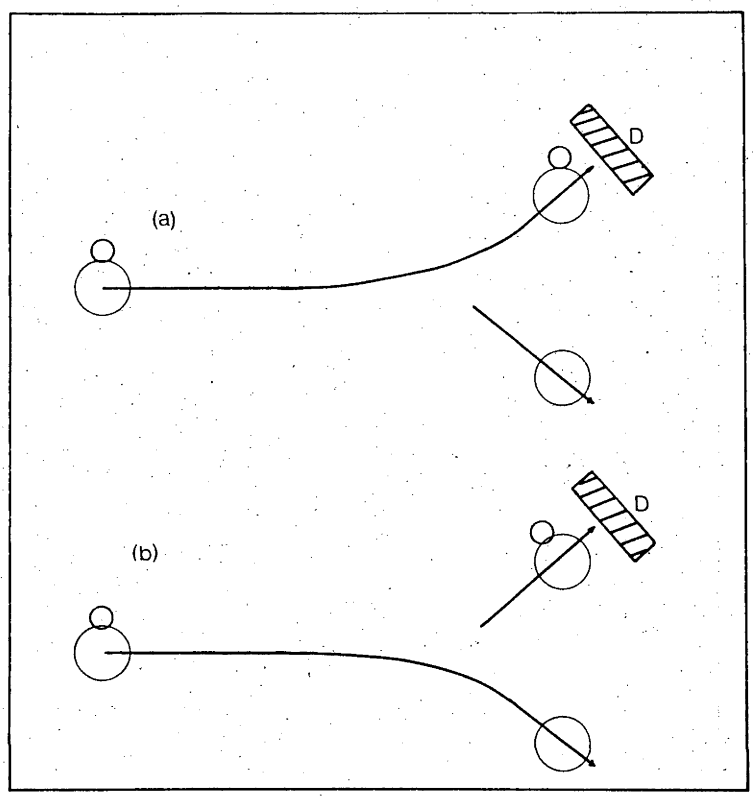

Fig.1.2. Indistinguishability of elastic transfer and elastic scattering. In (a), ^{13}C is elastically scattered into the detector D. In (b), ^{13}C transfers its neutron to the ^{12}C target, and ^{13}C is again detected with identical kinematics.

In Fig.1.2, the indistinguishability of elastic scattering and neutron transfer are illustrated. Since both processes are coherent, interference between them is expected giving rise to constructive and destructive components to the elastic scattering differential cross section.

The origin of the interference pattern in the cross section may be understood using semi-classical arguments, in particular, the association of well defined orbits with the particles. In the state where there is no relative motion of the cores, the time dependent wave function of the neutron is given by (eg. von Oe 70)

$$\Phi(t) = \phi_a \cos(J(R)t/\hbar) + i\phi_b \sin(J(R)t/\hbar) \quad \text{---} \qquad 1.5.$$

where ϕ_a and ϕ_b represent a neutron bound to a ^{12}C core to make the ^{13}C ground

Fig.1.3. A comparison of $^{12}C(^{13}C,^{12}C)^{13}C$ elastic scattering with and without an exchange interaction. Optical model parameters are those of Fig.1.1.

state. J(R) is the exchange energy which will be discussed later, (Sect.5) it is a function of the intercore separation R. A resonant transfer time is given by:

$$t_{res} = \pi\hbar(2J(R))^{-1} \quad ---- \qquad 1.6.$$

If the ions move along well defined trajectories, then a collision time may be defined. This has the form

$$t_{coll} = a(\theta)/V \quad ---- \qquad 1.7.$$

where $a(\theta)$ is a characteristic length which depends on the angle of scattering θ, and V is a characteristic velocity. The resonance exchange process will be most strongly excited if the collision time is an integral multiple of the transfer time, i.e.

$$t_{coll} = nt_{res} \qquad n = 1,2,3, \cdots$$

Constructive or destructive interference will depend on the value of n.

In Fig.1.3, calculations are shown graphically for the $^{12}C(^{13}C,^{12}C)$ ^{13}C reaction at 12 MeV. LAB. energy. The smooth curve is from an optical model calculation. When an exchange potential is added coherently to the optical potential, oscillations are introduced into the cross section.

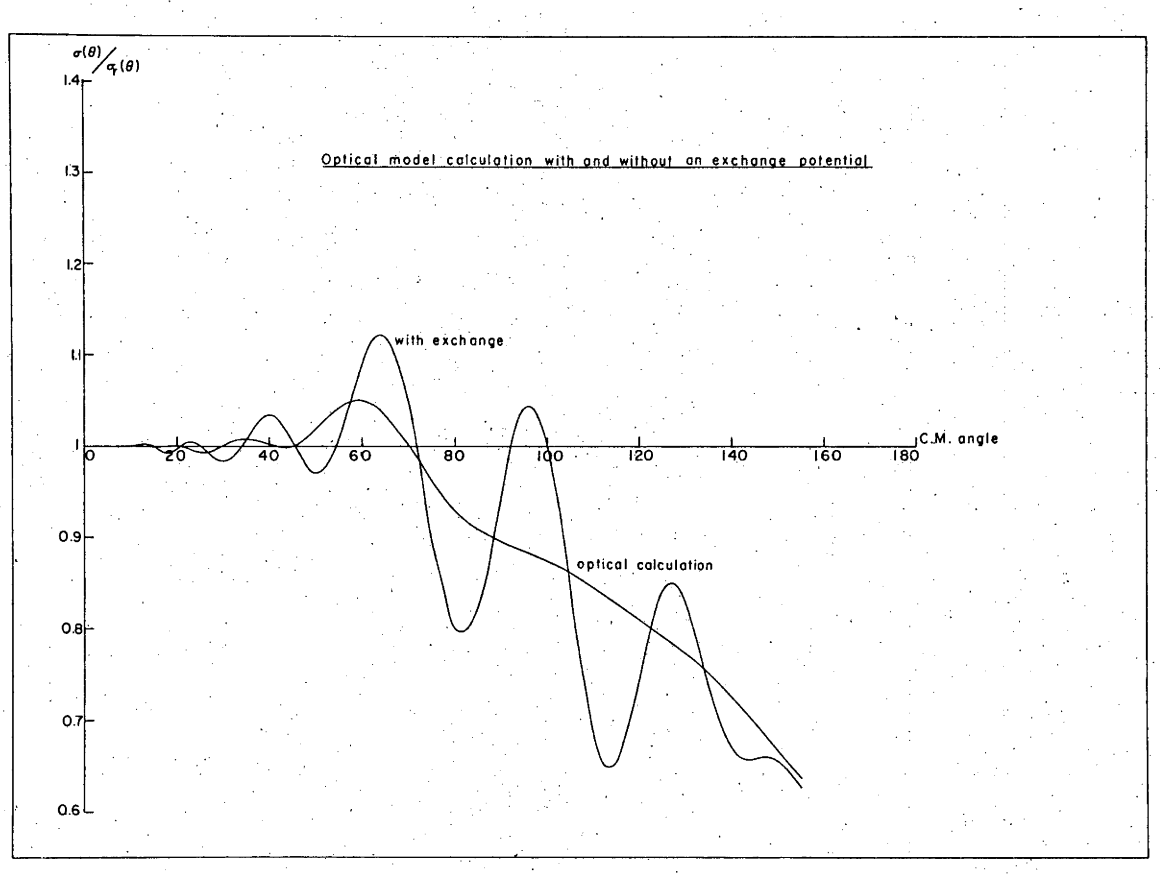

The exchange potential has been calculated using the Linear Combination of Nuclear Orbitals method (L.C.N.O.) which will be described in section 5.

1.1.4. Determination of Spectroscopic Factors by the Linear Combination of Nuclear Orbitals method.

Analyses of H.I. transfer reactions have generally been made using one of three methods, viz:

(i) The coupled channel Born approximation (C.C.B.A.). e.g.(Im 74).

(ii) The D.W.B.A. (Bu 66). This was adapted for H.I. processes by Trautman and Alder (Al 72) for the case where Coulomb scattering is dominant.

(iii) The Linear Combination of Nuclear Orbitals method (L.C.N.O.). This method has been pioneered in the last ten years or so principally by W. von Oertzen (von Oe 70), H.G. Bohlen and W. von Oertzen (Bo 71), K.D. Hildenbrand, R. Bock, H.G. Bohlen, P. Braun-Munzinger, D. Fick, C.K. Gelbke, W. von Oertzen and W. Weiss (Hi 72) and others. For example, Becker especially (Be 74), and a recent review paper (von Oe 75) with the references therein.

Single nucleon transfer reactions have been investigated for ^{28}Si,^{29}Si (Hi 72), ^{16}O,^{17}O (Ge 73), ^{13}C,^{12}C (Bo 71), ^{13}C,^{14}C (von Oe 75) as well as proton transfer reactions such as $(^{15}N,^{16}O)$,$(^{19}F,^{18}O)$ (von Oe 75). All these examples have been analysed in terms of nucleon or nucleon hole exchange using the L.C.N.O. method. At energies where the number of reaction channels is limited to essentially elastic scattering and elastic transfer, good fits to the data have been obtained.

In Fig.1.4., the data and fit obtained by Bohlen and von Oertzen (Bo 71) for the $^{13}C(^{12}C,^{13}C)^{12}C$ reaction are shown. ^{13}C was bombarded with ^{12}C at 15 and 19 MeV. LAB. energy, and the fits are generated by method (iii). In the lower part of Fig.1.4, data for the $^{28}Si(^{29}Si,^{28}Si)^{29}Si$ reaction are shown. These data were measured by Hildenbrand et.al. (Hi 72) and again method (iii) was used in fitting. From these analyses, reduced neutron widths for ^{13}C and ^{29}Si have been obtained.

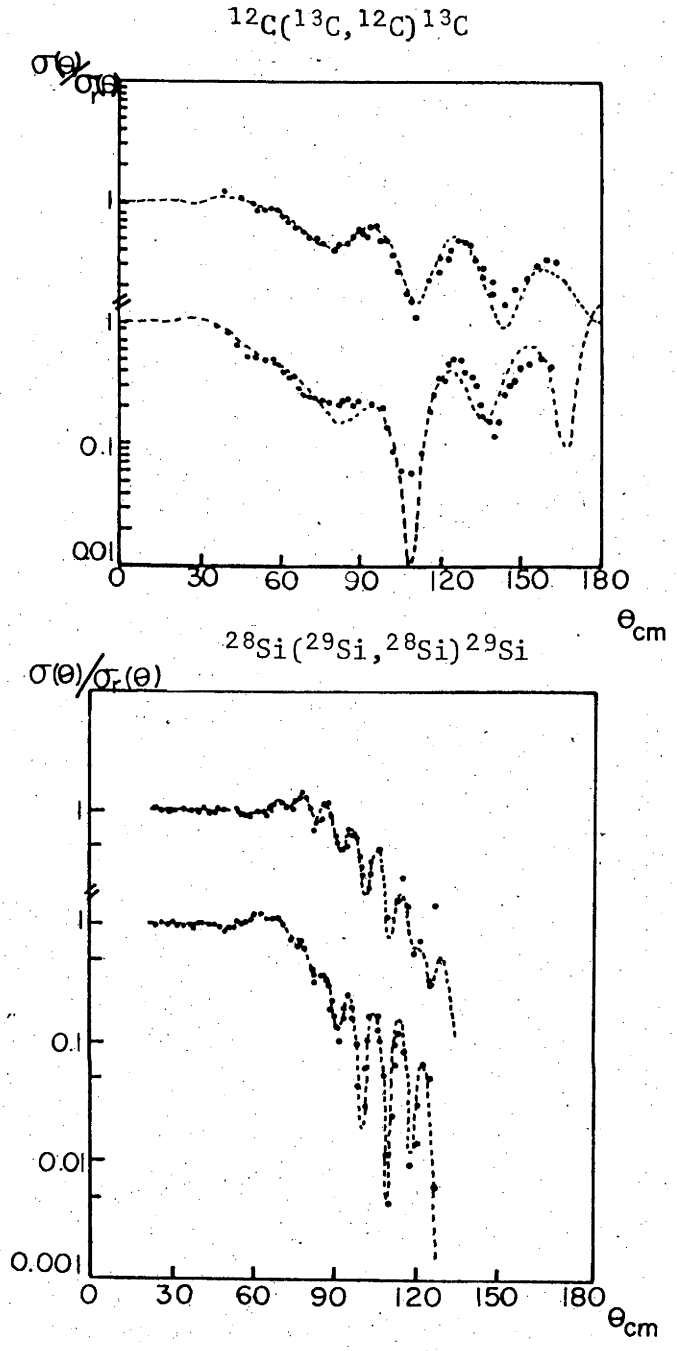

Fig.1.4. In the upper part of the figure are the data for $^{12}C(^{13}C,^{12}C)^{13}C$ at 15 and 19 MeV (upper set, lower set respectively). In the lower part of the figure, the $^{28}Si(^{29}Si,^{28}Si)^{29}Si$ data at 65 and 70 MeV LAB. energy are shown (upper and lower set respectively).

In Table 1.1, values of the spectroscopic factors obtained by method (iii) are compared with values obtained from (d,p) work and theoretical values.

Nuclide	(iii)	(d,p)	Theory
^{13}C	0.81 0.59±0.12*	0.58	0.613
^{29}Si	0.43	0.53	0.5

Table 1.1.

References for table 1.1.

	^{13}C	^{29}Si
Method (iii)	(von Oe 75)	(Hi 72)
	*(present experiment)	
(d,p)	(Mi 72)	(Me 71a)
Theory	(Co 67)	(Hi 72)

Experimental Method

1.2.1. Beam, target, target chamber, spectrometer and monitors

Thin Carbon 12 targets can be easily fabricated, and since ^{13}C beams are readily available from the A.N.U. tandem Van de Graaff generator, a thin (15μg cm^{-2}) ^{12}C target was bombarded with a ^{13}C beam. This was in charge state 3+ with an analysed energy of 12 MeV.

After magnetic analysis, the beam was directed to the appropriate line by a three way switching magnet. It was then focussed by a quadrupole doublet lens to pass through a 1mm x 5mm rectangular collimator about 30 cm. from the target. Reaction products were detected by the A.N.U. 61 cm. double focussing spectrometer which is described in detail elsewhere (e.g. El 68, Pa 74). A cylindrical target chamber was coupled to the spectrometer entrance via a sliding band which allowed rotation and maintainence of vacuum integrity. Reaction products could be observed at angles between zero and 150° to the beam direction by rotating the spectrometer. The sliding band chamber is described by Parkinson (Pa 74) and was constructed from a drawing supplied by the California Institute of Technology.

The chamber was not large enough to contain a properly suppressed Faraday cup. In any case, absolute beam integration is always difficult

Fig.2.1. The apparatus is held rigidly in the target chamber. The target position is in the middle of the box structure and the beam axis is defined by holes in the front and back plates.

The three surface barrier detectors are at 35° to the beam axis and subtend a solid angle of 0.2 msr. at the target. A Faraday cup can be inserted in the large hole in the front plate, the coiled up wire carries the current to a feed through in the chamber. Scattered particles pass through the slot on the right hand side of the front plate into the spectrometer entrance.

when using heavy ions because of the number of charge states involved. For this reason, the beam intensity was measured indirectly from the yield of elastically scattered particles. Three surface barrier detectors were mounted symmetrically about the beam axis and at 35° to it. In Fig.2.1, the special apparatus constructed to do this is shown. If the beam moves in a vertical plane, then the decrease in yield in one monitor should be compensated by an increase in yield in the opposite monitor. This is assuming that the cross section at 35° does not change too non-linearly with angle which is true over a small angular interval for Rutherford scattering.

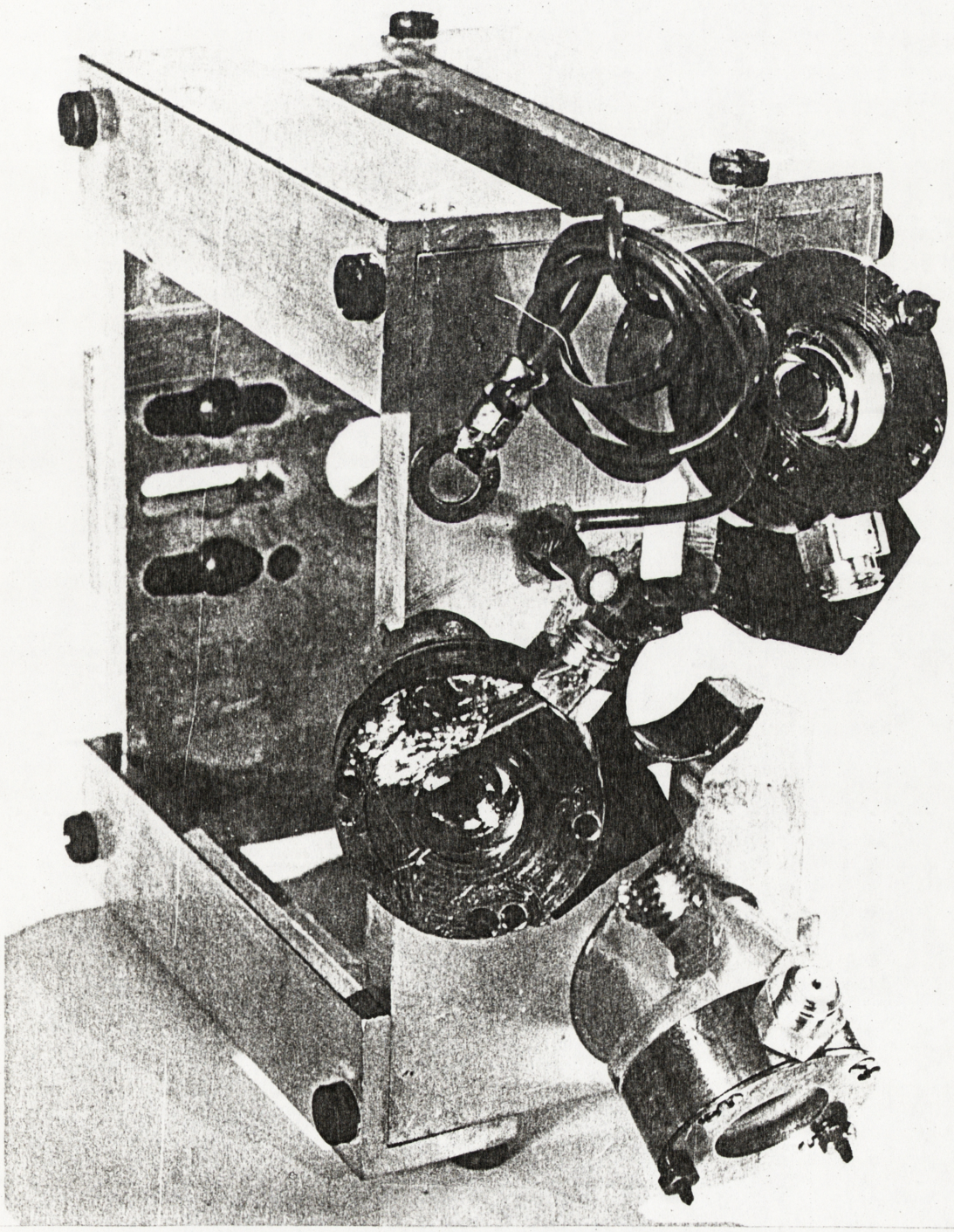

Unfortunately it was not possible to mount a corresponding monitor opposite to the one in the horizontal plane. From the geometry of the beam line, it is possible for the beam to move across the target by ± 1mm.

This would cause a corresponding change in the yield of the side monitor by ±3%*. However, the overall error is much less than this because the monitor yields are summed and the 3% error is buffered by the total yield. Nevertheless, it is desirable to obtain a number of independent estimates for each datum to verify that only a statistical error is present.

The yield in each monitor for an integrated number of beam particles I is given by:

$$Y_m \simeq At_{12_C} I(d\sigma/d\Omega)_m \delta\Omega_m \quad \text{---} \qquad 2.1.$$

where A is a constant which depends on the charge state of the incident beam and on the particular units used. t_{12_C} is the thickness of the carbon target. $(d\sigma/d\Omega)_m$ is the differential cross section at 35° LAB., and $\delta\Omega_m$ the solid angle subtended by each monitor at the target (0.2 msr).

The yield in the spectrometer for charge state j is given by:

$$Y_S(\theta) \simeq \varepsilon_j At_{12_C} I(d\sigma/d\Omega)\delta\Omega_S \quad \text{---} \qquad 2.2.$$

where ε_j is the equilibrium charge state fraction of the j'th charge state and $\delta\Omega_S$ the solid angle subtended by the spectrometer. Eliminating $At_{12_C} I$ from equation 2.2 using equation 2.1 gives:

$$\begin{aligned} Y_S(\theta) &\simeq \varepsilon_j Y_m (d\sigma/d\Omega)\delta\Omega_S ((d\sigma/d\Omega)_m \delta\Omega_m)^{-1} \\ &= \text{Constant} \times \varepsilon_j Y_m (d\sigma/d\Omega)\delta\Omega_S \quad \text{---} \end{aligned} \qquad 2.3.$$

where the Constant = $((d\sigma/d\Omega)_m \delta\Omega_m)^{-1}$. Consequently, by using the yield from the monitor detectors, the term It_{12_C} is eliminated in calculating the experimental cross section from equation 2.3. If the solid angle of the spectrometer is kept constant for all measurements, then:

---

* The relative error in the sum of the three monitors, ε/N, is given by

$$1/N\sqrt{n_1 + n_2 + n_3 + 0.03^2 n_3^2}$$

where $N = \sum_{i=1}^{3} n_i$

For example, a realistic case is $n_1 = n_2 = n_3 = 3000$. Then

$$\varepsilon/N = \pm 1.45\%$$

The statistical error is $1/\sqrt{N} = 1.05\%$.

$$d\sigma/d\Omega = \text{Constant} \times Y_s(\theta)(\epsilon_j Y_m(\theta))^{-1} \quad \text{---} \quad 2.4.$$

where Constant = $(d\sigma/d\Omega)_m \delta\Omega_m/\delta\Omega_s$.

This constant may be obtained by measuring the cross section where Rutherford scattering is valid, namely at small forward angles. By eliminating t_{12_C} as in equation 2.3, it is not necessary to allow for increase in target thickness during bombardment.

1.2.2. Charge State Fractions

Ions emerging from a stopping medium may be divided into two types depending on their history. The first kind are observed at essentially zero degrees and have an angular distribution which reflects a statistical accumulation of small angle scattering events with atoms. The second type arises from close collisions with nuclei and emerge at relatively large angles.

For the first class of ion, the probability of electron transfer is a function of V/V_e, where V is the ion velocity, and V_e an orbital electron velocity. (Usually in units of $e^2/\hbar \simeq 2.10^8 cm.s^{-1}$, the Bohr orbital velocity of the hydrogen electron in its ground state). If $V \gg V_e$, a bound electron may be treated as being essentially free. The minimum energy transfer is $0.5 m_e V_e^2$, and the maximum $4m_eE/M$, where m_e and M are the masses of the electron and H.I. respectively and E is the ion energy. On this basis, the cross section for electron loss is proportional to $(V/V_e)^n$ where n is integral of the order of 3 (Be 72). On the other hand, the electron capture cross section is proportional to $(V_e/V)^n$ (Ma 71).

This process, where the ion emerges at a small forward angle is essentially peripheral insofar as atomic collisions are of the screened Coulomb type. However, in large angle collisions, the overlap of projectile and target atom is large. Large rearrangements of the electrons may occur so that the emergent ion has a different electronic configuration than in the small angle case.

Equilibrium charge state fractions sometimes depend on the method in which they were measured, i.e. from forward scattering or large angle scattering processes. In the present experiment, the detected ions result from large angle collisions and so it is important to use equilibrium charge state fractions which are pertinent to this. Equilibrium charge state fractions have been measured in the laboratory by Parkinson (Pa 74). These data were obtained from backward angle scattering. They were incorporated in a computer program which listed the C.S.F. (charge state fraction) as a function of angle of the scattered particle.

In Fig.2.2, the values for the 4+ and 5+ states are shown as a function of velocity squared (MeV/A).

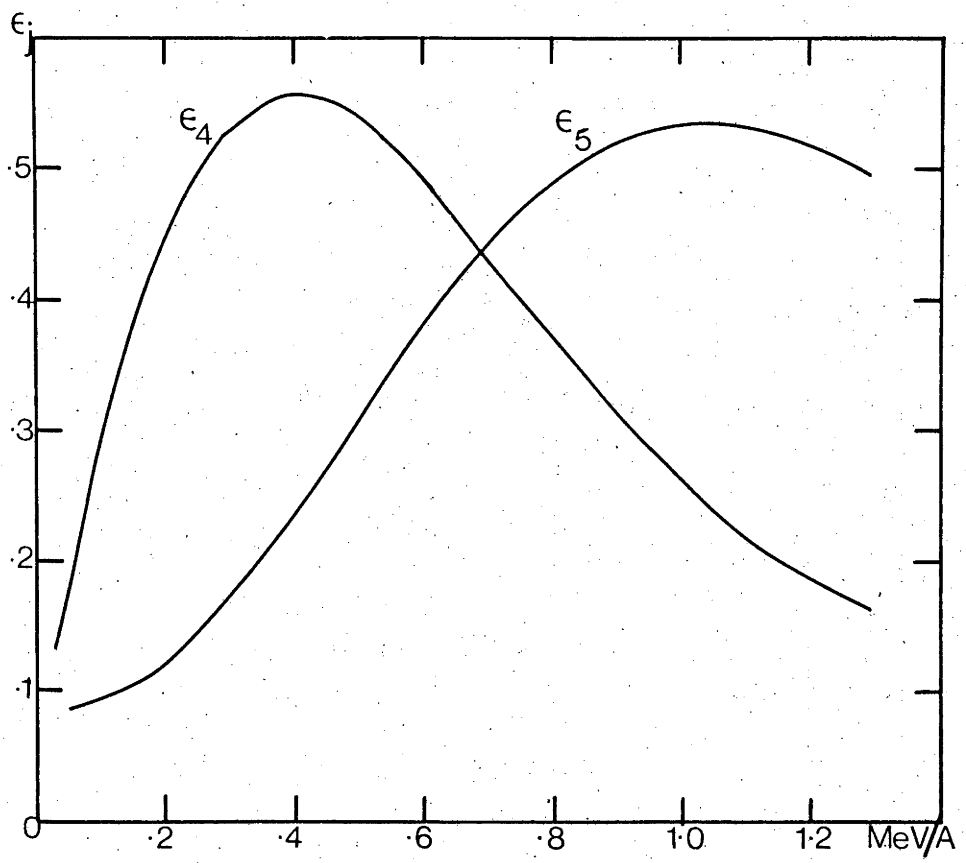

Fig.2.2. Equilibrium charge state fractions

1.2.3. Detection of reaction products

The advantage of using a magnetic spectrometer for this experiment is demonstrated in Fig.2.3. At small forward angles, the energies of ^{13}C and ^{12}C recoils are very similar. However, their mass-energy products (mE/ϵ_j^2, which is labelled rigidity in Fig.2.3) are sufficiently different for separation by magnetic analysis. At larger angles, the reverse is true, but ^{12}C and ^{13}C may be distinguished by their energy separation.

Reaction products were detected by an Ortec position sensitive detector at the focal plane of the spectrometer. It had a nominal length of 5 cm. and a width of 0.8 cm. As will be explained later, it was necessary to place the counter at an angle of 48° to the focal plane in order to increase its effective length. The energy and energy × position pulses from the detector were processed by the electronic system shown in Fig.2.4.

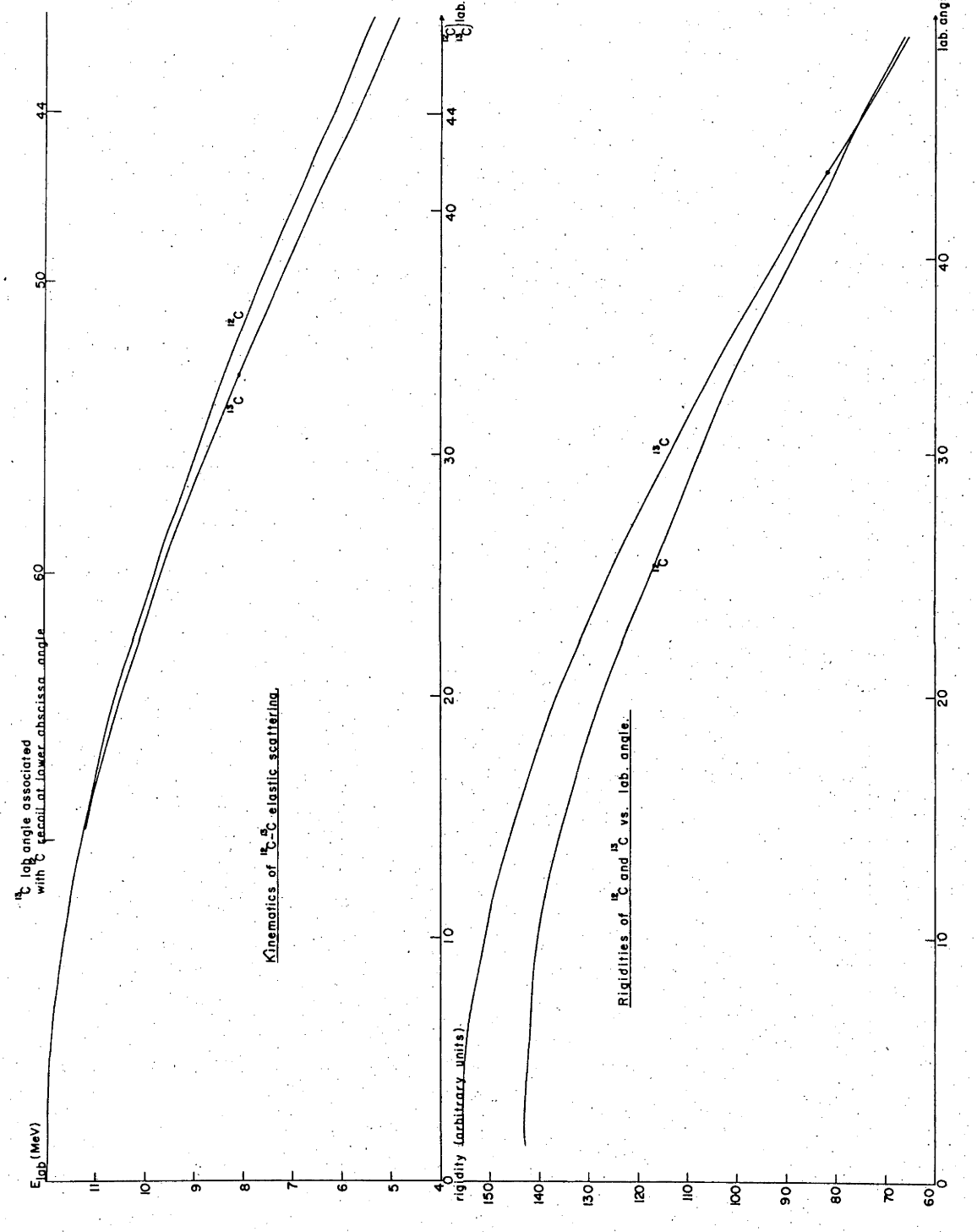

Fig.2.3. Kinematics of ^{13}C on ^{12}C at E_{LAB} = 12 MeV.

Fig.2.4. The electronic system used in the experiment. The top section shows the circuits associated with pulses from the P.S.D., and the lower section with pulses from the monitors.

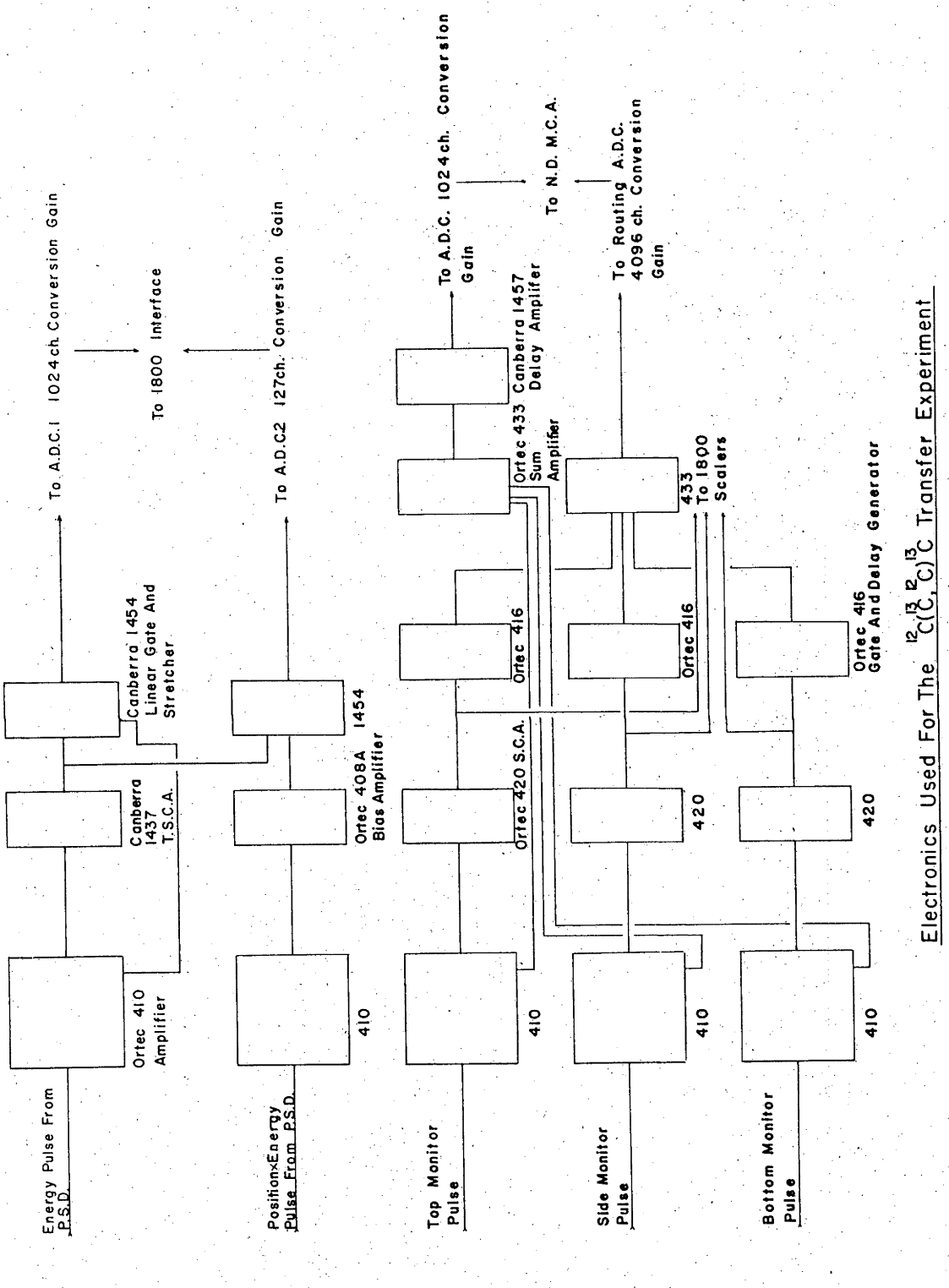

Electronics Used For The $^{12}C(^{13}C,^{12}C)^{13}C$ Transfer Experiment

Fig.2.4.

1.2.4. Energy spread in the detected particles

In evaluating the feasibility of an experiment, one aspect which deserves consideration is the energy spread in the detected particle group. This is intimately related to the solid angle subtended by a detector at the intersection of the beam axis and target, and also to the properties of the target itself. Limiting the energy spread necessarily limits the flux of scattered particles. For example, if one were to ask for an energy spread of 20 keV from a H.I. reaction where the cross section was of the order of microbarns per steradian, this could easily limit the target thickness and detector solid angle to prohibitively small values for experimental purposes.

The contribution from the kinematics of the reaction will be evaluated followed by effects due to the target.

Kinematic broadening

The energy of scattered particles depends on the angle through which they are scattered. To simplify the argument, the projectile and target ions will be taken to have equal mass, A = 12. The 8% mass difference of ^{12}C and ^{13}C will be neglected. Kinematic spread is $dE/d\theta_{LAB}$, and from a vector diagram of the collision,

$$dE/d\theta_{LAB} = E_{LAB} \sin 2\theta_{LAB} \text{ ---} \qquad 2.5.$$

where the relationship $\theta_{cm} = 2\theta_{LAB}$ has been used. Equation 2.5 is maximized when $\theta_{LAB} = 45°$, and the energy spread about 45° in a small interval $\delta\theta_{LAB}$ is

$$\delta E^{K}(45) = 12\delta\theta_{LAB} \text{ MeV ---} \qquad 2.6.$$

All further remarks will refer to scattering at 45° unless otherwise stated. If the incident energy is 12 MeV, then a particle scattered at 45° will have an energy of 6 MeV.

Target thickness effects

A finite target thickness causes a spread in energy for the following reasons:-

a) Energy straggling
b) Non-uniformity
c) Multiple scattering

a) and c) have not been so thoroughly investigated for heavy ions as in the case of light ions and protons. Nevertheless, estimates will be based on existing theories and supported by experimental evidence wherever possible.

Multiple scattering in target

In passing through the carbon foil, carbon ions undergo collisions with electrons and elastic screened collisions with nuclei. The relatively light electrons take up energy without significantly altering the trajectory of the massive carbon ion.

However, in a nuclear collision a large angular deflection may result. The emergent ion reflects its history in the foil as a statistical accumulation of nuclear collisions. If $\sigma(\theta)$ is the differential cross section for scattering, then if a number of small angle collisions occur in a foil, a mean square angle of the emergent ion may be calculated from:

$$\langle\theta^2\rangle = \int_\Omega \sigma(\theta)\theta^2 d\Omega / \int_\Omega \sigma(\theta) d\Omega \quad --- \qquad 2.7.$$

In order to make a quantitative estimate of this effect, the Thomas-Fermi model of the atom is used in deriving $\sigma(\theta)$. The electrostatic potential of the atom can be approximated by:

$$V(r) = \frac{Z_1 Z_2 e^2}{r} \exp(-r/a) \quad --- \qquad 2.8.$$

where Z_1 and Z_2 are the atomic numbers of the projectile and target respectively, and e is the electronic charge. The screening radius a is given by (Li 63):

$$a = 0.885 a_0 / (Z_1^{2/3} + Z_2^{2/3})^{1/2} \quad --- \qquad 2.9.$$

with $a_0 = 0.529\ 10^{-8}$cm.

For small angle collisions, $\sigma(\theta)$ is given by

$$\sigma(\theta) = 4d^2/(\theta^2+\theta_{min}^2)^2 \quad --- \qquad 2.10.$$

where $d = Z_1 Z_2 e^2 / 2E_{cm}$

θ_{min} is the angle below which classical Rutherford scattering becomes invalid.

Unlike Rutherford scattering, equation 2.10 gives more realistic results in the limit of zero energy or $\theta = 0$

$$\left.\begin{array}{ll} \lim_{E\to 0} & \sigma(\theta) = 0 \\ \lim_{\theta\to 0} & \sigma(\theta) = 0.25 r_0^4/d^2 \end{array}\right\} \quad --- \qquad 2.11.$$

Although $\sigma(\theta)$ has an identical form whether it is derived from classical or quantum mechanics, the total cross section depends on whether classical or quantum mechanical results are used. Validity of the classical treatment

may be judged by the value of the Born parameter:

$$\alpha = Z_1 Z_2 (137\beta)^{-1}$$

where $\beta = v/c$

In the present case (carbon on carbon at E_{LAB} = 12 MeV) $\alpha \simeq 6$ which implies that classical techniques may be used. In this case, the value of θ_{min} is determined by:

$$\int_{\Omega} \sigma(\theta) d\Omega = \pi r_0^2 \quad \text{---} \qquad 2.12.$$

where r_0 is the geometric radius of a scattering centre. If the target consists of N hard spheres of radius r_0 per unit volume, then $r_0 = 0.5N^{-1/3}$.

From equation 2.10,

$$\int \sigma(\theta) d\Omega = 4\pi d^2/\theta_{min}^2 \quad \text{---} \qquad 2.13.$$

which with equation 2.12 gives

$$\theta^2_{min} = 4d^2/r_0^2 \quad \text{---} \qquad 2.14.$$

For the particular case of interest,

$$\theta_{min} \simeq 0.8^\circ$$

Meyer (Me 71) has developed a classical theory for heavy ion multiple scattering using the Thomas-Fermi potential. He found that the angular distribution of multiple scattered ions was very similar to a Gaussian distribution. The F.W.H.M. is given by:

$$\phi_{1/2} = 4da^{-1}\{g_1(\tau) + (a/r_0)^2 g_2(\tau)\} \quad \text{---} \qquad 2.15.$$

where $\tau = \pi a^2 Nt$, t being the target thickness. Numerical tabulations of g_1 and g_2 are given in Meyer's paper. Hooton et al. (Ho 74) have compared the values of $\phi_{1/2}$ with experimental values for O, Cℓ and Fe incident on thin (<100μg.cm^{-2}) C, Aℓ and Ni foils. They found good agreement between theory and experiment. For C ions incident on a 15μg.cm^{-2}C foil, the values of $\phi_{1/2}$ are:

$\phi_{1/2} = 0.048^\circ$ $\qquad E_{LAB}$ = 12 MeV

$\phi_{1/2} = 0.096^\circ$ $\qquad E_{LAB}$ = 6 MeV

There is a non-negligible probability of ions being scattered up to $\pm\phi_{1/2}$, i.e., one F.W.H.M. deviation away from the mean.

$\left(\int_{\phi_{1/2}}^{\phi_{1/2}} P(\theta)d\theta / \int_0^{2\pi} P(\theta)d\theta = 98\%\right.$, where $P(\theta)$ is the probability of scattering at θ).

The contribution to the energy spread will therefore be:

$$\delta E^{MS} = (dE/d\theta_{LAB}) 2\phi_{1/2} \qquad 2.16.$$
$$= 40 \text{ keV } (\theta_{LAB} = 45°)$$

Energy loss and straggling

According to the calculations of Lindhard et.al. (Li 63) the ratio of electronic stopping to nuclear stopping is much greater than unity for the case of interest. Stopping powers are given in terms of dimensionless quantities,

$$\varepsilon = aA_2(Z_1Z_2e^2(A_1+A_2))^{-1}E$$
$$\rho = (4\pi a^2A_1A_2/(A_1+A_2)^2)Nt$$

The electronic stopping power is given by $k\varepsilon^{1/2}$, where $k = 0.133\ Z_2^{2/3}A_2^{-1/2}$ for $Z_1 = Z_2$, $A_1 = A_2$. However, where experimental data are available, for example, the semi empirical tables of Northcliffe and Schilling (No 70) these numbers are to be prefered. According to Blaugrund (Bl 66), the atomic stopping power is given by:

$$(d\varepsilon/d\rho)_n = (0.5\varepsilon)^{-1}\{0.3 + \ell n[(0.6+\varepsilon^2)/\varepsilon]\} \quad --- \qquad 2.17.$$

Consequently, $\frac{d\varepsilon_e}{d\varepsilon_n} \simeq 180$ for carbon ions at $E_{LAB} = 12$ MeV on carbon.

The value of $(dE/dx)_e$ has been taken from the tables of Northcliffe and Schilling and converted to $(d\varepsilon/d\rho)_e$ using their reference 32*. At very low energies, atomic stopping becomes important and dominates in the kilovolt energy region.

Energy straggling

Energy straggling of an ion passing through a stopping medium arises from statistical variation in the number of collisions and variation in energy transfer at each collision. When $\bar{n}$, the mean number becomes greater than about ten, the distribution of collision probability becomes symmetric about $\bar{n}$. An estimate of $\bar{n}$ is given by the parameter x which is the ratio of the mean energy loss to the maximum energy transfer to a free electron.

$$x = \xi/\varepsilon_{max} \quad --- \qquad 2.18.$$

where $\xi = (2\pi e^4Z_1^2Z_2/mv^2)(\rho A_0 t/A_1)$

and $\varepsilon_{max} = \frac{4mME}{(m+M)^2}$

m is the electron mass, ρ the mass density of the target, and A_0 Avogadros number. In this case:

---

* $d\varepsilon/d\rho = 0.196\ A_2(A_1+A_2)(Z_1^{2/3}+Z_2^{2/3})^{1/2}(Z_1Z_2A_1)^{-1}dE/dx$

$$\varepsilon_{max} \simeq 4mE/M \quad \text{---} \qquad 2.19.$$

which is the classical maximum energy transfer to a free electron. In the case of interest, $x \sim 20$.

From classical considerations, N. Bohr (Bo 15) derived an equation for stopping power.

$$dE/dx = (4\pi Z_1^2 Z_2 e^4/mv^2)(\rho A_0/A_1) \ell n\, B_c \quad \text{---} \qquad 2.20.$$

where $B_c = 1.123\ mv^3(Z_2 e^2 \langle\omega\rangle)^{-1}$

$\langle\omega\rangle$ is an average over the frequencies of the atomic electrons. It is tempting to identify $\hbar\langle\omega\rangle$ with the mean ionisation potential. Taking a value for this quantity from Evans (Ev 55), for a 15 μg cm^{-2} carbon target, the energy loss from equation 2.20 is about 186 keV. This compares with about 110 keV from the tables of Northcliffe and Schilling. The variance of the energy loss is given by Bohr as:

$$\sigma^2 = 4\pi e^4 Z_1^2 Z_2 (\rho A_0 t/A_2) \quad \text{---} \qquad 2.21.$$

This gives a value $\sigma \sim 10$ keV, or F.W.H.M. of the distribution as 24 keV. Recently, J. Barrette et.al. (Ba 75) have measured σ^2 for ^{12}C, ^{14}N, ^{16}O and ^{32}S in A/CH_4 mixture. They found $\sigma_{exp} \simeq 1.6\sigma$ (Bohr).

Uniformity of target

By moving a target whose diameter was large compared to the beam spot size over the beam spot, the effect of non-uniformity could be observed. The dispersion of the magnetic spectrometer is defined by:

$$D = \delta y 2E(R\delta E)^{-1} \quad \text{---} \qquad 2.22.$$

where the y plane is normal to the mean ray at the focal plane, and R is the radius of curvature of the mean ray. The relevant values are (El 68):

$$D = 3.38$$
$$R = 61 \text{ cm.}$$

The position resolution of the Ortec P.S.D. is about 2mm, which, projected from the focal plane onto the y axis, is 1.3mm. (The focal plane makes an angle of 48° with the y axis). Using equation 2.22, $\delta E/E = 0.0013$. Consequently, a change in target thickness of roughly 10% at 6 MeV should produce an observable movement in position. Since no such movement occurred when bombarding different parts of the target, the target non-uniformity is no worse than ±10%.

One further contribution remains, this is additional to the kinematic broadening and is due to the target spot size. The beam defining

collimator 30cm from the target is 1mm x 5mm. The entrance to the spectrometer is 36cm away from the target, and so the kinematic contribution is $12 \times 0.0029 \simeq 34$ keV.

Total energy spread

Summarising previous considerations, the contributions to the total energy spread are:

1)	Kinematic broadening	$\delta E^K = 12\delta\theta_{LAB}$
2)	Multiple scattering	$\delta E^{MS} \simeq 40$ keV
3)	Straggling	$\delta E^S \simeq 24$ keV
4)	Non-uniformity	$\delta E^U \lesssim 23$ keV
5)	Target spot effect	$\delta E^{TS} \simeq 34$ keV

2, 3 and 4 all have approximately Gaussian distributions, so these may be added in quadrature. The total energy spread is then:

$$\delta E \simeq 12\delta\theta_{LAB} + .034 + \sqrt{(\delta E^{MS})^2+(\delta E^S)^2+(\delta E^U)^2} \quad --- \quad 2.23.$$

From equation 2.22

$$3.38 = \frac{4\cos 48^\circ \; 2.6}{61(12\delta\theta_{LAB}+0.086)} \quad --- \quad 2.24.$$

Here the length of the detector has been taken as 4cm in order to ensure that the group was well on the counter. From equation 2.24, the value of $\delta\theta_{LAB}$, which satisfies the conditions listed previously, can be obtained. This turns out as

$$\delta\theta_{LAB} \simeq 0.33^\circ$$

The outcome of these considerations is that at $\theta_{LAB} = 45^\circ$, the elastically scattered carbon group will be completely intersected by the P.S.D. if the horizontal slits of the spectrometer are set at approximately $\pm 0.15^\circ$. This is for a 15 $\mu g\ cm^{-2}$ target. These parameters give a satisfactory count rate when beam intensity is taken into consideration. For example, with $\sim$300na. of 3+ ^{13}C striking the target, the count rate in the spectrometer would be about $6s^{-1}$ with the following aperture settings.

Vertical slits	$\pm 2^\circ$
Horizontal slits	$\pm 0.15^\circ$

These values make $\delta\Omega_S \simeq 0.5$msr.

However, when the experiment was performed, it was found that about 10% of the particle group was off the counter with the above parameters. Upon examination of the monitor spectra, it was noticed that a low energy tail was

Fig.2.5. Vector diagram of ^{13}C, ^{12}C kinematics. As the ^{12}C LAB. angle decreases, the ^{13}C LAB. angle increases up to $\theta_{MAX} = 67°$ LAB. By observing ^{12}C recoils forward of 44° LAB, the ^{13}C range 44° - 67° LAB. was covered. $\underline{V}_{cm}$ is the velocity of the c.m. $\theta^{12}_{cm}C$ is the scattering angle of ^{12}C in the c.m. system, and $\theta^{LAB}_{^{13}C}$ and $\theta^{LAB}_{^{12}C}$ are the appropriate LAB. angles.

present. This was ascribed to small angle scattering from the defining collimator. The problem was overcome by modifying the focal plane of the spectrometer so that the P.S.D. was held normally to the mean ray. This means that its length in the y plane (in which it now lies) is roughly 5cm. The value of $\delta E/E$ is increased from 0.026 to 0.049 and, at $\theta_{LAB} = 45°$, $\delta E = 291$ keV. It was now found that the particle group occupied about 80% of the counter, or $\delta E \simeq 230$ keV. The calculated value of δE, not allowing for a low energy tail on the beam, is roughly 200 keV. Therefore the beam profile has a low energy tail of about 30 keV. With the counter in its new position, the experiment was successfully executed.

1.2.5. Detection of ^{12}C recoils

Instead of detecting ^{13}C at LAB. angles greater than 44° with the implicit reduction in energy, it is expedient to detect associated ^{12}C recoils. At $\theta_{LAB} = 44°$, ^{13}C and ^{12}C recoils are scattered at the same angle. ^{13}C angles greater than 44° correspond to the ^{12}C recoil angles less than 44°, so by looking at these in the forward direction, the range of ^{13}C angles 44° to 67° may be covered. This can be seen from the vector diagram, Fig.2.5.

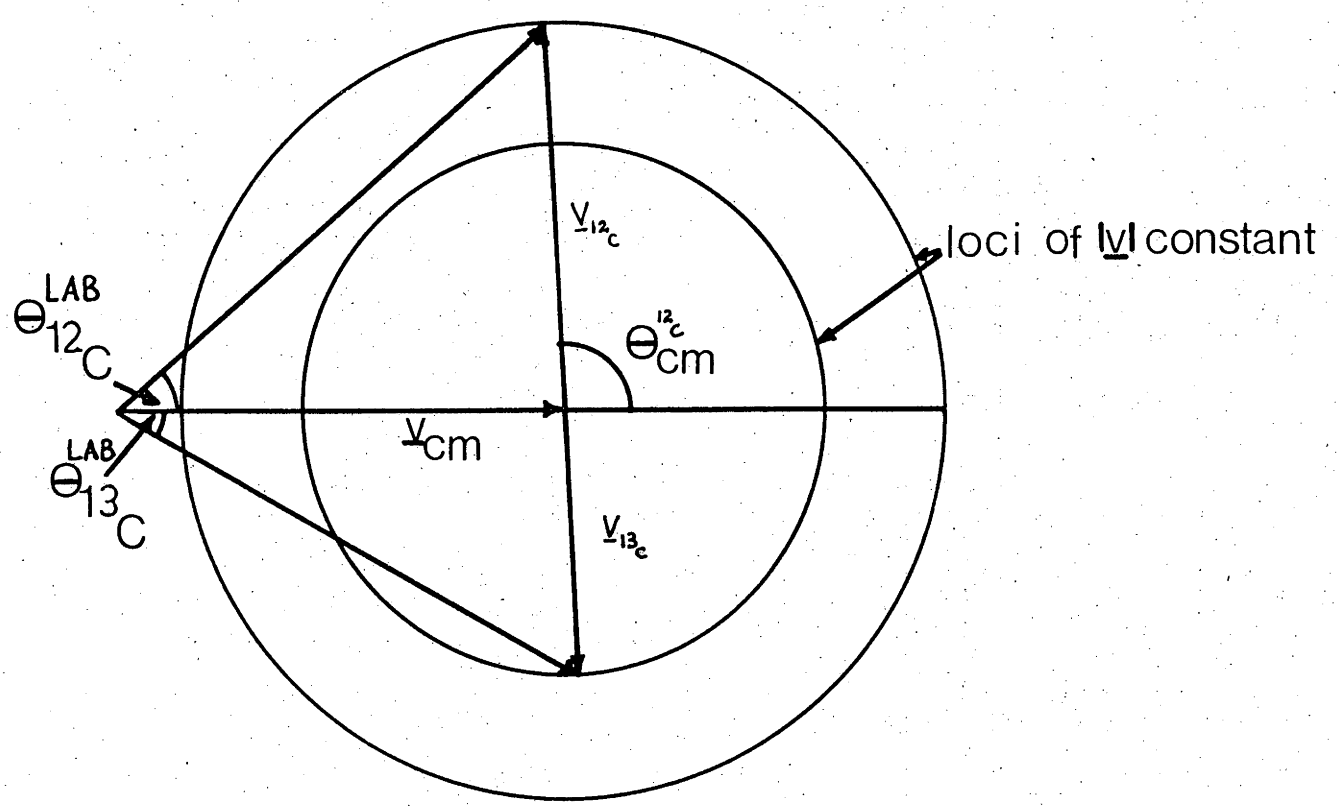

Fig.2.5.

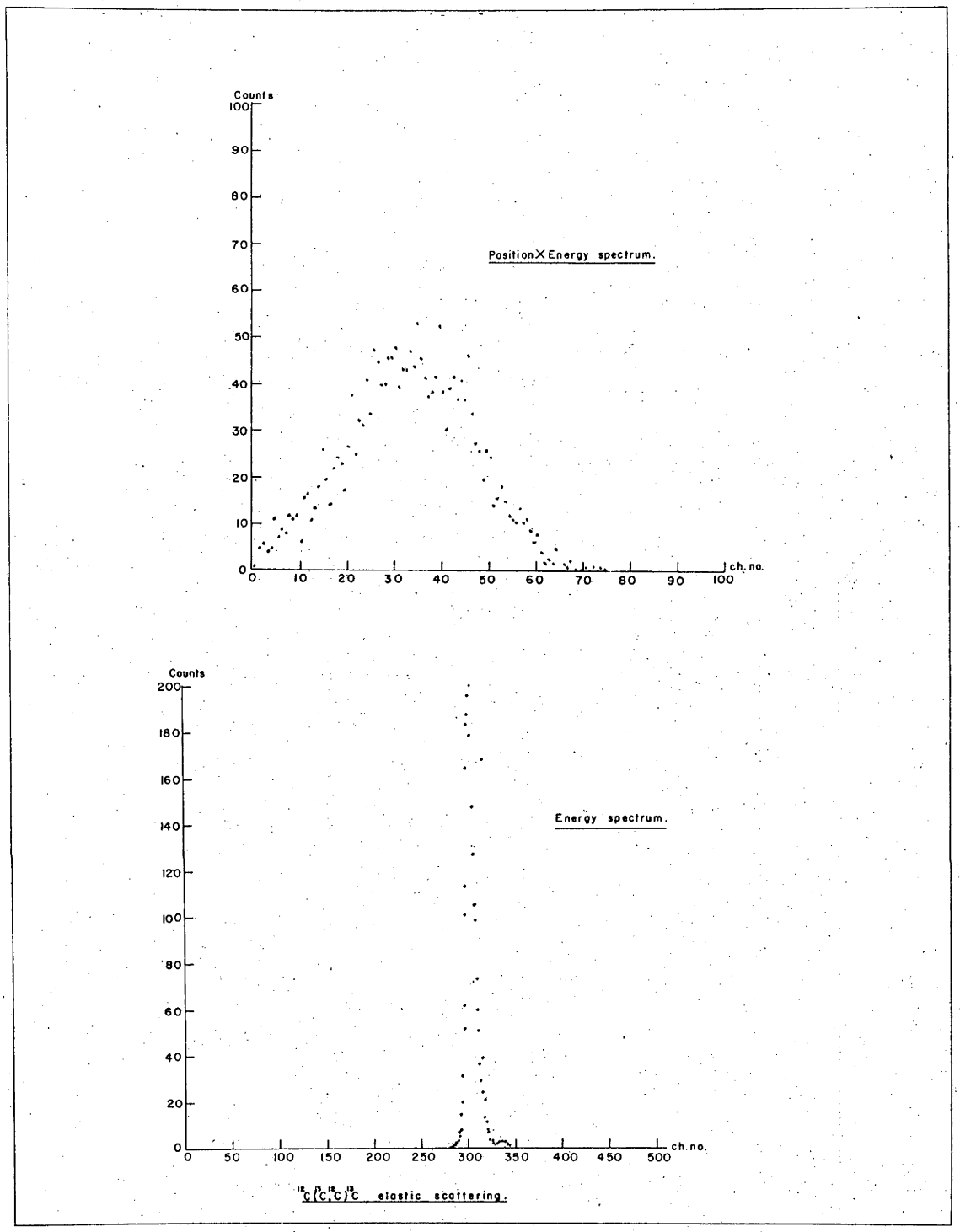

Fig.3.1. An example of a ^{13}C energy spectrum together with its associated position spectrum.

1.3.1. Signal analysis

Signals from the Ortec P.S.D. and the three monitor detectors were processed by the electronic system shown in Fig.2.4. Energy and Energy x Position pulses were recorded in event by event mode by an IBM 1800 computer and stored on a magnetic disc. On line sorting of the data was possible and it could quickly be ascertained whether a group was correctly positioned on the Ortec P.S.D. for example. Dead time was measured by comparing gate enable signals recorded by a scaler with the integrated spectrum. This turned out to be less than 0.5%.

The three monitor signals were routed to three subsets of a Nuclear Data P.H.A. memory. Dead time was checked in the same way as the P.S.D. dead time and found to be negligible.

An example of a P.S.D. position spectrum, together with its associated energy spectrum is shown in Fig.3.1. At angles where the rigidities of ^{12}C and ^{13}C are not sufficiently different, then both peaks appear in the spectra. They were completely resolved in the energy spectrum at all angles. No background was present in the region of the peak, so the yield was determined by simple summation.

1.3.2. Test of angular scale alignment.

An initial test of the accuracy of the spectrometer was carried out by investigating $^{197}Au(^{13}C,^{13}C)^{197}Au$ elastic scattering at E_{LAB} = 12 MeV. It was found that the ratio of the measured cross section to Rutherford was not constant with angle. This is shown by Fig.3.2. It can be seen that the ratio $\sigma(\theta)/\sigma_R(\theta)$ deviates strongly from unity at forward angles. However, by adding half a degree to each angle and recalculating the ratio, the data fall on a straight line within their statistical accuracy. This led to the conclusion that the angular scale of the spectrometer was misaligned by 0.5°.

1.3.3. $\sigma_{exp}(\theta)/\sigma_R(\theta)$

The purpose of the experiment was to measure the quantity:

$$\sigma_{exp}(\theta)/\sigma_R(\theta) = \text{Constant} \times Y_s(\theta)(\varepsilon_j(\theta)Y_m(\theta)\sigma_R(\theta))^{-1} \quad \text{---} \quad 3.1.$$

In actual fact, the yield due to Rutherford scattering is

$$Y_R(\theta) = \varepsilon_j A I t_{^{12}C} \int_{\delta\Omega_s} \sigma_R(\theta) d\Omega \quad \text{----} \quad 3.2.$$

where A is the constant of equation 2.2 and $\delta\Omega_s$ the solid angle subtended by the spectrometer. Therefore equation 3.1 is replaced with

$$\sigma_{exp}(\theta)/\langle\sigma_R(\theta)\rangle = \sigma_{exp}(\theta)/\frac{1}{\delta\Omega_s}\int_{\delta\Omega_s}\sigma_R(\theta)\delta\Omega_s \quad \text{---} \quad 3.3.$$

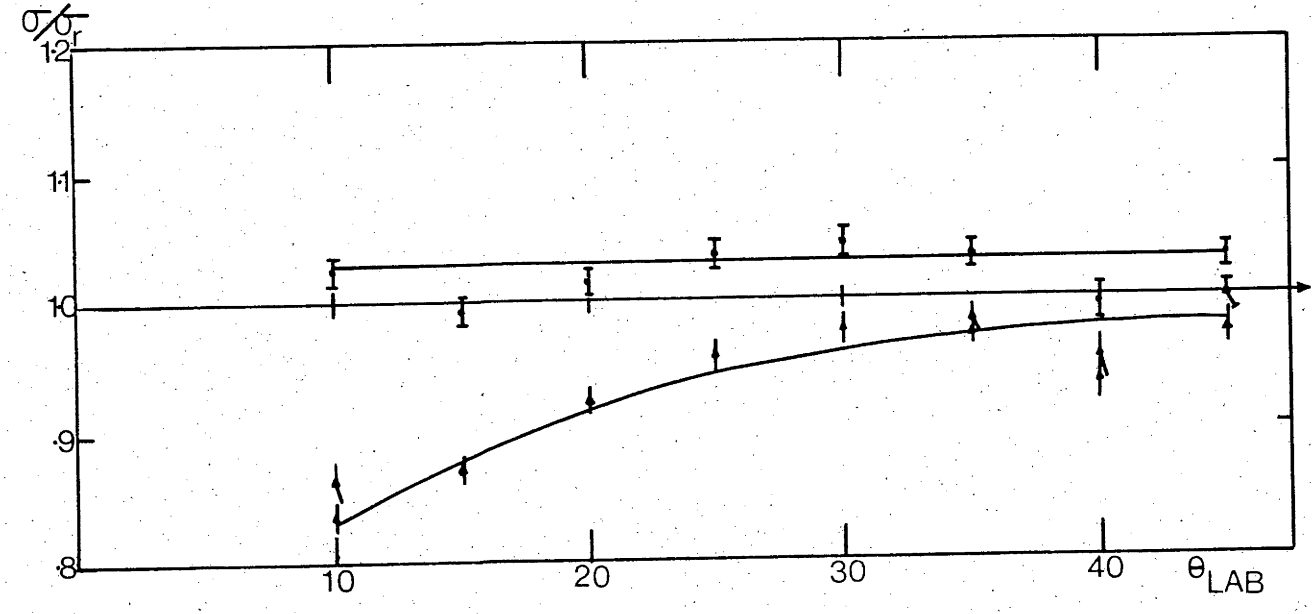

Fig.3.2. $\sigma(\theta)/\sigma_R(\theta)$ for the elastic scattering of ^{13}C on ^{197}Au at E_{LAB} = 12 MeV. The effect of adding 0.5° to each LAB. angle and calculating $\sigma(\theta)/\sigma_R(\theta+0.5)$ is to make the data fall on a straight line. (There is an arbitrary offset from unity for the sake of clarity).

By equation 2.3,

$$\sigma_{exp}(\theta) = \text{Constant} \times Y_s(\theta)(\varepsilon_j(\theta)Y_m)^{-1} \quad --- \quad 3.4.$$

where the constant is now

$$(d\sigma/d\Omega)_m \delta\Omega_m/\delta\Omega_s \quad --- \quad 3.5.$$

At small forward angles, $\sigma_{exp}(\theta) = \sigma_R(\theta)$, so that the constant, equation 3.5, may be determined by measuring $\sigma_{exp}(\theta)$ at small angles.

A FORTRAN program was written to calculate $\int_{\delta\Omega_s} \sigma_R(\theta) d\Omega_s$ in equation 3.3 for any $\delta\Omega_s$ which might be used in the experiment. Only at small forward angles was $<\sigma_R(\theta)>$ significantly different from $\sigma_R(\theta)$.

1.3.4. Evaluation of errors

The error in $\sigma_{exp}(\theta)/<\sigma_R(\theta)>$ is compounded from three different sources. Firstly, there is the error in the monitor yield Y_m. This is given by (p.9)

$$\varepsilon_m = \frac{1}{N}\{N+(0.3n_3)^2\}^{1/2} \quad --- \quad 3.6.$$

Secondly, the error in the spectrometer yield Y_s which is taken to be $Y_s^{1/2}$. The third error is due to uncertainty in the charge state fraction $\varepsilon_j(\theta)$. This is estimated to be $\pm 1\frac{1}{2}\%$. Adding these three errors in quadrature gives:

$$\sigma_{exp}(\theta)/<\sigma_R(\theta)> = \text{Constant } Y_s(\varepsilon_j Y_m <\sigma_R(\theta)>)^{-1}$$

$$\{1 \pm \sqrt{1/Y_m + (0.03n_3)^2/Y_m^2 + 1/Y_s + 0.00023}\} \quad --- \quad 3.7.$$

A realistic case ($n_1 = n_2 = n_3 = 3000$, $Y_s = 5000$) gives an error of $\pm 2\frac{1}{2}\%$. In the actual experiment it was found that 1% statistics could be achieved on Y_s at all angles, and the statistical error on Y_m made negligible.

1.4.1. Experimental results

The data from this experiment are shown in Fig.4.1. The solid line is a fit with the parameter S^2 (explained in section 5) of 0.702, and the broken line with $S^2 = 0.468$. In the upper part of Fig.4.1, the value of χ^2 per degree of freedom is shown as a function of $(SN)^2$.

As seen in Fig.4.1, the minimum value of χ^2 is about 4 which corresponds to an extremely low probability of the data belonging to the parent population given by the fitted lines. (The 30% confidence limits for χ^2 are 1.118 and 0.850). Consequently, it is difficult to estimate the error on the spectroscopic factor by examining χ^2 for different fits. The error quoted was obtained from the best visual fits to the data which

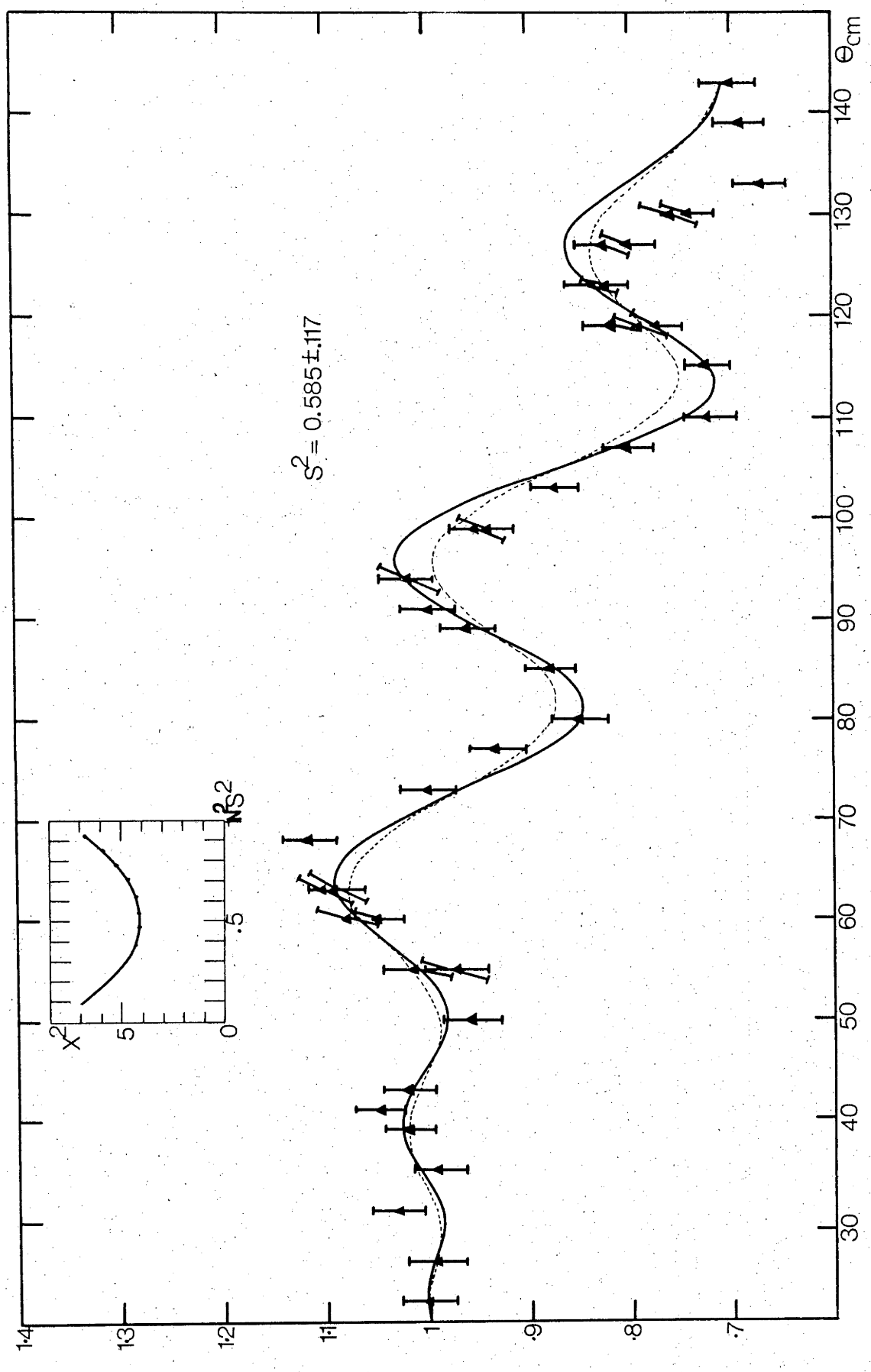

Fig.4.1. Experimental data of $^{12}C(^{13}C,^{12}C)^{13}C$ elastic scattering at E_{LAB} = 12 MeV. The fits to the data are explained in the text.

corresponded to about 5% change from the minimum value of χ^2. A large contribution to χ^2 arises from the data in the 130° region, but even when χ^2 is calculated without these 'bad' data, the minimum value of χ^2 is still outside the 30% confidence limits.

From this it may be concluded that the L.C.N.O. method gives a good semiquantitative description of the experiment, but it is hard to pin down S^2 with good accuracy.

1.5.1. The L.C.N.O. theory

In this section, the theory behind the fits shown in Fig.4.1 will be developed. The model to be used is shown in Fig.5.1.

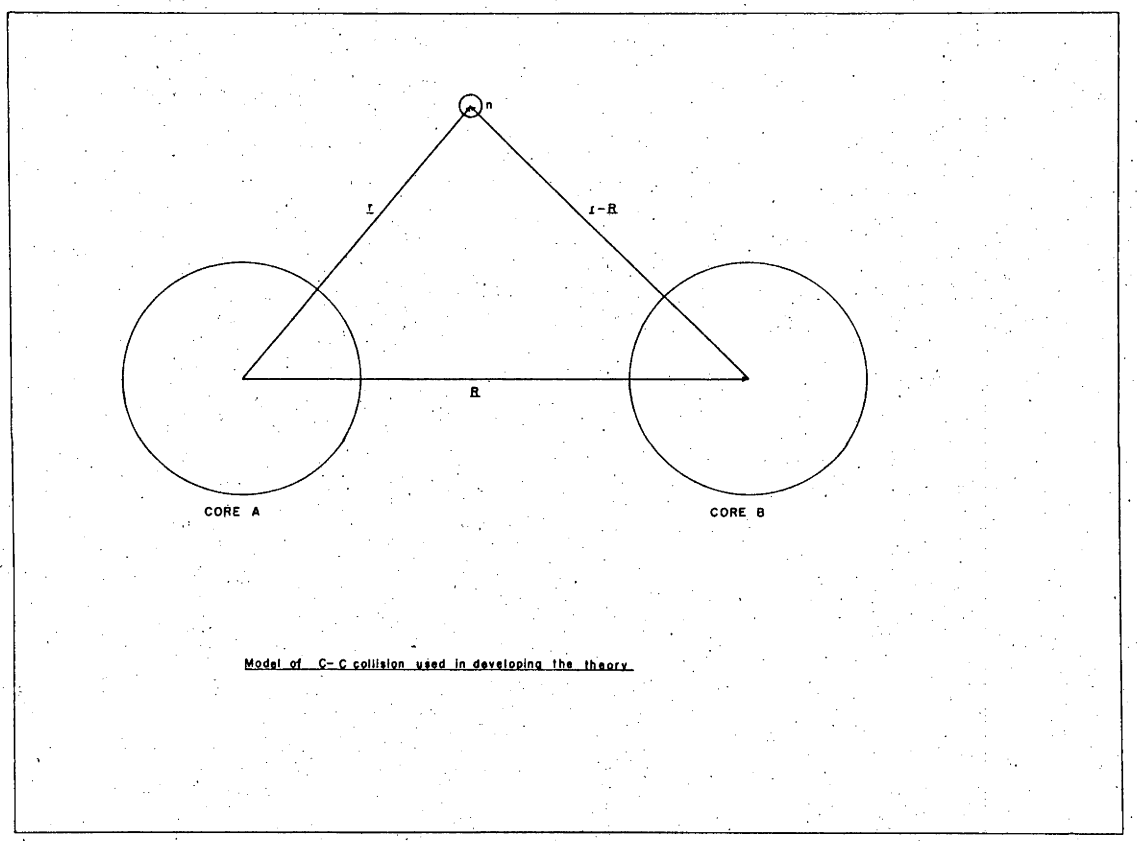

Model of C-C collision used in developing the theory

Fig.5.1. Cores A and B represent inert ^{12}C cores separated by R. The valence neutron n moves in the combined field of the two cores.

There are two stages in developing the theory. Initially the static situation is considered. Cores A and B are at fixed separation R, with the neutron n moving in their combined fields. The energy of this system is calculated. The second stage is to consider relative motion of the cores and the influence of the exchange process on the scattering is evaluated.

1.5.2. Collisional adiabaticity

If the ^{13}C valence neutron receives a violent impulse from the field of the passing ^{12}C core, the collision will be diabatic. On the other hand, if the collision is slow compared with the orbital period of the neutron, it will make many revolutions during the collision and adiabaticity will prevail. For this to be true,

$$t_{coll} >> \tau$$

where t_{coll} is the collision time, and τ is an orbital periodic time. In order to put some numbers into the discussion, a semi-classical derivation of τ will be made. Taking the $p_{1/2}$ neutron to be in an orbit of radius $r_0 A^{1/3}$, the classical angular momentum can be equated to the expectation value of this quantity:

$$(r_0 A^{1/3} m_n v_n)^2 \simeq 2\hbar^2 \quad \text{---} \qquad 5.1.$$

If we take the orbital periodic time to be

$$\tau = 2\pi r_0 A^{1/3}/v_n \quad \text{---} \qquad 5.2.$$

where v_n is the average velocity of the neutron, then $\tau \sim 4.10^{-22}$s.

There are various ways of defining a collision time, but in this case it will be defined as the time during which the exchange interaction has a value greater than J_{max}/e, where J_{max} is the maximum value of the exchange potential. ($J_{max} = J(R_{min})$). For ^{13}C on ^{12}C at E_{LAB} = 12 MeV, the collision time is approximately 24.10^{-22}s.

$$t_{coll}/\tau \sim 6$$

so the adiabatic condition is quite well fulfilled. The collision process is represented in Fig.5.2.

Returning now to the stated approach to the problem, the energy of the system will be evaluated for fixed separation of the cores. The cores play a spectator role in the transfer, they are treated as inert. This is justified from the energy separation of the first excited state in ^{12}C from the ground state (4.43 MeV), since the CM energy in the collision is only 5.76 MeV. (It is essentially the same condition as adiabaticity demands). At infinite separation of ^{13}C and ^{12}C, the wave function of the nucleon is assumed to be a single particle $p_{1/2}$ state. However, at separations where the neutron is influenced by the fields of both cores, a molecular orbital is constructed using unperturbed shell model states as a basis. The probability of the reaction proceeding through channels other than transfer

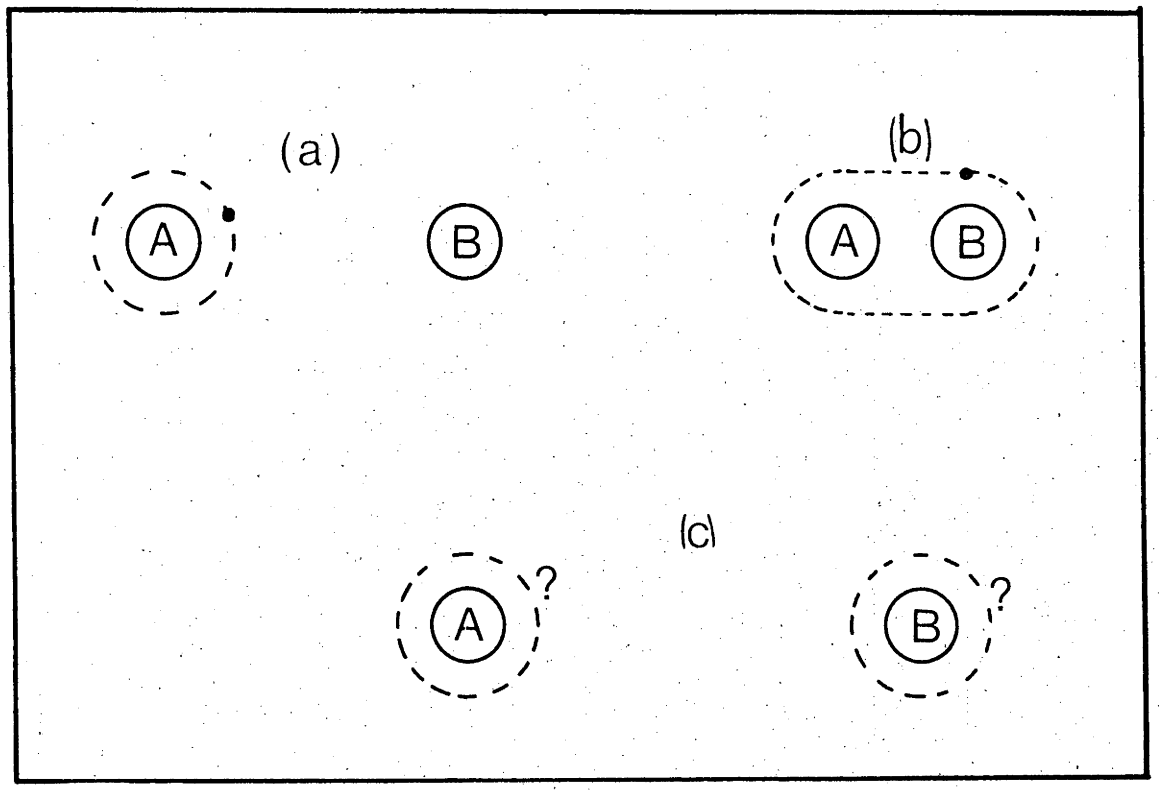

Fig.5.2. Core A with a neutron in a bound state approaches core B (Part a). The two cores collide, and if $t_{coll} >> \tau$, the neutron can make several orbits in the combined field of A and B (Part b). Finally, the two cores separate. There is a probability for the neutron remaining with either core (Part c).

between two $p_{1/2}$ orbitals is small, and the orbital wave function is written

$$\psi_{MOL}^{I,II} = \frac{1}{\sqrt{2}} \{\phi_a(\underline{r}) \pm \phi_b(\underline{r}-\underline{R})\} \quad --- \quad 5.3.$$

where the I,II superscripts refer to the +ve and -ve signs respectively. These are the familiar g and u states of molecular theory, (Gerade, ungerade) ϕ_a is a $p_{1/2}$ wave function centred on core A and similarly for ϕ_b. The energies of the g and u states are degenerate at large intercore separations, but this is removed for small values of R. Then the energy splitting between the g and u states is given by 2J(R) where

$$J(R) = \int \phi_a^*(\underline{r}) V_{cn}(\underline{r}) \phi_b(\underline{r}-\underline{R}) d^3r \quad --- \quad 5.4.$$

with V_{cn} the core-neutron potential. Certain assumptions about the integrand

lead to a simple analytic form for J(R). A single particle neutron wave function may be approximated in its asymptotic region by a spherical hankel function. Using an addition theorem (Bu 66), $\phi_b(\underline{r}-\underline{R})$ may be expanded in functions with $\underline{r}$ as coordinate. (Appendix A). Replacing ϕ_a and ϕ_b with spherical hankel functions, and for $r \leq R$, the exchange energy becomes

$$J(R) = \frac{(SN)^2}{\alpha^3} E_B \exp(-\alpha R)/\alpha R \quad --- \quad 5.5.$$

where $(SN)^2$ is the reduced width for the separation of the neutron from ^{13}C. E_B is the separation energy, and $\alpha^2 = 2m_n E_B/\hbar^2$, where m_n is the reduced mass of the exchanged neutron ($^{12}/_{13}$ 931 MeV/c^2). The other approach is to generate single particle wave functions using a shell model potential and obtain J(R) by numerical integration. This has been done (Bo 71) and J(R) can be quite well approximated by the analytic form at large separations of the cores ($\gtrsim$ 8fm). Since the classical minimum separation is 9 fm., the analytic form equation 5.5 was used in this analysis.

1.5.3. The scattering process

When the scattering process is taken into account, the total wave function is:

$$\Psi(\underline{R}) = \frac{1}{\sqrt{2}} \{\chi_I(\underline{R})\Psi^I_{MOL} + \chi_{II}(\underline{R})\Psi^{II}_{MOL}\} \quad --- \quad 5.6.$$

where $\chi_{I,II}(\underline{R})$ are scattering wave functions which satisfy

$$[\nabla_R^2 + k^2 - 2\mu/\hbar^2\{V_c + V_{AB} \pm J(\underline{R})\}]\chi_{I,II}(\underline{R}) = 0 \quad --- \quad 5.7.$$

$$k^2 = 2\mu E/\hbar^2$$

V_c is the core-core Coulomb potential, $J(\underline{R})$ the exchange potential and μ the reduced mass of the system. V_{AB} is the core-core nuclear potential. In order to solve this equation, specific forms for the potentials have to be taken. The nuclear potential is parameterised with the optical potential. (Eq.1.4.).

The real and imaginary well radii are given by

$$R_{o,i} = r_{o,i}(A_1^{1/3} + A_2^{1/3}) \quad --- \quad 5.8.$$

where o,i stands for real and imaginary respectively. $r_{o,i}$ are the real and imaginary well radii parameters. The parameters used are those for the scattering of ^{12}C on ^{12}C given by von Oertzen (von Oe 75). They are

$V_o = 17.00$	$r_o = 1.35$	$a_o = 0.46$
$W = 2.60$	$r_i = 1.35$	$a_i = 0.30$

(Units are MeV and fm.)

Following the analysis of Voos et.al. (Vo 69), the Coulomb radius R_c is set equal to the radius of the real part of the potential well, R_o.

The Coulomb potential is taken as

$$V_c(R) = \begin{cases} Z_1 Z_2 e^2/R_c\{1.5 - 0.5(R/R_c)^2\} & R \leq R_c \\ Z_1 Z_2 e^2/R & R > R_c \end{cases} \quad \text{---} \quad 5.9.$$

The exchange potential has been discussed and the analytic form due to Buttle and Goldfarb (Bu 66) is used. (See Appendix A). This expression contains Clebch-Gordon coefficients which define the selection rules for the transferred angular momentum ℓ_n.

$$\left.\begin{array}{l} |\ell_1-\ell_2| \leq \ell_n \leq \ell_1+\ell_2 \\ |j_1-j_2| \leq \ell_n \leq j_1+j_2 \\ \ell_1+\ell_2+\ell_n \text{ even} \end{array}\right\} \quad \text{----} \quad 5.10.$$

j_1 and j_2 are the total nuclear spins of projectile and core B+n ($\frac{1}{2},\frac{1}{2}$) and ℓ_i (i = 1,2) are the orbital angular momenta of the bound neutron ($p_{1/2} \rightarrow p_{1/2}$, $\ell_1=\ell_2=1$). This gives $\ell_n = 0$ as the only possible transfer.

If the scattering wave functions χ_j (j=I,II) are decomposed into products of radial and angular parts:

$$\chi_j = \sum_\ell c_\ell u_\ell^j(R)/R \; P_\ell(\cos\theta) \quad \text{---} \quad 5.11.$$

and substituted into the Schrodinger equation 5.7, the radial wave equation emerges, of which u_ℓ^j is a solution. If the nuclear and exchange potentials vanish (V_{AB}=J(R)=0), only the Coulomb potential remains, and the solution of equation 5.7 is (Pr 62, for example)

$$u_\ell^{coul}(R) = C_\ell\{F_\ell(R) + \tan\delta_\ell G_\ell(R)\} \quad \text{---} \quad 5.12.$$

where $F_\ell(R)$ and $G_\ell(R)$ are the regular and irregular Coulomb wave functions. The solutions of the radial equation are computed when the nuclear and exchange potentials are not zero, and then equated to equation 5.12 at asymptotic values of R. (Asymptotic values of R imply $V_{AB}(R) = J(R) = 0$). The phase shifts δ_ℓ^j (j=I,II) are extracted from

$$\tan\delta_\ell^j = \frac{F_\ell(R)u_\ell^j(R+\varepsilon) - u_\ell^j(R)F_\ell(R+\varepsilon)}{u_\ell^j(R)G_\ell(R+\varepsilon) - u_\ell^j(R+\varepsilon)G_\ell(R)} \quad \text{---} \quad 5.13.$$

where $u_\ell^j(R)$ is obtained with potentials $V_{AB}(R) \pm J(R)$ for j = I(+ sign) and j = II(- sign). It is implicit that R has an asymptotic value, and ε is an increment in R.

In Fig.5.2, calculations of the real part of $u_\ell(R)$ are shown for the case where $J(R) = 0$, and for $J(R) \neq 0$. Both $u_\ell(R)$ (optical model wave function) and $u^I_\ell(R)$ (exchange wave function) are normalised at small distances, and the larger amplitude of $u^I_\ell(R)$ is a consequence of an increased potential barrier, $V_{AB}(R) + J(R)$.

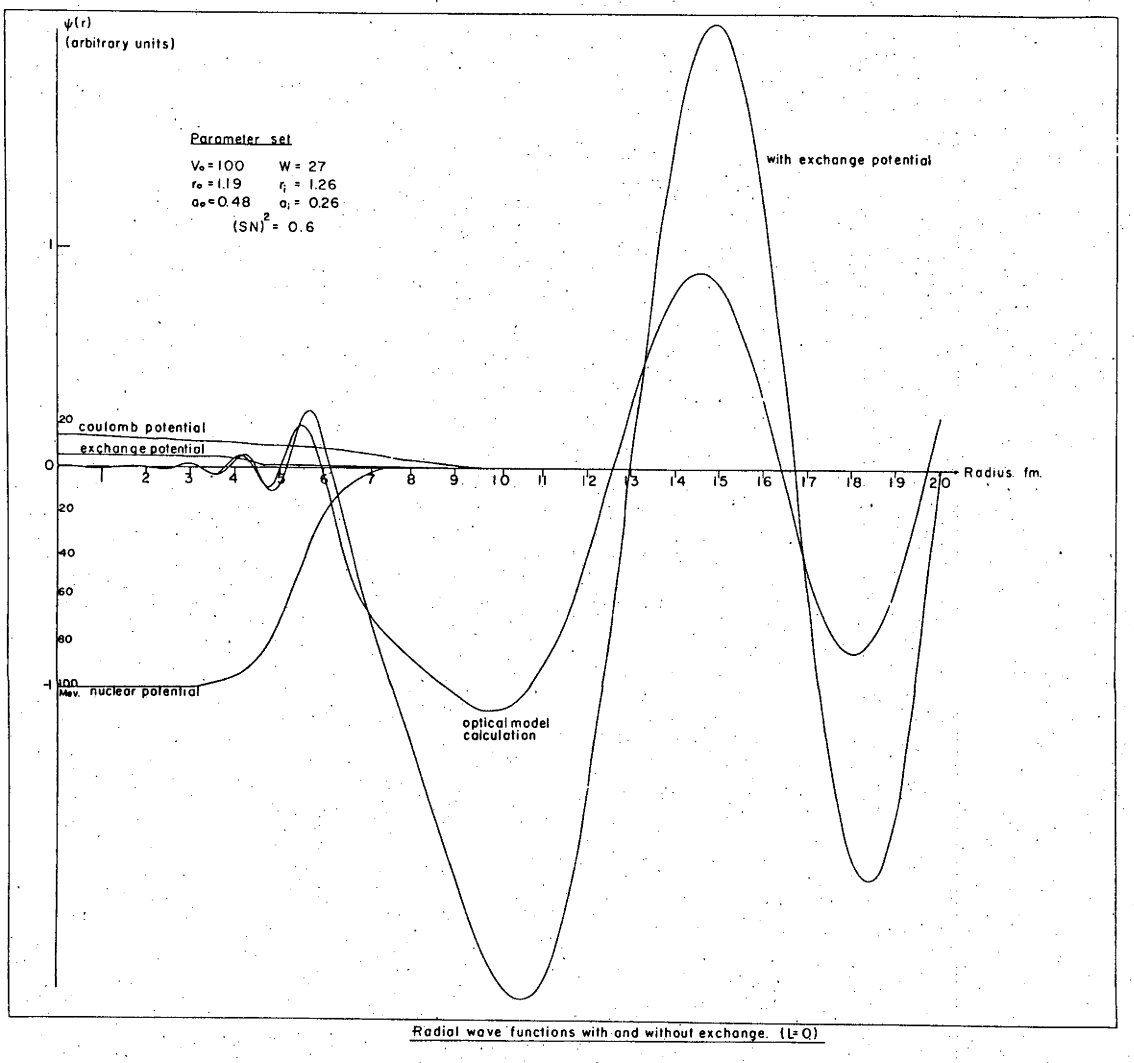

Radial wave functions with and without exchange. (L=0)

Fig.5.2.

The ^{12}C cores are collectively Bosons and, rather than become involved in antisymmeterisation under interchange of any two nucleons, the problem is circumvented by asking for even symmetry under core interchange (von Oe 71, Bo 71).

Since $$\Psi(\underline{R}) = \frac{1}{\sqrt{2}}\{\chi_I(\underline{R})\Psi^I_{MOL} + \chi_{II}(\underline{R})\Psi^{II}_{MOL}\} \quad \text{---} \quad 5.14.$$

and the partial waves into which $\chi_j(\underline{R})$ is decomposed have symmetry $(-1)^\ell$

by virtue of the Legendre Polynomials, then the following association of $X_j^{\ell}(\underline{R})$ and $\Psi_{MOL}^{j}(j=I,II)$ must occur. $(X_j(\underline{R}) = \Sigma_{\ell} X_j^{\ell}(\underline{R}))$.

It is required that $\Psi(-\underline{R}) = \Psi(\underline{R})$, so $X_I^{\ell}(\underline{R})$ must have even symmetry in the first term in brackets of equation 5.14, and odd in the second term. In a self explicit notation, this requires

$$\Psi(\underline{R}) = \frac{1}{\sqrt{2}} \{\Psi_{MOL}^{I} \sum_{\ell even} + \Psi_{MOL}^{II} \sum_{\ell odd}\} \quad --- \quad 5.15.$$

Furthermore, this definite association of ℓ = even partial waves with Ψ_{MOL}^{I} and ℓ = odd with Ψ_{MOL}^{II} means that

(i) even partial waves are incident on a barrier $V_{AB} + J(R)$.

(ii) odd partial waves are incident on a barrier $V_{AB} - J(R)$.

The reflection coefficients, $\eta_{\ell} = \exp - 2Im(\delta_{\ell})$ should therefore be larger for ℓ even than for ℓ odd, and this was found to be so. In keeping with these considerations, the nuclear scattering amplitude splits into two parts

$$f_N(\theta) = -\frac{1}{2ik} \{\sum_{\ell even}(2\ell+1)a_{\ell}^{I}P_{\ell}(\cos\theta) + \sum_{\ell odd}(2\ell+1)a_{\ell}^{II}P_{\ell}(\cos\theta)\} \quad --- \quad 5.16.$$

where $a_{\ell}^{j}(j=I,II)$ are scattering matrix elements for potentials $V_{AB} \pm J(R)$. They may be parameterised in terms of nuclear and Coulomb phase shifts:

$$a_{\ell}^{I,II} = (1-\exp 2i\delta_{\ell}^{I,II})\exp 2i\sigma_{\ell} \quad --- \quad 5.17.$$

where σ_{ℓ} are Coulomb phase shifts given by

$$\sigma_{\ell} = \sigma_0 + \sum_{s=1}^{\ell} \arctan(\eta/s) \quad --- \quad 5.18.$$

and η is the Sommerfeld parameter. The total scattering amplitude is written:

$$f(\theta) = f_c(\theta) + f_N(\theta) \quad --- \quad 5.19.$$

where

$$f_c(\theta) = -Z_1Z_2e^2(4E_{cm}\mathrm{cosec}^2(\theta/2))^{-1} \times \exp\{-2i\eta\ell n \sin(\theta/2) + i\pi\} \quad --- \quad 5.20.$$

Once f_c and f_N have been evaluated, the differential cross section is simply $|f(\theta)|^2$.

The computor code RAMOC was written to calculate the exchange cross section based on the previous discussion. In Fig.5.3, a schematic flow chart displays the basic steps in the calculation. This FORTRAN V program ran on the A.N.U. Univac 1108, and a typical run time was five minutes of C.P.U. time.

Various parameter sets were tried (e.g. for ^{10}B on ^{12}C at E_{LAB} = 18 MeV, Fig.1.1). As expected, the calculation was quite insensitive to different sets of parameters. The set finally used was that for the elastic scattering of ^{12}C on ^{12}C which von Oertzen has used which enables a direct comparison of spectroscopic factors obtained by him and in this experiment (von Oe 75). After fixing the nuclear potential, the only remaining parameter is the reduced width $(SN)^2$ in equation 5.5. N is a normalisation constant which approximates a Spherical Hankel function to the radial bound state neutron eigenfunction at asymptotic distances. This has a value of 0.89. The experimental data are then fitted by varying $(SN)^2$.

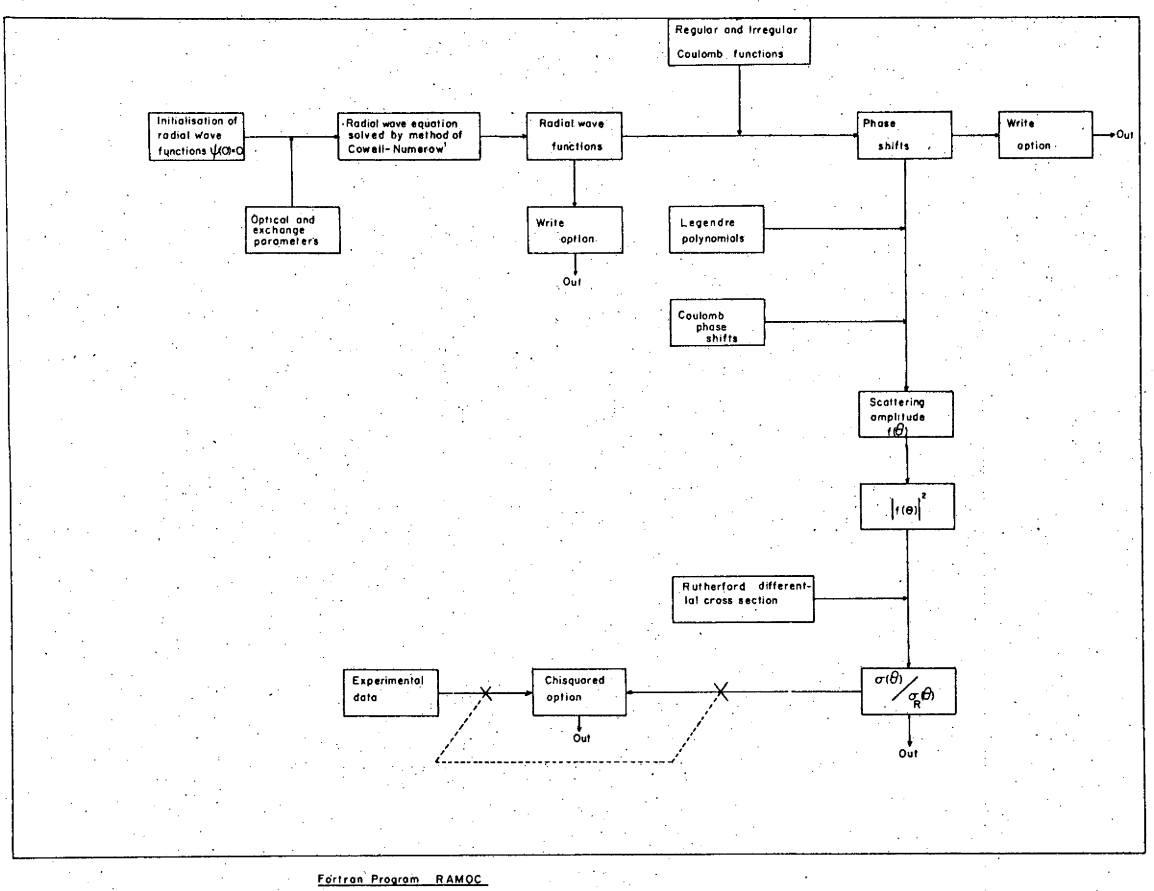

Fig.5.3. Flow chart of the Fortran program RAMOC.

1.5.4. Conclusion

The results of the experiment are shown in Fig.4.1. The data are quite well fitted over most of the angular interval. However, χ^2 changes quite slowly with $(SN)^2$ about the minimum value of χ^2, so the error is quite large - 20%. The value of $S^2 = 0.59 \pm 0.12$ agrees well with

the theoretical value and that obtained from (d,p) experiments. It disagrees with the work of von Oertzen et.al. who carried out the same experiment at 15 and 19 MeV (Table 1.1).

The reduced neutron width of ^{13}C has been satisfactorily determined from analysis of the data. Unfortunately, the error on this number is large and this is because the C.M. energy is low. As explained above χ^2 is a slowly varying function of $(SN)^2$ at this energy. A dilemma is apparent in this type of experiment. The assumptions of the theory (insensitivity to optical parameters, adiabaticity) are better satisfied at low energies ($E_{cm} << E_{coul}$), but the exchange interaction is so weak that the perturbation is small and sensitivity to $(SN)^2$ also small. To reduce the error requires a much greater precision in the data, say $\pm\frac{1}{2}\%$ of each datum. It is easy to reduce the statistical errors to insignificance, but the error in the measured charge state fractions remains. To remeasure these with greater precision would involve an unjustifiably large amount of machine time.

In a quest to improve the fit in the 130° region of the present experiment, a surface absorption term was added to the original optical potential. It is clear that the surface potential is the only relevant region of the nuclear interaction. The surface absorption term was

$$W = -ia_i W_D df(r)/dr \quad --- \quad 5.21$$

where f(r) is the normal Woods-Saxon radial function (e.g. equation 1.4). The effect of varying W_D was studied, and it was found that for any value of W_D the oscillatory structure of the angular distribution was damped and the fit to the data degraded.

CHAPTER 2

Photonuclear Giant Resonances

2.1.1. Introduction

This chapter is an introduction to the subject of photonuclear giant resonances. The remainder of this thesis is an investigation of four medium mass (A≈50) nuclides with excitation energies in the continuum. There are many systematic data available on the giant dipole resonances of nuclides, and the aim of the present study was to add to these and to seek evidence for giant quadrupole resonances. Considerable work has recently been done in the latter field, and giant quadrupole resonances have been observed in many nuclides using (e,e'), (p,p') and particle capture reactions (e.g. Wa 73, Ha 75). As discussed at length in later sections, (α,γ) reactions on targets with zero spin is in principle an especially useful method of observing E2 strength.

In section 2.2.1, the reactions investigated will be detailed together with some general remarks on experimental aspects of particle capture radiative studies.

In the third section, an outline of the theory used in estimating the compound, direct and semi-direct contributions to the (α,γ) cross sections will be given.

2.1.2. The Giant Dipole Resonance

The first evidence of a photonuclear reaction was in the photo-disintegration of deuterium and beryllium (Ch 34, Sz 34). This was in the early days of accelerator technology, and once electron beams of variable energy became available, the whole field of photonuclear work was opened up. Review articles of progress up to 1953 and 1965 are given by Strauch (St 53) and Danos and Fuller (Da 65) respectively. A more recent review is by Spicer (Sp 69).

The G.D.R. is a characteristic resonance of all nuclides which occurs at energies in the continuum. A classical dipole oscillator has an absorption cross section (e.g. Ja 62)

$$\sigma_{abs}(E) = \sigma_o \Gamma^2 E^2 / \{(E^2 - E_o^2)^2 + \Gamma^2 E^2\} \qquad \text{---} \qquad 2.1.$$

that is, a Lorentz line shape. It is a well-known feature of resonances excited by zero rest mass particles that their line shape is of the form

2.1. For this reason, experimental line shapes are sometimes fitted with a Lorentz line, and in this case the parameters σ_0, Γ and E_0 classify the nuclide (σ_0 = peak cross section, Γ = line width, E_0 = resonance energy). In Fig.2.1, the total γ absorption cross section for ^{208}Pb is shown as a function of energy. This has an approximately Lorentzian shape.

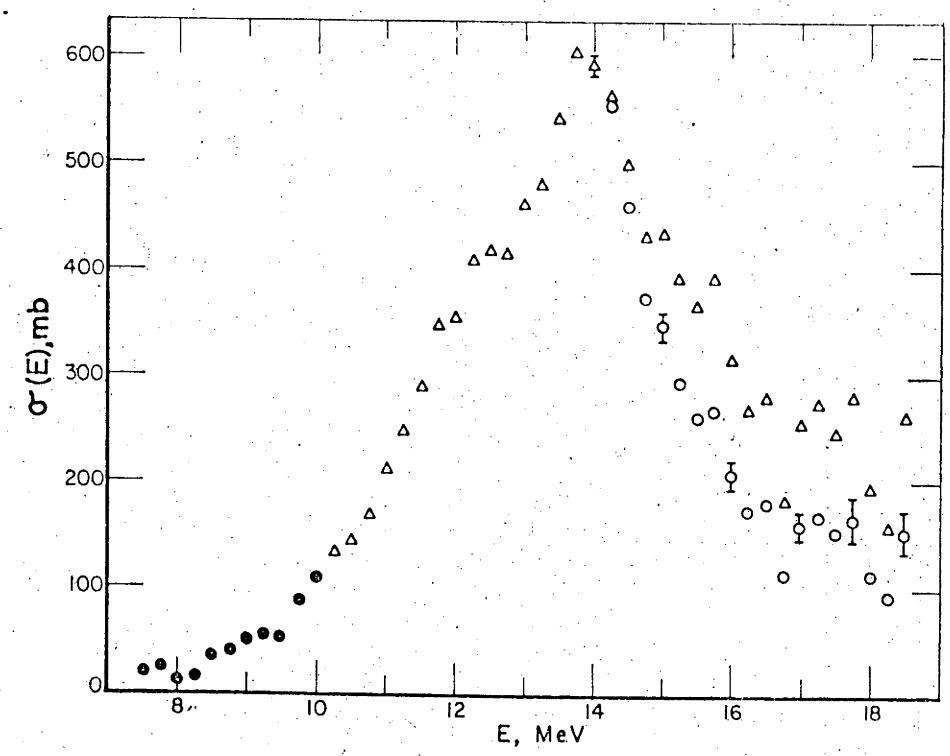

Figure 2.1. (After Danos & Fuller, Da 65). The total gamma absorption cross section of ^{208}Pb. The open circles are the triangles corrected for neutron multiplicity.

The nuclear G.D.R. is usually the dominant feature of the absorption spectrum, and it has been found that

$$\int \sigma_{abs}^{exp}(E)\,dE \qquad \text{---} \qquad 2.2.$$

always exhausts a sizeable fraction, and in some cases is larger than the classical dipole sum rule. The integrated absorption cross section (eq.2.2) normalized to the classical dipole sum (C.D.S.) rule (eq.2.9) varies between about 60% in A$\sim$10 to $\sim$130% in A$\sim$180 nuclides. All available experimental data up to 1972 are collected in the National Bureau of Standards publication, NBS 380.

2.1.3. Classical and Quantum Equivalence

A system of n discrete charges at positions $\underline{r}_i'$ (i=1,n) with respect to some origin has a dipole moment given by

$$\underline{D} = \sum_{i=1}^{n} q_i \underline{r}_i' \qquad \text{---} \qquad 2.3.$$

where q_i is the charge at position $\underline{r}_i'$. In the quantum mechanical formalism, equation 2.3 becomes an operator and an expectation value of the dipole moment is written as

$$\langle \underline{D} \rangle = \langle | \sum_{i=1}^{n} q_i \underline{r}_i | \rangle \qquad \text{---} \qquad 2.4.$$

where the empty Dirac brackets are state amplitudes. Since nuclei have state amplitudes of definite parity, then $\langle \underline{D} \rangle = 0$ in the ground state. However, if a sufficiently strong electromagnetic field interacts with a nucleus, polarization of the nucleons may result and a dipole moment with respect to the centre of gravity exists. Equation 2.3 may be transformed to the centre of gravity (centre of mass = cm) coordinates. Using the same origin as for $\underline{r}_i'$, the c.m. of the nucleus is located by a vector $\underline{R}$, where

$$\underline{R} = \frac{1}{A} \sum_{i=1}^{A} \underline{r}_i' \qquad \text{---} \qquad 2.5.$$

The position of the j^{th} proton with respect to the c.m. is $\underline{r}_j = \underline{r}_j' - \underline{R}$, and substituting for $\underline{r}_j$ in the operator in eq.2.4

$$\underline{D} = e \sum_{i=1}^{Z} (\underline{r}_i' - \underline{R})$$

$$= e[\sum_{i=1}^{Z} (N/A)\underline{r}_i' - \sum_{i=1}^{N} (Z/A)\underline{r}_i'] \qquad \text{---} \qquad 2.6.$$

Since the operator separates into a sum over Z protons and N neutrons, (N/A)e is taken as the effective charge of a proton, and (-Z/A)e the effective charge of the neutron. In a later section the isospin formalism is introduced, and then eq.2.6 can be written as a single summation over A nucleons using proton and neutron projection operators.

A classical expression for absorption of dipole radiation by a single non-relativistic oscillator is given in most text books (e.g. Ja 62). The absorption line shape is of the form eq.2.1.

$$\sigma_{abs}(\omega) = 4 \frac{e^2}{mc} \frac{\omega^2 \Gamma}{(\omega_o^2 - \omega^2)^2 + \omega^2 \Gamma^2} \qquad \text{---} \qquad 2.7.$$

$$\int_0^\infty \sigma_{abs}(\omega)\,d\omega = 2\pi^2 e^2 (mc)^{-1} \qquad \text{---} \qquad 2.8.$$

and for a system of n charges, eq.2.8. is simply summed. It has been seen that the effective charge of a proton is (N/A)e and a neutron (-Z/A)e. Consequently, equation 2.8 becomes

$$\frac{2\pi^2}{mc}\hbar\sum_i e_i^2 = \hbar\frac{2\pi^2}{mc}\{\sum_{i=1}^{Z}[(N/A)e]^2 + \sum_{i=1}^{N}[(-Z/A)e]^2\}$$

$$= \frac{2\pi^2}{mc}\frac{NZ}{A}\hbar e^2$$

$$= 60\ NZ/A \quad \text{MeV.mb.} \qquad \text{---} \qquad 2.9.$$

($\hbar$ has been inserted to change ω to energy, m = nucleon mass). This result is the C.D.S. rule for nuclei and will be used in future sections.

Quantum mechanically, a set of linear energy weighted sum rules (L.E.W.S.R.) may be defined for the λ multipole operator as (Wi 69)

$$S(\lambda) = \sum_B (E_B - E_A) \sum_{M_B} |\langle J_B M_B T_B T_{3B} | \Omega_{\lambda m} | J_A M_A T_A T_{3A} \rangle|^2 \qquad \text{---} \qquad 2.10.$$

where a state with isospin T_A, projection T_{3A}, spin J_A and projection M_A makes a transition to a state B with a similar notation for its quantum numbers. $\Omega_{\lambda m}$ is the m^{th} component of a 2^λ multipole operator. If equation 2.6 is inserted in equation 2.10, then it can be shown that

$$S(1) = 2\pi^2\hbar e^2 NZ (mcA)^{-1}$$

$$= 60\ NZ/A \quad \text{MeV.mb.} \qquad \text{---} \qquad 2.11.$$

There is exact correspondence between the C.D.S. rule and the quantum mechanical L.E.W.S.R.

2.1.4. Deviations from the C.D.S. Rule

The manner in which the rule was derived leads one to expect deviations from it for real nuclei. As mentioned earlier, integrated experimental photoabsorption cross sections normalised to the C.D.S. rule do not lie on a straight line, but show rapid fluctuations with A. There are several reasons for this.

Quantum mechanically, the dipole interaction is represented by the electromagnetic field interacting with the nuclear current, j_N. If the only components of j_N are convective and spin currents, then the C.D.S. rule is obtained. If there is a contribution from the meson current, a modified sum rule results.

This may be understood since the q/m ratio for mesons is much larger than for nucleons and the C.D.S. rule is increased above its expected value. For example, Gell-Mann (Ge-Ma 54) gives the result

$$\int_{\circ}^{\mu} \sigma_{abs}(E)\,dE = 60NZA^{-1}\{1+0.1A^{2}(NZ)^{-1}\} \quad --- \quad 2.12.$$

where μ is the meson production threshold. In fact $\sigma_{abs}(E)$ includes all multipole orders in equation 2.12, but the correction given by Levinger (Le 50) is similar, that is

$$S = 60NZA^{-1}\{1+x\} \quad --- \quad 2.13.$$

where $x \simeq 0.3$.

This value is substantiated by the experimental work of Veyssiere et.al. (Ve 70) who deduced $x = 0.28 \pm 0.1$ in ^{208}Pb and ^{197}Au. Other departures from the value 60NZ/A are caused by:

1) The integration is not taken to high enough energy.

2) Not all decay channels are included from (γ,particle) reactions, i.e. $\int\sigma(\gamma,n) + \sigma(\gamma,p) + \sigma(\gamma,d) + \ldots\, dE \leq \int\sigma_{abs}(E)dE$.

3) All multipole orders are included.

2.1.5. Quadrupole Sum Rule

The L.E.W.S.R. for quadrupole radiation is given by equation 2.10 for $\lambda = 2$ as

$$S(2) = (50e^{2}\hbar^{2}/8\pi m)Z\langle r_{p}^{2}\rangle \quad --- \quad 2.14.$$

where $\langle r_p^2\rangle$ is the mean square charge radius averaged over Z protons. The sum can be split into two terms corresponding to $\Delta T = 0$ and $|\Delta T| = 1$ transitions

$$S(2, \Delta T = 0) = \hbar^{2}50e^{2}Z^{2}(8\pi mA)^{-1}\langle r_{m}^{2}\rangle \quad --- \quad 2.15.$$

$$S(2, |\Delta T| = 1) = \hbar^{2}50e^{2}NZ(8\pi mA)^{-1}\langle r_{m}^{2}\rangle \quad --- \quad 2.16.$$

where the averaged squared radius is over the matter distribution. There is a more familiar $\lambda = 2$ sum rule due to Gell Mann and Telegdi (Ge Ma 53). It is for isoscaler E2 radiation and is weighted by the inverse second power of the energy.

$$\int\sigma(E2)/E^{2}dE = \pi^{2}Z^{2}(137.3mc^{2}A)^{-1}\langle r^{2}\rangle \quad --- \quad 2.17.$$

If $\langle r^2\rangle$ is taken as $^{3}/_{5}R^{2}$ where $R = 1.2A^{1/3}$, then

$$\int\sigma(E2)/E^{2}dE = 0.22Z^{2}A^{-1/3}\mu b.MeV^{-1} \quad --- \quad 2.18.$$

This value is frequently used in comparing the quadrupole strength over a region of excitation.

2.1.6. Isospin

With the early ideas of charge independence and charge symmetry came the representation of a nucleons charge in isospin space. In this space, protons and neutrons are represented by their isovector projection on the three axis. This is $t_3 = \pm \frac{1}{2}$ for a neutron (+) and proton (-). $\underline{t} = (t_1 t_2 t_3)$ has modulus $\frac{1}{2}$. The same formalism as for spin space is adopted. An operator $\underline{\tau}$ is defined by $\underline{t} = \frac{1}{2}\underline{\tau}$ and

$$\tau_3 \chi_p = -\chi_p$$

$$\tau_3 \chi_n = \chi_n$$

(χ_p and χ_n are proton and neutron wave functions respectively).

This is particularly convenient when sums over neutrons and protons are involved. Projection operators are written $\frac{1}{2}(1 \pm \tau_3)$ which obviously satisfy

$$\tfrac{1}{2}(1+\tau_3)\chi_p = 0 \qquad \tfrac{1}{2}(1+\tau_3)\chi_n = \chi_n$$

$$\tfrac{1}{2}(1-\tau_3)\chi_p = \chi_p \qquad \tfrac{1}{2}(1-\tau_3)\chi_n = 0$$

Using these operators, equation 2.6 can be written

$$\underline{D} = \tfrac{1}{2} e \sum_{i=1}^{A} \{(-Z/A)(1+\tau_3^{(i)}) + (N/A)(1-\tau_3^{(i)})\}\underline{r}_i' \quad \text{---} \qquad 2.19.$$

This separates $\underline{D}$ into terms which are linearly dependent on τ_3 and terms independent of τ_3. The former are isovector terms and connect states of different isospin, and the latter isoscalar terms which connect states of the same isospin. In this thesis, the mass range of concern is about A=40 to 60. Prior to 1961, it was thought that the concept of isospin in this region of the periodic table would be of little or no value because of increasing Coulomb energy which is fundamentally opposed to T being a good quantum number. For example, MacDonald (Ma 55,56,58) calculated the ground state isospin mixing of $T^<$ and $T^< + 1$ states in nuclides with $A \lesssim 20$. Based on a Fermi gas model, he deduced a steadily increasing intensity of $T^>$ states in the ground state rising from <1% (A=8) to ~4% (A=20).

However, the experiments of Anderson and Wong (An 61) implied the unexpected result that sharp isobaric analogue states existed in $A \simeq 90$ systems. This prompted a new theoretical approach to isospin mixing in heavy nuclei. Calculations of ground state isospin mixtures were made in the framework of the shell model.

The magnitude of isospin mixing in the ground state of medium mass and heavy nuclei has been explained in terms of quenching. In a simple shell model approach, the neutrons and protons move in identical nuclear one body potentials which are taken as harmonic oscillator potentials. The bound protons experience an electrostatic potential which is (in operator form)

$$V_c^i = \frac{(Z-1)e^2}{2R}(1-\tau_3^{(i)})\{3/2 - 1/2 r_i^2/R^2\} \quad --- \quad 2.20.$$

i.e. that of a uniformly charged sphere of total charge Z-1. This simply modifies the oscillator constant, since both nuclear and Coulomb potentials are quadratic in r. For a neutron, the oscillator constant is

$$\alpha = \frac{(mk)^{1/2}}{\hbar} \quad --- \quad 2.21.$$

and for protons,

$$\alpha' = \alpha(1-\delta) \quad --- \quad 2.22.$$

where

$$\delta = \frac{(Z-1)e^2m}{2\alpha^2\hbar^2R^3} \quad --- \quad 2.23.$$

where R is the nuclear radius.

The single proton wave function is now written using single neutron wave functions as basis states. The proton state with quantum numbers $(n\ell)$ are thus written (to first order in δ)

$$\phi_{n\ell}(\alpha') = \phi_{n\ell}(\alpha) + \beta_{n\ell}\phi_{n+1,\ell}(\alpha) \quad --- \quad 2.24.$$

where

$$\beta_{n\ell} = \frac{1}{4}\sqrt{2n(2n+2\ell+1)}\ \delta$$

The total wave function (which consists of a Slater determinant of single neutron and proton wave functions) is written as

$$\psi = \phi_{T_o} + \gamma\ \phi_{T_o+1} \quad --- \quad 2.25.$$

where $|\gamma|^2$ is the intensity of the T_o+1 mixture. It can be shown that $|\gamma|^2$ is given by

$$|\gamma|^2 = \frac{1}{N-Z+2}\Sigma' N_{n\ell}|\beta_{n\ell}|^2 \quad --- \quad 2.26.$$

$N_{n\ell}$ is the number of protons in the state (n,ℓ), and the primed sum is over all states (n,ℓ) for which the state $(n+1,\ell)$ lies above the neutron Fermi surface. This may be simply understood in terms of the Pauli principle. To form a state T_o+1, the isospin raising operator T_+ has to change a proton in state $(n\ell j)$ to a neutron in the same state. If this state is below the neutron

Fermi level, then the Pauli exclusion principle forbids the new neutron state since it is already occupied. However, if the proton state (nℓj) is above the neutron Fermi surface, then a neutron state (nℓj) is allowed. This is the first type of isospin quenching in nuclei, only a few protons can take part in generating T_o+1 states in the ground state. For the obvious reason it is usually called Pauli quenching. The second type of quenching is called geometric quenching and is due to the term $(N-Z+2)^{-1}$ in equation 2.26. The third form of quenching is due to an isospin dependent potential of the form

$$4\frac{V_1}{A}\,\underline{t}\cdot\underline{T} \qquad \text{---} \qquad 2.27.$$

This acts explicitly on the T_o+1 component of a particle hole excitation, and its effect is to increase the energy splitting of the T_o and T_o+1 states. This effect is called analogue quenching.

Taking these effects into account, calculations by Soper (So 69) gave the intensities of $T^>$ states in the ground state as shown in Table 2.1.

Table 2.1.

Nuclide	$T_>$ intensity %
^{16}O	0.11
^{40}Ca	1.81
^{48}Ca	0.15
^{90}Zr	1.20

His conclusion was that even in heavy nuclides, isospin mixing in the ground state is $\lesssim$1%. It is interesting to notice that in ^{40}Ca where one would expect the geometric quenching to be maximised, the isospin mixing is an order of magnitude larger than in ^{48}Ca.

Some of the work in this thesis is concerned with isospin forbidden reactions. Clearly, if isospin is a good quantum number, then (α,γ) reactions $(T_\alpha=0)$ on T = 0 targets cannot excite T = 1 levels as required for electric dipole radiation. If the ground state T = 1 intensity is <1%, this cannot account for a substantial cross section ($\sim\mu$b.), and the likely alternative is appreciable T = 1 intensity in T = 0 levels in the region of the G.D.R. In all (α,γ) reactions on self conjugate nuclides, dipole radiation to the ground state has been seen, and mixing of $T^<$ and $T^>$ levels in the continuum proposed as the probable reason (e.g. Wa 72, Me 67).

2.1.7. Selection Rules

The radiative width for a dipole transition can be written

$$\Gamma\gamma(1) = 8\pi k \sum_{MM_B} |\langle J_B M_B T_B T_{3B} | \underline{D}_M | J_A M_A T_A T_{3A} \rangle|^2 \quad \text{----} \quad 2.28$$

Writing $\underline{D}_M$ as a combination of isoscalar and isovector terms

$$\underline{D} = \underline{D}^{(0)} + \underline{D}^{(1)} \quad \text{---} \quad 2.29.$$

then the width $\Gamma\gamma(1)$ separates into an isoscalar term

$$\langle |\underline{D}^0| \rangle = (T_A 0 T_{3A} 0 | T_B T_{3B}) \langle J_B M_B T_B || \underline{D}^0 || J_A M_A T_A \rangle \quad \text{---} \quad 2.30$$

where the empty Dirac brackets have the quantum numbers of eq.2.28. The geometrical dependence on the projection of T_A and T_B on the 3 axis has been separated using the Wigner-Eckart theorem.

From eq.2.19

$$\underline{D}^{(0)} = \tfrac{1}{2} e \sum_{i=1}^{A} (N-Z)\ A^{-1} \underline{r}_i'$$

$$= \tfrac{1}{2} e (N-Z) \underline{R} \quad \text{----} \quad 2.31.$$

Thus, eq.2.30 is a matrix element of an external operator taken between states orthogonal in their internal coordinates, and consequently vanishes. On the other hand, doing the same thing for the isovector matrix element leads to a Clebsch Gordan coefficient

$$(T_A 1 T_{3A} 0 | T_B T_{3B}) \quad \text{---} \quad 2.32.$$

Therefore isovector transitions proceed by $\Delta T = 0, \pm 1 \quad \Delta T_3 = 0$ selection rules. In isovector $\Delta T = 0$ transitions,

$$(T_A 1 T_{3A} 0 | T_B T_{3B})$$

$$= (T_A 1 T_{3A} 0 | T_A T_{3A}) \propto T_{3A} \quad \text{---} \quad 2.33.$$

and so in self conjugate nuclides where $T_{3A} = 0$, only $\Delta T = \pm 1$ isovector electric dipole transitions are allowed.

2.1.8. Proton and Alpha Particle Capture.

The most successful approach to the G.D.R. has been made using one particle - one hole basis states (ph) (e.g. Br 59, Gi 64). The particle and hole are correlated strongly in angle so that their angular momenta couple to produce a 1^- state. Absorption of dipole radiation occurs when a single proton is lifted above the Fermi level leaving a hole below. This proton may

then escape taking with it the excitation energy of the nucleus, or the 1p1h state may dissolve into more complicated np-nh states. The widths for these two processes are Γ and 2W respectively, and the fraction of protons which escape directly is $\Gamma/(\Gamma+2W)$. It has been found that (p,γ) reactions often proceed by a direct mechanism. An incident proton is captured from a continuum scattering state to a bound state with emission of dipole radiation. The width for this process is $\sim$few MeV and gives rise to gross structure in a (p,γ) excitation function. Alternatively, the incident proton may form a so-called doorway state. A proton from the target is raised above the Fermi level, so that a 2p-1h state results. This can proceed through hallway states of 3p-2h, 4p-3h, etc. states into the compound nucleus. It is these hallway states which have widths intermediate between direct reaction widths and compound nucleus widths, i.e. $\Gamma_D > \Gamma_{HW} > \Gamma_{CN}$. For example, in Fig.2.3 the $^{39}K(p,\gamma_0)^{40}Ca$ excitation function is shown over the excitation energy range 15-25 MeV. Gross, intermediate and fine structure are present which suggests both direct and compound nuclear processes.

In contrast to this, it has been found that alpha particle radiative capture is mostly a compound process. In Fig.2.2, data from the $^{40}Ar(\alpha,\gamma)^{44}Ca$ reaction are shown. These data represent averages over any finer structure present as will be explained more fully in Chapter 4.

Fluctuation analysis usually shows no correlation between different exit channels (e.g. γ_0 and γ_1) in agreement with the postulates of Ericson's fluctuation theory. Some data can be well fitted by Hauser-Fesbach theory, but in subsequent sections the possibility of a direct or semi-direct alpha capture mechanism will be investigated.

2.1.9. Splitting of the G.D.R.

The photonuclear G.D.R. has been investigated in the framework of 1p-1h excitations (Sect.2.1.8). Fallieros et.al. (Fa 65) showed that, by coupling 1p-1h pairs to 2p-2h excitations, the G.D.R. was split into two components of isospin $T^< = T_{gs}$ and $T^> = T_{gs}+1$ where T_{gs} is the ground state isospin quantum number ($T_{gs}>0$). The energy splitting between the two components is given by

$$\Delta E = U(T_{gs}+1)/T_{gs} \qquad \text{---} \qquad 2.34.$$

where U is a symmetry energy equal to the difference in the nuclear interaction of a neutron and a proton in the same state with the nucleus (Br 71, Fa 65).

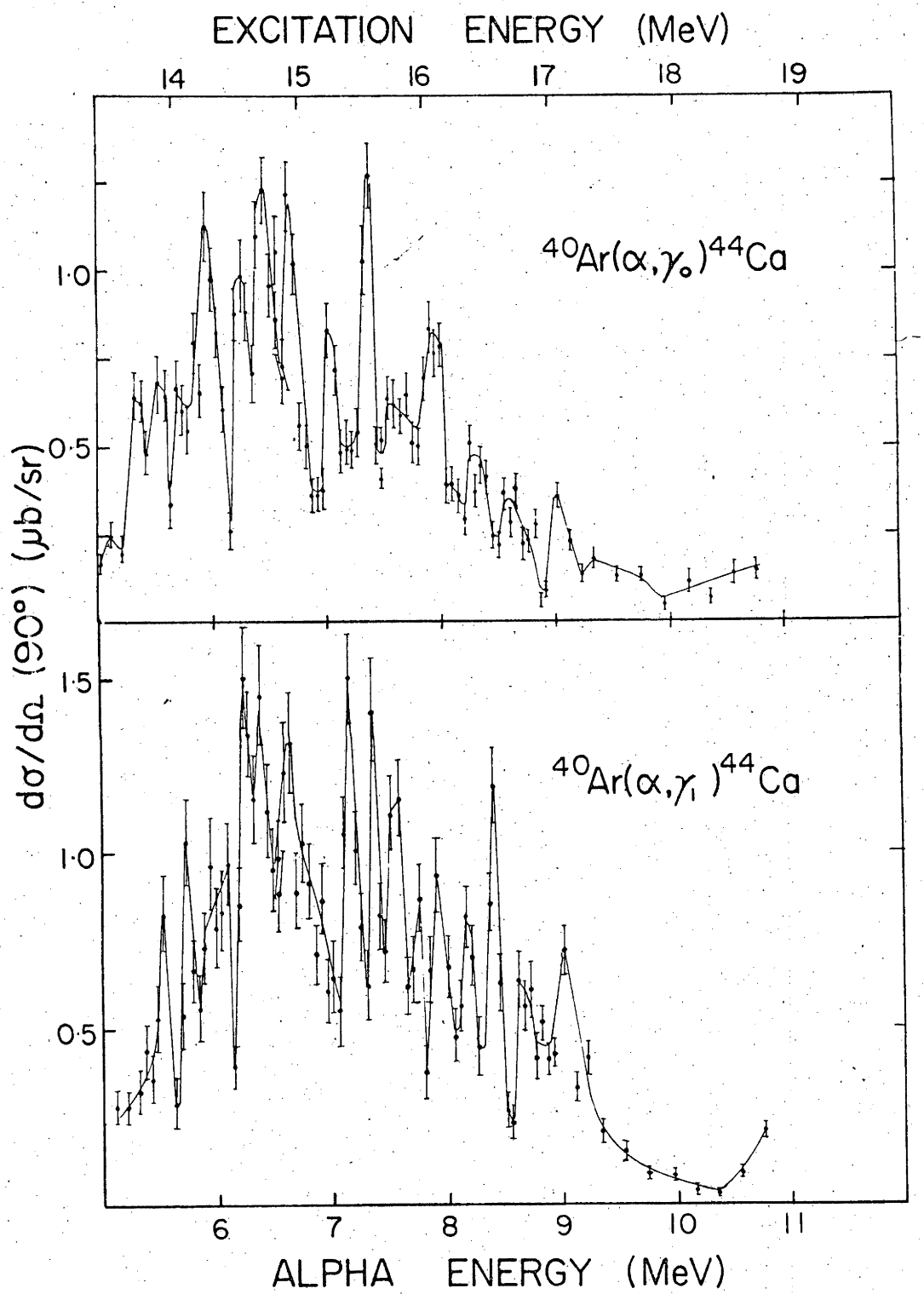

Fig.2.2. The absolute differential cross sections for the $^{40}Ar(\alpha,\gamma_0)^{44}Ca$ and $^{40}Ar(\alpha,\gamma_1)^{44}Ca$ reactions measured at 90° to the beam direction as a function of bombarding energy. (Ref. Fo 74).

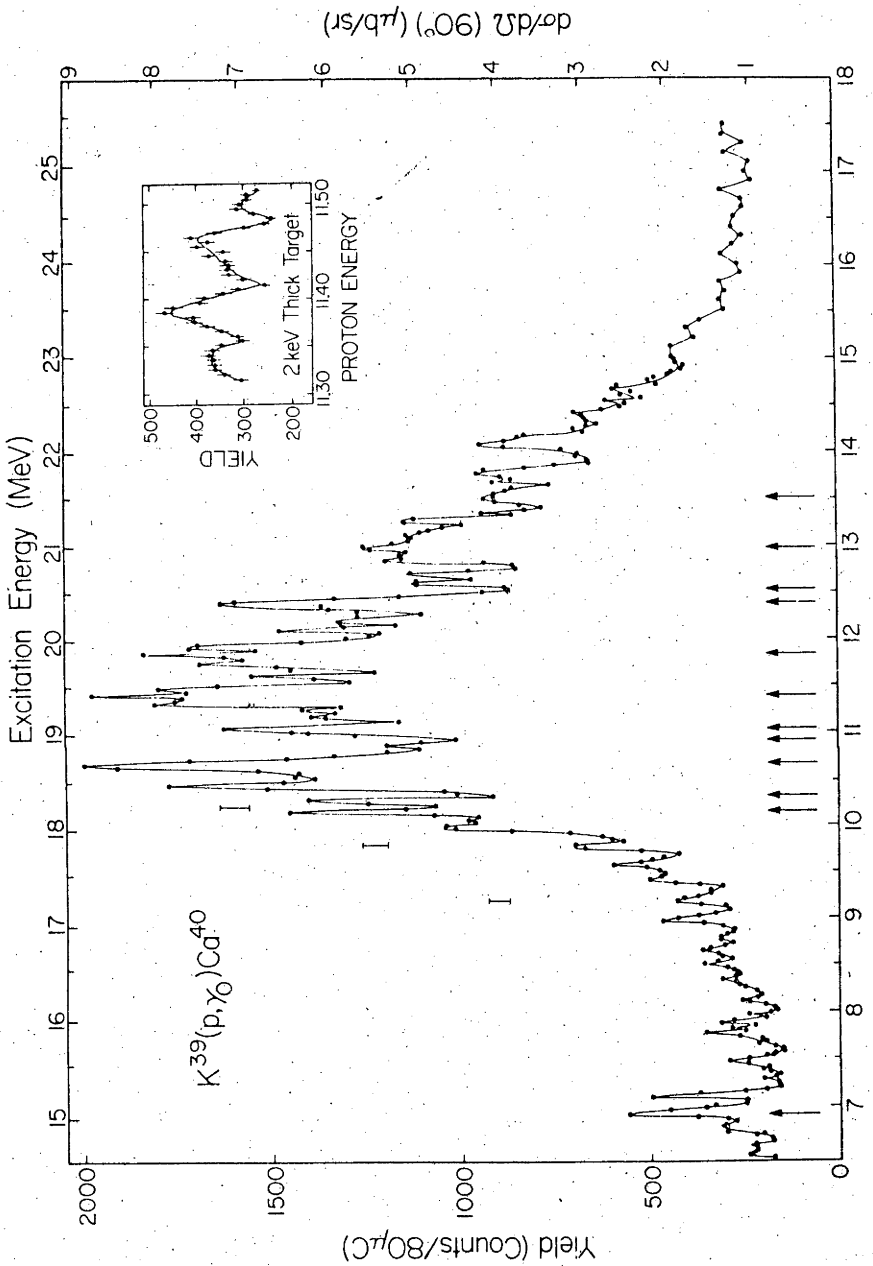

FIG. 2. Excitation function (mostly in 20-keV steps) of the γ_0 yield at 90° over the GDR regions of ^{40}Ca. Complete angular distributions were taken at energies indicated by arrows. The insert shows the portion from 11.30 to 11.56 MeV taken in 2-keV steps.

Fig. 2.3.
Ref. Di 73.

The ratio of the two widths is

$$\Gamma_{T>}/\Gamma_{T<} = (1/T_{gs})(E_{T>}/E_{T<})^3 \quad --- \quad 2.35.$$

Since this proposal was first made, many experiments have verified that splitting of the G.D.R. does occur. Some of the evidence for this will briefly be discussed in following sections.

2.1.10. The Hydrodynamic Model

The hydrodynamic model provides justification for the $A^{-1/3}$ energy dependence of the G.D.R. and G.Q.R. which is borne out by systematics.

Microscopic densities ($\rho(\underline{r},t)$) are ascribed to neutron and proton fluids which are continuous inside a rigid, non-permeable spherical boundary. Under the influence of an electromagnetic field, the proton and neutron fluids separate. A restoring force acts through the potential

$$V = \chi[\rho_n(\underline{r},t) - \rho_p(\underline{r},t)]^2/\rho_o \quad --- \quad 2.36.$$

where $\rho_o = \rho_n(\underline{r},t) + \rho_p(\underline{r},t)$, and a constant χ' is related to the symmetry energy of the semi-empirical mass formula by (Da 68)

$$V_s = \chi'(N-Z)^2/A \quad --- \quad 2.37.$$

and $\chi = \chi'/m$ (m = nucleon mass)

A frictional force is also included which is proportional to the relative velocity of the two fluids. Using the formulation of classical mechanics (e.g. Ei 70), the problem is one of calculating the normal modes of density vibration of the fluid. An harmonic time dependence is assumed for the proton fluid, viz.

$$\rho_p(\underline{r},t) = \rho(o)\{1+\eta(\underline{r})\exp(-i\omega t)\} \quad --- \quad 2.38.$$

($\rho(o)$ = equilibrium density)

then it can be shown that $\eta(\underline{r})$ satisfies the Helmholtz equation

$$\nabla^2\eta(\underline{r}) + k^2\eta(\underline{r}) = 0 \quad --- \quad 2.39.$$

where $k^2 = \omega^2\{1+i\Gamma/\omega\}A^2(8\chi NZ)^{-1}$ and the boundary condition of no radial flux is

$$\nabla\eta(\underline{r})\big|_{R_o} = 0 \quad --- \quad 2.40.$$

(R_o = nuclear radius)

Equation 2.39 has the solutions

$$j_\ell(kr)Y_{\ell m}(\hat{\underline{r}})$$

(A product of an ℓ^{th} order spherical Bessel function and spherical harmonic).

Solving eq.2.39 with the boundary condition (eq.2.40) leads to

$$kR_o = 2.0815 \qquad \ell = 1$$
$$kR_o = 3.3421 \qquad \ell = 2$$

Since $E_\ell = \hbar\omega_\ell$, the respective energies of the G.D.R. and G.Q.R. are

$$\left.\begin{aligned} E_1 &\simeq 70A^{-1/3} \\ E_2 &\simeq 112A^{-1/3} \end{aligned}\right\} \qquad \text{---} \qquad 2.41.$$

The exact values of the coefficients depend on the value of the radius parameter r_o ($R_o = r_o A^{1/3}$) and X. The normal dipole mode exhausts about 84% of the C.D.S. rule and so this is identified with the G.D.R. Systematics of medium and heavy nuclides show that the resonance energy of the G.D.R. is given by $\sim 77A^{-1/3}$ which is in good agreement with the hydrodynamic model. Modifications to the model and quantisation of the fluctuation eigenmodes are discussed by Bertsch (Be 75) and Eisenberg and Greiner (Ei 70).

Returning for a moment to the question of isospin mixing in the ground state, the admixture of $(0^+,0)$ and $(0^+,1)$ (J^π,T) states has been calculated using the hydrodynamical model. Bohr, Damgård and Mottleson have evaluated the admixed intensity as

$$P(T=1) = 5.55.10^{-7}Z^{8/3}$$
(e.g. ^{40}Ca, $\simeq 0.2\%$, ^{208}Pb, $\simeq 7\%$)

However, the three quenching effects discussed previously will reduce P.

So far the treatment has been for spherical nuclei. In the case of a nucleus with intrinsic prolate deformation, three fundamental modes of vibration are possible, one parallel to the major axis, and two degenerate vibrations parallel to the minor axes. The relationship between the energies of the different modes is given by (Da 58)

$$E_a/E_b = 0.911(a/b) + 0.089 \qquad \text{---} \qquad 2.42.$$

where a and b are semi major and semi minor axes respectively. Using this expression, good agreement (e.g. Fu 58) was found between quadrupole moments measured by Coulomb excitation and determination of Q_o from the expression

$$Q_o = \frac{2}{5}ZR_o^2A^{2/3}(d^2-1)/d^{2/3} \qquad \text{---} \qquad 2.43.$$

where $d = a/b$ (see Fig.2.4.).

Degeneracy of vibrations parallel to the minor axes is removed if quadrupole surface vibrations are introduced (e.g. Da 68).

Nucleus	E_a, MeV	σ_a^0, mb	Γ_a, MeV	E_b, MeV	σ_b^0, mb	Γ_b, MeV	$\sigma^0\Gamma_b/\sigma_a^0\Gamma_a$	Γ_b/Γ_a	Q_0, barns $R_0 = 1.2$ fm	Q_0, barns Coul. Ex.
V^{51}	17.5	41	3.60	20.25	46	6.5	2.03	1.8	0.61	0.64
Mn^{55}	16.5	45.9	3.0	19.5	62.7	4.5	2.05	1.5	0.81	1.1
	16.8	70	2.7	19.8	64	4.0	1.35	1.5	0.78 ± 0.1	1.1
Co^{59}	16.5	78	2.0	19.0	78	4.0	2.0	2.0	0.76 ± 0.1	1.1
	16.5	40	3.75	19.25	43.4	7.0	2.02	1.86	0.84	1.1
Rh^{103}	14.5	104	3.4	17.0	164	4.5	2.08	1.3	1.8	2.3
	14.25	150	3.0	17.5	240	3.8	2.03	1.3	2.7 ± 0.3	2.3
Ag^{107}	13.5	—	2.5	16.0	—	4.5	—	1.8	1.9 ± 0.7	1.8
In^{115}	14.0	166	3.0	16.25	240	3.8	1.8	1.3	2.3 ± 0.4	2.0
Tb^{159}	12.5	258	2.4	16.3	310	4.0	2.0	1.7	6.8 ± 0.6	6.9
	12.5	267	3.4	16.4	317	3.4	1.19	1.0	6.6 ± 0.6	6.9
Ho^{165}	12.2	318	2.3	16.0	328	4.5	2.0	2.0	7.7 ± 0.6	7.8
	12.1	200	2.65	15.75	249	4.4	2.07	1.66	7.4 ± 0.9	7.8
Er	12.2	318	2.3	16.0	328	4.5	2.0	2.0	7.7 ± 0.6	
Ta^{181}	12.5	308	2.3	15.5	348	4.4	2.15	1.9	6.9 ± 0.3	6.8
	12.5	317	2.3	15.5	444	3.6	2.19	1.6	6.9 ± 1.6	6.8
	12.6	500	2.0	15.3	450	4.0	1.8	2.0	6.1	6.8
	12.75	198	3.0	15.5	224	5.0	1.9	1.7	6.71 ± 0.74	6.8
	12.4	350	2.4	15.5	400	3.8	1.8	1.6	7.1 ± 0.8	6.8
U^{235}	10.85	—	2.5	14.1	—	4.00	—	1.6	12.8 ± 1.3	~ 10

Fig.2.4. Some parameters of the split G.D.R. in deformed nuclei. Comparison of quadrupole moments obtained from eq.2.43 and from Coulomb excitation is made in the last two columns.

If nuclei with intrinsic prolate deformation are randomly oriented then the measured cross section will be

$$\langle\sigma(E)\rangle = \frac{1}{3}\sigma_a(E) + \frac{2}{3}\sigma_b(E) \quad --- \quad 2.44.$$

due to the twofold degeneracy mentioned above. The maximum values of the cross sections are related to the widths by:

$$\sigma_a(max)/\sigma_b(max) = \Gamma_b/2\Gamma_a \quad --- \quad 2.45.$$

2.2.1. Experimental Aspects

A convenient method for exciting the nuclear G.D.R. is provided by (particle,γ) reactions with large positive Q values (several MeV). A further advantage of this method is the good energy resolution of particle beams provided by Tandem Van de Graaff generators.

This thesis concerns studies of (α,γ) reactions on nuclides in the mass range 40 to 66. All are even-even, so that population of excited states occurs in the $m_z = 0$ substate. The z direction is defined by the beam axis. If isospin is a good quantum number, then alpha capture to excited states should proceed via isospin coupling rules; that is, $T_{ex} = T_{gs}$ where the subscripts ex and gs refer to excited and ground states respectively. Emission of λ=1 radiation is restricted by $\Delta T = 0,\pm1$ isospin selection rules, and in self conjugate nuclides, $|\Delta T| = 1$ transitions only are allowed. Consequently, excitation of the G.D.R. in self conjugate nuclides is forbidden. Many reactions of this type have been studied (e.g. Pe 74) and in all cases decay by dipole radiation observed from regions where the G.D.R. is located. This has been explained in terms of the high level density of medium mass nuclides around 15 MeV where $\Gamma/D>>1$. It is assumed that an appreciable $T^>$ component (T=1) is mixed with T=0 states at this excitation. To provide further data on self conjugate nuclides, the $^{40}Ca(\alpha,\gamma)^{44}Ti$ reaction was investigated with reasonable resolution ($\rho\approx 10\Gamma$, ρ = resolution, Γ = mean level width) over the energy range of the G.D.R.

In non self conjugate nuclides, $\Delta T = 0$ isovector E1 radiation is allowed. The $^{54}Fe(\alpha,\gamma)^{58}Ni$ reaction was investigated over the G.D.R. energy region which has been located in $^{58}Ni(\gamma,n)^{57}Ni$ (Mi 68) and $^{58}Ni(\gamma,p)^{57}Co$ (Ca 59) measurements. Two other non self conjugate nuclides in the same region of the periodic table were investigated by the (α,γ) reaction. They were $^{60}Ni(\alpha,\gamma)^{64}Zn$ and $^{62}Ni(\alpha,\gamma)^{66}Zn$. Since excitation of $T = T^<$ states by alpha capture is allowed and this state can then decay by E1 emission, it might be expected that dipole intensity should be greater than for N = Z nuclides.

However, the situation is a little more complicated than this. Decay of the compound nucleus into a channel c depends on the factor $T_c/\sum_d T_d$, where T_d is the transmission coefficient for channel d. (This is only roughly correct as will be seen in the next section). As the excitation energy increases, more and more channels become available for decay, and so the demonimator, $\sum_d T_d$, makes the probability for decay in one particular channel quite small. This argument has frequently been used to explain the small (α,γ) cross section in the region of the G.D.R. (e.g. Fo 74).

Analyses of the fine structure in excitation functions have been based on the fluctuation theory of Ericson which will be briefly described.

This theory was applied to the narrow overlapping resonances which characterize the compound nucleus. At energies where individual levels are separated from their neighbours by more than the level width, $(\Gamma/D<<1)$, each resonance can be described by a Breit-Wigner amplitude

$$f^j_{\alpha\beta} = A^j_{\alpha\beta}/(E-E_j+i\Gamma_j/2) \qquad \text{---} \qquad 2.46.$$

α and β are entrance and exit channels respectively, j labels the level. At energies where $\Gamma/D>>1$, and if no direct reaction component is present, the cross section is given by $|f|^2$, where f is a coherent sum of terms like eq.2.46.

Thus

$$\begin{aligned}\sigma &= |f|^2 \\ &= |\textstyle\sum_j f^j_{\alpha\beta}|^2 \\ &= \textstyle\sum_{j=1}^{N} |f^j_{\alpha\beta}|^2 + \sum_{j\neq j'} f^{j*}_{\alpha\beta} f^{j'}_{\alpha\beta} \qquad \text{---} \qquad 2.47.\end{aligned}$$

If the $f^j_{\alpha\beta}$ are random both in magnitude and sign, then the second term will average out as zero. However, it will have a standard deviation about zero. For example, if each $f^j_{\alpha\beta} = \pm(\sigma'/N)^{\frac{1}{2}}$, then we obtain

$$\sigma = \sigma' \pm \sqrt{N(N-1)}\sigma'/N$$

$$\lim_{N\to\infty} \sigma = \sigma' \pm \sigma' \qquad \text{---} \qquad 2.48.$$

so that σ can fluctuate within the range o to several times σ'. It is the interference between the different amplitudes which gives rise to the fluctuating cross section. Specific forms for the correlation between the fluctuations in an excitation function have been derived, and will be applied to the data in Chapter 4. As mentioned before, many (α,γ) reactions have been

analysed in terms of the fluctuation theory and compound nuclear reaction mechanisms deduced as a result. This contrasts with (p,γ) work which has been shown to be dominated by direct and semi direct processes. A few exceptions have been noted. For example, Bearse et.al. (Be 68) measured the $^{23}Na(p,\gamma)^{24}Mg$ reaction in the region of the G.D.R. energy. Based on fluctuation analysis, they deduced equal contributions from compound and direct processes. This was attributed to a small value of the spectroscopic factor of a $d_{3/2}$ proton in the ground state of ^{24}Mg which would inhibit a direct type mechanism.

2.2.2. Alpha Particle and Proton Radiative Capture

A further use of radiative capture reactions using alpha particles is in testing the theory of isospin splitting (Sect.2.1.9.) of the G.D.R. In principle, alpha capture can selectively excite $T^<$ components. On the other hand, proton capture can excite both $T^<$ and $T^>$ components. Comparison of $^{A-4}_{Z-2}(\alpha,\gamma)^{A}_{Z}$ data with $^{A-1}_{Z-1}(p,\gamma)^{A}_{Z}$ might therefore demonstrate the splitting. However, as discussed in Sect.2.2.1., p.51, the (α,γ) cross section usually falls rapidly once above neutron and proton thresholds, and so a negligible cross section at the $T^>$ resonance region would not be clear evidence of isospin selection rules operating. The G.D.R. of ^{64}Zn has been investigated by Paul et.al. (Pa 71) through the $^{63}Cu(p,\gamma)^{64}Zn$ reaction. The excitation function indeed displayed two distinct components in both γ_0 and γ_1 channels which obeyed the predictions of Goulard and Fallieros. Both the energy separation of the components, ΔE, and the integrated yields agreed with theoretical predictions. In table 2.2, the energy splitting ΔE, and the symmetry energy U are shown for various nuclides in the mass range 42 to 91.

One of the objectives of the $^{60}Ni(\alpha,\gamma)^{64}Zn$ study was to make a comparison with the data of Paul et.al. in the region of the $T^<$ and $T^>$ G.D.R. energies.

2.2.3. The Giant Quadrupole Resonance

The Giant Quadrupole Resonance (G.Q.R.) has received less attention in photonuclear physics than the G.D.R. This is principally because it is more difficult to investigate than the latter resonance. For example, in the long wave-length approximation ($ka \ll 1$), the ratio of λ and λ+1 transition probabilities goes as $\tau(\lambda)/\tau(\lambda+1) \sim \frac{(ka)^2}{(\lambda+1)(2\lambda+3)^2}$ (e.g. Ja 62) where τ is the lifetime of the state for gamma emission. If ^{40}Ca emits a 20 MeV gamma ray, $ka \simeq 0.5$, and the ratio of E2 to E1 transition probabilities is about .5%.

Nucleus	ΔE(MeV)	T	$\tilde{V}$(MeV)
^{42}Ca	3.0±0.2	1	63±4
^{49}Sc	4.8±0.2	7/2	52±2
^{60}Ni	3.0±0.2	2	60±4
^{64}Zn	3.2±0.3	2	68±6
^{64}Zn*[a]	2.9±0.3	2	62±6
^{88}Sr	3.7±0.5	6	47±6
^{89}Y	3.9±0.5	11/2	54±7
^{89}Y*[a]	3.8±0.4	11/2	52±6
^{90}Zr	3.9±0.5	5	58±7
^{91}Nb	3.6±0.7	9/2	59±10

[a] First excited state.

Ref. Pa 71. Table 2.2. $U = \tilde{V}T/A$

Secondly, a much larger fraction of the quadrupole sum rule is exhausted by low lying collective states than in the dipole case (∿20-40%).

Unlike dipole radiative transitions, both $\Delta T = 0$ isoscalar and $\Delta T = \pm 1,0$ isovector transitions are allowed for quadrupole radiation. According to Fukuda and Torizuka (Fu 72), the positions of the isoscalar and isovector G.Q. resonances are given by $\sim 65A^{-1/3}$ and $\sim 120A^{-1/3}$ MeV respectively. These coefficients of $A^{-1/3}$ were deduced from (e,e') data on a number of spherical nuclides. The isovector estimate is quite close to the hydrodynamic model prediction of $\sim 112A^{-1/3}$ MeV. Calculations by Suzuki (Su 73) predict that the isoscalar and isovector G.Q. resonances should lie at about $58A^{-1/3}$ and $130A^{-1/3}$ MeV respectively. The available experimental data support the isovector assignment within error bars, but the isoscalar systematics suggest a value of $62A^{-1/3}$ (Wa 73). Calculations are usually based on the G.Q.R. exhausting the appropriate sum rule which has not been verified experimentally.

Some of the experimental data will now be reviewed.

Lewis and Bertrand (Le 72) investigated inelastic scattering of 62 MeV protons from ^{27}Al, ^{54}Fe, ^{120}Sn and ^{209}Bi. Based on a careful examination of the proton continuua spectra in the excitation range 6-41 MeV, and

with the G.D.R. location from (γ,n) studies, they deduced an isoscalar G.Q.R. located at $\sim 63A^{-1/3}$ MeV. The same authors made measurements on ^{nat}Cu, ^{nat}In and ^{nat}Pb. In table 2.3, values of the G.Q.R. peak position from these experiments are shown

Nuclide	$E^{G.Q.R.}$	$E^{GQR} \times A^{1/3}$
^{27}Al	19 ± 1 19.5 ± 0.8	57 ± 3
^{54}Fe	16 ± 1	60 ± 4
^{120}Sn	13.5 ± 1	67 ± 5
^{209}Bi	11.5 ± 1	68 ± 6
^{nat}Cu	15.5 ± 0.6	62 ± 2
^{nat}In	13.7 ± 0.6	74 ± 3
^{nat}Pb	11.2 ± 0.5	66 ± 3

$< >=65$

Table 2.3.

Dahmen et.al. (Da 71) measured the $^{208}Pb(\gamma,p)^{207}Tl$ reaction from threshold to 33 MeV. ^{208}Pb was bombarded with bremstrahlung, and the 4.8m. β^- activity of ^{207}Tl measured. Above 25 MeV, the competing $^{208}Pb(\gamma,np)^{206}Tl$ reaction with an associated 4.3 min β^- activity could not be resolved from the (γ,p) reaction. The cross section for the (γ,p) and (γ,np) reactions increased from about zero at 15 MeV to about 2mb at 30 MeV in a linear fashion. At 25 MeV, a peak was present on the increasing background which was about 2 MeV wide and had a peak value of 3.4 mb. This was attributed to an E1 $\Delta T=1$ transition to an isobaric analogue state in ^{208}Pb. The smoothly increasing background was attributed to E2 transitions in qualitative agreement with the calculations of Bunatyan (Bu 67).

Dreyer et.al. (Dr 72) measured the (γ,n) and (γ,p) reaction on ^{160}Gd. Activation analysis was used to deduce absorption cross sections from theshold to 33 MeV. A broad peak appeared in the cross section at 23.5 MeV, and it was argued that this was the G.Q.R. predicted by the hydrodynamic model at 1.6 times the G.D.R. energy, about $123A^{-1/3}$ MeV. The $^{160}Gd(\gamma,xn)(x=1,3)$ cross section had previously been measured by Berman et.al. (Be 69). Their data exhibited the doublet structure of the G.D.R. predicted by Danos for deformed nuclei, and also the broad resonance at 23.5 MeV which Dreyer et.al. attribute to the isovector G.Q.R.

Lewis (Le 72a) has analysed the available data for ^{40}Ca in terms of contributions from dipole, quadrupole and octupole resonances. The G.D.R. was placed at 20 MeV and almost exhausted the isovector energy weighted sum rule. The G.Q.R. had a resonance energy of 17 MeV and exhausted 72% of the isoscalar energy weighted sum rule, and about 100% if low lying bound 2^+ states were included.

The multipole resonance strength in ^{16}O appears to be fragmented into isolated resonances over the energy range 12 to 26 MeV excitation. For example, Snover et.al. (Sn 74) studied the $^{12}C(\alpha,\gamma_0)^{16}O$ reaction from E_x = 12 to 28 MeV. They deduced T=0 E2 strength over this range which exhausted about 17% of the isoscalar energy weighted sum rule. If other channels were included, they estimated that about 70% of the sum rule would be exhausted. ^{16}O has been subjected to considerable attention both theoretically and experimentally. Other recent experimental studies have been made by Paul et.al. (Pa 75) on the $^{15}N(p,\gamma)^{16}O$ reaction, and Knöpfle et.al. (Kn 75). Hanna et.al. used inelastic scattering of alpha particles to excite E2 strength in ^{16}O (Ha 75) together with polarised proton reactions on ^{15}N.

It was found that in ^{24}Mg and ^{26}Mg from (α,γ) reactions that the E2 strength is spread out over about eight MeV (Ku 75). There is as yet no unambiguous knowledge of how the quadrupole strength is distributed in different parts of the periodic table. It was hoped that the present study might indicate whether E2 strength in the nuclides investigated was concentrated into single resonances or spread over an appreciable region of the continuum. Where isolated resonance strength has been observed, the isoscalar E2 strength has been below the G.D.R. in the vicinity of $63A^{-1/3}$, and isovector strength above the G.D.R. in the vicinity of $124A^{-1/3}$ MeV.

In table 2.3, the E2 strength for various even-even nuclides is shown normalised to the isoscalar Gell-Mann sum rule, $0.22Z^2A^{-1/3}$ μb.MeV. Where it was available, the strength from low lying quadrupole states has been included. In the continuum, only the E2 strength determined from (α,γ) reactions is used. It is clear that in most cases, if an estimate of the decay through channels other than α_0 is made, then the cross section exhausts the sum rule below $E_x = 63A^{-1/3}$, the predicted position of the isoscalar G.Q.R. For $^{24,26}Mg$, the (γ,n) cross section is included in the terms in brackets. (Ku 75). This exemplifies the total E2 strength of these nuclei.

Table 2.3. After Hanna (Ha 75a)

Nuclide	$\int\sigma(E2)/E^2dE/0.22Z^2A^{-1/3}$%	
^{16}O	55	
^{24}Mg	47	(120±30)
^{26}Mg	40	(290±80)
^{28}Si	50	
^{30}Si	36	
^{32}S	51	
^{34}S	27*	
^{40}Ca	26	
^{42}Ca	64*	
^{44}Ti	14*	
^{52}Cr	17*	
^{60}Ni	15*	

* The data for these nuclei is incomplete.

2.3.1. Cross Section Calculations

In this section, the theory used in estimating the fraction of compound, direct and semi-direct processes which contribute to (α,γ) reactions will be considered. As will be seen, the expression for the compound process differs from the conventional Hauser-Fesbach expression. The theory is due to Shikazono and Terasawa (Sh 75).

Three possible meachnisms are considered for the reaction:

(i) Compound process. The incident alpha particle penetrates the potential barrier and coalesces with the target. A collective state is formed at high excitation, one of its decay modes is by gamma emission.

(ii) Direct process. The alpha particle is captured from a continuum scattering state to a bound orbital in the target. As it changes states a gamma ray is emitted.

(iii) Semi-direct process. The target is excited by a Coulomb interaction with the alpha particle. The alpha particle makes a radiationless transition to a bound state, and the excited core decays by gamma emission. A second type of E1 semi-direct mechanism is considered. For N=Z nuclei, a 1^- T=0 mode may be excited by a nuclear interaction between the target and incident alpha particle. If this state is mixed with the 1^- T=1 G.D.R., then the G.D.R. can be excited through this two step mechanism.

Using S matrix formalism, the total reaction amplitude is written in the usual way:

$$S_{\alpha'\alpha} = \bar{S}_{\alpha'\alpha} + S^{Fl}_{\alpha'\alpha} \qquad \text{---} \qquad 2.49.$$

where α and α' are entrance and exit channels respectively. $\bar{S}_{\alpha'\alpha}$ is an average amplitude associated with direct and semi direct processes. The cross section is proportional to $|S_{\alpha'\alpha}|^2$, and the average cross section is

$$\bar{\sigma}(\gamma,\alpha) = \frac{\pi g}{k_\gamma^2}\{|\bar{S}_{\alpha\gamma}|^2 + \overline{|S^{Fl}_{\alpha\gamma}|^2}\}$$

$$= \sigma^{D.S.D.}(\gamma,\alpha) + \bar{\sigma}^{Fl}(\gamma,\alpha) \qquad \text{---} \qquad 2.50.$$

Here, the (γ,α) cross section is considered which is related to the (α,γ) cross section by detailed balance, viz.

$$\sigma(\alpha,\gamma) = \frac{2(2I+1)}{(2I'+1)}\frac{k_\gamma^2}{k_\alpha^2}\sigma(\gamma,\alpha) \qquad \text{---} \qquad 2.51.$$

where I is the ground state spin of the target, and I' that of the residual nucleus for the (γ,α) reaction. k_γ and k_α are gamma and alpha wave numbers respectively. g is the statistical factor, $g = \frac{1}{2}(2J+1)/(2I+1)$ where J is the spin of the compound nucleus.

(i) Compound processes.

The fluctuating part of the cross section averaged over energy is written

$$\bar{\sigma}^{Fl}(\gamma,\alpha) = \frac{\pi}{k_\gamma^2} g T_\gamma B_\alpha \qquad \text{---} \qquad 2.52.$$

where T_γ is a gamma ray transmission coefficient. It is defined by

$$T_\gamma = 1 - \sum_\alpha |\bar{S}_{\alpha\gamma}|^2 \qquad \text{---} \qquad 2.53.$$

It is shown by Shikazono and Terasawa that

$$\bar{\sigma}^{Fl}(\gamma,\alpha) \simeq \frac{\pi}{k_\gamma^2} g \frac{\Gamma_{G\gamma}\Gamma_G^{\downarrow}}{(E-E_G)^2+\frac{1}{4}\Gamma_G^2} B_\alpha \qquad \text{---} \qquad 2.54.$$

where Γ_G is the total width for the giant resonance, and $\Gamma_{G\gamma}$ is the partial width for γ decay. $\Gamma_G^{\downarrow}$ is called the spreading width of the resonance and is expressed by

$$\Gamma_G^{\downarrow} = \Gamma_G - 2\pi\sum_\alpha |\gamma_{G\alpha}|^2 \qquad \text{---} \qquad 2.55.$$

where $\gamma_{G\alpha}$ is a reduced width for decay in channel α.

Comparing equation 2.52 with 2.54 shows that

$$T_\gamma = \frac{\Gamma_{G\gamma}\Gamma_G^{\downarrow}}{(E-E_G)^2 + \frac{1}{4}\Gamma_G^2} \qquad \text{---} \qquad 2.56.$$

Eq.2.54 is then written in the form

$$\bar{\sigma}^{F1}(\gamma,\alpha) = \bar{\sigma}_{\gamma G}\, \Gamma_G^{\downarrow}/\Gamma_G\, B_\alpha \qquad \text{---} \qquad 2.57.$$

where $\bar{\sigma}_{\gamma G}$ has the Breit-Wigner form

$$\bar{\sigma}_{\gamma G} = \frac{\pi}{k_\gamma^2}\, g\, \frac{\Gamma_{G\gamma}\Gamma_G}{(E-E_G)^2 + \frac{1}{4}\Gamma_G^2} \qquad \text{---} \qquad 2.58.$$

The only factor which remains to be determined is B_α, the decay probability for channel α. From eq.2.50 and 2.52

$$\overline{|S_{\alpha\gamma}^{F1}|^2} = T_\gamma B_\alpha \qquad \text{---} \qquad 2.59.$$

Under the assumption that a compound nucleus level $|a\rangle$ can be decomposed into a linear combination of $T^<$ and $T^>$ states, it can then be shown that for N=Z nuclei

$$B_\alpha = T_{\alpha o}\left[\frac{(1-\varepsilon^2)\varepsilon'^2}{(1-\varepsilon^2)\Sigma\frac{1}{2}(T_p+T_n) + \varepsilon'^2\{\Sigma\frac{1}{2}(T_p+T_n) + \Sigma T_\alpha\}} + \frac{\varepsilon^2(1-\varepsilon'^2)}{\varepsilon^2\Sigma\frac{1}{2}(T_p+T_n)+(1-\varepsilon'^2)\{\Sigma\frac{1}{2}(T_p+T_n)+\Sigma T_\alpha\}}\right] \qquad 2.60.$$

One of the parameters of the decay probability is the isospin mixing parameter ε. ε' is given by

$$\varepsilon'^2 = \varepsilon^2\langle D_<\rangle/\langle D_>\rangle \qquad \text{----} \qquad 2.61.$$

The transmission coefficients are calculated in the framework of the optical model. The method will be explained in Chapter 4.

(ii) E1 and E2 direct processes.

The direct process cross sections are proportional to matrix elements taken between initial and final states of the E1 or E2 operator. The initial state is that of the target in its ground state plus an alpha particle in a scattering state. The final state consists of the core plus alpha particle in a bound orbital. For E1 direct capture,

$$\bar{\sigma}_{E1}^{D}(\alpha,\gamma) = \frac{64\pi^2 m_\alpha k_\gamma^3}{9\hbar^2 k_\alpha} \sum_{\ell\ell' m}(2\ell'+1)\left|\bar{T}^{(1)}_{\ell\ell' m}\right|^2 \qquad \text{---} \qquad 2.62.$$

where

$$\overline{T}^{(1)}_{\ell\ell'm} = \langle\overline{\Psi}_{\ell m}|\tfrac{1}{2}e\Sigma_i(1-\tau_{3i})r_i Y_{1m}(\Omega_i)|\Psi_{\ell' o}\rangle \quad --- \quad 2.63.$$

and for E2 capture

$$\overline{\sigma}^{D}_{E2}(\alpha,\gamma) = \frac{16\pi^2 m_\alpha k_\gamma^5}{75\hbar^2 k_\alpha}\Sigma_{\ell\ell'm}(2\ell'+1)\overline{|T^{(2)}_{\ell\ell'm}|^2} \quad --- \quad 2.64.$$

where

$$T^{(2)}_{\ell\ell'm} = \langle\Psi_{\ell m}|\tfrac{1}{2}e\Sigma_i(1-\tau_{3i})r_i{}^2 Y_{2m}(\Omega_i)|\Psi_{\ell' o}\rangle \quad --- \quad 2.65.$$

(iii) E1 and E2 semi direct processes.

Two types of semi direct process are considered for E1 radiative capture. In the first, the G.D.R. is excited by a Coulomb interaction with the alpha particle. In the second, the existence of a 1^- T=0 resonance is postulated (On 70) which excites the 1^- T=1 resonance through isospin mixing of the two states. The cross section for these two processes is

$$\sigma^{SD}_{E1} = \frac{2\pi m_\alpha k_\gamma{}^3}{27\hbar^2 k_\alpha}\Sigma_{\ell\ell'}(\ell+\ell'+1)e^2 S_\ell |m^{(1)}_{\ell\ell'}|^2 \quad --- \quad 2.66.$$

where

$$m^{(1)}_{\ell\ell'} = \frac{9(\hbar c)^3\Gamma_{G\gamma}}{E_G{}^3}\ \frac{\int u^*_\ell F\Psi_{\ell'} r^2 dr}{E_\alpha - E_\ell - E_G + \frac{1}{2}i\Gamma_G} \quad --- \quad 2.67.$$

where F is a form factor for the two processes given in Sh 75.

Excitation of a collective E2 excitation of the core can occur by a nuclear interaction of the alpha particle and core. The particle-vibration coupling is assumed to be of the form

$$H = R_o\frac{\partial V_\alpha}{\partial R_o}\Sigma_m Y_{2m}\alpha^*_{2m} \quad --- \quad 2.68.$$

where α^*_{2m} is the operator creating a collective E2 state, and V_α is the alpha-core nuclear potential. The matrix element for this process is

$$m^{(2)}_{\ell\ell'} = \frac{2S(\hbar c)^5\Gamma_{G\gamma}}{e^2 A R_o E_G{}^5}\ \frac{\int u^*_\ell(\partial V_\alpha/\partial R_o)\Psi_{\ell'} r^2 dr}{E_\alpha - E_\ell - E_G + \frac{1}{2}i\Gamma_G} \quad --- \quad 2.69.$$

and the cross section

$$\overline{\sigma}^{SD}_{E2}(\alpha,\gamma) = \frac{16\pi m_\alpha k_\gamma^5}{15\hbar^2 k_\alpha}\ \Sigma_{\ell\ell'}(2\ell'+1)(\ell'200|\ell 0)^2 e^2 S_\ell |m^{(2)}_{\ell\ell'}|^2 \quad --- \quad 2.70$$

where S_ℓ is a spectroscopic amplitude of the alpha particle in the residual nucleus.

Methods of calculating the wave functions which appear in these equations will be discussed in Chapter 4.

CHAPTER 3

Experimental Considerations

3.1.1. Introduction

The A.N.U. 10" NaI(Tℓ) spectrometer is designed to detect high energy (∿10-30 MeV) gamma rays from low cross section (∿1μb) radiative capture reactions in the presence of high background rates. It is similar to one constructed at Stanford University (Su 68). Detailed reports have been made of its construction (Bl 71, Fo 74) and these will not be repeated here. In Fig. 3.1, a schematic diagram of the spectrometer is shown. Its operational features will be described together with the electronics system designed to process signals from the instrument.

3.1.2. Description of the Spectrometer

(i) The crystal and 60 A.V.P. photomultiplier

The spectrometer is based on a $9\frac{3}{8}$" diameter by 10" cylindrical NaI(Tℓ) crystal supplied by the Harshaw Chemical Company. This is optically coupled through a short light pipe ($d/\ell >> 1$) to an Amperex 60 A.V.P. photomultiplier tube. The 60 A.V.P. has a gain of 10^8 at 3000 volts, and an intrinsic pulse rise time of 2.5ns. It is operated with negative H.V. on the photocathode, and the anode is D.C. coupled using a 50Ω load resistor. In practice, the voltage waveform had a rise time of approximately 70ns. with saturation occurring at about 8 volts. Timing was improved by cable clipping this pulse with 14ft. of 50Ω cable at the receiving end of the anode transmission line. The clipping line was terminated with a 3Ω resistor which reduced positive overshoot of the falling pulse edge. After clipping, the rise time was about 50ns.

Because the photocathode is at a negative high potential (∿2000 V), a large field gradient can exist across the glass face of the tube which is at ground potential. This can cause a high initial dark current, and so the H.V. power supply was always left on.

(ii) The NE102 plastic A.C.S.

An annulus of type NE102 scintillator plastic surrounds the crystal. This is about 3" thick. The front face of the crystal is covered with a piece of NE102 about $1\frac{1}{2}$" thick, and this assembly acts as the anti-

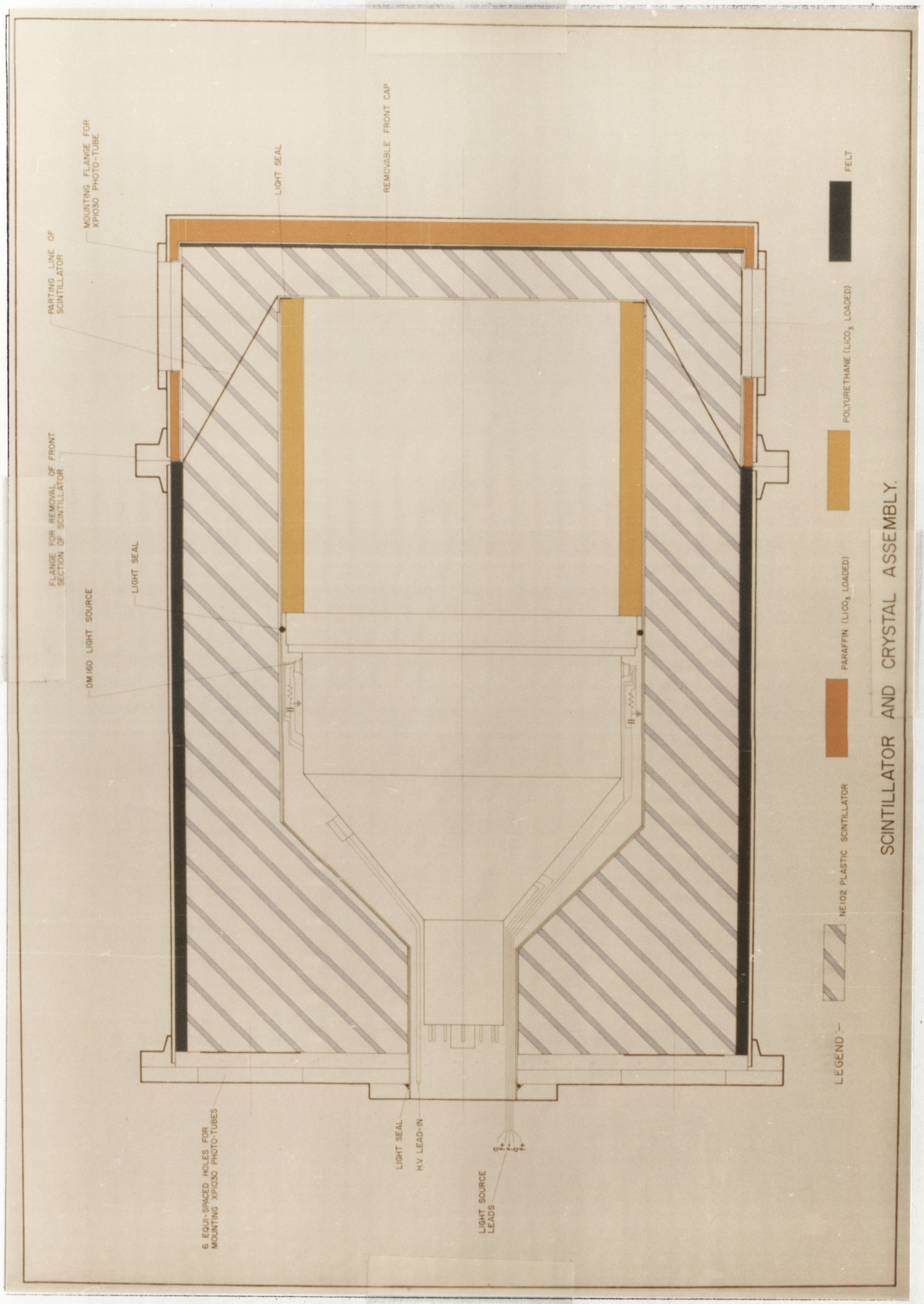
SCINTILLATOR AND CRYSTAL ASSEMBLY.
LEGEND :-
NE102 PLASTIC SCINTILLATOR
PARAFFIN ($LiCO_3$ LOADED)
POLYURETHANE ($LiCO_3$ LOADED)
FELT
6 EQUI-SPACED HOLES FOR MOUNTING XP1030 PHOTO-TUBES
LIGHT SEAL
H.V LEAD-IN
LIGHT SOURCE LEADS
8
7
9
LIGHT SEAL
DM160 LIGHT SOURCE
FLANGE FOR REMOVAL OF FRONT SECTION OF SCINTILLATOR
PARTING LINE OF SCINTILLATOR
MOUNTING FLANGE FOR XP1030 PHOTO-TUBE
LIGHT SEAL
REMOVABLE FRONT CAP

Fig 3.1

coincidence shield. The front cap is faced with a 2cm thick layer of $LiCO_3$ doped paraffin wax, its purpose is to moderate and remove neutrons in the non-radiative $^6Li(n,\alpha)T$ reaction (^6Li has an isotopic abundance of about 7.5%). The mass absorption coefficient for paraffin wax is roughly $10^{-1}cm^2g^{-1}$, so that the neutron flux will be attenuated by 20% in 2cm of wax. σ_{th} for the $^6Li(n,\alpha)T$ reaction is 1000 b. The concentration of $LiCO_3$ is unknown in the wax so the effect of this is not known. Experiments did show, however, that with concentrations of about 30 or 40% of $LiCO_3$ in wax, Compton scattering of high energy gamma rays was increased over wax with no $LiCO_3$ present.

The plastic scintillator has a rise time of $\lesssim$20ps. (Ca 74). The whole A.C.S. is viewed by eight XP1030 phototubes. These are ten stage photomultiplier tubes with an intrinsic pulse rise time of 7ns. at 1400 V. The anodes are D.C. coupled to a summing impedence matching network.

(iii) Construction and collimation of spectrometer

Surrounding the crystal and A.C.S. is a lead shield about 12cm thick. In addition to this, another 12cm of lead bricks are placed on the top of the spectrometer. The front face of the A.C.S. has a 12cm thick plate shielding the crystal from radiations emanating from the reaction under investigation.

The complete assembly which consists of the crystal, A.C.S. and lead shield is supported in a steel case. This is mounted on a rotating carriage so that the spectrometer may be rotated about a vertical axis containing the target, allowing angles of observation from zero to 150° to the beam direction. The separation of the spectrometer from the target may be varied by means of a lead screw which slides the spectrometer on its bed which is an integral part of the rotating carriage.

The centre of the front lead shielding plate is removed to allow different collimators to be inserted. Two collimators were used in these experiments. They were lead cylinders about 14cm. thick with conical sections removed from their interiors. A $LiCO_3$ doped wax frustrum fills their interiors. The collimator used depends on the reaction under investigation and the resolution required. The geometries used in the present experiments are shown in Fig.3.3. Collimation with the smaller solid angle gave slightly better resolution which was about 6% F.W.H.M. of the full energy peak. Excitation functions were measured with the 110 msr. geometry

Fig.3.2. The perspex target chamber. The two collimation geometries used to measure excitation functions (no.2) and angular distributions (no.1). The whole spectrometer and collimator assembly was moved forwards or backwards on its carriage to achieve the correct separation from the target. With collimator no.1 angles of observation could be made between 0 and 150 degrees to the beam direction. (Dimensions are in inches).

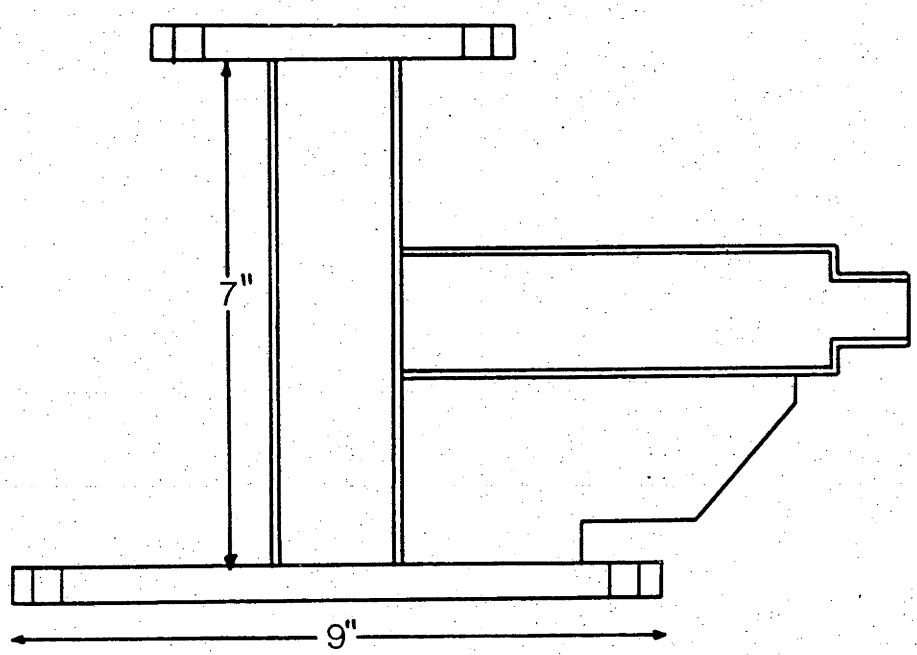

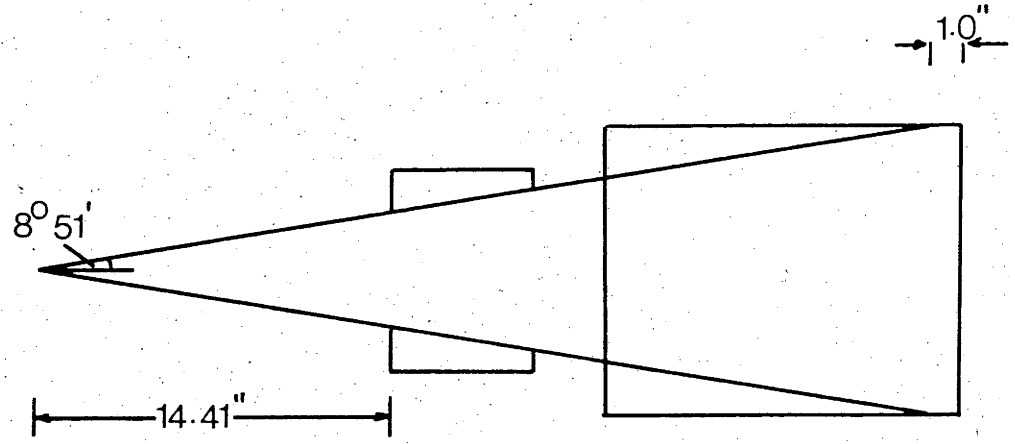

no.1 angular distributions

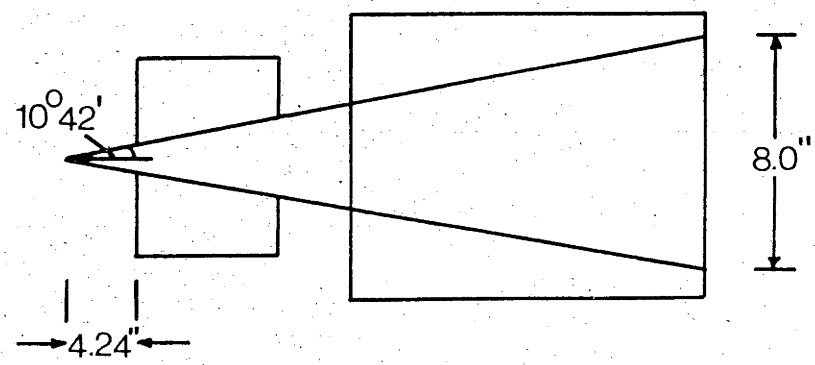

no.2 excitation functions

and angular distributions with the 75 msr. geometry. The attenuation of the gamma flux in the paraffin wax inserts is about 20%, whereas the fast neutron flux attenuation is roughly 70%.

3.1.3. Target Chamber

The same target chamber was used in all the experiments described here. It was a simple perspex tube 1.5" in diameter and with a wall thickness of $\frac{3}{16}$". This attenuates the gamma flux by roughly 1% ($E_\gamma \gtrsim 10$ MeV). The target chamber is shown in Fig.3.2.

3.1.4. Attenuation by the Target Backing

Gamma rays emerge from the target in either transmission or reflection geometry depending on the angle at which the spectrometer is. For angles less than 90°, transmission geometry was employed. All targets were evaporated onto Au blanks 1" x 1" and thickness t. The actual distance a gamma ray had to travel through the gold depended on the scattering angle θ as:

$$x = t.10^{-6}/\cos(\theta-45) \qquad \theta<90° \qquad --- \qquad 3.1.$$

where t is the thickness of Au in $\mu g.cm^{-2}$ ($9.8.10^5 \mu g.cm^{-2}$). The gamma ray attenuation is then given by:

$$n(x) = n(o)\exp(-\alpha(E)x) \qquad --- \qquad 3.2.$$

where α(E) is the attenuation coefficient in cm^2g^{-1}. α(E) was obtained from a curve given by Marion and Young (Ma 68) for Pb. It was parameterised as:

$$\alpha(E) = 0.0378 + 0.001279E \qquad --- \qquad 3.3.$$

with E in MeV.

For example, the maximum attenuation occurs when θ = 0, then for a 13 MeV gamma ray the attenuation is 13%. This correction was incorporated into a computer code which fitted angular distributions.

3.1.5. Interactions in the Crystal

A complete history of the energy of a gamma ray from the time it entered the crystal to the time an equivalent light pulse occurred would demand a complete treatise on the interaction of gamma rays with matter (e.g. Se 60). Only the major aspects will be briefly touched upon.

Theoretical calculations and experiment show that in the energy interval under consideration (10-20 MeV), the dominant cross section is pair

production with its well-known Z^2 dependence. The energy of the pair is $E_\gamma - 2m_oc^2$ where m_o is the rest mass of an electron. There is a small asymmetry in the energy distribution due to the electrostatic field of the nucleus. The average angle between the pair is defined by

$$\langle\theta\rangle = \int\theta\sigma(\theta)d\Omega/\int\sigma(\theta)d\Omega \quad --- \quad 3.5.$$

which is given approximately by

$$\langle\theta\rangle \simeq 2m_oc^2/E_\gamma \quad --- \quad 3.6.$$

Consequently, most pairs produced travel into the crystal with a small angular divergence (e.g. $\langle\theta\rangle\sim6°$ at E_γ = 10 MeV).

If it is assumed that the energy is divided equally between the pair, then for a 15 MeV gamma ray each lepton will have roughly 7 MeV kinetic energy. These leptons may then propagate through the crystal losing energy in bremsstrahlung and collisions with electrons. A 7 MeV electron is ultra relativistic ($v/c\sim99.8\%$), but its interactions with atomic nuclei depends on the effective interaction distance. This is given by the uncertainty principle as

$$\Delta x\sim\hbar/\Delta p \quad --- \quad 3.7.$$

where Δp is the momentum transfer involved. If $\Delta x<<R_o$ where R_o is the atomic radius, then the interaction takes place essentially in the Coulomb field of the nucleus. On the other hand, if $\Delta x>>R_o$, the interaction is outside the atom and the nuclear field is screened by the atomic electrons.

For an incident energy E_o, a screening parameter is defined by

$$\Gamma = 100\hbar\omega\, m_oc^2(E_oEZ^{1/3})^{-1} \quad --- \quad 3.8.$$

where $E = E_o - \hbar\omega$.

In the complete screening limit ($\Gamma\simeq0$), the electron passes the nucleus at large distances compared with the atomic radius. In the limit of no screening ($\Gamma>>1$), the electron moves close to the nucleus and radiates in a potential Ze. Since for NaI, $\langle Z\rangle$ = 45, the screening parameter eq.3.8 becomes

$$\Gamma_{NaI} = 14.37\,\frac{\hbar\omega}{E_oE} \quad --- \quad 3.9.$$

If E_o = 7 MeV, for small $\hbar\omega$, $\Gamma_{NaI}\simeq0$, that is, the no screening limit applies. In this limit, the differential energy loss (total energy radiated per cm. of path) can be written (e.g. Jackson p.518)

$$dE_{RAD}/dx = \frac{16}{3} N \frac{Z^2e^2}{\hbar c} \left(\frac{z^2e^2}{m_0c^2}\right)^2 \ell n(\lambda\gamma)\gamma m_0c^2 \quad --- \quad 3.10.$$

where γ is defined by $E_0 = \gamma m_0c^2$, N is the number of nuclei per cm^3 and λ is a numerical adjustment of the order of 2*. At E_0 = 7 MeV, eq.3.10 gives

$$dE_{RAD}/dx\Big|_{7\ MeV} \simeq 2.7\ MeV.cm^{-1} \quad --- \quad 3.11.$$

On the other hand, the collisional energy loss is approximately

$$dE_{coll}/dx \simeq \frac{4\pi NZe^4}{m_0v^2} \{\ell n \left(\frac{\gamma^{3/2}m_0c^2}{\sqrt{2}\hbar<\omega>}\right)^2 - \frac{v^2}{c^2}\} \quad --- \quad 3.12.$$

where $\hbar<\omega>$ is the mean ionisation potential of the target atoms. For NaI. $\hbar<\omega>$ = 562 ev (Shafroth p.283). Consequently, at E_0 = 7 MeV,

$$dE_{coll}/dx\Big|_{7\ MeV} \simeq 8.6\ MeV.cm^{-1} \quad --- \quad 3.13.$$

and the ratio of radiative to collisional energy loss is about 32%.

The leptons penetrate into the crystal losing energy by radiation and collision. A 6 MeV electron has a mean range of ≈6.8 mm in NaI and a maximum range of ≈13.38 mm. Both positrons and electrons behave similarly until they become thermalised. The positron is able to annihilate with an electron producing two gamma rays which will have a combined energy of 1.02 MeV if the positron annihilated at rest. It was found that an escape peak could be seen in good statistics spectra. This is from the undetected escape of one 0.511 MeV quantum which leaves via the front face of the crystal. The geometry of collimation is such that the escape of two quanta is unlikely. One escaping gamma ray implies that the other is propagating into the crystal or through appreciable NaI (greater than the mean free path of 2.7 cm.).

---

* Some parameters for NaI are:

ρ = 3.665 $g.cm^{-3}$

<Z> = 45

<A> = 111

N = 1.824 10^{22} atoms cm^{-3}

Mean free path of 1 MeV gamma ray is 4.67 cm.

The average range of an electron in NaI is given by (Shafroth, p.288)

$$\bar{S} \simeq 0.0603[\varepsilon(1-0.003\varepsilon) - 0.29]\ cm.$$

where ε is in units of m_0c^2.

3.1.6. Cosmic Rays

Scintillation detectors on the earth's surface are subjected to the cosmic ray flux. This is divided into two approximate classes, hard and soft radiation.

The former consists of fast mesons which have energies up to several GeV, and the latter of photons and electrons up to 100 MeV. It is relatively easy to shield from the soft component with lead for example, but the meson component is extremely penetrating radiation. The average energy loss of a fast μ meson in Pb is 10 $MeV.cm^{-1}$, and in NaI 5 $MeV.cm^{-1}$. Careful calculations of the thickness of Pb required to absorb the secondary radiation produced by a μ meson in the shield have been made. For example, for an incident energy E_o, some values are as below:

E_o	10^2 keV	10^4 BeV	10^6 BeV
Thickness (cm)	19	28	36

The A.N.U. spectrometer is shielded by cylindrical Pb shielding and has additional lead shielding bricks on top. The combined thickness is about 24 cm. The plastic A.C.S. serves to reject radiation which penetrates the Pb. Fast mesons lose roughly 15 MeV in the plastic scintillator, and about 45 MeV in the crystal. The Pb shield on top of the spectrometer is about 24 cm thick, or 240 MeV equivalent energy loss for fast mesons. This is sufficient to absorb all the soft component of the cosmic flux, but not sufficient to absorb secondary cosmic radiation produced in the lead by μ mesons. The A.C.S. effectively rejects showers caused by fast mesons in the lead. One particular component of the hard meson flux requires special rejection techniques. μ^+ mesons which have energies less than about 350 MeV pass through the lead shield losing about 240 MeV. These may then come to rest in the NaI, and decay into positrons with a well-known half life of 2.2μs.

Consequently, delayed radiation with respect to a pulse in the A.C.S. can occur. If the timing requirement for coincidence of a plastic A.C.S. and NaI pulse is less than 2.2μs, a considerable number of these pulses will be accepted as genuine events in the crystal. According to Suffert et.al*, the count rate of delayed events is roughly $4s^{-1}$ in the region 10 to 60 MeV in a similar spectrometer to this one. These are approximately uniformly distributed over the energy interval so that in the range 10-20 MeV, roughly $\frac{2}{3}$ count per second can be expected. This would be unacceptable in radiative capture experiments. The electronic logic necessary to discriminate against this type of event will be described below.

* (Su 68).

3.1.7. Rationale of Signal Analysis

The problem of cosmic originated pulses in the spectrometer has been described above. The requirement of the logic system to discriminate against these types of signal is to sample pulses from the A.C.S. and NaI and test for coincidence. If this exists, to reject the NaI event. This same logic will reject events in the crystal which subsequently loose energy outside the volume of NaI in bremstrahlung or annihilation radiation.

Secondly, at high count rates pile up of lower energy pulses into the full energy peak can occur. It is therefore desirable to minimise this.

3.1.8. Electronics System

In Fig.3.3, a block diagram of the system used to process signals from the spectrometer is shown. All the modules are standard Ortec or Canberra units except for the 20μs gate generator. Not shown in the Fig. are the phototube power supplies which are two Fluke H.V. units. The 60 A.V.P. tube is driven by one of these units which can supply the high standing current requirement of 15ma in the dynode resistor chain. This is set at a nominal voltage of -2160V on the dials. The second Fluke supply drives the eight XP1030 tubes through a voltage divider mounted on the spectrometer. This has a nominal output of -2250V. Other items not shown in Fig.3.3 are an Ortec 113 preamplifier connected to the 9^{th} dynode of the 60 A.V.P. tube, and the fast summing amplifier for the eight XP1030 tubes. Fast timing signals are transmitted to the control room via several hundred feet of high quality 50Ω cable (UR67) which gave negligible distortion or attenuation of the pulse.

Fast anode signals from the 60 A.V.P. phototube are cable clipped from about 70ns. rise time to about 50ns. This clipped pulse is applied to the input of an Ortec 453 C.F.T.D. set in leading edge mode. If the pulse height is above threshold as determined by a front panel helipot setting, the 453 is triggered and generates standard positive and negative logic pulses. The positive logic pulse then opens the Canberra 1454 linear gate (after suitable delay in a Canberra 1455A logic shaper and delay) to allow the corresponding linear signal through. Linear signals are derived from the 9^{th} Dynode of the 60 A.V.P. phototube, preamplified by an Ortec 113 and amplified by an Ortec 410 amplifier in double delay line mode. One of the fully buffered outputs drives an Ortec 449 ratemeter through a Canberra 1437 S.C.A. The level of this S.C.A. is set to correspond to about 1 MeV, so that the

total rate in the NaI above 1 MeV is indicated by the ratemeter. Small pulses which originate mostly in bremstrahlung processes are removed from the amplified linear signal by an Ortec 408 bias amplifier. It was found that if this were not done, the 1454 linear gate became paralysed. The Canberra 1457 delay is necessary for correct timing between linear and gate signals.

On the plastic A.C.S. side, summed anode pulses from the 8 XP1030 phototubes are delayed for 65ns in an A.N.U. delay box. This pulse is amplified by an Ortec 454 T.F.A., the output of which triggers a 100 MHz discriminator. As mentioned earlier, the 60 A.V.P. anode pulse generates a negative logic signal if above threshold of the 453 C.F.T.D. This pulse starts a 1443 T.A.C. which is stopped by the output of the 436 100 MHz discriminator. (Through suitable delay in two Canberra 31ns. delays). The resolving time of the T.A.C. was 500ns. This resolving time was found adequate to include the complete time spectrum generated by 60 A.V.P. anode start signals and plastic A.C.S. stop signals. If two pulses arrive within this time interval, an internal S.C.A. pulse is generated. This standard positive logic pulse triggers an A.N.U. gate generator which is modified to provide a 20μs. output pulse. This pulse has two purposes:

(a) To route the rejected spectrum into part of the IBM 1800 memory.
(b) To block the accepted spectrum routing pulse.

20μs is chosen as the blocking pulse time because it is roughly ten half lives for the decay

$$\mu^+ \rightarrow \bar{\nu}_\mu + \nu_e + e^+$$

and can therefore be expected to effectively reject pulses associated with this event in the crystal

$$e^+ + e^- \rightarrow 2\gamma \quad .$$

The accepted spectrum routing signal is essentially the positive logic signal from the 453 C.F.T.D. This is passed by the Canberra 1446 Coincidence unit to route the linear signal into the accepted spectrum unless it is blocked by the 20μs reject pulse.

Consequently, every NaI linear pulse which is passed by the 1454 linear gate has associated with it a routing signal directing it to either the accepted or rejected parts of the I.B.M.1800 memory. An advantage of this system is that both spectra are processed by identical linear electronics, thereby avoiding problems of gain normalisation in two independent amplifiers.

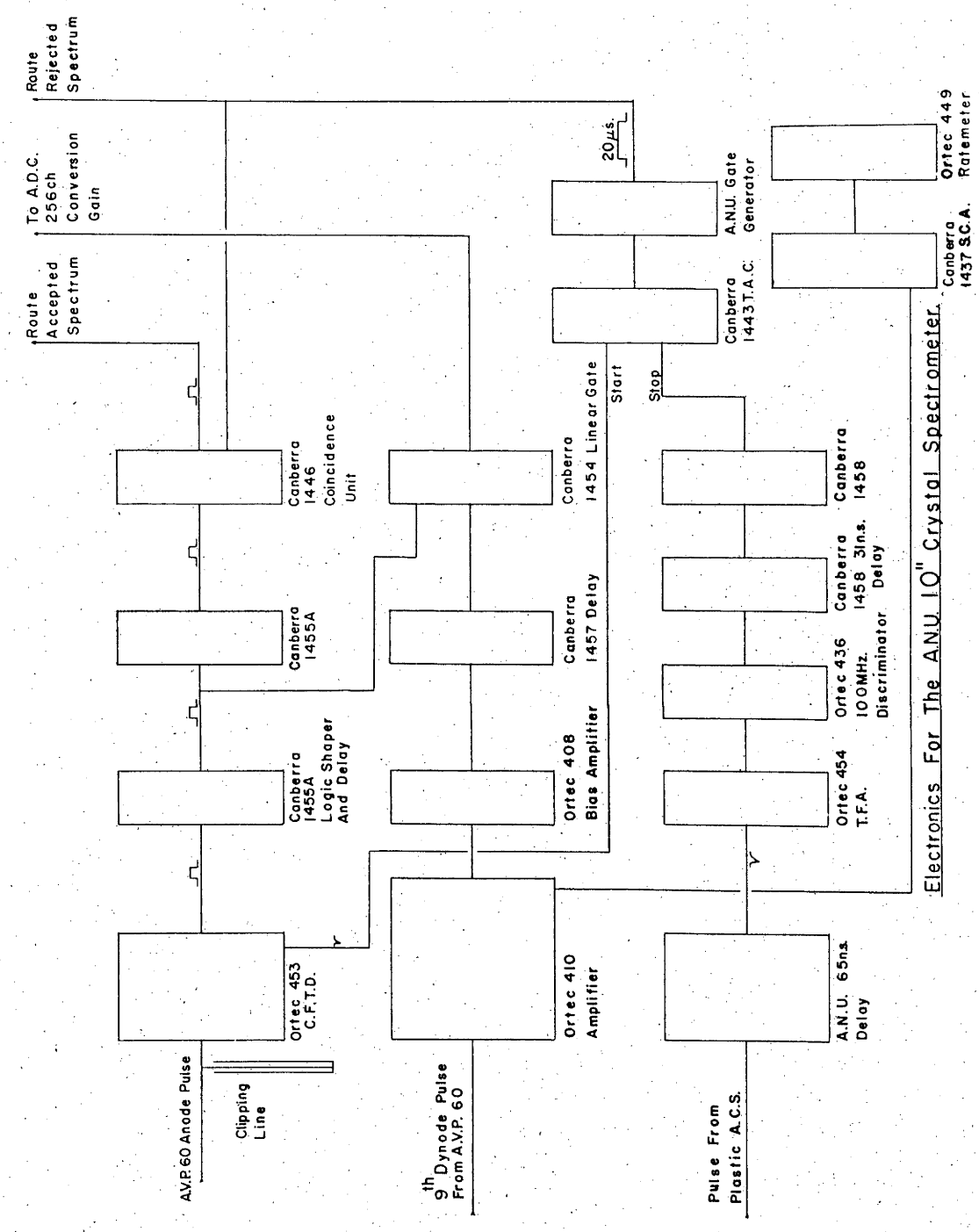

Fig.3.3. Block diagram of electronics system for spectrometer.
Electronics For The A.N.U. 10" Crystal Spectrometer.

Both the accepted and rejected spectra can be viewed on a visual display unit, and a nominated fraction of one may be subtracted from the other.*

Gain changes of 60 A.V.P. phototube.

It was found that the gain of the photomultiplier tube varied with the count rate (and hence the current in the dynode chain). This could be checked using the built-in light sources of the spectrometer. These are two Mullard D.M.160 light emitting triodes inserted in the light pipe coupling the NaI crystal to the face of the phototube, and are driven by a power supply with 0.1% stability which ensures that the emission spectrum is constant. A region of the spectrum from 3600-5000Å is selected by using Kodak 47B filters over the light source.

If the pulse from the light sources (the two sources were pulsed simultaneously) was set in a particular channel of the pulse height analyzer display, then changes in gain of the phototube with count rate could be monitored. For a change in beam intensity of two, then the reference peak changed by about 1½%. To overcome this problem, at the start of each run, the reference peak was set in a particular channel (the same channel for each run), and the beam intensity monitored. The beam current meter had provision for automatically stopping data collection if the current increased or decreased outside preset limits. By keeping the intensity constant to within about ±15%, no change in gain due to count rate occurred during a run. The stability of the EN tandem is such that this condition is easily met, and the collection of data is not continuously stopping and starting. In fact, the stability of the beam was generally about ±5% over the duration of a run, about one hour.

3.1.9. Pulse Pile-up

Anode pulses from the 60 A.V.P. phototube arrive at a rate R s^{-1}. The probability of n pulses arriving in a time interval t is:

$$P(n,t) = [(t/\tau)^n/n!]\exp(-t/\tau) \qquad \text{---} \qquad 3.14.$$

where τ is the average time between successive pulses. $\tau = 1/R$.

Pile up of anode pulses occurs when two or more pulses arrive within the resolving time of the anode discriminator circuit. The number of pulses arriving in this time, τ_a also has a Poisson distribution. The probability

---

* In Appendix B, a list of typical instrument settings is given for future users of the system.

of n pulses arriving in a time interval τ_a is

$$[(R\tau_a)^n/_{n!}]\exp(-R\tau_a) \quad --- \quad 3.15.$$

The number of events per second where n pulses arrived in a time interval $\leq\tau_a$ will therefore be

(no. of intervals per sec. of length τ_a) $\times$ (probability of n pulses arriving in time interval $\leq\tau_a$)

$$\text{i.e. } (^1/_{\tau_a}) \times [(R\tau_a)^n/n!]\exp(-R\tau_a) \quad --- \quad 3.16.$$

For example, the rate of single pile up (n=2) is

$$[(^1/_{\tau_a})(R\tau_a)^2/2!]\exp(-R\tau_a) \quad --- \quad 3.17.$$

double pile up

$$[(^1/_{\tau_a})(R\tau_a)^3/3!]\exp(-R\tau_a) \quad --- \quad 3.18.$$

and so on.

The measured rate of anode pulses is about $20.10^3 s^{-1}$ in the range 1 to 20 MeV, and the resolving time of the anode circuit about 100ns. Consequently, the single pile up rate is about $20.s^{-1}$. The double pile up is down by three orders of magnitude. However, this is the total pile up rate to any amplitude. What we require is the pile up rate into the region of interest, $E_o + \Delta$ say.

The number of pulses per second per MeV is dR(E)/dE, and the rate in an interval dE

$$(dR(E)/dE)dE \quad --- \quad 3.19.$$

The total rate R is just eq.3.19 integrated over energy, i.e.

$$R = \int_a^\infty (dR(E)/dE)dE \quad --- \quad 3.20.$$

where a is an arbitrary lower limit of integration. In the discussion above it was taken as 1 MeV.

The probability of a pulse of energy E and one of energy E' occurring in a time τ_a will be

$$P = 0.5\tau_a^2 R(E)R(E') \quad --- \quad 3.21.$$

and

$$d^2P/dEdE' = 0.5\tau_a^2 (dR(E)/dE)(dR(E')/dE') \quad --- \quad 3.22.$$

A reasonably realistic form of R(E) is

$$R(E) = A\exp(-kE) \quad --- \quad 3.23.$$

and with this functional form,

$$d^2P/dEdE' = 0.5k^2A^2\tau_a{}^2\exp(-kE)\exp(-kE') \quad --- \quad 3.24.$$

It is required that the energies of the two pulses should satisfy

$$E_o \leqslant E + E' \leqslant E_o + \Delta \quad --- \quad 3.25.$$

that is, the piled up pulse should have an energy in the interval E_o to $E_o + \Delta$. The probability for this is

$$P = 0.5k^2A^2\tau_a{}^2\{\int_0^{E_o} e^{-kE}dE \int_{E_o-E}^{E_o-E+\Delta} e^{-kE'}dE' + \int_{E_o}^{E_o+\Delta} e^{-kE}dE \int_0^{E_o-E+\Delta} e^{-kE'}dE'\} \quad 3.26.$$

This turns out to be

$$P = kA^2\tau_a{}^2 e^{-kE_o-\frac{1}{2}k\Delta}\{\mathrm{Sinh}\tfrac{1}{2}k\Delta\{E_o + {}^1/_k\} - \tfrac{\Delta}{2}e^{-\frac{1}{2}k\Delta}\} \quad --- \quad 3.27.$$

The number of pulses which pile up per second into the region E_o to $E_o + \Delta$ is

$$P/\tau_a = kA^2\tau_a e^{-kE_o-\frac{1}{2}k\Delta}\{\mathrm{Sinh}\tfrac{1}{2}k\Delta\{E_o + {}^1/_k\} - \tfrac{\Delta}{2}e^{-\frac{1}{2}k\Delta}\} \quad --- \quad 3.28.$$

To find the pile up rate in the interval (o,∞), $E_o = 0$, $\Delta = \infty$. Then

$$n_\infty = 0.5\tau_a A^2 \ s^{-1} \quad --- \quad 3.29.$$

But the total rate is A from eqs.3.23 and 3.20, so the total pile up rate will be

$$(0.5/\tau_a)(A\tau_a)^2 \quad --- \quad 3.30.$$

using eq.3.14 and ignoring the exponential term since $A\tau_a \simeq 2.10^{-3}$. Eq.3.30 is the same as eq.3.29 which shows that eqs.3.26 to 3.29 have the correct limiting behaviour.

The values of A and k which roughly fit eq.3.23 to the observed spectrum of anode pulses are $A \simeq 20.10^3$ and $k = 1.3$. Hence with $\tau_a = 100$ns, the pile up rate in the interval 10 to 20 MeV will be approximately one every 30 mins.

The effects of pulse pile up were investigated by comparing spectra taken at various count rates. As a general rule, if the total pulse rate above 1 MeV was kept below $20.10^3 s^{-1}$, no observable pile up occurred.

3.1.10. Sources of Background

Residual radioactivity in the crystal produces a well defined spectrum without beam on target.

Apart from the normal contaminants in NaI and radiation from surrounding materials, radioactive nuclides are produced in neutron capture. During bombardment of the target, neutrons can initiate 'prompt' events in the crystal such as $^{127}I(n,\gamma)^{128}I$ (σ_{th} = 6.2b, Q = 6.8 MeV) and $^{23}Na(n,\gamma)^{24}Na$ (σ_{th} = 400mb. Q = 7 MeV). ^{24}Na decays to ^{24}Mg by β^- emission with a half life of 15 hours, and ^{24}Mg then decays to its ground state with a total gamma energy of 4.12 MeV. This pulse is frequently observed in the low energy spectrum. ($\lesssim$9 MeV).

Bombardment of carbon with alpha particles produces neutrons from the $^{13}C(\alpha,n)^{16}O$ reaction. At E_α = 7.88 MeV fast neutrons can have a maximum energy of 9.7 MeV. Although there is about 11.5cm of paraffin wax in each collimator, roughly 30% of the fast neutron flux will not be stopped. A few of these fast neutrons may be thermalised in the NaI crystal in scintillation type processes. Finally, the neutrons may be captured by ^{127}I. This series of events could generate pulses in the crystal which had an equivalent pulse height of the neutrons kinetic energy plus the Q value for capture by ^{127}I. Since thermalisation times of fast neutrons are roughly of the order of milliseconds, it is unlikely that this energy would appear as one coherent pulse. Rather, it would be spread out over a time interval of a m.s. or so. A more probable explanation is the radiative capture of fast neutrons by ^{127}I.

For example, the $^{127}I(n,\gamma)$ cross section at 6 MeV is 0.03 barns, or there is roughly a 1% chance of radiative capture in 10" of NaI.

3.1.11. Calibration of the Spectrometer

The low energy part of the spectrum can be calibrated using an Am/Be source. ^{241}Am decays by alpha emission with a half life of 458 y. 4.43 MeV gamma rays are produced in the $^{9}Be(\alpha,n)^{12}C^*$ reaction. These are prominant in the spectrum. The neutrons produced can give the following gamma rays $^{127}I(n,\gamma)^{128}I$ Q = 6.8 MeV. $^{23}Na(n,\gamma)^{24}Na$ Q = 7.0 and $p(n,\gamma)d$ Q = 2.2 σ_{th} = 0.3b. The 4.12 MeV pulse from the decay of ^{24}Mg ($^{24}Na \xrightarrow{\beta^-} {}^{24}Mg^* \rightarrow$ 4.12 MeV γ) is unresolved from the 4.43 MeV $^{12}C^*$ gamma ray.

The high energy part of the spectrum was calibrated with three radiative capture reactions. These were

1)	$^{12}C(\alpha,\gamma)^{16}O$	E_α = 7.88	E_{γ_0} = 13.07
2)	$^{27}Al(p,\gamma)^{28}Si$	E_p = 6.75	E_{γ_0} = 18.08
3)	$^{11}B(p,\gamma)^{12}C$	E_p = 4.75	E_{γ_0} = 20.31

(Energies are in MeV)

These three gamma rays interpolate the region of interest in radiative capture reactions. In Fig.3.4, measured line shapes for reactions (1) and (2) are shown. The associated rejected spectra are drawn on a reduced scale with vertical lines drawn 500 keV below the centroids of the full energy peaks. There is some evidence of the first escape peak in both the accepted and rejected spectra.

The resolution of the spectrometer depends on the collimation geometry employed, being slightly improved for the smaller solid angle collimation (Fig.3.2.). It was generally better than 6% F.W.H.M. of the full energy peak.

3.1.12. Rejection Efficiency

Measurements of the rejection efficiency depend on

a) The region of the spectrum under consideration.
b) The beam intensity.

Rejection ratio is defined as:

R = Counts in accepted spectrum ⁄ Counts in rejected spectrum.

The region of the spectrum where R is measured was taken as 1 MeV above the highest energy gamma ray in the spectrum to 25 MeV. In the case of the $^{12}C(\alpha,\gamma)^{16}O$ reaction, this is 14-25 MeV. (E_{γ_0} = 13.07 MeV). The results obtained were

R = 5008:1 Beam off.
R = 2008:1 600na of $^{4}He^{++}$ on a C target.

The difference is attributable to the neutron flux from the $^{13}C(\alpha,n)^{16}O$ reaction.

3.1.13. Lineshape Fitting

Gamma ray yields were extracted from the measured spectrum using a standard line shape from a mono-energetic decay. It was found that the measured lineshape changed very little with energy over the region 10 to 20 MeV. Therefore one standard lineshape was used, the 13.07 MeV gamma ray from the $^{12}C(\alpha,\gamma_0)^{16}O$ reaction. As this lineshape is moved over the energy interval, its shape is altered so that the resolution remains constant.

From the calibration of the energy spectrum, the position of the γ_0 decay is specified. Separation of the first excited state and ground state locates the γ_1 peak and likewise for γ_2.

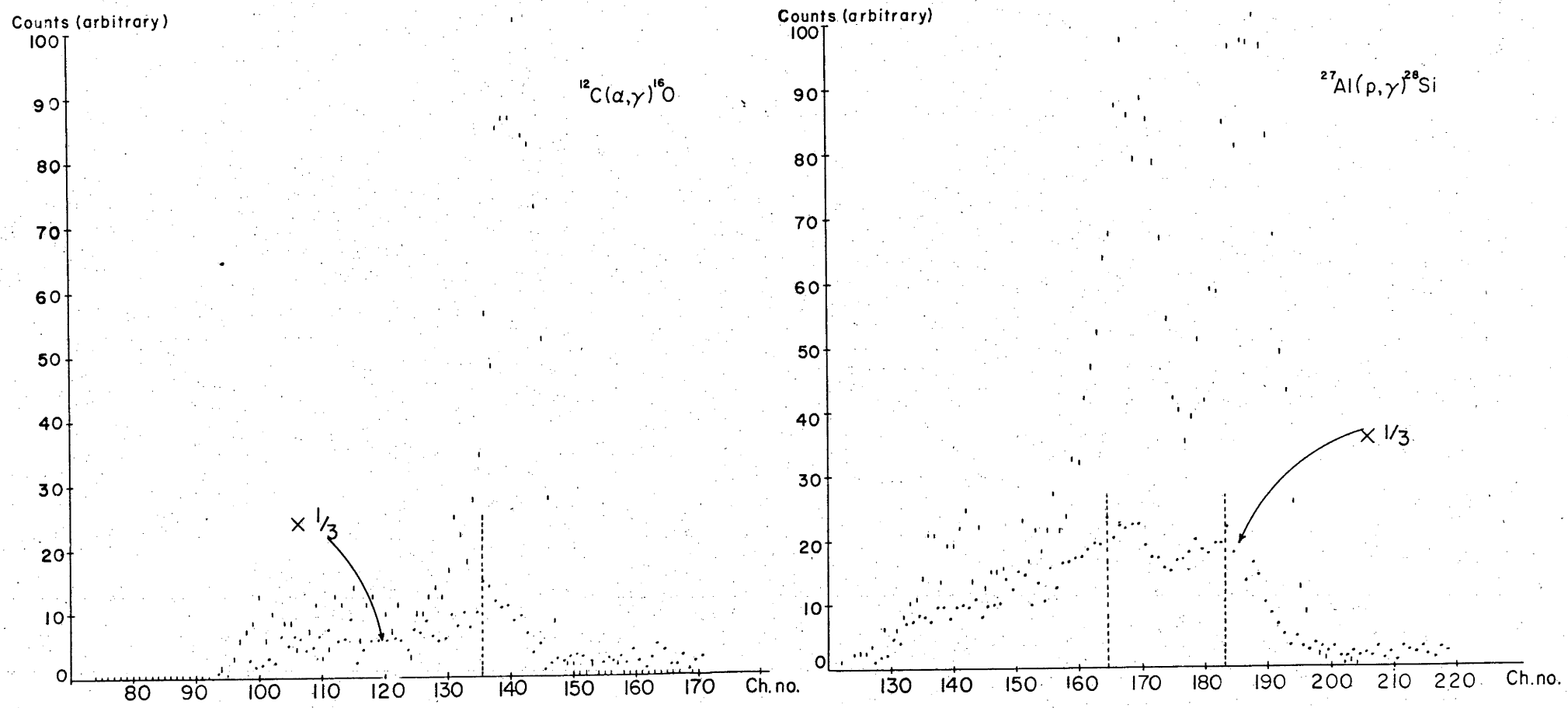

Fig.3.4. The $^{27}A(p,\gamma)^{28}Si$ decays to the ground and first excited state of ^{28}Si. The .... are the rejected spectra drawn on a reduced scale. (Collimator no.1).

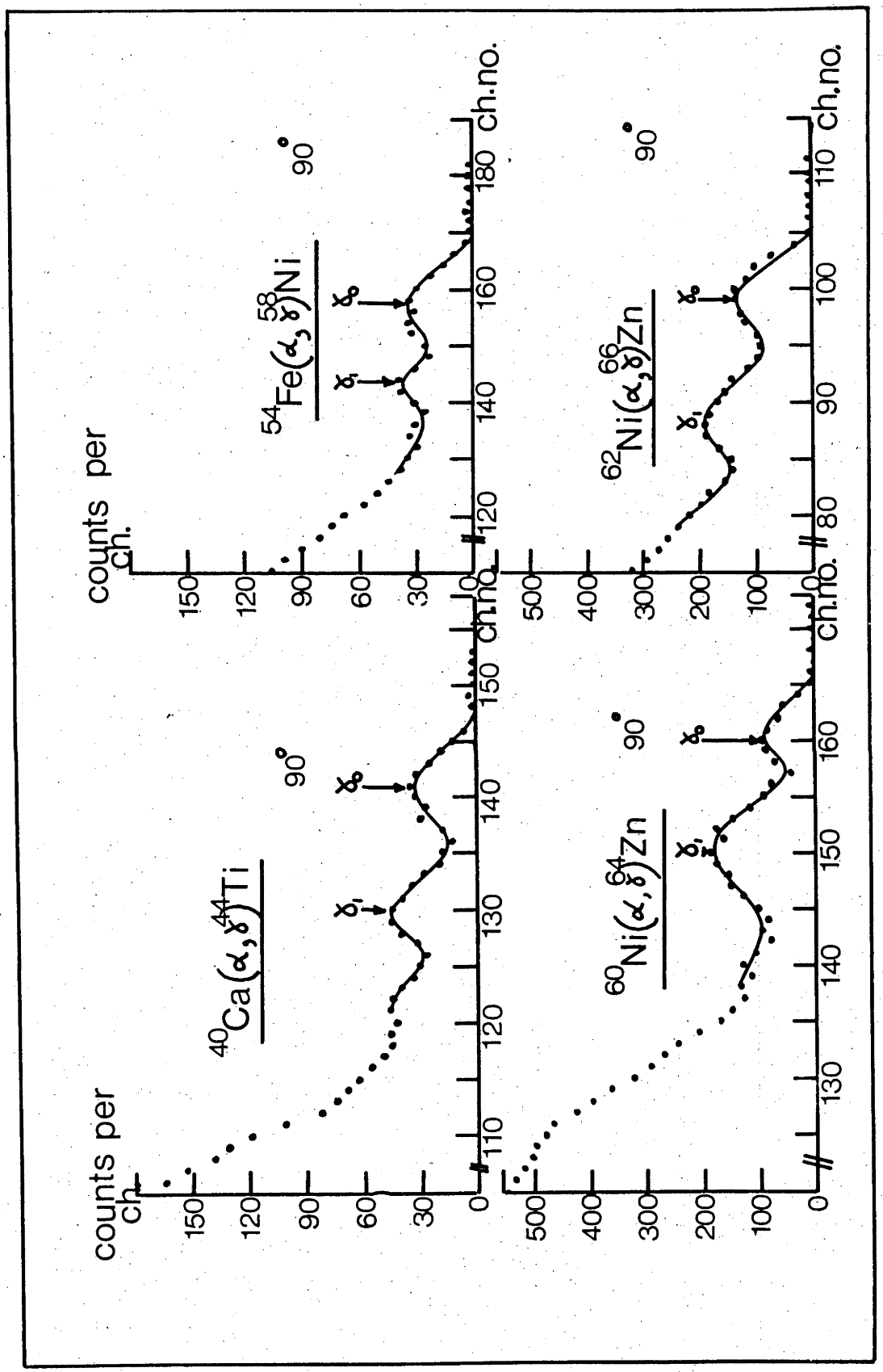

Fig.3.5. Examples of spectra taken for the reactions investigated. The smooth lines are fits generated by the method described in Section 3.1.13.

The appropriately broadened lineshape is moved to each peak position, and a linear least squares routine fits the standard components to the complex spectrum. If each standard component is labelled $f_\mu(x_i)$ where x_i denotes channel i and μ has values 1, 2, 3, then the quantity δ is minimised where

$$\delta = \sum_i \frac{1}{\sigma_i^2}\{S_i - \sum_\mu a_{\mu i} f_\mu(x_i)\}^2 \qquad --- \qquad 3.31.$$

S_i is the number of counts in channel i and σ_i^2 the variance. The intensities of the fitted components is then derived from the values of the coefficients $a_{\mu i}$. The uncertainties in the intensities are obtained from the diagonal elements of the inverse curvature matrix (e.g. Bevington p.154).

In some spectra a flat background was present above the highest energy peak due to neutron events and some cosmic radiation which was not rejected by the electronic circuitry. In this case, a flat background was subtracted from the entire spectrum before fitting the standard line shapes. Fitted lines were displayed superimposed on the data on a visual display unit. This was used in evaluating the quality of the fit together with the value of chisquared which was defined by

$$\chi^2 = \sum_i \frac{1}{\sigma_i^2}[S_i - \sum_\mu a_{\mu i} f_\mu(x_i)]^2 \qquad --- \qquad 3.32.$$

By changing the peak positions by one channel, a new fit could be obtained, and the best position was taken to be that which gave a good visual fit and a minimum value of χ^2. In some cases these criteria were mutually exclusive, in which case a compromise was made between the visual quality of the fit and χ^2.

In Fig.3.5 examples of fitted data are shown for the reactions investigated.

3.1.14. Absolute Cross Sections

The efficiency of the spectrometer was defined as

$$\varepsilon = \text{no. detected in } \delta\Omega / \text{ no. emitted into } \delta\Omega \qquad --- \qquad 3.33.$$

where $\delta\Omega$ is the solid angle of the spectrometer. In order to determine this quantity, three standard reactions for producing high energy gamma rays were used. These have cross sections which have been reliably measured.

$^{12}C(\alpha,\gamma_0)^{16}O$.

From the widths given by Ophel et.al. (Op 75) $\sigma(\alpha,\gamma) = 37\mu b$ at $E_\alpha = 7.88$ MeV. This agrees quite well with the value given by Snover

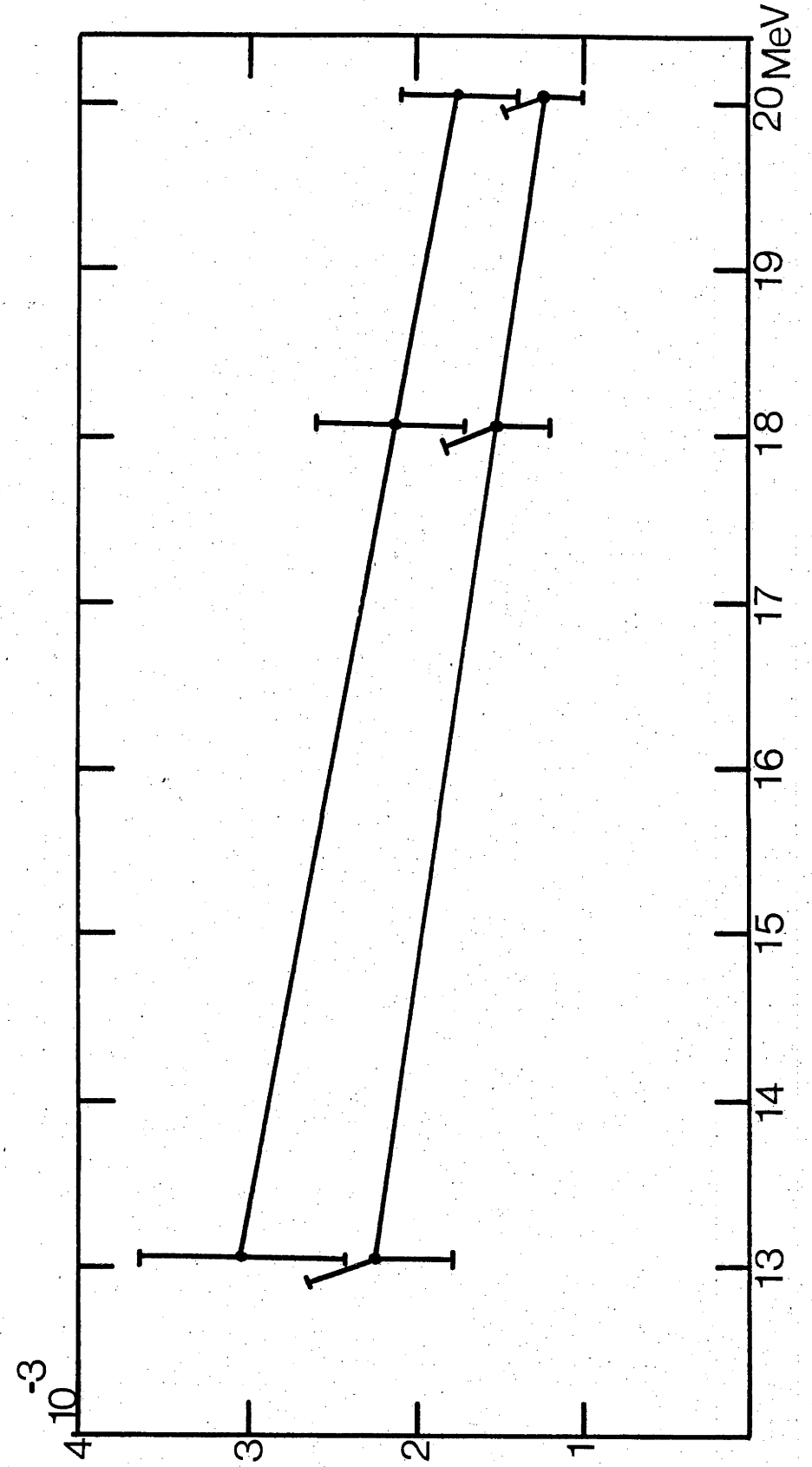

Fig.3.6. Total efficiency of the crystal for collimators 1 and 2. (Lower line, upper line respectively).

et.al. (Sn 74) of $\sigma(\alpha,\gamma_0)$ = 44μb. Since there was no preference for either value, a mean was chosen of

$$\sigma(\alpha,\gamma_0) = 41 \pm 2.5\mu b.$$

$^{27}Al(p,\gamma)^{28}Si$.

The cross section for this reaction has been measured by Allas (Al 64a). At E_γ = 18.08 MeV, $d\sigma/d\Omega = 6.4 \pm 0.4\mu b.sr^{-1}$.

$^{11}B(p,\gamma_0)^{12}C$.

This has also been measured by Allas (Al 64). The cross section at E_γ = 20.31 MeV is $d\sigma/d\Omega = 4 \pm 0.3\mu b.sr^{-1}$.

The uncertainty in the efficiency arises from counting statistics target thickness uncertainty and errors in the above cross sections. The error bars in Fig.3.6 estimate the total uncertainties involved.

The absolute differential cross section is determined by

$$d\sigma/d\Omega = 0.0637n\ m(It\varepsilon^i)^{-1} \quad nb.sr.^{-1} \qquad --- \qquad 3.34.$$

where n is the number of gamma rays detected using collimator number i. (i = 1 or 2). m is the mass number of the target. I is the integrated beam current in mC. t is the target thickness in $\mu g.cm^{-2}$ and ε^i is the total efficiency using collimation geometry i. ε^i is given in Fig.3.6.

3.1.15. Errors

The error in the determination of the absolute cross section arises from the following causes. They may be divided into statistical and systematic errors.

The error in the number of counts in the full energy peak contains an error due to the fitting procedure and a statistical error given by $\sqrt{n}$. The error in the fitted intensity varied between about 3 and 15%, and the statistical error varied between about 3 and 15% giving a total error of between 4 and 21%. The error in the integrated beam intensity was taken to be 5%. The error in target thickness measurement was about 8%. The error in the efficiency of the crystal was 15%.

The statistical error of each datum is about 7% on the average, while the systematic error in the absolute differential cross section is about 20%.

3.2. Experimental method

3.2.1. The Alpha Beam

Negatively charged alpha particles were produced in a H.V.E.C. duoplasmatron and lithium exchange negative ion source. These were accelerated by the A.N.U. EN Tandem Van de Graaff generator, magnetically analysed and directed down the appropriate beam line by a switching magnet. The beam was focussed through a $\frac{3}{16}$" diameter tantalum collimator about 1 foot from the target by a quadrupole doublet lens. Typically, 3μa of $^4He^-$ would be produced by the ion source giving about 1.2μa of $^4He^{++}$ on target at a terminal voltage of 4.5 MV. In order to obtain maximum beam on target, both the object and image slits of the analysing magnet were set at ±0.150". The measured beam resolution under these conditions was about 15 keV. Most data were obtained for an integrated beam charge of 2mC. The running time per datum was about 45 minutes, so the time factor was an important consideration. The statistics were often of the order of 10%, but this had to be tolerated in order to complete a reasonable survey.

Beam was maximised by focussing through the $\frac{3}{16}$" collimator and monitoring the current on it. At most energies it was possible to focus so that the collimator current was zero.

3.2.2. Vacuum

Vacuum in the beam line and target chamber was maintained by a well-baffled water-cooled oil diffusion pump. Typically, pressure in the line was about 10^{-6}torr. Protection interlocks closed valves at a threshold of about 10^{-5}torr.

3.2.3. Targets and Beam Integration

Tests showed that integrating the beam on a gold disc in the perspex target chamber and in a Faraday cup several meters from the target gave consistent results within 5%. For this reason integrating the beam on the target was considered a reliable way of measuring the absolute beam charge. This allowed observation at zero degrees to the beam direction. The integrated beam charge was digitised by an Ortec charge digitiser and recorded on a preset stop scaler which controlled data collection by the IBM 1800 computer.

In the bombarding energy range of interest (4-18 MeV alpha energy) it was found that a clean gold blank produced a negligible flux of high energy

gamma rays. Consequently, a 0.020" thick Au blank was used as a backing material for all the targets. Isotopically enriched target material was evaporated from a tantalum boat by R.F. induction heating. Monitor foils were used to assess the target thickness by precision weighing, and a Sloane thickness monitor provided continuous deposition rate information during evaporation. Targets susceptible to oxidation (Ca, Fe) were kept under vacuum and handled in an atmosphere of dry high purity argon.

Thickness measurements.

Besides precision weighing and continuous monitoring of target thickness during evaporation, a variety of other methods were used. All the methods are summarised below.

(1) Precision weighing.

A weighed monitor foil was placed symmetrically to the target during evaporation and weighed afterwards. The accuracy of this method is estimated to be about 10% for targets about 1 $mg.cm^{-2}$.

(2) Deposition monitor.

This method relies on the change in resonant frequency of a quartz crystal due to material evaporated onto it. In principal this method is very accurate. The change in frequency is measured by the beat frequency. A thickness of 1 $\mu g.cm^{-2}$ should cause a change of approximately 10 Hz and the accuracy of the method should be a few percent.

(3) $^{13}C(p,\gamma)^{14}N$ resonance measurement.

In the case of the carbon calibration target used, a convenient $^{13}C(p,\gamma)^{14}N$ resonance exists at E_p = 1.7476 MeV, E_γ = 9.172. The principal uncertainty is in estimating the width of the yield curve. This was estimated to be about 10%.

(4) Energy loss technique.

This method relies on knowledge of the stopping power of a material. Alpha particles are scattered from the target backing material (Au) into a magnetic spectrometer described in Chapter 1. The elastic continuum spectrum is observed, and by changing the magnetic field, the position spectrum is moved on the P.S.D. The Au backed target is now placed in the beam, and the continuum spectrum is again recorded. From the position on the counter and calibration of position v.s. field from the first two measurements, the energy loss in the target material may be calculated. The uncertainties of this method are:

i) Ascertaining the exact channel numbers of the position spectra. The channel number where the distribution had fallen to half its maximum height was used.

ii) Uncertainty in the stopping power tables. The tables of Williamson et.al. (Wi 66) were used to determine the thickness in $\mu g.cm^{-2}$ from the energy loss. The error of this method was estimated to be about 5%.

iii) If the target material contains contaminants such as oxygen or nitrogen, this method will give an unreliable estimate of the thickness of the isotope of interest.

(5) Proton fluorescence

Some of the target thicknesses were determined by the proton induced fluorescence method. An H.V.E.C. 2 MV Van de Graaff generator exists in the laboratory mainly for atomic physics studies. The apparatus is described by Newton (Ne 75). Basically, a Kevex X ray detector detects the X radiation from the atomic rearrangement of electron shells after a proton has collided with a target atom. The apparatus is calibrated by detecting backscattered particles from a thin target of the material to be measured. The yield of backscattered protons is given by

$$Y_p = AIt\sigma_R\delta\Omega_D \qquad \text{---} \qquad 3.35.$$

where A is a constant which depends on the units used. I is the integrated beam current, t the target thickness, σ_R the Rutherford cross section and $\delta\Omega_D$ the solid angle subtended by the particle counter (which is at 160° to the beam direction). If the yield of X rays is written

$$Y_x = BIt \qquad \text{---} \qquad 3.36.$$

where B is a function of E_p.

Using equation 3.35,

$$Y_x = BY_p(A\sigma_R\delta\Omega_D)^{-1}$$

$$\text{or} \quad B = A\sigma_R\delta\Omega_D Y_x/Y_p \qquad \text{---} \qquad 3.37.$$

The procedure adopted was to determine B of eq.3.36 using a thin self supporting target of carbon and iron. (The two targets measured by this method). The advantages of using thin targets for this are:

i) The energy spectrum of backscattered protons contains a well-defined narrow peak.

ii) The constant B is determined at energy E_p rather than being averaged over the energy loss in a thick target. The targets were about 10 $\mu g.cm^{-2}$ thick.

Having fixed B for each element, the procedure was repeated with the gold backed targets and their thickness determined from eq.3.36. The accuracy of this method is between 5 and 10%.

3.2.4. Contamination of Targets

The principal contaminant was carbon which built up during bombardment. As discussed earlier, the gamma ray from the $^{12}C(\alpha,\gamma)^{16}O$ reaction may lie in the region of interest. Also, the neutron flux from the $^{13}C(\alpha,n)^{16}O$ reaction is a potential threat. Extensive studies of these reactions have been made and they were used to assess the importance of carbon contamination. ($^{12}C(\alpha,\gamma)^{16}O$: Su 67, Op 64. $^{13}C(\alpha,n)^{16}O$: Wa 57, Bo 56). Carbon contamination of the targets was monitored by the $^{12}C(\alpha,\gamma_0)^{16}O$ reaction at E_α = 7.88 MeV, or the $^{13}C(p,\gamma)^{14}N$ resonance at E_p = 1.749 MeV. If more than 1 $\mu g.cm^{-2}$ of carbon built up on the target under study, then it was changed to a new one.

The other possible contaminants in the readily oxidizable targets were ^{16}O and ^{14}N. ^{16}O contamination was checked by the $^{16}O(\alpha,\gamma)^{20}Ne$ resonances at E_α = 6.93 and 7.94 MeV (Pe 64). By careful handling of the Ca and Fe targets in vacuum and dry argon, oxygen contamination was avoided.

Nitrogen contamination was checked for by the $^{14}N(p,\gamma)^{15}O$ reaction at E_p = 2.48 MeV (Ev 67). This corresponds to an excitation energy of 9.60 MeV in ^{15}O with a strong gamma decay to the ground state. No radiation was observed at this resonance energy implying that ^{14}N contamination was not a problem.

3.2.5. Measurements

Excitation functions were measured at 90° to the beam direction using collimator number 2. This has a half angle of 10°42'. The basic incremental step in the excitation function was chosen according to the target thickness and the time available to survey a region of the continuum. These steps ranged from 50 keV in the $^{40}Ca(\alpha,\gamma)^{44}Ti$ reaction to 250 keV in the $^{62}Ni(\alpha,\gamma)^{66}Zn$ reaction.

Angular distributions were measured with collimator number 1 which has a half angle of 8°51'. Seven angles were chosen so that the emerging

gamma ray was not obstructed by the target frame. Usually about ten angular distributions were measured for each nuclide at energies corresponding to extrema in the excitation function.

CHAPTER 4

Experimental Data and Analysis

4.1.1. Introduction

In this chapter, the experimental data of the work done will be presented, and the methods of analysis discussed. In the second part, interpretation of the data in terms of the theory described in Chapter 2 will be made. The conclusions will be left until Chapter 5.

In Table 4.1, a summary of the experimental data taken is given together with some other relevant information.

Table 4.1.

Target/Product	$Q(\alpha,\gamma_0)$ (MeV)	Step size of ex.funct.(keV)	Range of E_x(MeV)	No.of angular distributions
$^{40}Ca/^{44}Ti$	5.1	50	12.5-18.5	10
$^{54}Fe/^{58}Ni$	6.4	150	14.0-19.5	9
$^{60}Ni/^{64}Zn$	4.0	250	10.0-18.5	9
$^{62}Ni/^{66}Zn$	5.3	250	8.0-18.0	12

4.1.2. Excitation Functions

Excitation functions were measured for both γ_0 and γ_1 decay channels in the step sizes shown in Table 4.1. They were taken with the spectrometer at 90° to the beam direction using collimator number 2. (Half angle 10°42'). The results are shown in Figs.4.1 to 4.4. The error bars on the data are statistical errors only. Typical spectra for these reactions are shown in Fig.3.5, together with fits generated by the line shape fitting procedure described in Section 3.1.13.

In Fig.4.5, the low-lying levels of the residual nuclei are shown. In all cases, the first excited state has a $J^\pi = 2^+$ lying about 1 MeV above the 0^+ ground state.

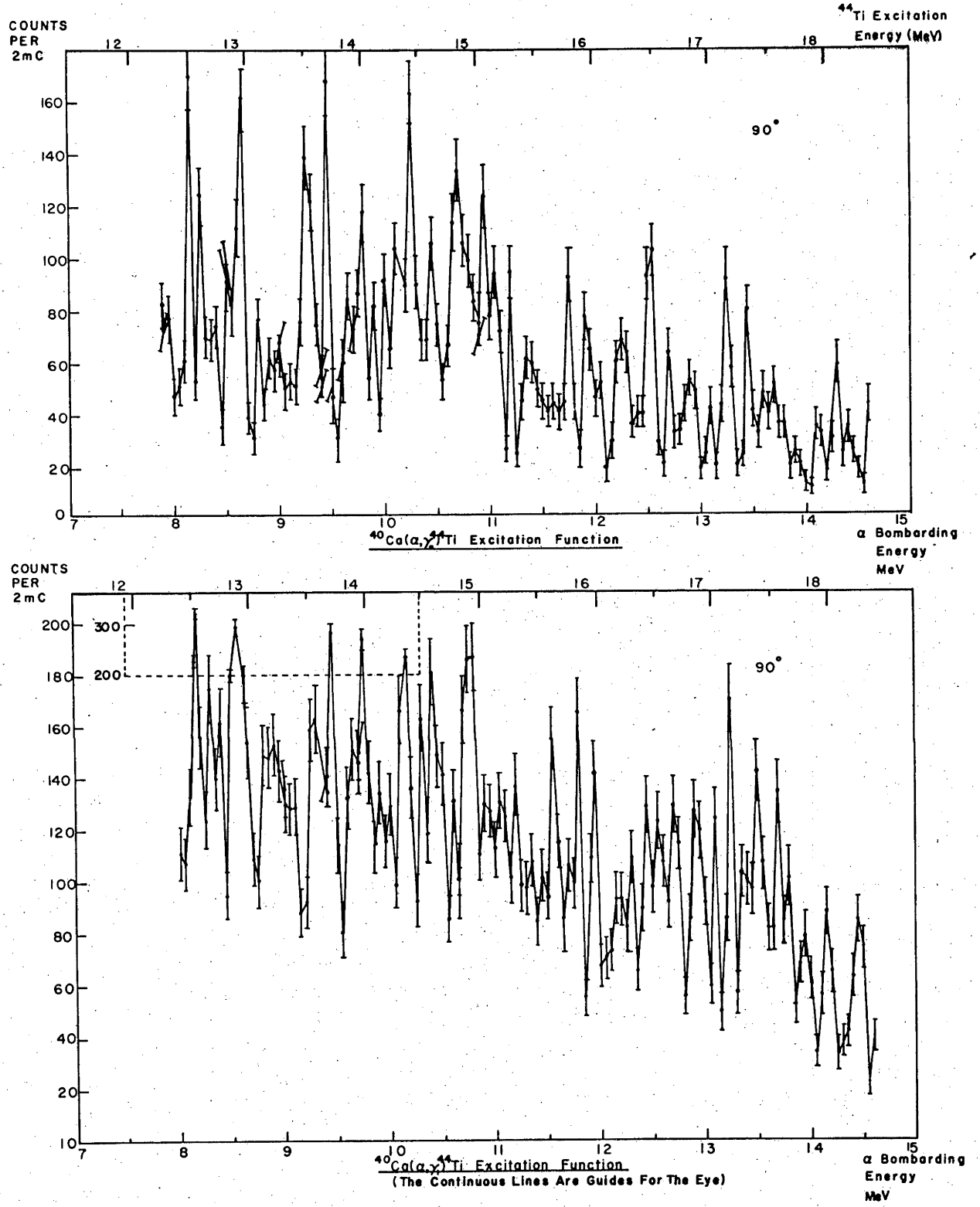

Fig.4.1. The $^{40}Ca(\alpha,\gamma_0)^{44}Ti$ and $^{40}Ca(\alpha,\gamma_1)^{44}Ti$ excitation functions.

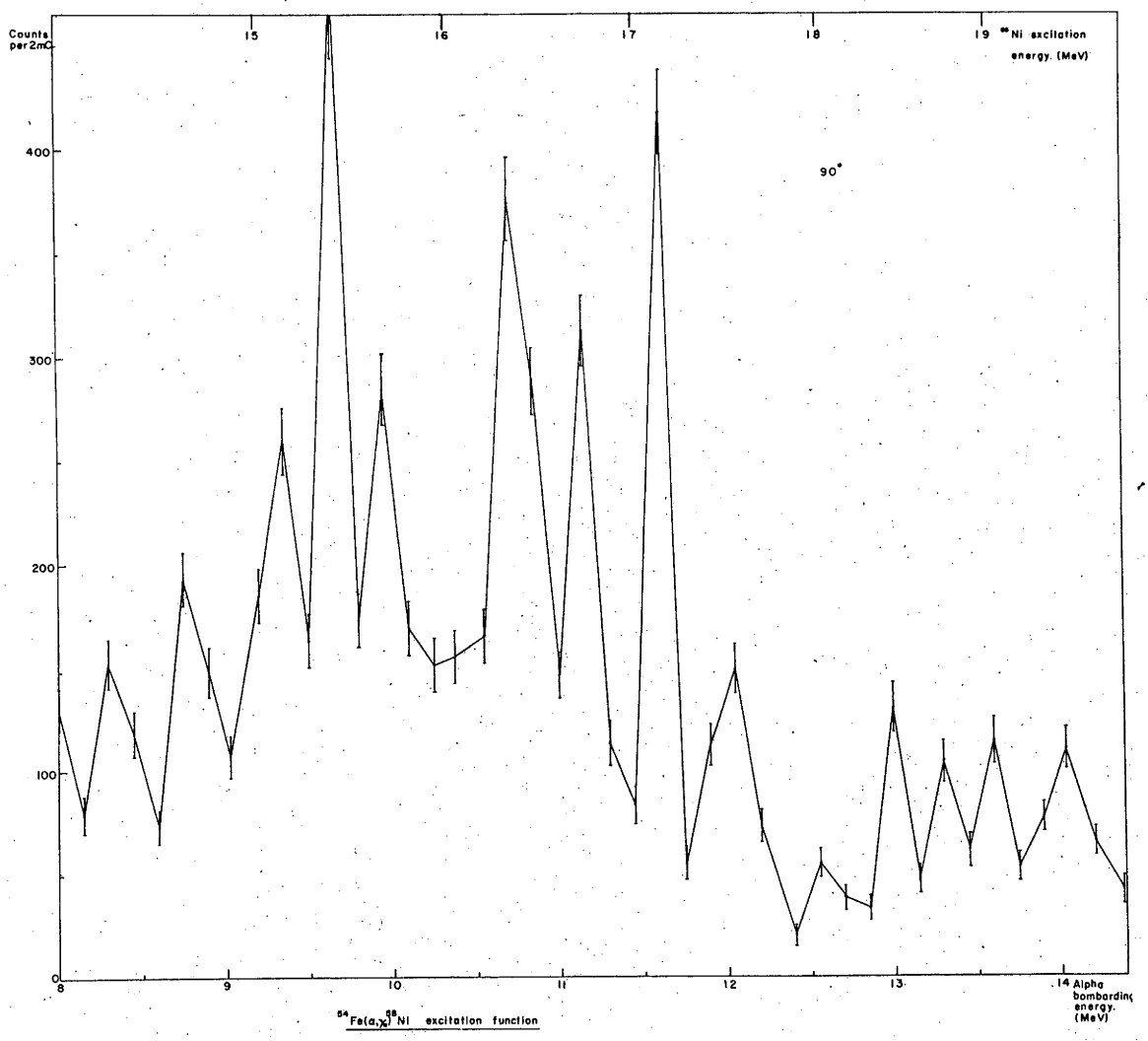

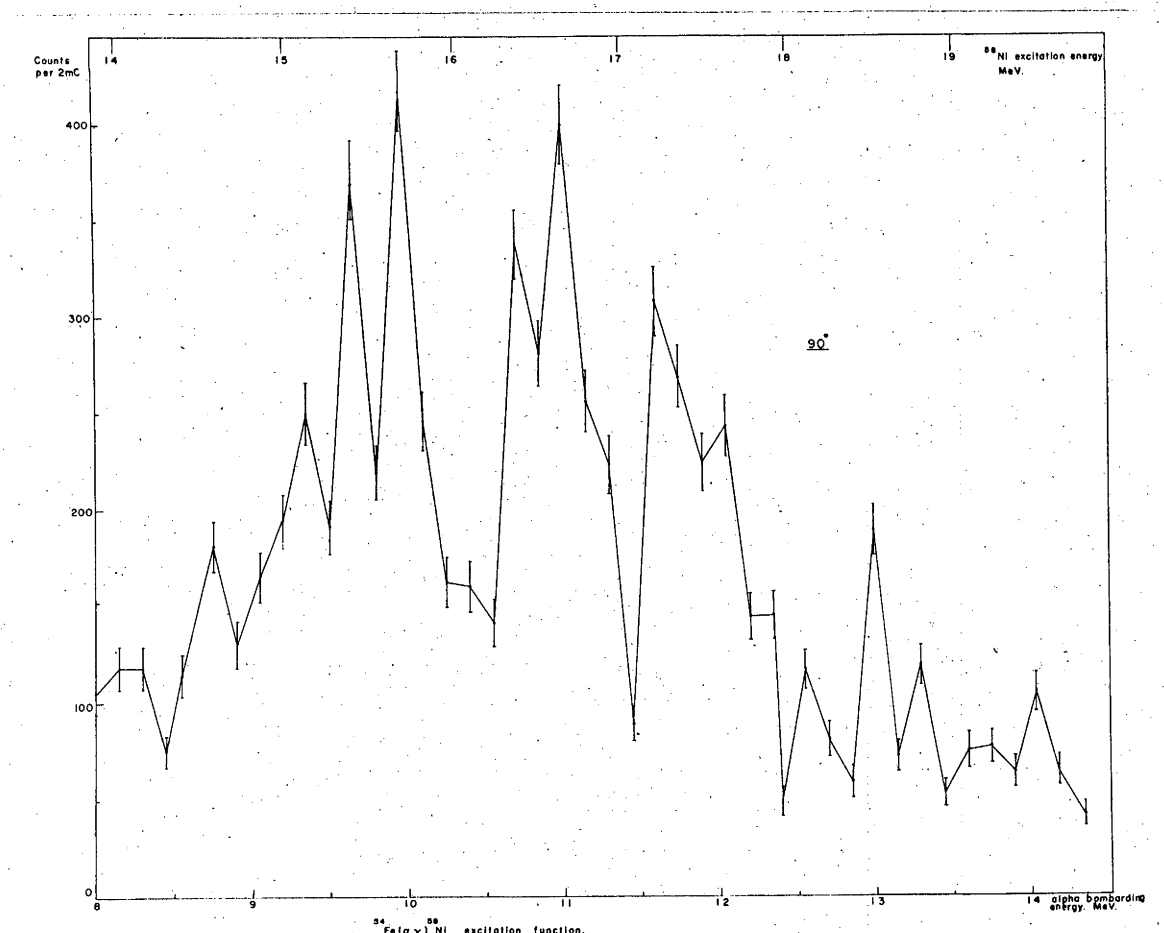

Fig.4.2. $^{54}Fe(\alpha,\gamma_0)^{58}Ni$ and $^{54}Fe(\alpha,\gamma_1)^{58}Ni$ excitation functions.

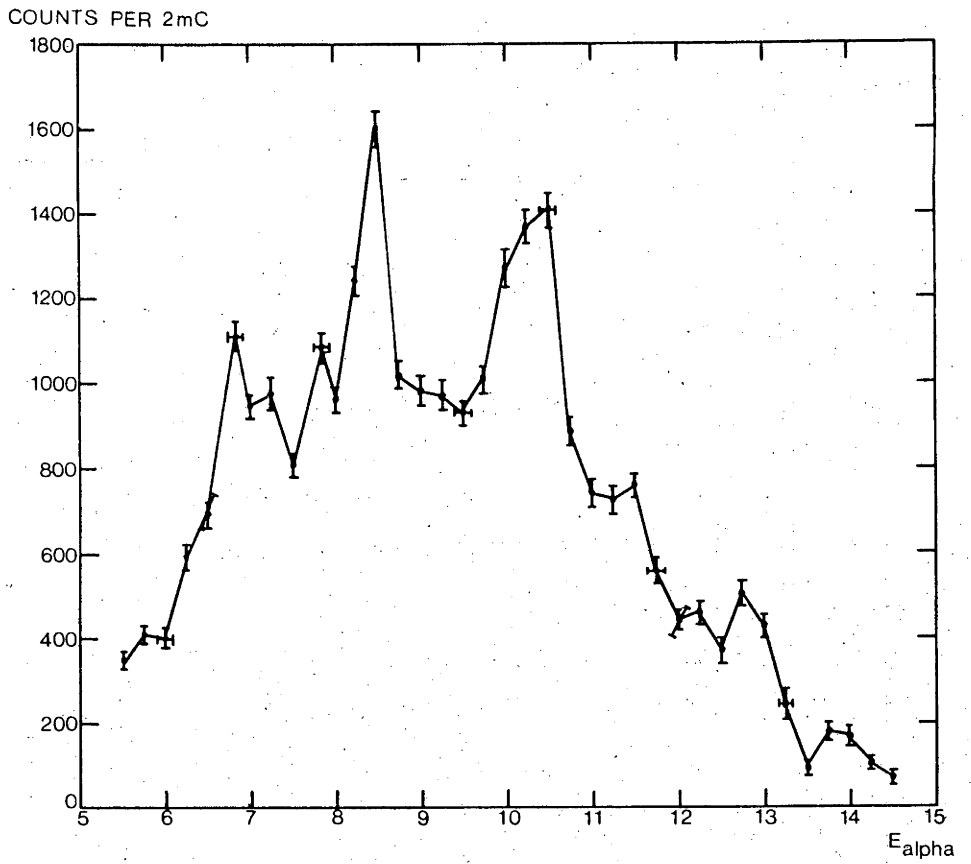

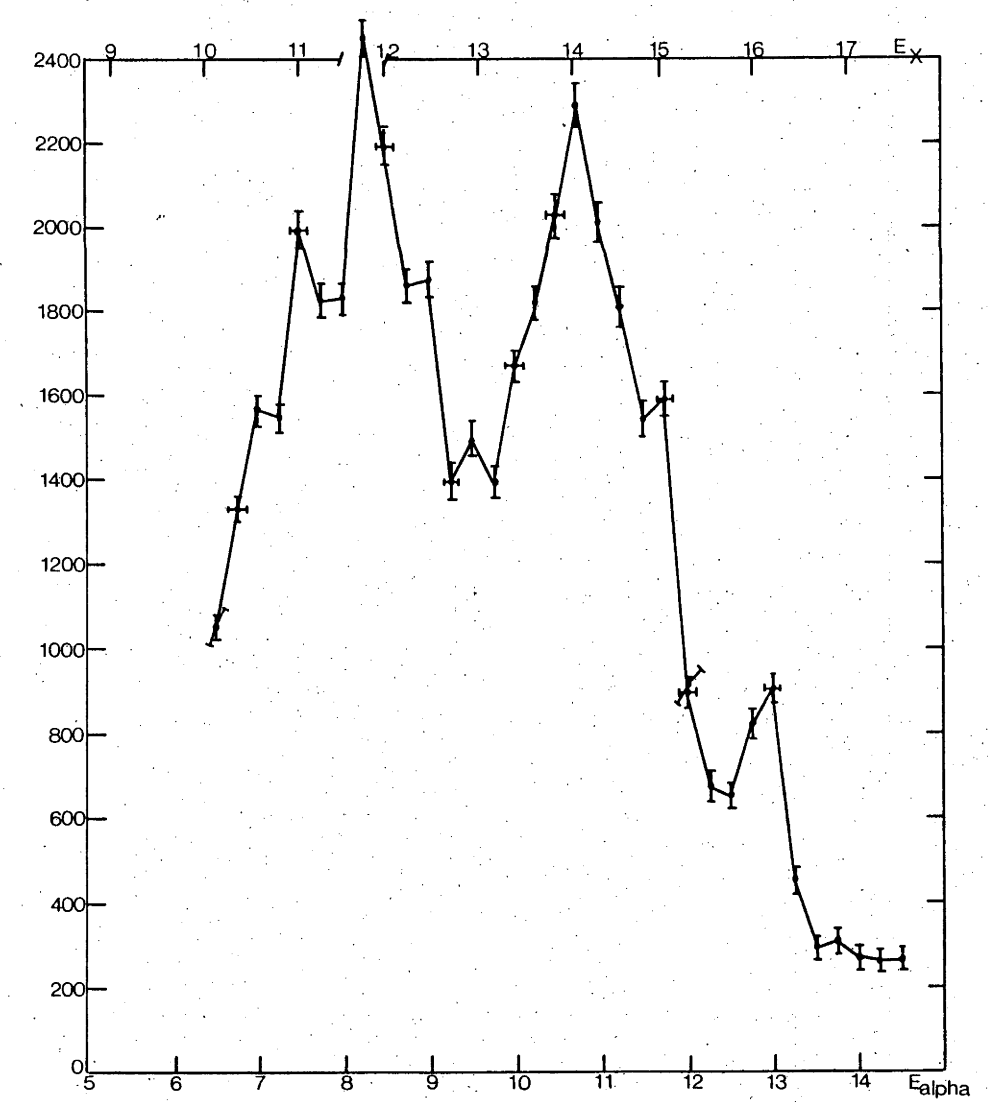

Fig.4.3. $^{60}Ni(\alpha,\gamma_0)^{64}Zn$ and $^{60}Ni(\alpha,\gamma_1)^{64}Zn$ excitation functions.

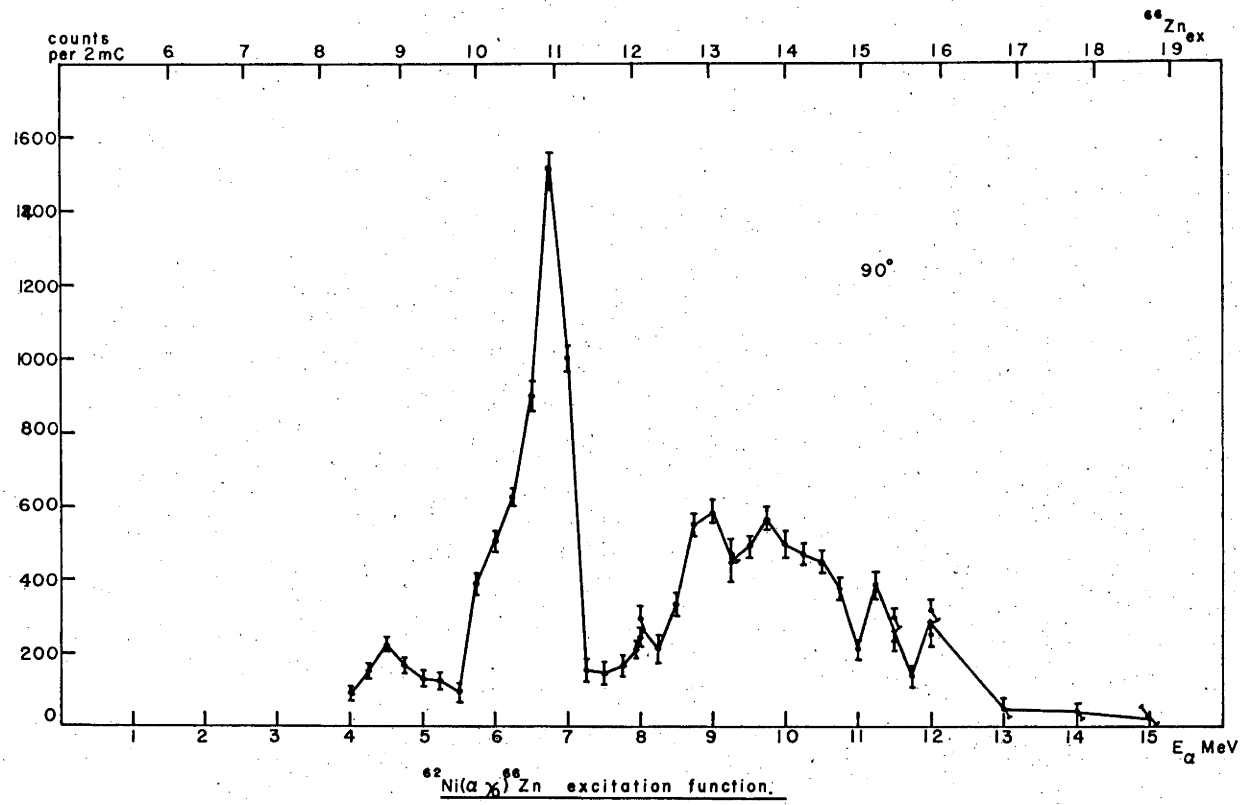

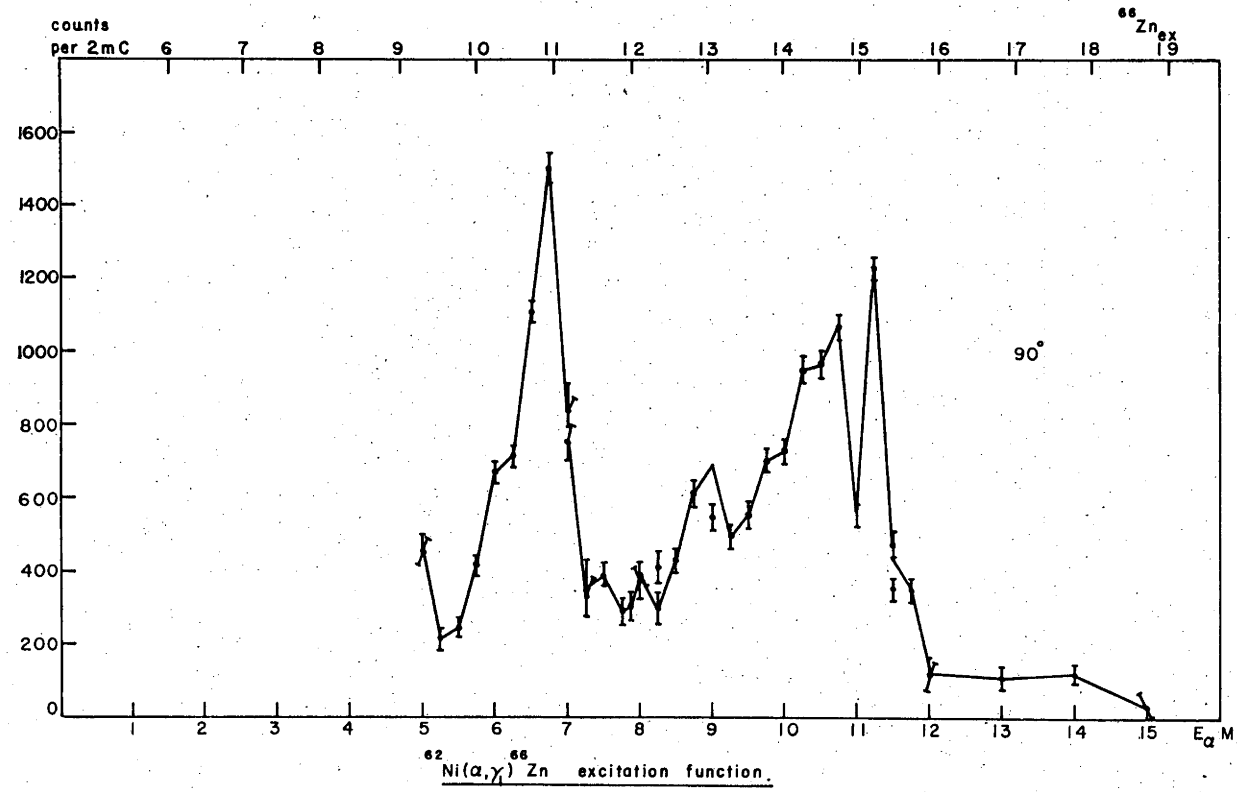

Fig.4.4. $^{62}Ni(\alpha,\gamma_0)^{66}Zn$ and $^{62}Ni(\alpha,\gamma_1)^{66}Zn$ excitation functions.

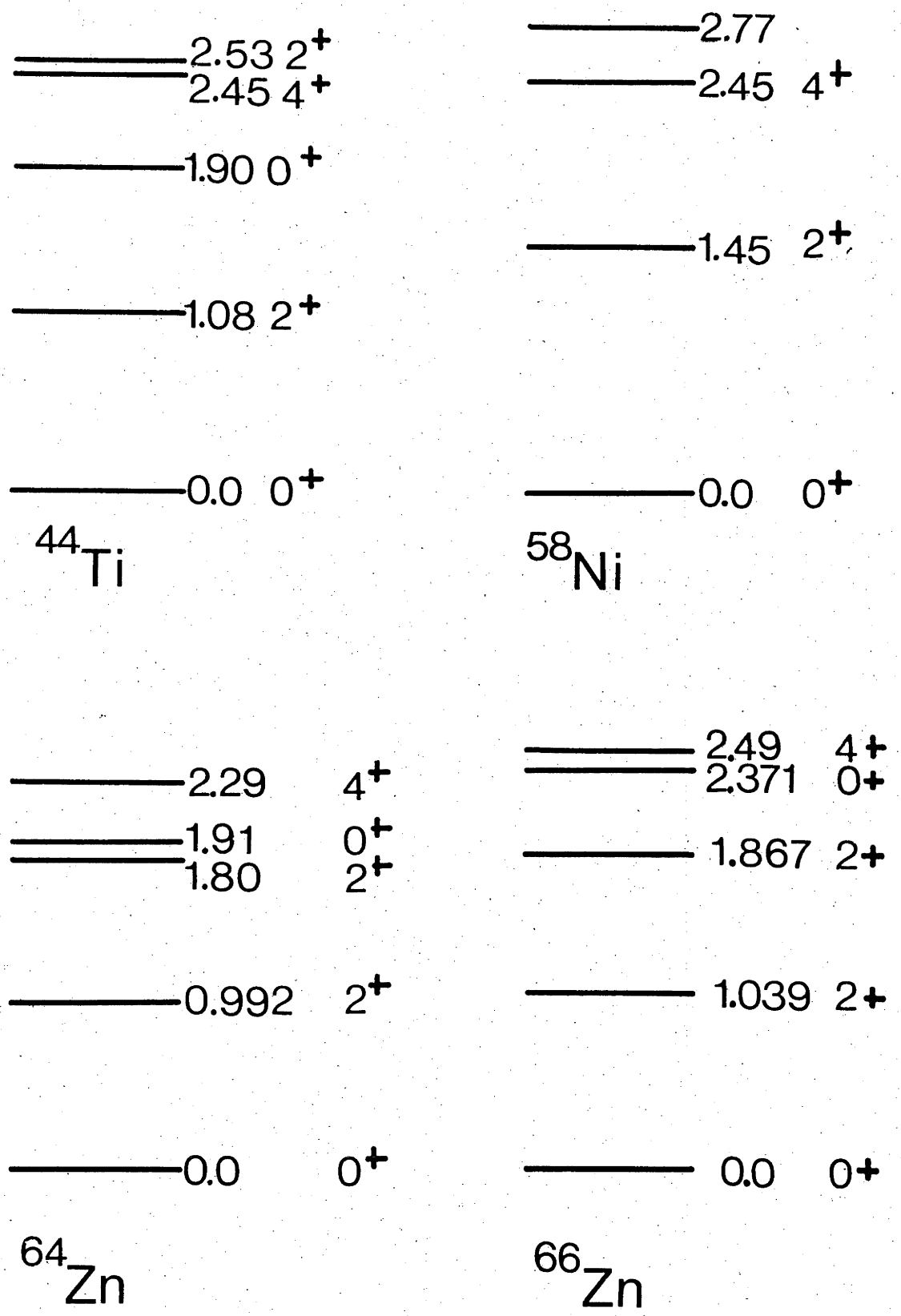

Fig.4.5. Low-lying levels of the residual nuclei from the reactions studied. The data for ^{58}Ni, ^{64}Zn and ^{66}Zn are taken from Le 67, those for ^{44}Ti from En 73.

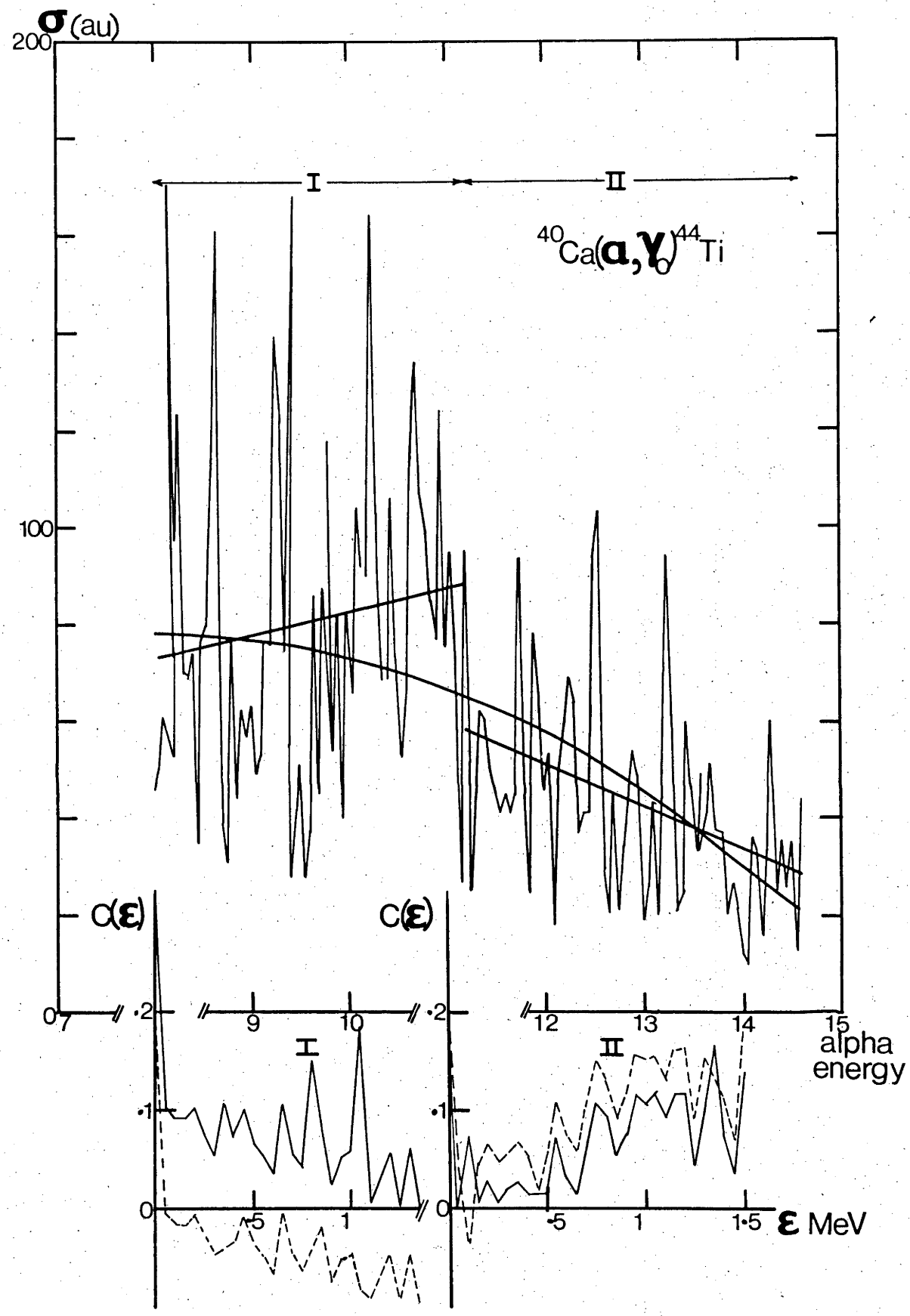

Fig.4.6. The $^{40}Ca(\alpha,\gamma_0)^{44}Ti$ excitation function. The data are smoothed with (a) two straight lines over the regions 8-11 MeV and 11-14.5 MeV, (b) a quadratic fit $a+bE+cE^2$ over the entire region. In the lower part of the figure, the autocorrelation functions are shown for the two regions (I and II) using a value of $\langle\sigma(E)\rangle$ calculated from the two methods of smoothing the data (a and b). Solid lines are using a and broken lines using b. Note the characteristic offset from the ordinate and sloping trend.

4.1.3. Correlation of Fluctuation Structure

According to the fluctuation theory of Ericson (Er 63), fluctuations in an excitation function which are caused by overlapping states in a compound nucleus should be correlated over an energy interval Γ which is the average width of the states involved. It is implicit in the theory that the experimental resolution (beam resolution plus energy loss in target) ρ is much smaller than Γ. While this is quite easy to achieve in (p,γ) reactions for example, in the present experiments it may be assumed that $\rho \gg \Gamma$ and there will be an averaging of the fluctuation structure.

A measure of the correlation between fluctuations is given by

$$C(\Gamma,\varepsilon) = \frac{\langle\sigma(E)\sigma(E+\varepsilon)\rangle}{\langle\sigma(E)\rangle\langle\sigma(E+\varepsilon)\rangle} - 1 \qquad \text{---} \qquad 4.1.$$

If the structure is caused by interference between overlapping levels in the compound nucleus, then it has been shown that

$$C(\Gamma,\varepsilon) = \frac{1}{N}(1-y_d^2)\,\frac{\Gamma^2}{\Gamma^2+\varepsilon^2} \qquad \text{---} \qquad 4.2.$$

N is sometimes called the fluctuation damping parameter and is the number of magnetic substates contributing to the reaction. In the γ_0 channel N=1. y_d is the fraction of direct component contributing to the reaction. It will be seen later that for the E1 radiative capture $y_d \simeq 0$. From eq.4.2, it is seen that $C(\Gamma,\varepsilon)$ should have a Lorentz shape as a function of ε with a F.W.H.M. of Γ and a value

$$C(\Gamma,0) = \frac{1}{N}(1-y_d^2)$$

In fact, eq.4.2 was derived for an infinite set of data, and since all measurements involve finite sets, a correction for this should be made. It has been shown (e.g. Al 65) that the finite range of data allows the tail of the function $C(\Gamma,\varepsilon)$ to fluctuate about the abscissa with a standard deviation given by:

$$C(\Gamma,\varepsilon) = 0 \pm \frac{1}{N}\sqrt{\pi/2n} \qquad \text{---} \qquad 4.3.$$
$$\varepsilon \gg \Gamma$$

n is referred to as the number of independent cross sections. There is some confusion in the literature as to whether $n = I/\Gamma$ or $n = I/\pi\Gamma$ where I is the range of the excitation function. Since the fluctuations should be correlated over an energy width Γ, the former definition of n is used (e.g. Al 65, El 66, Gi 65). There is also an error on the value of Γ due to the finite range of data as measured by the F.W.H.M. of the curve; this is given by (B-M 68)

$$\frac{\Delta\Gamma}{\Gamma} = \pm \left[\frac{3\pi}{4} \frac{(N+1)}{nN}\right]^{1/2} \qquad \text{---} \qquad 4.4.$$

4.1.4. Modulation of Fluctuation Structure

It has been found (e.g. Al 65, Ga 65) that excitation functions which do not have a constant value of the average cross section reflect this in the autocorrelation function. If the data have an average cross section which is a function of energy, then using the definition of $C(\Gamma,\varepsilon)$ from eq.4.1 leads to a curve which has an offset from the abscissa (Fig.4.6). In fact, the offset can be arbitrarily set by varying the average values in the denominator of eq.4.1. Often the curve is not only offset from the abscissa but also tilted with respect to it, and it is clear that this distortion is due to the modulation of the fluctuation structure by the changing average value. For example, in Fig.4.6, the $^{40}Ca(\alpha,\gamma_0)^{44}Ti$ data are shown with $C(\Gamma,\varepsilon)$ calculated using different averages of $\sigma(E)$. The data are divided into two sections. The first section below about 11 MeV alpha energy has a monotonic increasing trend, and that above 11 MeV a monotonic decreasing trend. In the lower part of the figure, $C(\Gamma,\varepsilon)$ is shown where $\langle\sigma(E)\rangle$ has been obtained from the straight line fits (straight lines) and from the quadratic fit to the entire set of data (curved line). This demonstrates the distortion referred to previously. To remove this distortion (or to demodulate the fluctuation structure), $\sigma(E)$ is averaged over intervals Δ which are small enough to average out the fine structure but which are not so large that any broader structure is averaged over. According to Elliott and Spear (El 66), this interval is best chosen by calculating $C(\Gamma,0)$ for various intervals Δ

$$C(\Gamma,0) = \left\langle \left[\frac{\sigma(E) - \langle\sigma(E)\rangle_\Delta}{\langle\sigma(E)\rangle_\Delta}\right]^2 \right\rangle \qquad \text{---} \qquad 4.5.$$

When this is done, a curve is obtained as shown in Fig.4.7. The initial increase is due to the fine structure being averaged over. It then levels off before increasing again when broader structure is starting to be averaged over.

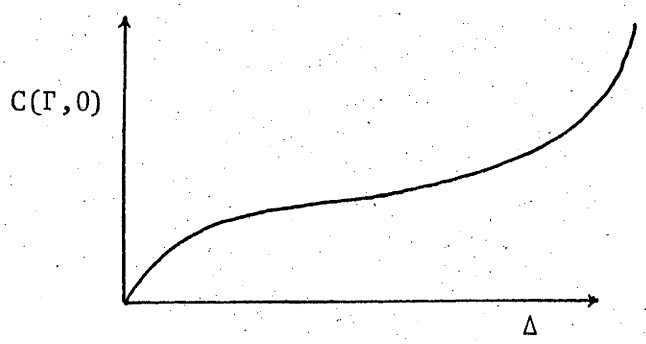

Fig.4.7.

A suitable value of Δ is where the curve is inflecting in Fig.4.7. This procedure was carried out for the ^{40}Ca data in Fig.4.6, and the autocorrelation function recalculated using this value of Δ as an averaging interval. The result is shown in Fig.4.8 and it can be seen that it has the correct Lorentzian shape for small ε and an oscillating tail for $\varepsilon>>\Gamma$. As mentioned earlier, the $^{40}Ca(\alpha,\gamma)^{44}Ti$ reaction is expected to proceed almost entirely through a compound process, and later calculations show this to be so. In this case, $y_d\simeq 0$ and in the γ_0 channel N=1. Therefore, $C(\Gamma,0)=1$ according to the theory, but it can be seen from Fig.4.8, for example, that $C(\Gamma,0)<1$. This is due to the phenomenon of resolution damping which will now be discussed.

4.1.5. Resolution Damping

It is possible to use a new value of N such that the expected value of $C(\Gamma,0)$ agrees with the experimental value. This may be understood from the fact that approximately $\rho/\pi\Gamma+1$ fluctuations are averaged over with an experimental resolution ρ. In fact, Fessenden et.al. (Fe 65) suggest that the value of $C(\Gamma,0)$ is damped by this factor and the mean level width Γ can be obtained from the expression:

$$C(\Gamma,0) = \frac{1}{N(\rho/\pi\Gamma+1)}(1-y_d^2) \qquad \text{---} \qquad 4.6.$$

Corti et.al. (Co 66) have used a different technique to obtain Γ when $\rho>>\Gamma$. The normalised variance is defined by:

$$C(\Gamma,0) = \left\langle \frac{[\sigma(E)-\langle\sigma(E)\rangle]^2}{\langle\sigma(E)\rangle^2} \right\rangle \qquad \text{---} \qquad 4.7.$$

and it has been shown that this is given by

$$C(\Gamma,0) = \frac{1}{N}(1-y_d^2)\,\frac{2\rho/\Gamma \arctan \rho/\Gamma - \ell n(1+\rho^2/\Gamma^2)}{\rho^2/\Gamma^2} \qquad \text{---} \qquad 4.8.$$

which reduces to eq.4.6. when $\rho>>\Gamma$. In fact, the relative error between the two expressions is only about 13% for $\rho=\Gamma$. Eq.4.8 is now generalised to arbitrary resolution $k\rho$, that is, the argument of eq.4.8 is changed from ρ/Γ to $k\rho/\Gamma$, $k = 1,2,3,\cdots$. The experimental values of $C(\Gamma,0)$ are obtained by averaging over $1,2,3,\cdots$ data. Eq.4.8 is then fitted to these values using Γ as a parameter. In such calculations, the value of $\langle\sigma(E)\rangle$ is taken to be the value of $\sigma(E)$ when the data are smoothed by some analytic form. In the ^{40}Ca data, straight lines reproduce the average trends as in Fig.4.6.

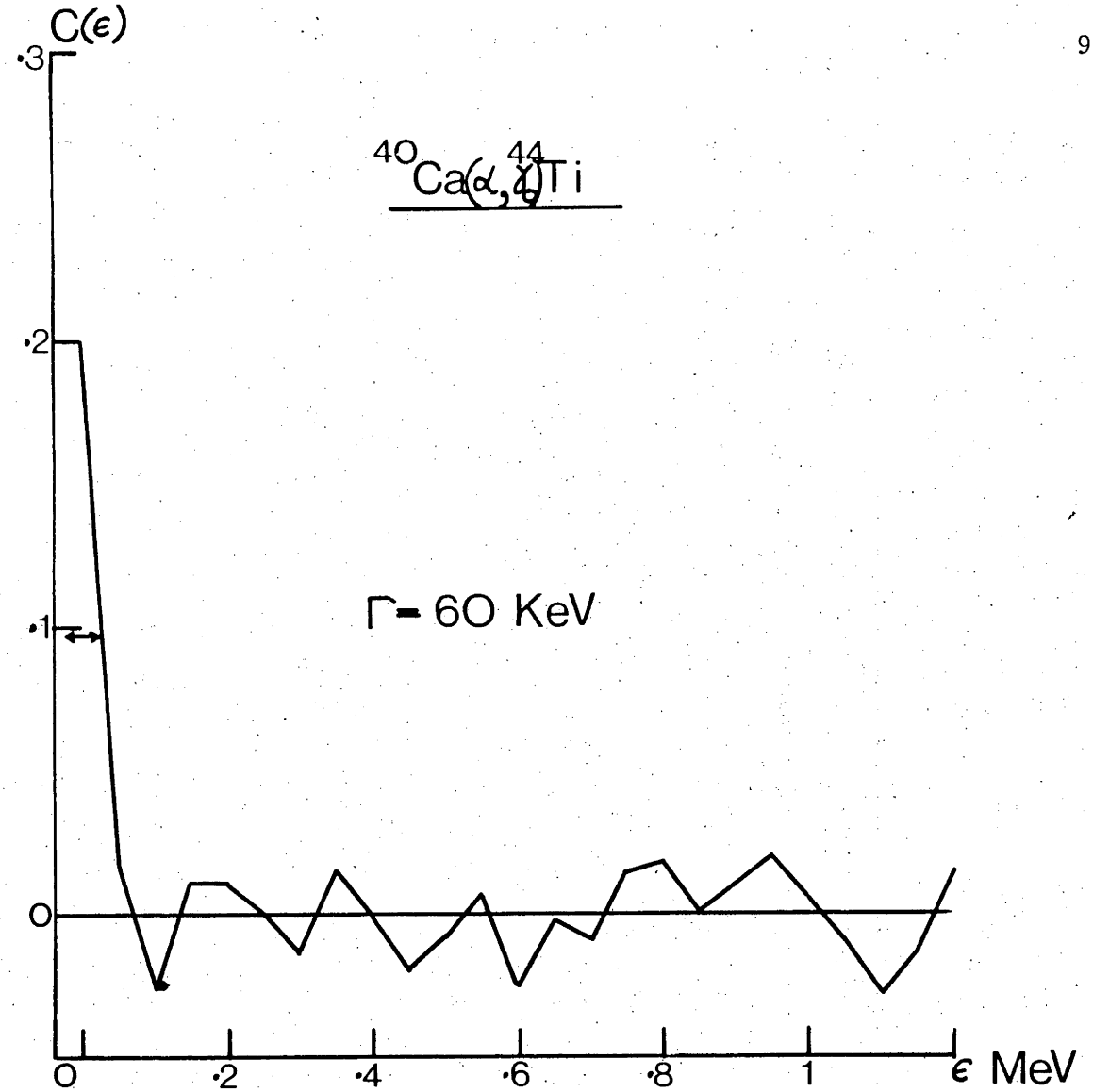

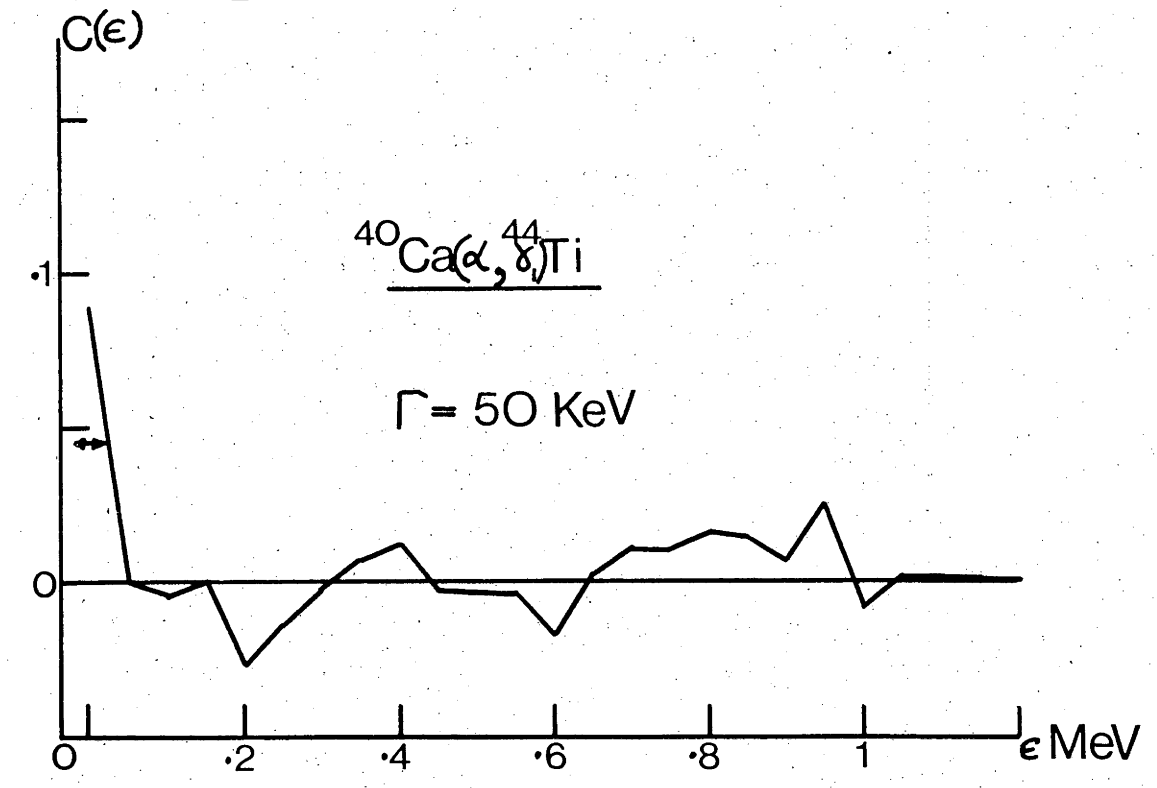

Fig.4.8. The autocorrelation functions for the ^{40}Ca(α,γ_0 and γ_1)^{44}Ti excitation functions calculated using a changing value of the average cross sections.

However, in the other cases the average trend is better represented by a quadratic expression, i.e. $\sigma(E) = a + bE + cE^2$ where the origin of the function is suitably chosen on the energy interval. According to Hodgson (Ho 71) there is a correction to $C(\Gamma,0)$ given by

$$C_1 = \frac{I^2(a^2I^2+b^2)}{12<\sigma(E)>^2} \qquad --- \qquad 4.9.$$

where I is now the energy interval on which the data are measured. Then

$$C_1(0) = C(\Gamma,0)-C_1 \qquad --- \qquad 4.10.$$

where $C(\Gamma,0)$ is defined by eq.4.7. There is a further correction to $C_1(0)$ due to the finite range of data. It is called the bias and is given by:

$$\frac{(N+1)}{N(nN-1)}$$

where $n = I/\Gamma$. In the case of the present analyses the bias is a negligible correction to $C_1(0)$ and is neglected.

4.1.6. Cross Correlation

One of the results of Ericson's fluctuation theory is that different exit channels should be uncorrelated in their fluctuation structure. A function which tests for cross correlation is $C'(\varepsilon)$ where

$$C'(\varepsilon) = \frac{<\sigma_1(E)\sigma_2(E+\varepsilon)>}{<\sigma_1(E)><\sigma_2(E+\varepsilon)>} - 1 \qquad --- \qquad 4.11.$$

where σ_1 and σ_2 are the cross sections of the two channels. (In this case γ_0 and γ_1). If the fluctuation structure arises from interference effects, then $C'(\varepsilon) = 0$. However, this result is only true for an infinite set of data. Again, the finite range of data allows $C'(\varepsilon)$ to fluctuate about the base line with a standard deviation given by

$$\pm\left(\frac{\pi}{2nN_1N_2}\right)^{1/2} \qquad --- \qquad 4.12.$$

here N_1 and N_2 are the fluctuation damping parameters in the two channels.

4.1.7. Probability Distribution of the Cross Section

The probability distribution of the fluctuating cross section is given by

$$P(y) = \frac{N^N}{(N-1)!}\, y^{N-1}\, e^{-Ny} \qquad --- \qquad 4.13.$$

where $y = \sigma/<\sigma>$.

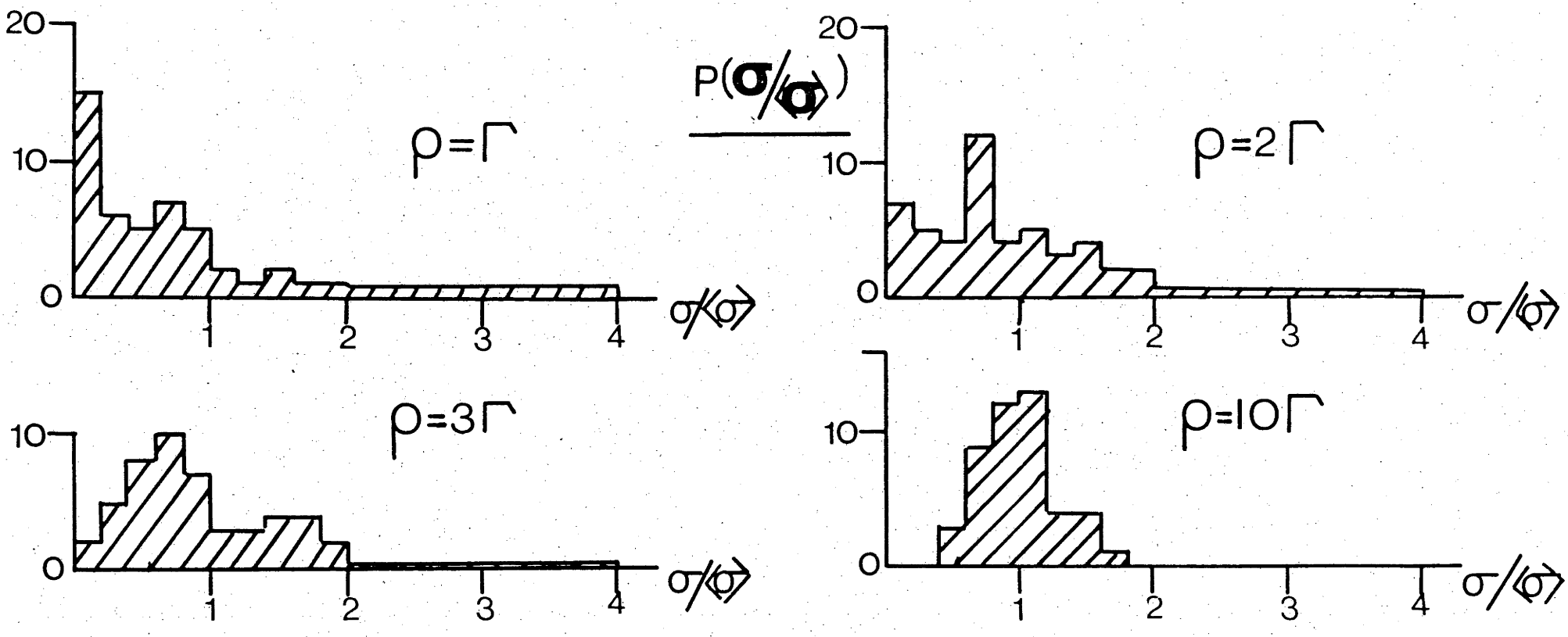

Fig.4.9. Distribution of the cross section for various resolution ρ. The analysis was made on an artificial excitation function with $\Gamma/D = 10$.

In the γ_0 channel where N=1, this becomes simply e^{-y}. However, the effect of energy averaging of the fluctuation structure has the effect of giving a distribution with an apparently larger value of N than the real value. This is demonstrated in Fig.4.9. An artificial excitation function was generated by computing the sum S where

$$S = \sum_{i=1}^{201} \frac{A_i}{(E-E_i+i\Gamma/2)} \qquad \text{---} \qquad 4.14.$$

The A_i are real numbers with random signs. The E_i were equally spaced energies such that $\Gamma/D = 10$. The cross section as a function of energy was then obtained from

$$\sigma(E) = |S(E)|^2 \qquad \text{---} \qquad 4.15$$

In Fig.4.9, $P(\sigma/\langle\sigma\rangle)$ is shown for various values of the resolution ρ. When $\rho=\Gamma$, $P(\sigma/\langle\sigma\rangle)$ is quite close to the expected exponential distribution. As ρ is increased, however, values of $\sigma/\langle\sigma\rangle$ near unity become more probable, and by the time $\rho=10\Gamma$, the distribution is symmetric (within the statistics of the histogram) about unity and has a shape given by eq.4.13 for large N. This demonstrates the equivalence of large N values and what will be called resolution damping.

4.1.8. Discussion of the Data

The data from the four reactions will now be discussed separately with respect to the methods of analysis discussed in the above sections.

$^{40}Ca(\alpha,\gamma)^{44}Ti$

Of the four alpha capture reactions investigated, this one is in a class of its own since isoscalar emission of dipole radiation is forbidden by the isospin selection rules. Since E1 radiation is observed, then it becomes necessary to explain this violation.

Both γ_0 and γ_1 channels show rapid fluctuations in their respective excitation functions. These are characteristic of compound nuclear reactions at excitation energies where $\Gamma/D>>1$. However, a cross correlation analysis between the two channels revealed an apparent cross correlation of the fluctuation structure. This is shown in Fig.4.10. The standard deviation about zero of C'(E) is given by

$$\pm \sqrt{\frac{\pi}{2nN_1N_2}}$$

which in this case turns out to be about 0.025. (Assuming $N_1=1$, $N_2=2$, $n=I/\Gamma$

Fig.4.10. The cross correlation function for the ^{40}Ca data.

Fig.4.11. The cross section probability distribution in the γ_0 and γ_1 channels for the ^{40}Ca data. The solid line in the histogram is the predicted $\exp(-\sigma/\langle\sigma\rangle)$ distribution. In the γ_1 data, the smooth curve is eq.4.13 for large N.

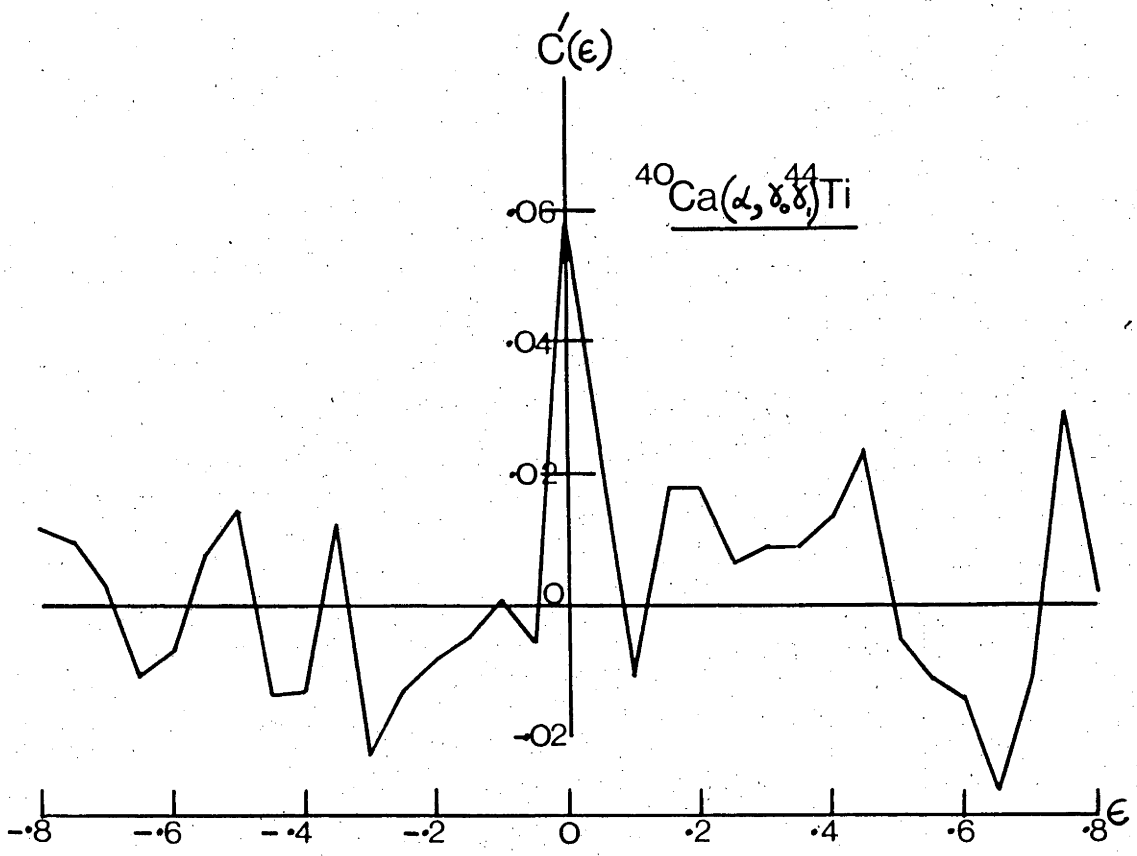
C'(ε)
^{40}Ca(α, γ$_0$γ$_1$)^{44}Ti
·06
·04
·02
0
-·02
-·8
-·6
-·4
-·2
0
·2
·4
·6
·8
ε

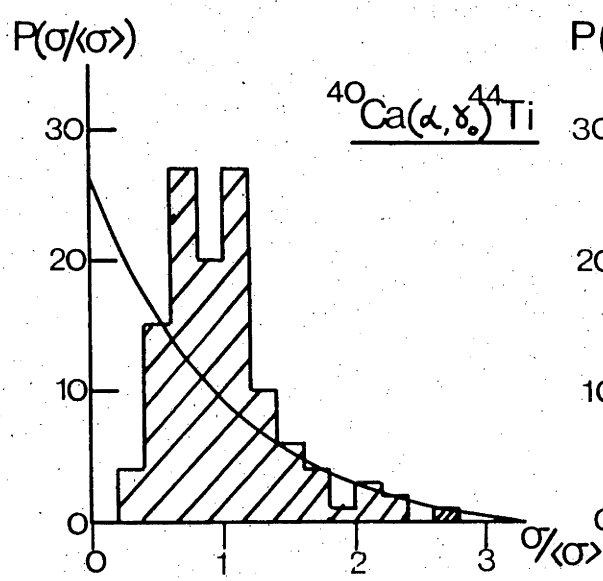
P(σ/⟨σ⟩)
^{40}Ca(α, γ$_0$)^{44}Ti
30
20
10
0
0
1
2
3
σ/⟨σ⟩

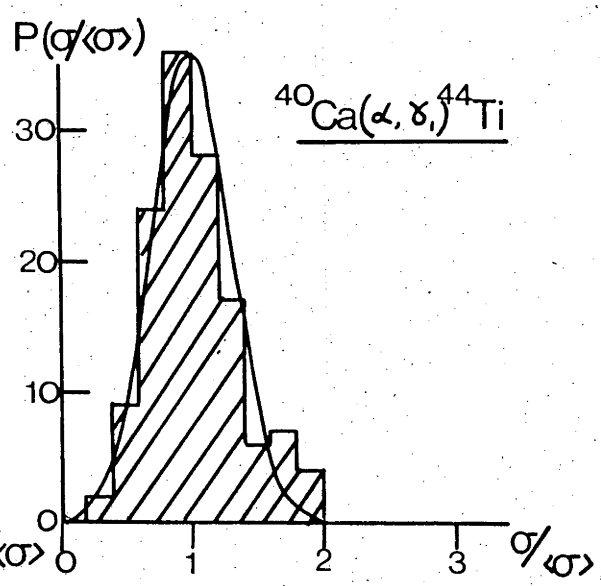
P(σ/⟨σ⟩)
^{40}Ca(α, γ$_1$)^{44}Ti
30
20
10
0
0
1
2
3
σ/⟨σ⟩

with Γ=5 keV). From Fig.4.10, the actual standard deviation about zero is 0.015 which suggests that N_1N_2 should be larger than 2. The systematics of mean level widths in this region of the periodic table suggests a value of Γ around 5 keV, and so $\rho/\Gamma \gg 1$. If $N_1N_2 \simeq 6$, the observed standard deviation is obtained. The value of $C'(\Gamma,0)$ is about three standard deviations greater than the expected error. However, the fact that the data are damped by resolution damping probably leads to an apparent cross correlation. In Fig. 4.11, the function $P(\sigma/\langle\sigma\rangle)$ has been calculated for the γ_0 and γ_1 channels. In both cases the distributions are almost Gaussian implying that $\rho \gtrsim 5\Gamma$.

A mean level width was extracted by the two methods described in Section 4.1.5. In the γ_0 channel, and assuming no direct component to the reaction,

$$C(\Gamma,0) = 1/(\rho/\pi\Gamma+1)$$

Using the value of $C(\Gamma,0)$ in Fig.4.8, Γ turns out to be 4.4 ± 0.3 keV. In the γ_1 channel, N=2 and Γ turns out to be 3.8 ± 0.2 keV.

The second technique involved calculating $C(k\rho)$ in eq.4.8. The results are shown in Fig.4.12, together with two curves for ρ/Γ = 10 and ρ/Γ = 20. The value of Γ obtained by this procedure was Γ = 3±1 keV in the γ_0 channel and Γ = 2.5±1 keV in the γ_1 channel. The average value of all the measurements is Γ = 3.4±0.45 keV.

$^{54}Fe(\alpha,\gamma)^{58}Ni$

The excitation functions for this reaction (Fig.4.2.) show a general Lorentzian trend in the averaged data similar to the generalised G.D.R. shape. However, the systematics suggest that the peak energy should be about 19 MeV whereas the observed peak is at around 16 MeV excitation.

These data were smoothed with a quadratic function, $a + bE + cE^2$, where the mid point of the interval I is taken at a suitable point on the abscissa. For $\rho/\Gamma \gtrsim 50$, eq.4.8. is equal to equation 4.6, so in the γ_0 channel $C(\Gamma,0) = \frac{1}{\rho/\pi\Gamma+1}$. A value of $C(\Gamma,0)$ was calculated with the smoothing procedure shown in Fig.4.13, and this gave a value of Γ = 9.15±1 keV (γ_0), and 5.36±2 keV (γ_1). The mean value is 7.26±1.12 keV.

$^{60}Ni(\alpha,\gamma)^{64}Zn$

The excitation functions for the γ_0 and γ_1 channels are shown in Fig.4.3. In Fig.4.14, a comparison of the γ_0 data is made with the $^{63}Cu(p,\gamma_0)^{64}Zn$ excitation function over the same energy region. Paul et.al. attribute the double humped structure peaking at about 16 and 19 MeV to the $T^<$ and $T^>$

Fig.4.12. Calculation of the mean level width of the ^{44}Ti compound nucleus using eq.4.8:

$$C(k\rho) = \frac{1}{N}(1-y_d^2)\,\frac{\frac{2k\rho}{\Gamma}\arctan\frac{k\rho}{\Gamma} - \ln\left(1+\frac{k^2\rho^2}{\Gamma^2}\right)}{k^2\rho^2/\Gamma^2}$$

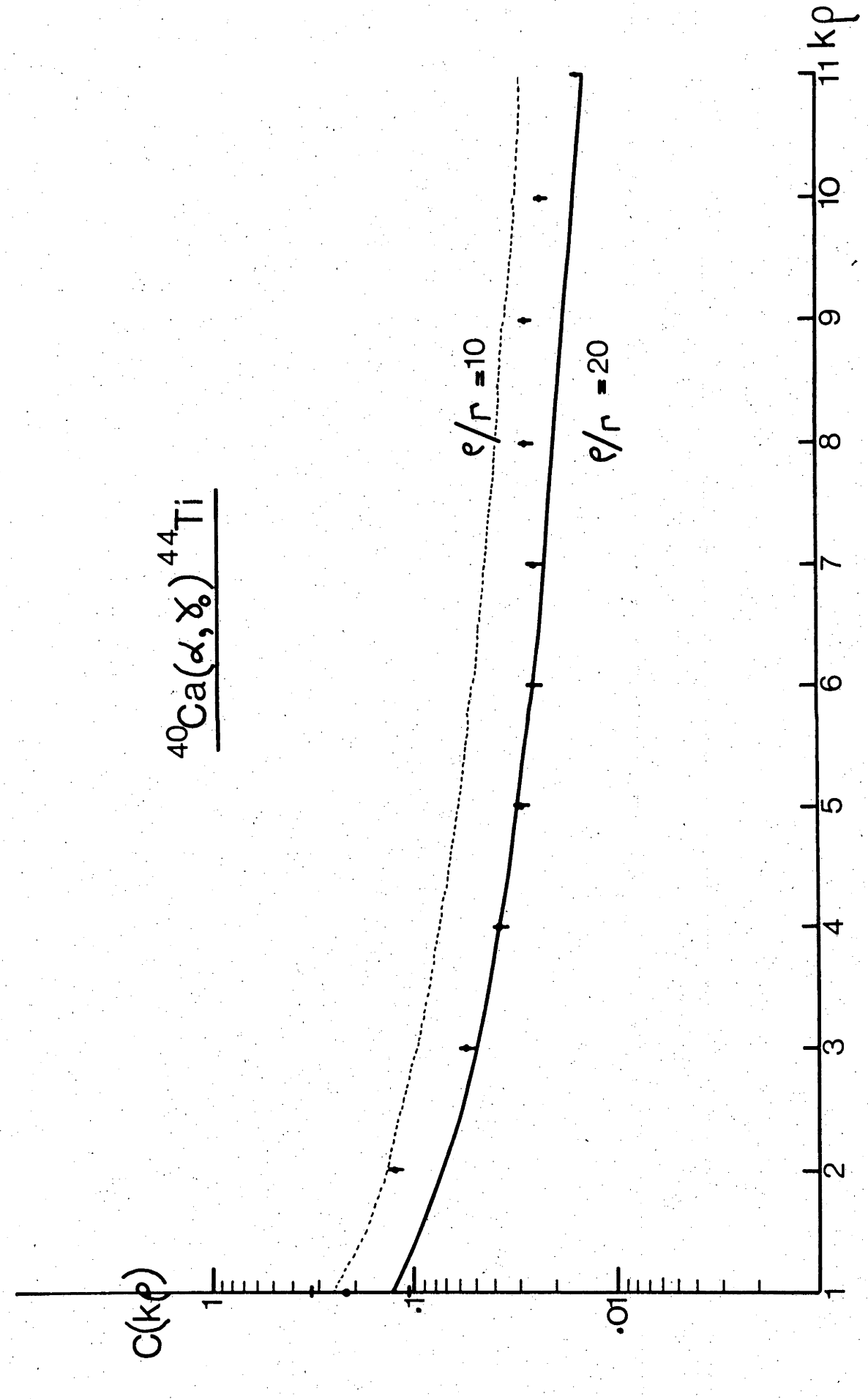
$^{40}Ca(\alpha,\gamma_0)^{44}Ti$
C(kρ)
1
.1
.01
1
2
3
4
5
6
7
8
9
10
11 kρ
ρ/r =10
ρ/r =20

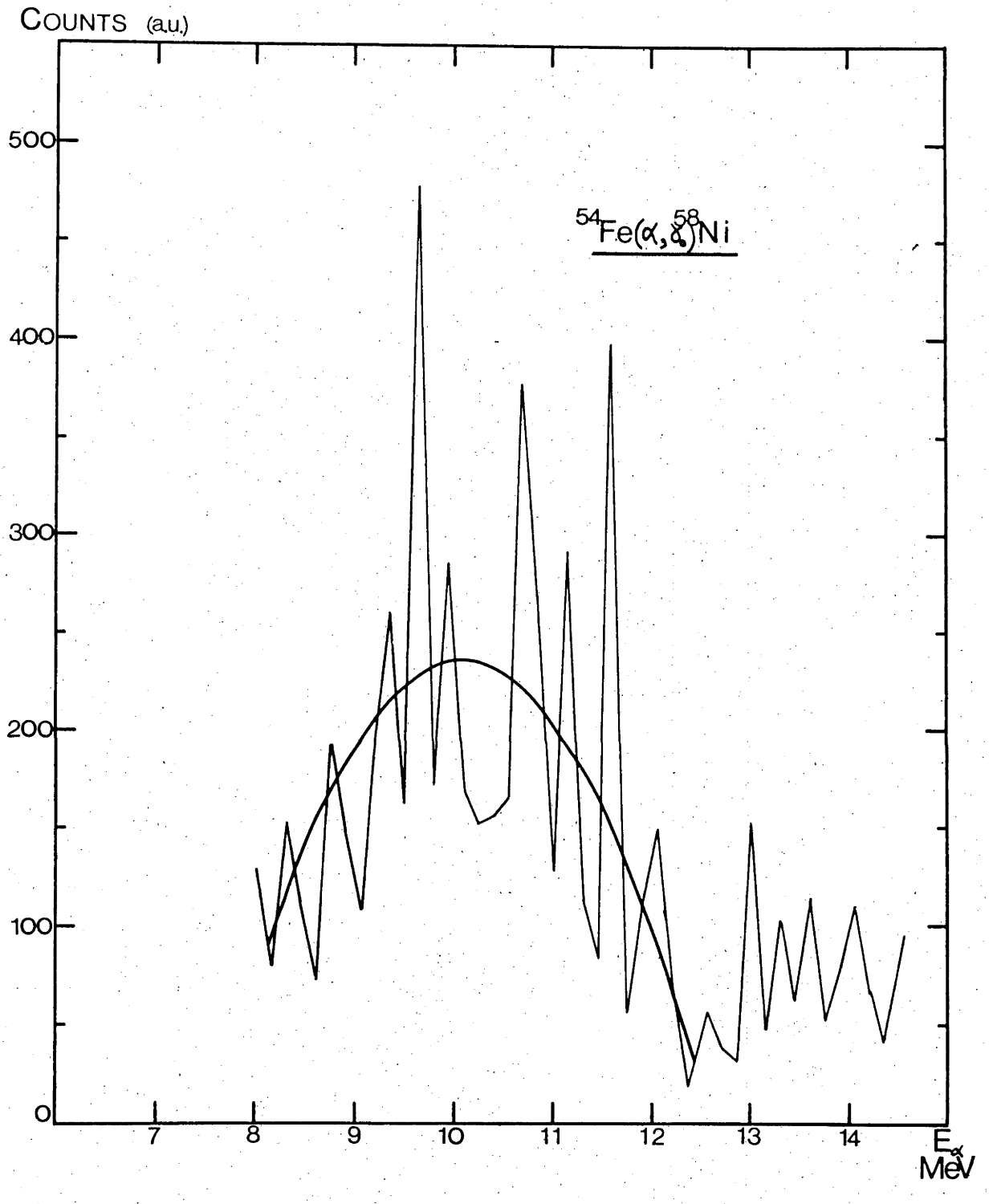

Fig.4.13. The $^{54}Fe(\alpha,\gamma_0)^{58}Ni$ data smoothed with a quadratic function. The last 1½ MeV was not included in the fit.

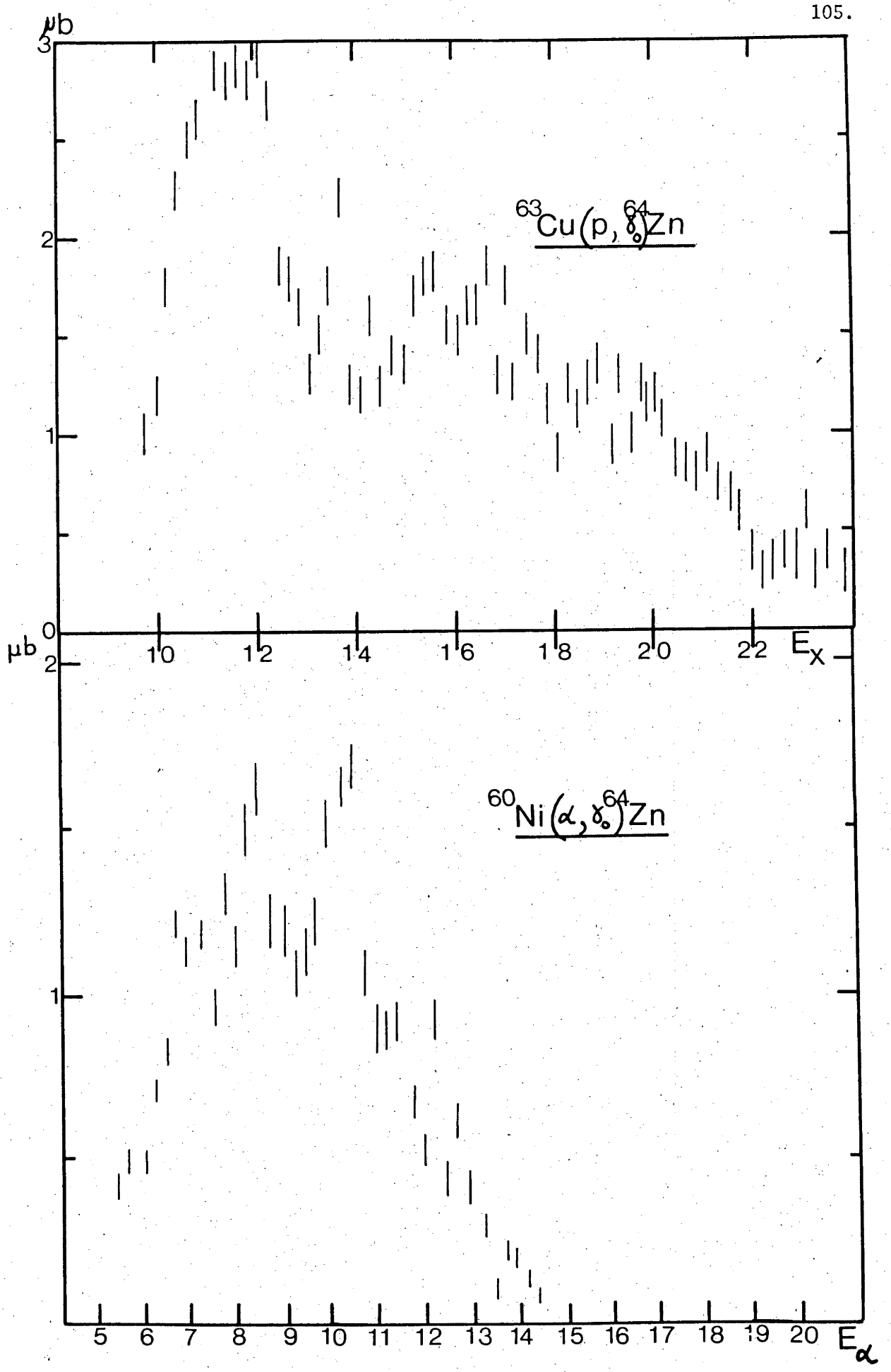

Fig.4.14. Comparison of the $^{63}Cu(p,\gamma_0)^{64}Zn$ and $^{60}Ni(\alpha,\gamma_0)^{64}Zn$ excitation functions. The upper set of data are taken from Paul et.al. (Pa 71).

G.D.R. If this is true, then the (α,γ_0) data barely has any cross section for the $T^>$ resonance. This point will be discussed in the next section where calculations of the cross section are made.

To calculate the mean level width, the data were smoothed with a quadratic function, and the normalised variance calculated. This gave a value for Γ of 5.2±2 keV.

$^{62}Ni(\alpha,\gamma)^{66}Zn$

The excitation functions for the γ_0 and γ_1 channels are shown in Fig.4.4. There is a spectacular fall of the (α,γ) cross section at the (α,n) threshold energy of 6.92 MeV. This is well reproduced in the calculations in a subsequent section.

The data were smoothed above the (α,n) threshold with a quadratic function as before and a value of Γ determined. This was Γ = 3.7±1 keV (γ_0) and 2.9±1 keV (γ_1).

Summary of mean level widths

Nuclide	Ex. energy range (MeV)	$\langle\Gamma\rangle$ (keV)
^{44}Ti	12.5-18.5	3.4 ±0.45
^{58}Ni	14.0-19.5	7.26±1.12
^{64}Zn	10.0-18.5	5.2 ±2.00
^{66}Zn	8.0-18.0	3.3 ±1.41

The errors on $\langle\Gamma\rangle$ are due to the counting statistics and the F.R.D. error, eq.4.4. The statistical error of the normalised variance is given by

$$\frac{1}{N-k+1}\left[\left(\sum_i (f(x_i) - \sigma(x_i))^2\ \sigma(x_i)/f(x_i)^4\right)2.0/k\right]^{1/2}$$

where N is the number of experimental data, and k the number of data which have been averaged over.

4.1.9. Angular Distributions

An important advantage of reactions involving zero spin projectiles on zero spin targets is the restriction to m=0 substates of the excited product nucleus. Such is the case for all the alpha capture reactions investigated. If the excited state decays directly to the ground state by gamma ray emission, then the projection of the gamma ray angular momentum

on the z axis will also be zero. Consequently, the ℓ^{th} order multipole radiation will exhibit an $(\ell,0)$ angular distribution. For example, the decay of a $(1^-,0)$ state will have the well-known $Sin^2\theta$ angular distribution characteristic of an oscillating dipole lying along the z axis. If states of different angular momentum can be excited coherently, then they will interfere and the emitted radiation will reflect this interference. As with all interference phenomena, the amplitudes of the processes must be added. In (α,γ_0) reactions on zero spin nuclides 1^- and 2^+ excited states are likely to decay to the ground state by electric $\ell=1$ and 2 radiation respectively. The amplitude for this process is therefore

$$f(\theta) = a^{1/2}\sin\theta + b^{1/2}\frac{e^{i\theta_{12}}}{2}\sin 2\theta \qquad \text{---} \qquad 4.16.$$

where the absolute cross sections for the E1 and E2 radiations are given by

$$\sigma(1^-) = \frac{8\pi}{3}\,a$$

$$\sigma(2^+) = \frac{8\pi}{15}\,b$$

θ_{12} is the difference in phase between $\ell=1$ and $\ell=2$ ingoing alpha partial waves. For pure E1 and E2 radiation, the $Sin^2\theta$ and $Sin^2 2\theta$ distributions can be written as Linear combinations of Legendre polynomials:

$$W(\theta) = 1 - P_2(\cos\theta) \qquad 1^-\rightarrow 0^+ \text{ E1}$$

$$W(\theta) = 1 + 0.71\,P_2(\cos\theta) - 1.71\,P_4(\cos\theta) \qquad 2^+\rightarrow 0^+ \text{ E2}$$

If there is interference between the 1^- and 2^+ levels, then the odd order polynomials P_1 and P_3 have non-zero coefficients. The angular distributions were fitted with the expressions:

$$W(\theta) = \sum_{\ell=0}^{4} A_\ell Q_\ell P_\ell(\cos\theta) \qquad \text{---} \qquad 4.17.$$

where the Q_ℓ's are attenuation coefficients. They are present in eq.4.17. because $W(\theta)$ is actually an average measurement over a finite solid angle. These have been calculated previously for the collimation geometries employed. The ratios of the $A_j/Ao(j=1,4)$ give the relative strengths of the E1 and E2 components. If pure E1 radiation is present, $A_2/A_0 = -1$ $A_1 = A_3 = A_4 = 0$. In all the angular distributions measured, most of the A_j's were non-zero indicating interference between 1^- and 2^+ levels. This may be seen qualitatively by the assymetry about 90° of the angular distribution.

Both eqs.4.16 and 4.17 were fitted to the measured angular distributions in the usual manner, i.e. the term δ was minimised with respect to the parameters (a, b, θ_{12}, or A_j, j=0,4)

$$\delta = \sum_i ((\sigma_{exp}(\theta_i) - W(\theta_i))/\sigma_i)^2 \qquad \text{---} \qquad 4.18.$$

$\sigma_{exp}(\theta_i)$ is the experimental value of the cross section at angle θ_i and σ_i^2 is the variance. The values of the coefficients are

$$A_j \pm \varepsilon_{jj}$$

where ε_{jj} is a diagonal element of the inverse curvature matrix which is formed from the normal equations.

The γ_1 decay channel is more complicated because there are more possibilities for allowed radiation, and non-zero magnetic substates are involved in the final level. The possibilities may be written in terms of Clebsch-Gordan coefficients.

γ_1 transitions

$(J_i\ 0\ \ell\ m_\ell \mid 2\ m_f)$

J_i = spin of compound state

ℓ = multipolarity of gamma ray

m_ℓ = substate of ℓ

m_f = substate of 2^+ first excited state

Possibilities

$(0\ 0\ell m_\ell \mid 2m_f)$ $\ell=2$

$(1\ 0\ell m_\ell \mid 2m_f)$ $\ell=1,2$

$(2\ 0\ell m_\ell \mid 2m_f)$ $\ell=1,2$

$(3\ 0\ell m_\ell \mid 2m_f)$ $\ell=1,2$

$(4\ 0\ell m_\ell \mid 2m_f)$ $\ell=2$

$\rightarrow$ E1, E2, E2/M1

E1	E2	E2/M1
$1^- \rightarrow 2^+$	$0^+ \rightarrow 2^+$	$2^+ \rightarrow 2^+$
$3^- \rightarrow 2^+$		

The competing decays are E2/M1 as well as pure E1 and E2 radiation being possible. This will be discussed further in Chapter 5.

In Figs.4.15 to 4.21, the measured angular distributions for the γ_0 and γ_1 decays are shown. (L.H. and R.H. side of page respectively). The energy label for each pair of distributions refers to the alpha bombarding energy in MeV. The reaction is labelled by the target nucleus, i.e. ^{40}Ca, ^{54}Fe, ^{60}Ni, ^{62}Ni. The smooth lines represent the five parameter Legendre polynomial fits to the data.

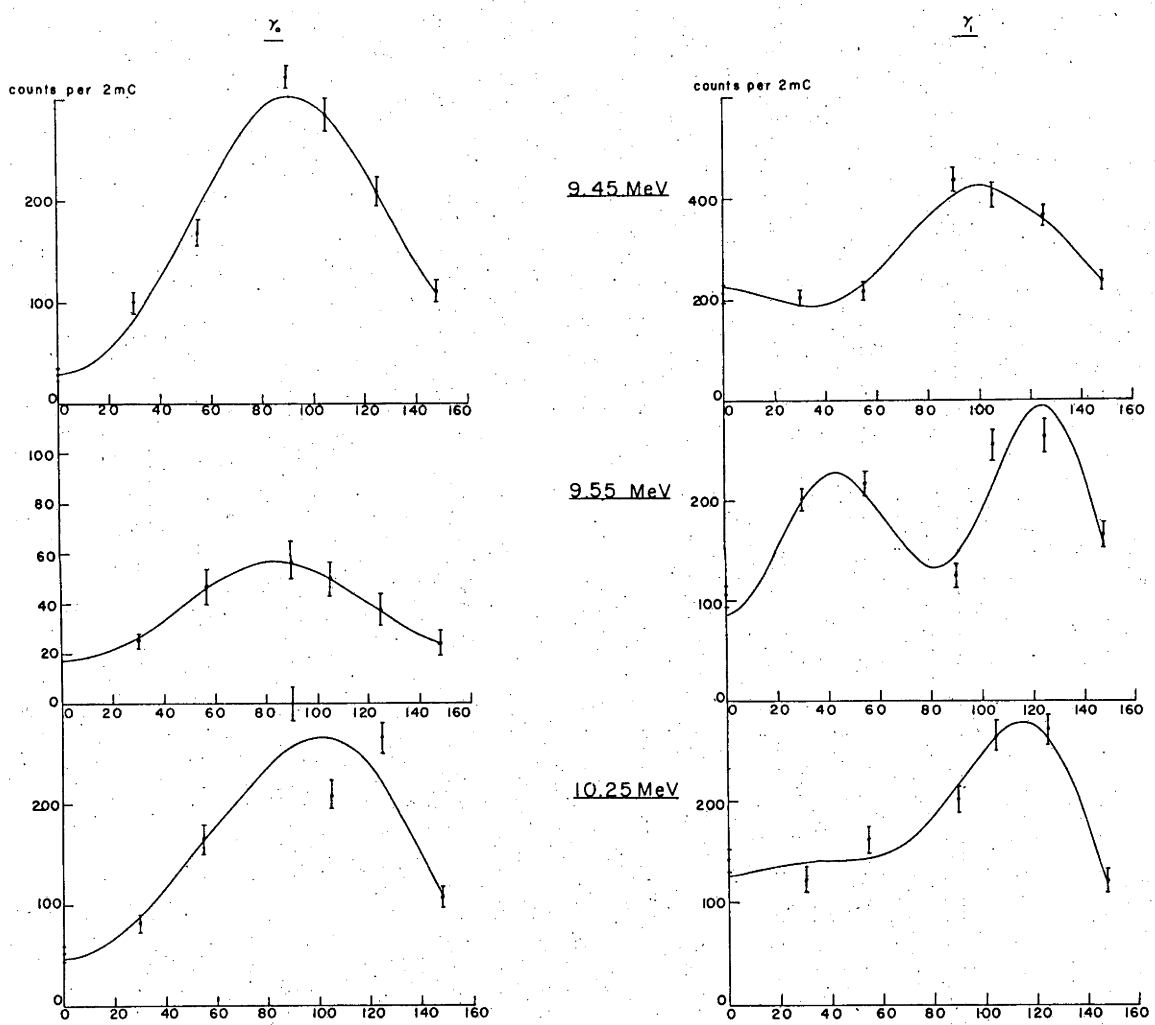

Fig.4.15. ^{40}Ca. (see page 109)

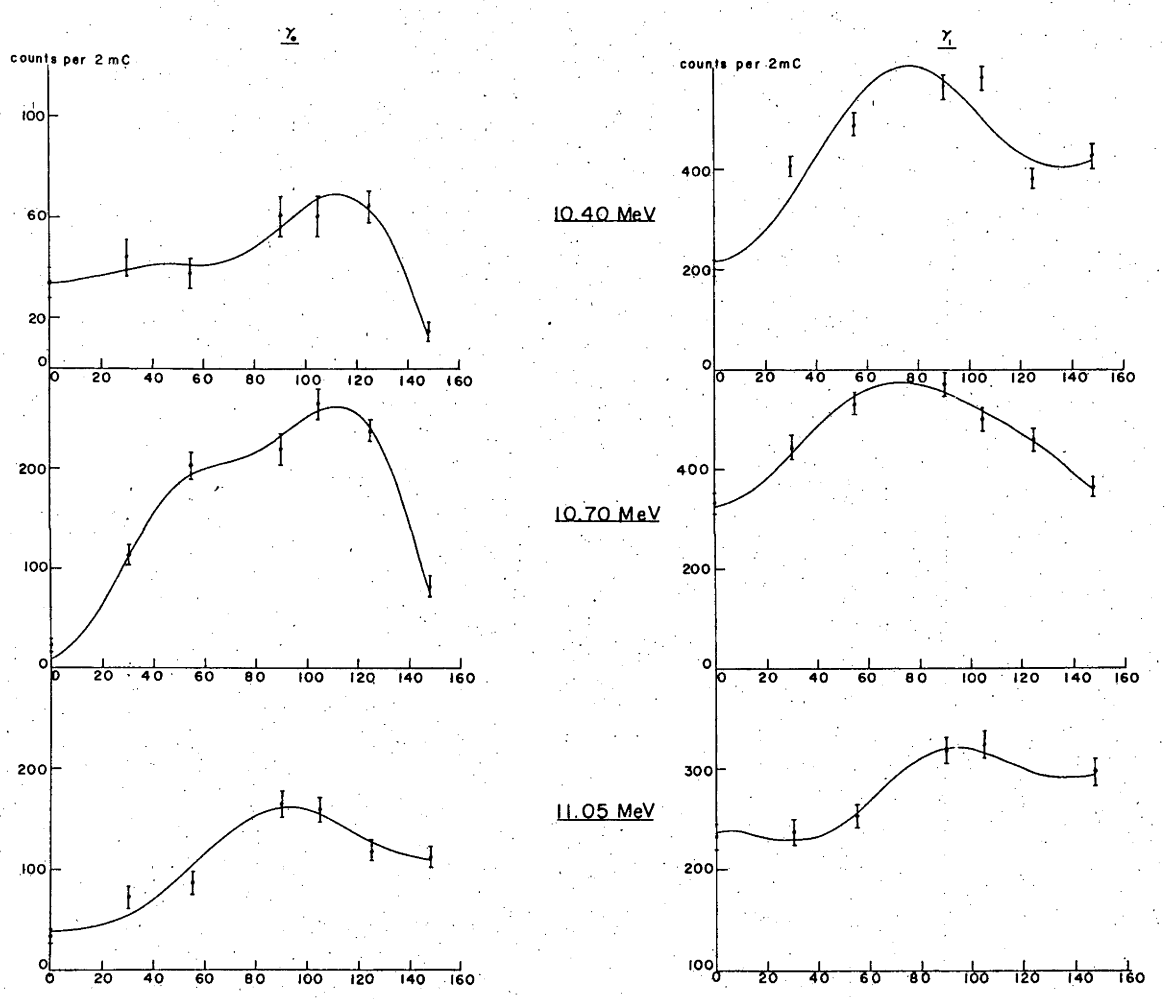

Fig.4.15a. ^{40}Ca. (See page 109)

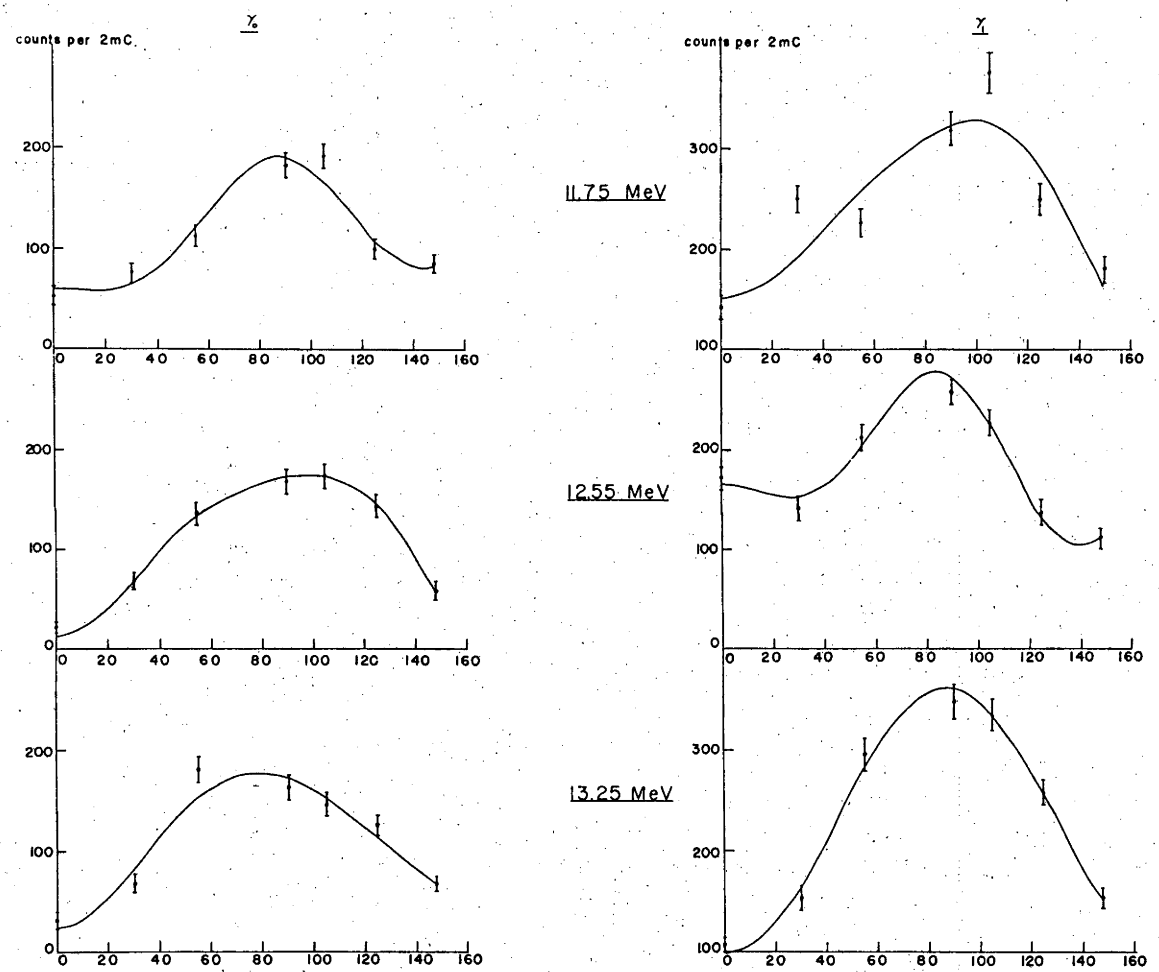

Fig.4.16. ^{40}Ca. (See page 109)

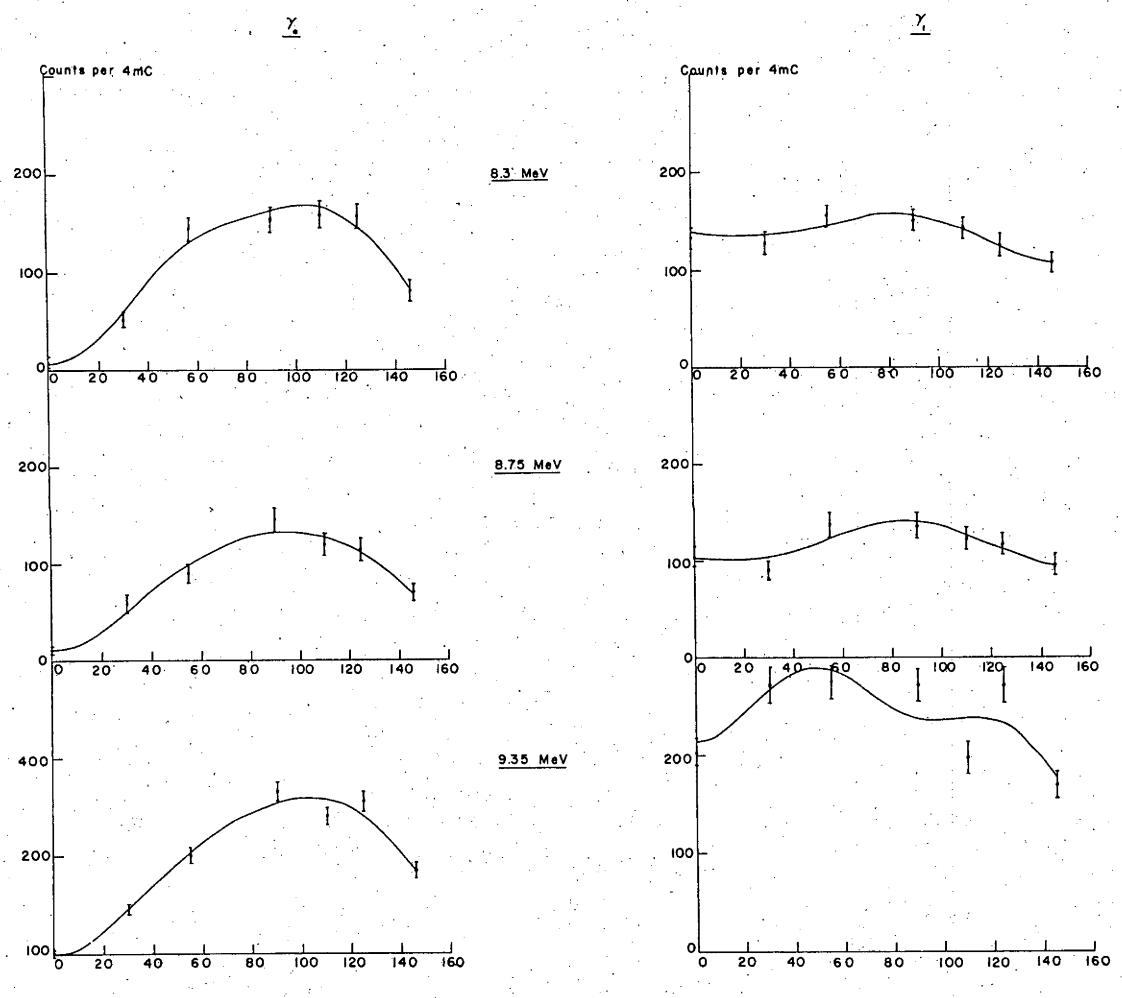

Differential cross sections. Abscissa values are Lab. angle in degrees.

Fig.4.16a. ^{54}Fe. (See page 109).

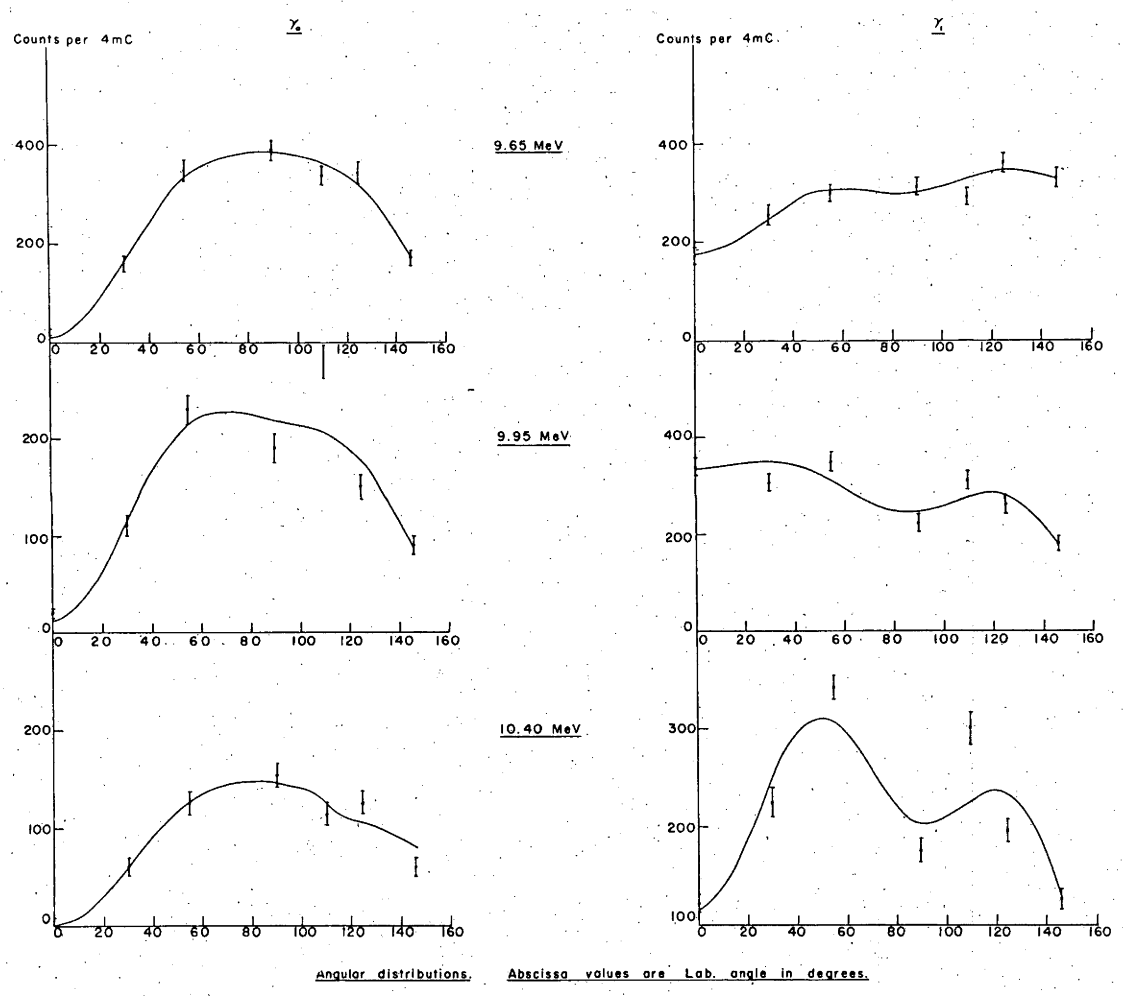

Fig.4.17. ^{54}Fe. (See page 109).

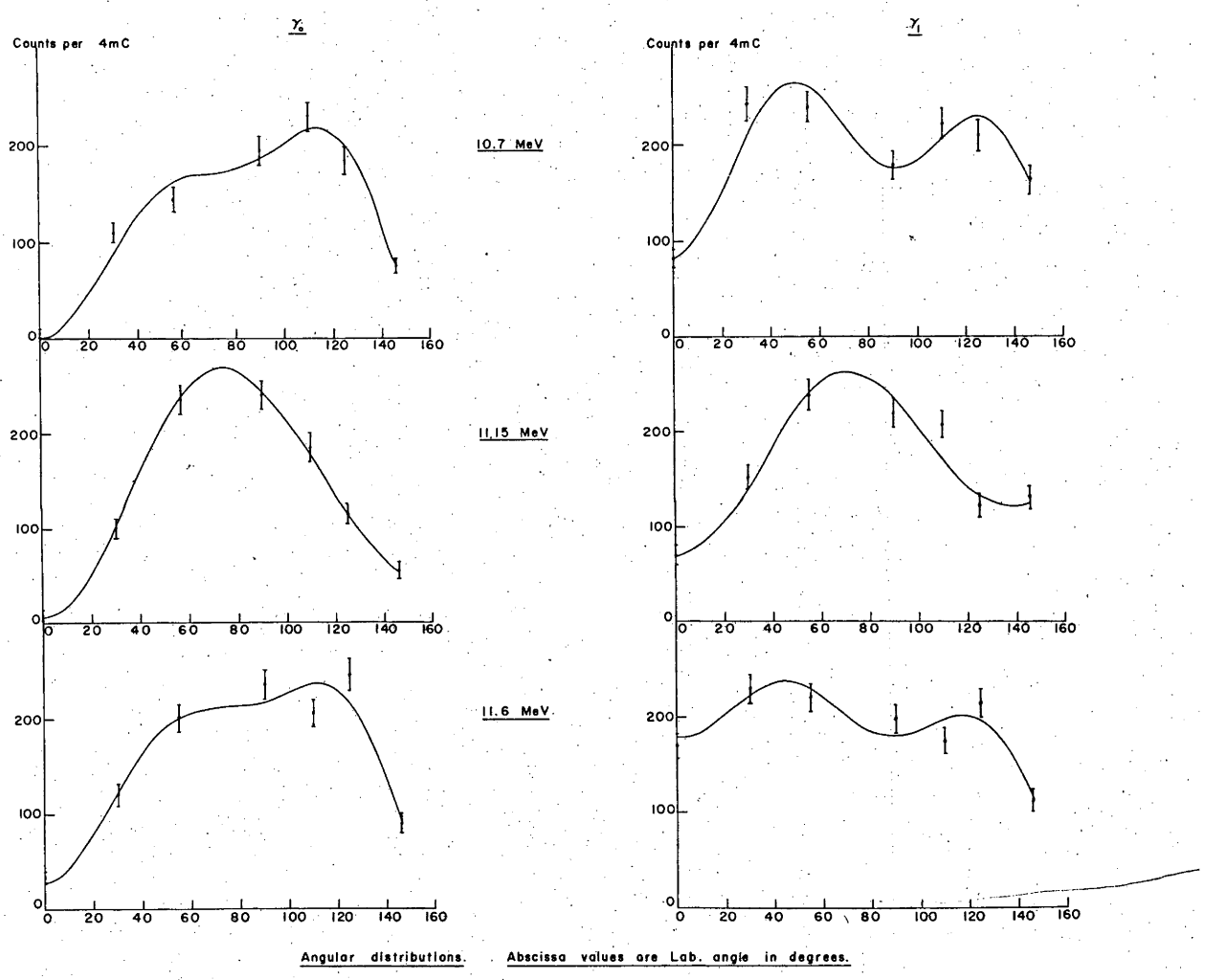

Fig.4.17a. ^{54}Fe. (See page 109).

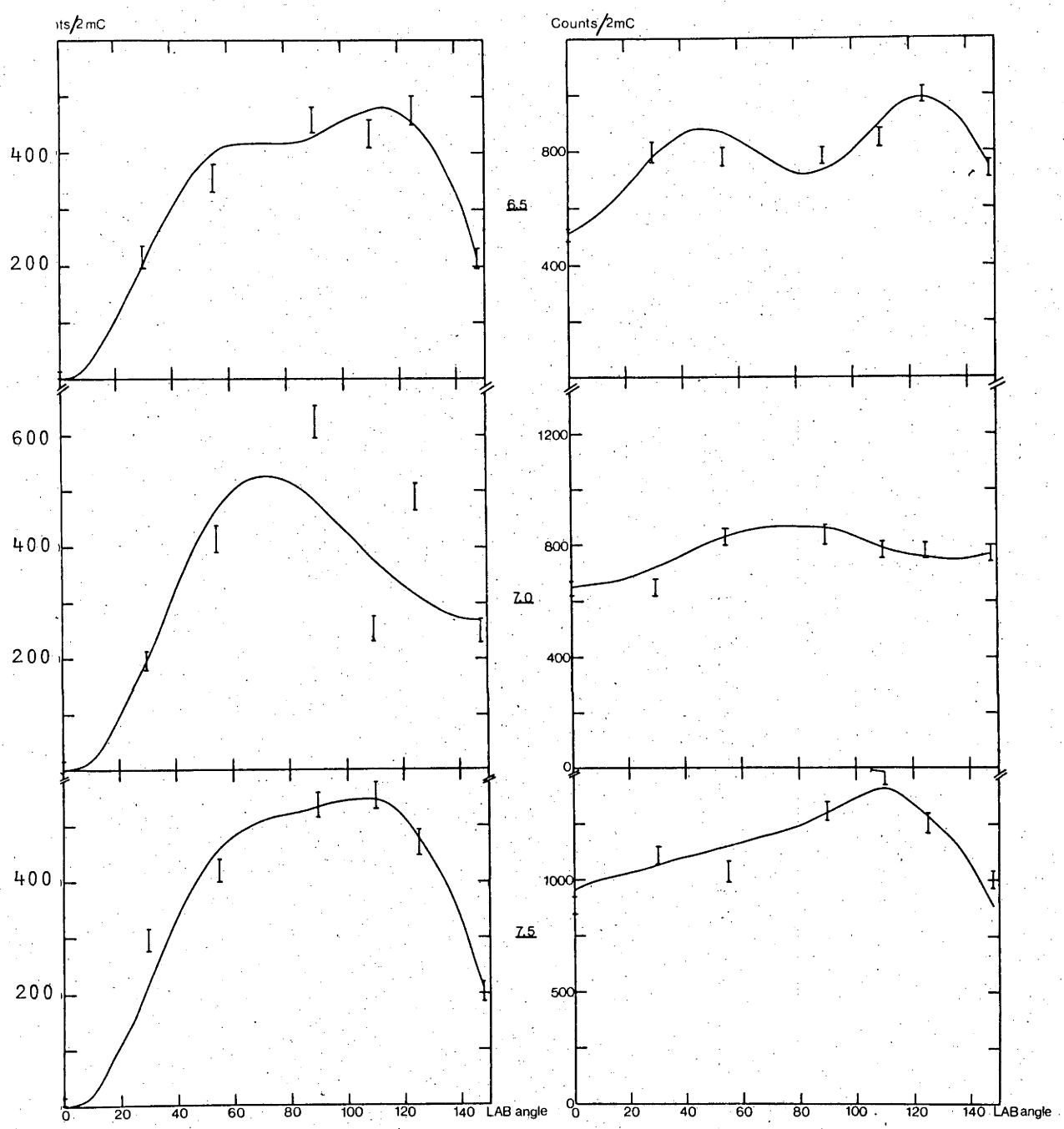

Fig.4.18. ^{60}Ni. (See page 109).

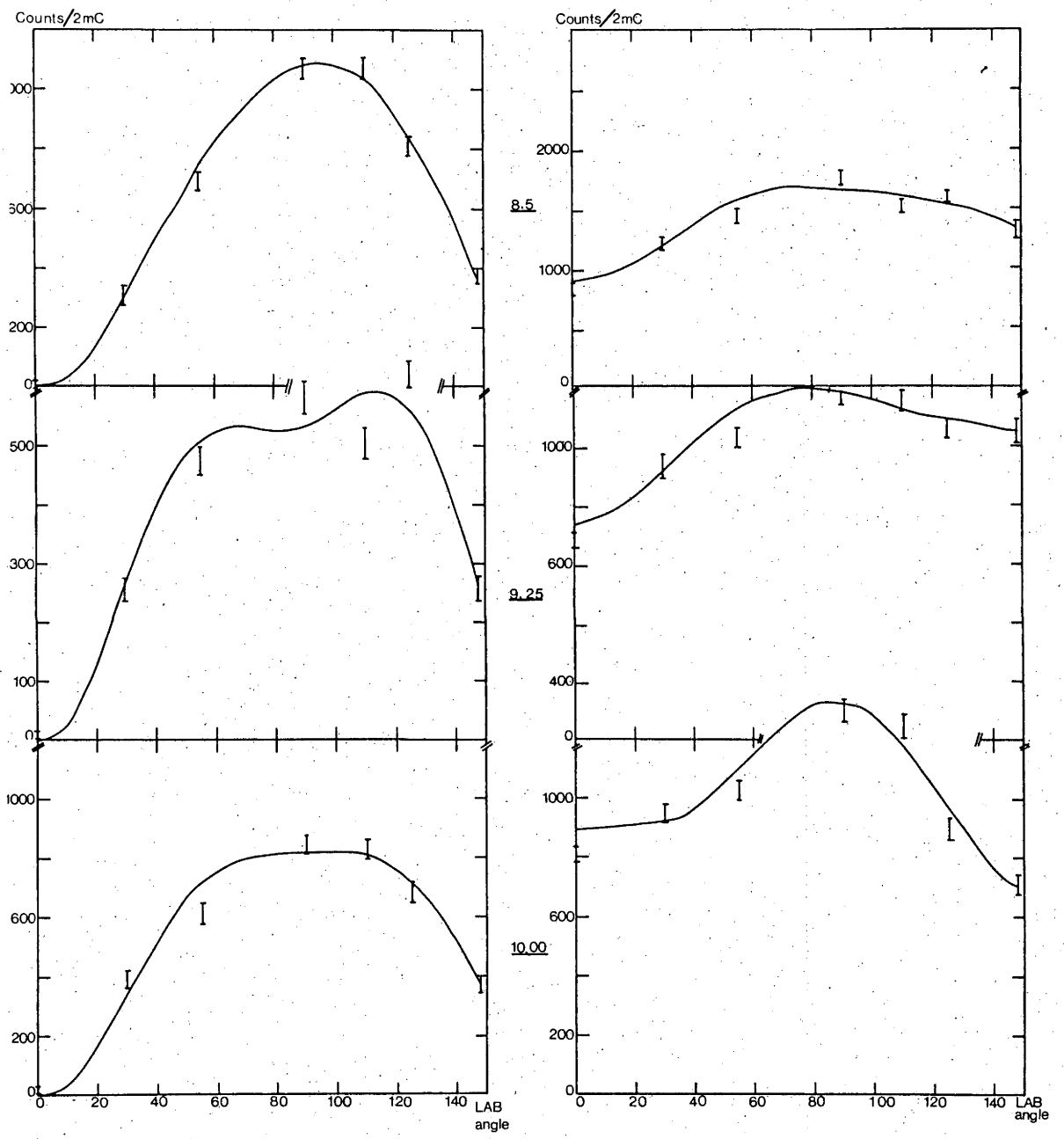

Fig.4.18a. ^{60}Ni. (See page 109).

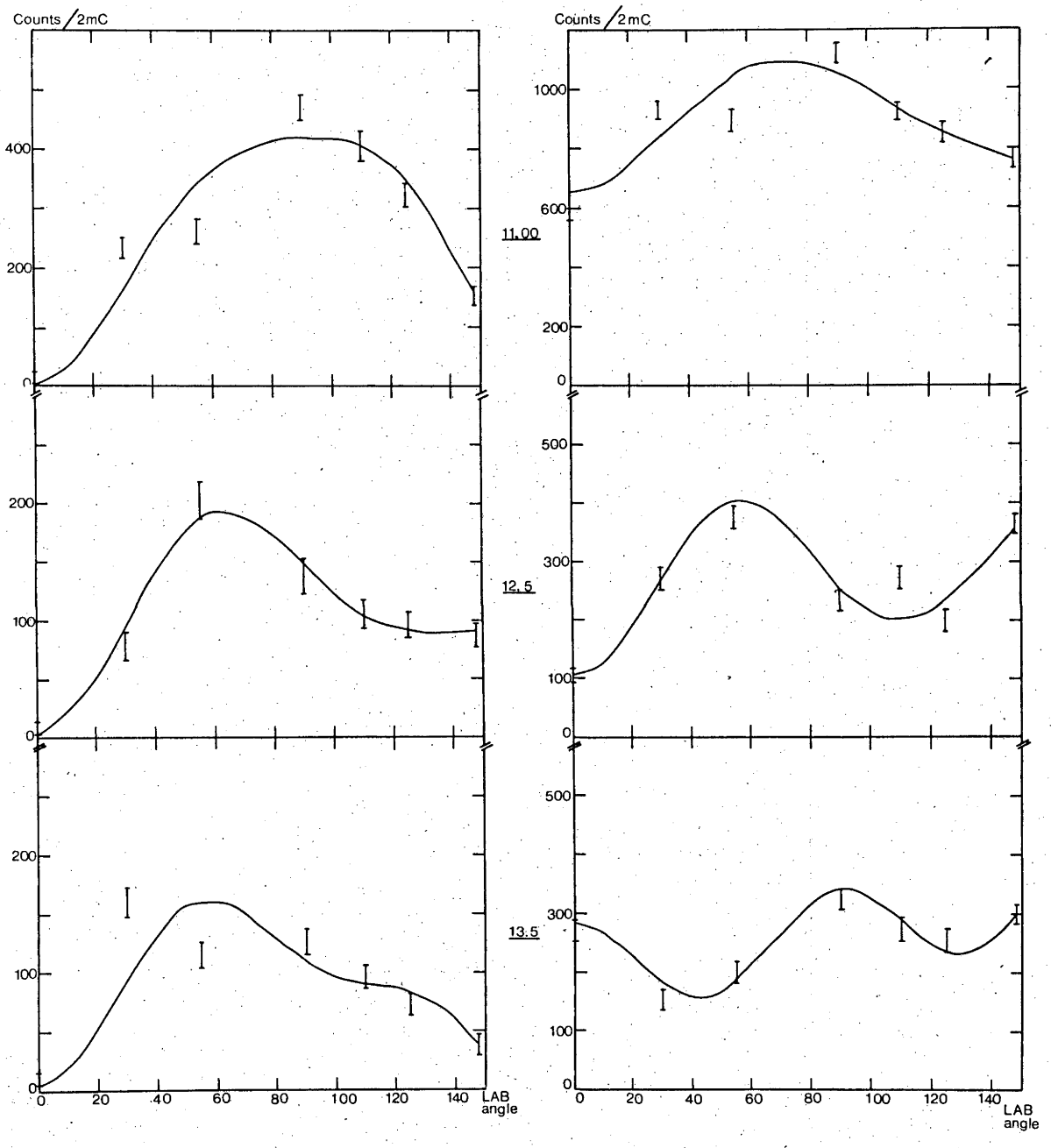

Fig.4.19. ^{60}Ni. (See page 109).

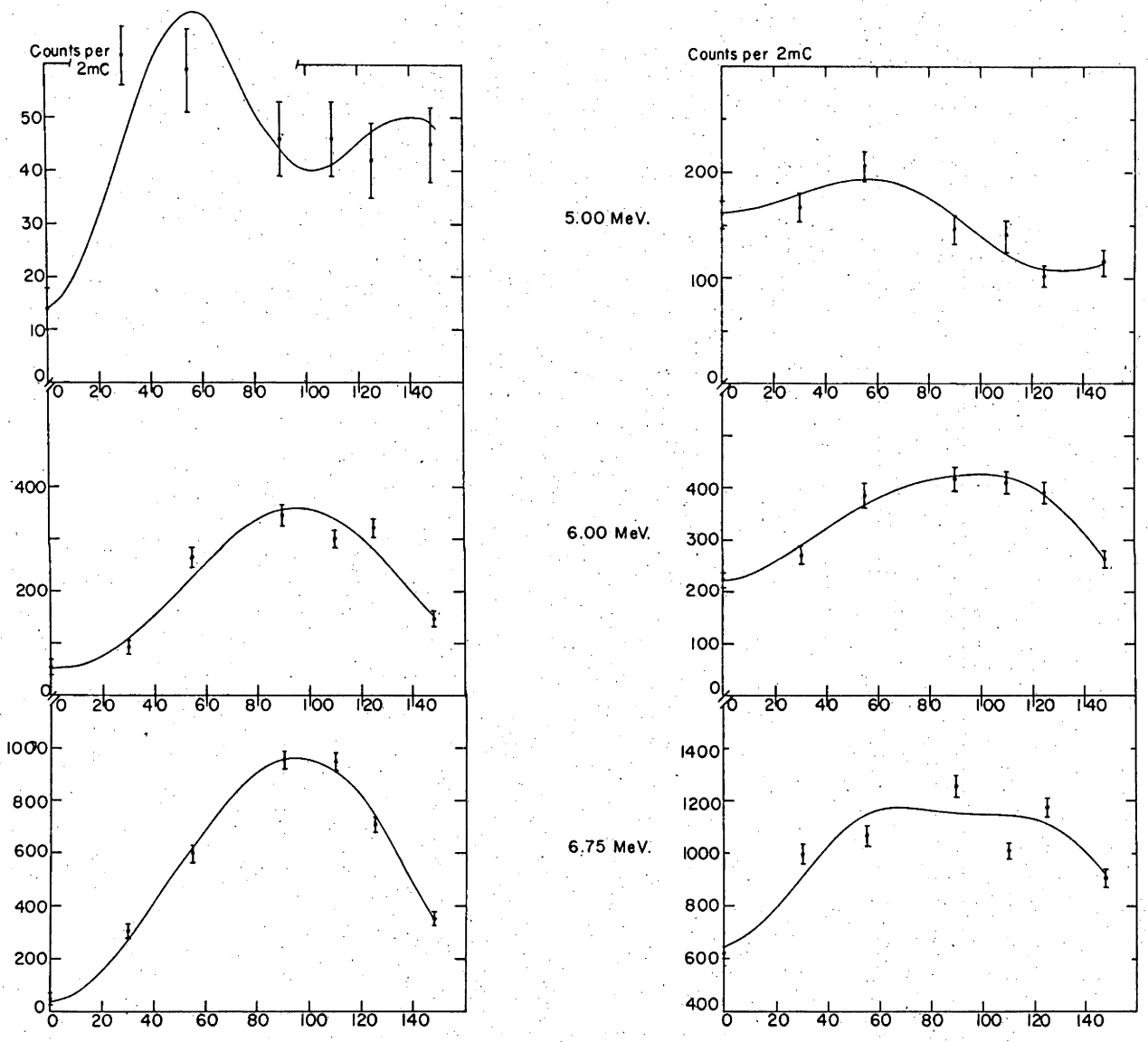

Fig.4.19a. ^{62}Ni. (See page 109).

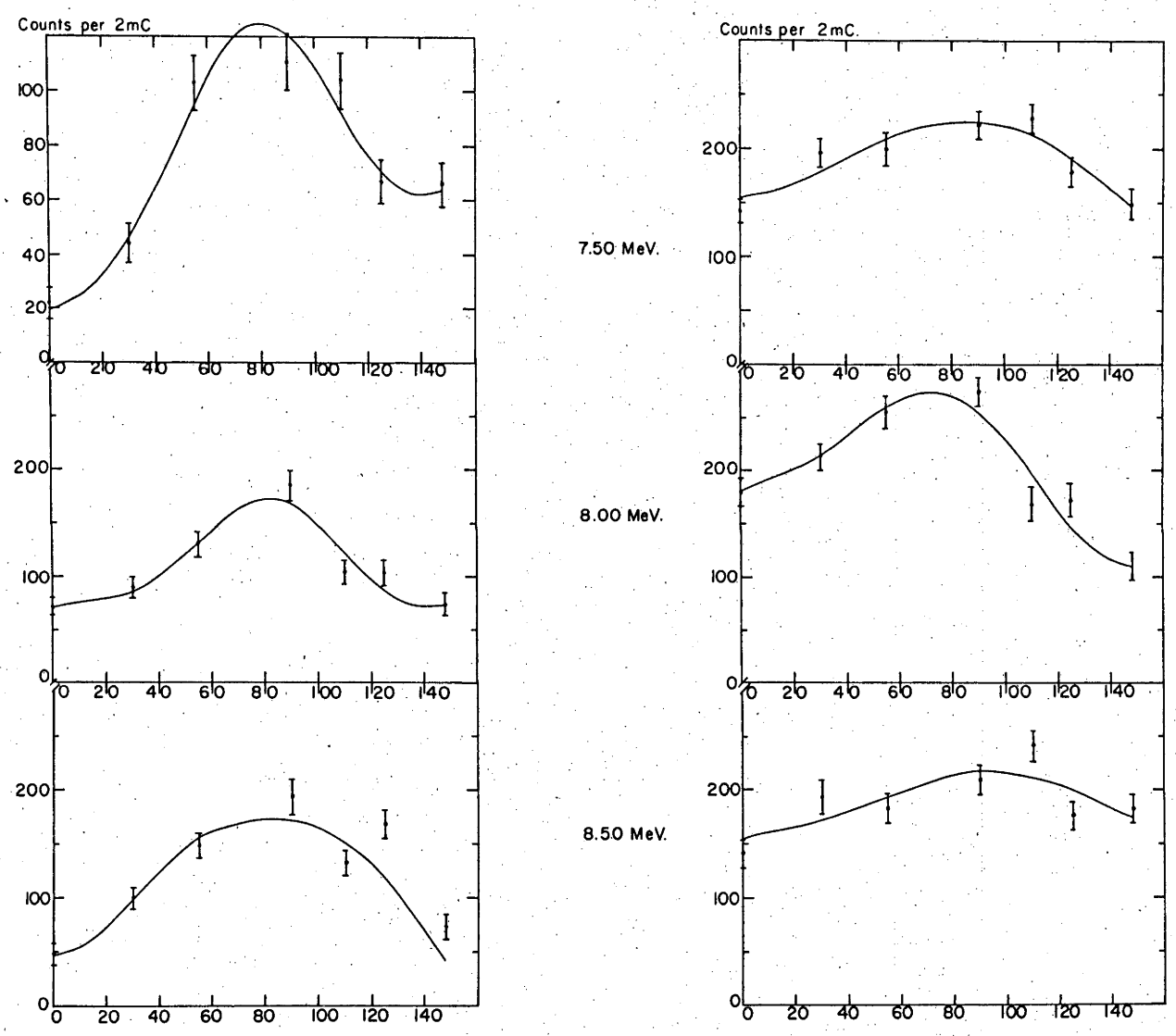

Fig.4.20. ^{62}Ni. (See page 109).

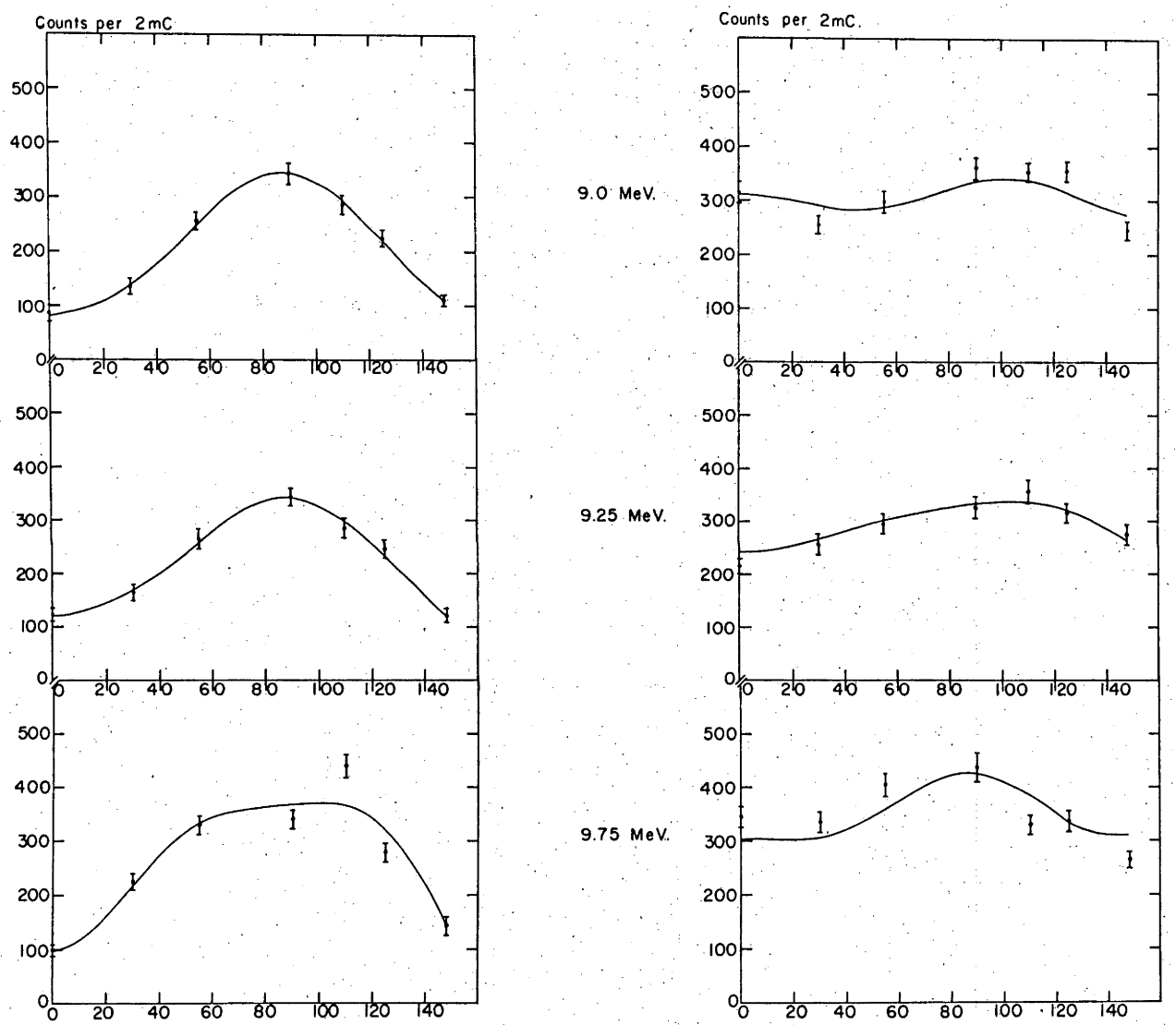

Fig.4.20a. ^{62}Ni. (See page 109).

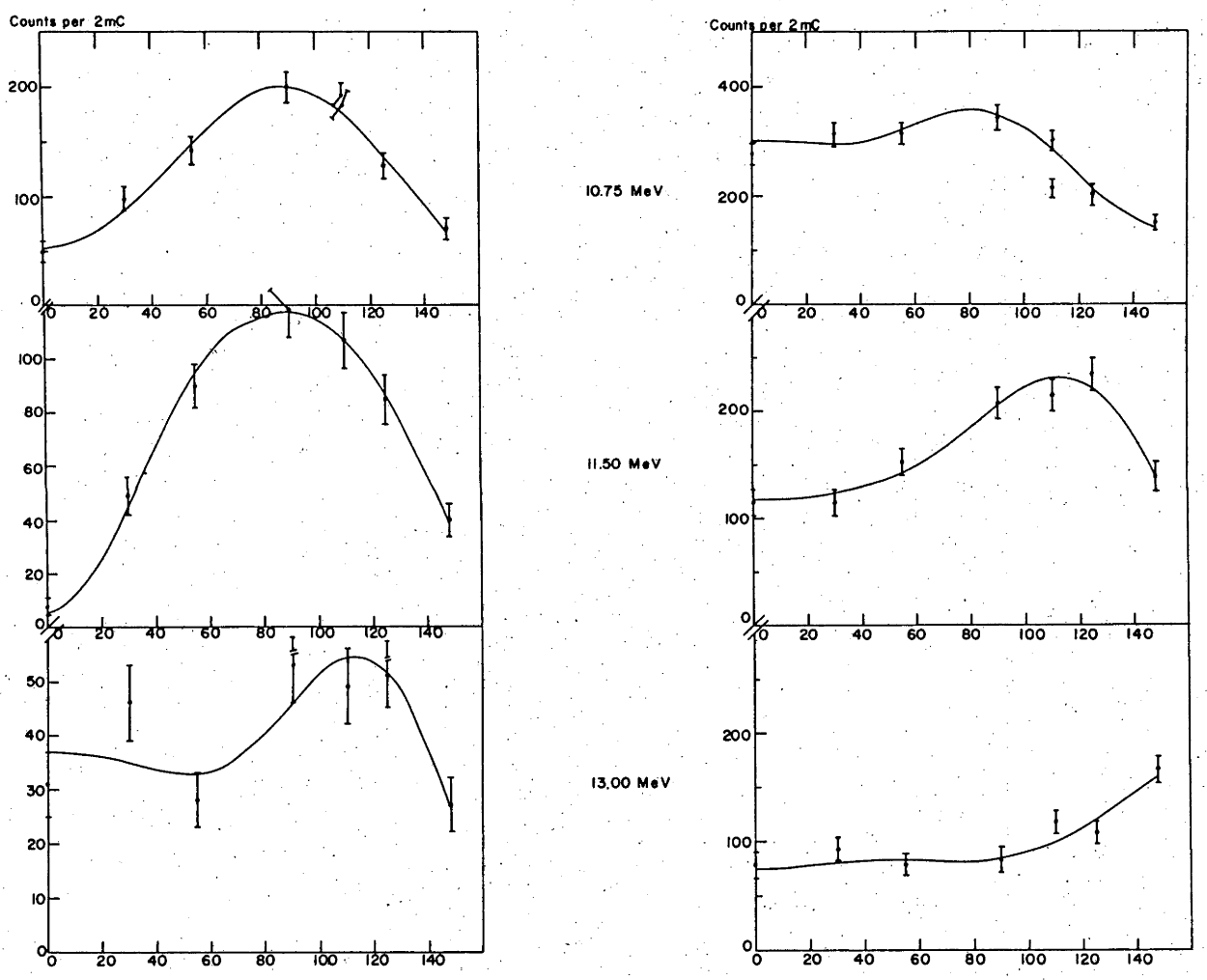

Fig.4.21. ^{62}Ni. (See page 109).

In Figs.4.22 to 4.29, the ratio of the Legendre polynomial coefficients A_j/A_o (j=1,2,3,4) are shown for the γ_0 and γ_1 angular distributions. The reaction is labelled by the target nucleus, ^{40}Ca, ^{54}Fe, ^{60}Ni or ^{62}Ni.

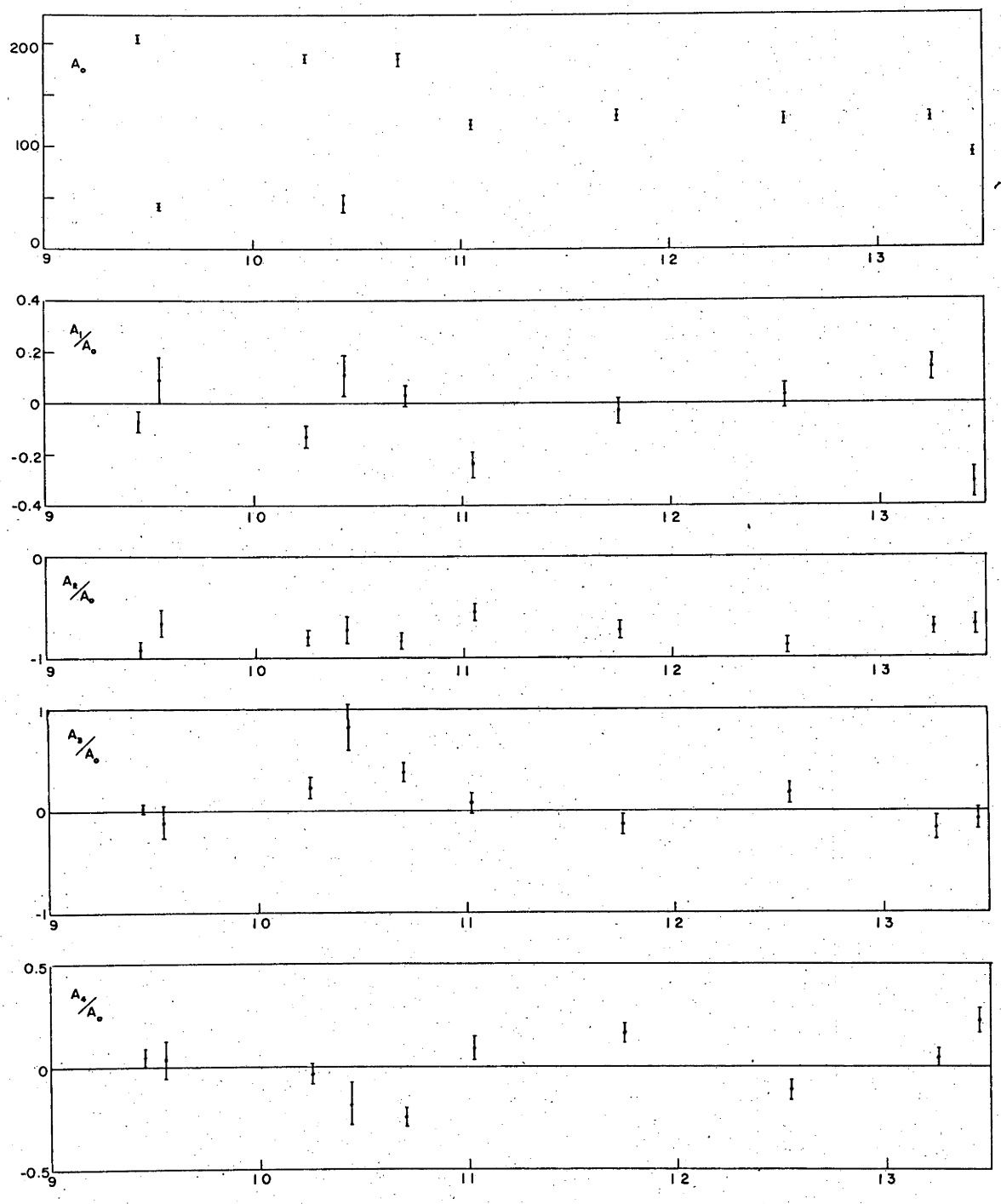

Normalised Legendre polynomial coefficients. Abscissa values are alpha bombarding energy.

Fig.4.22. ^{40}Ca γ_0

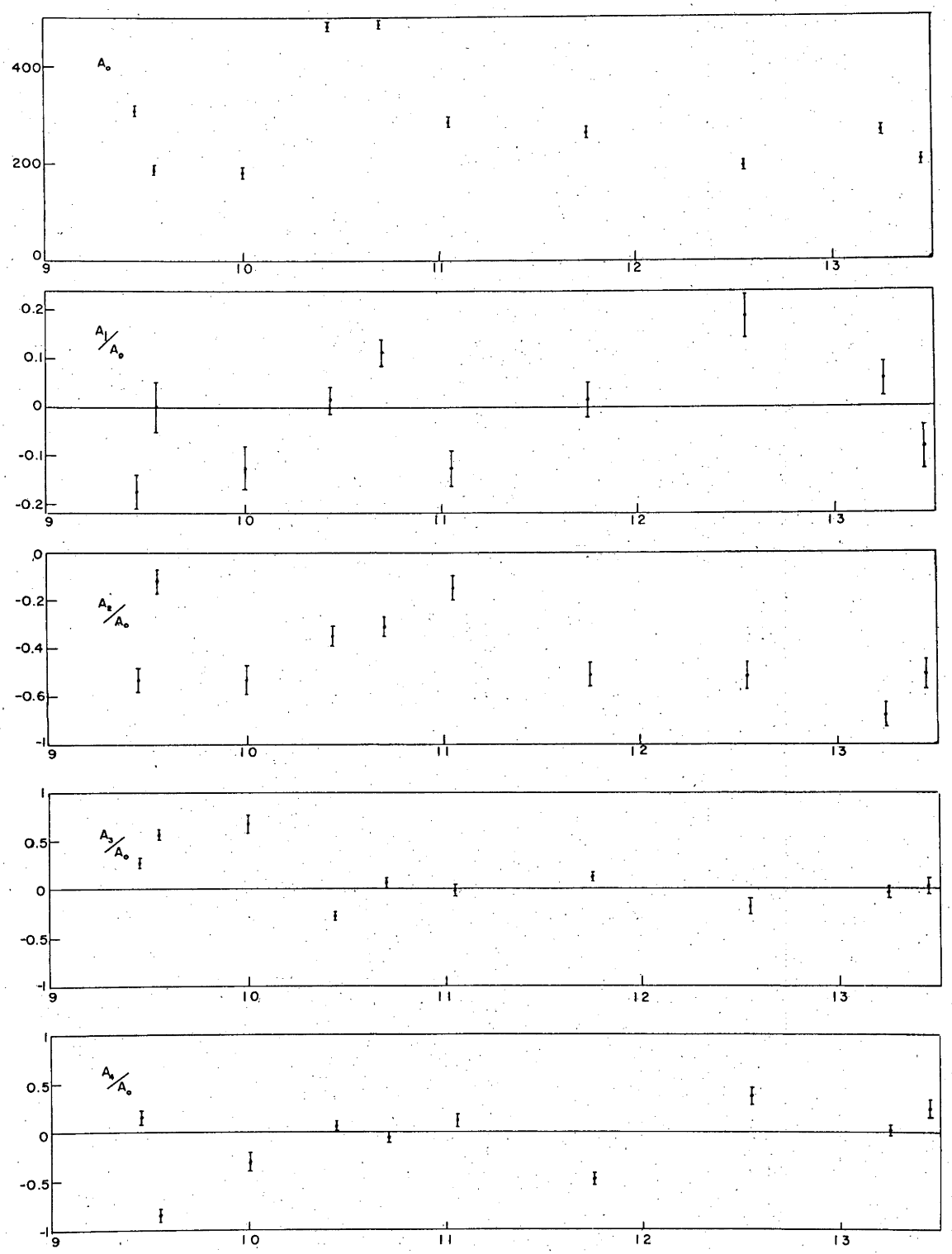

Normalised Legendre polynomial coefficients. Abscissa values are alpha bombarding energy.

Fig.4.23. ^{40}Ca γ_1

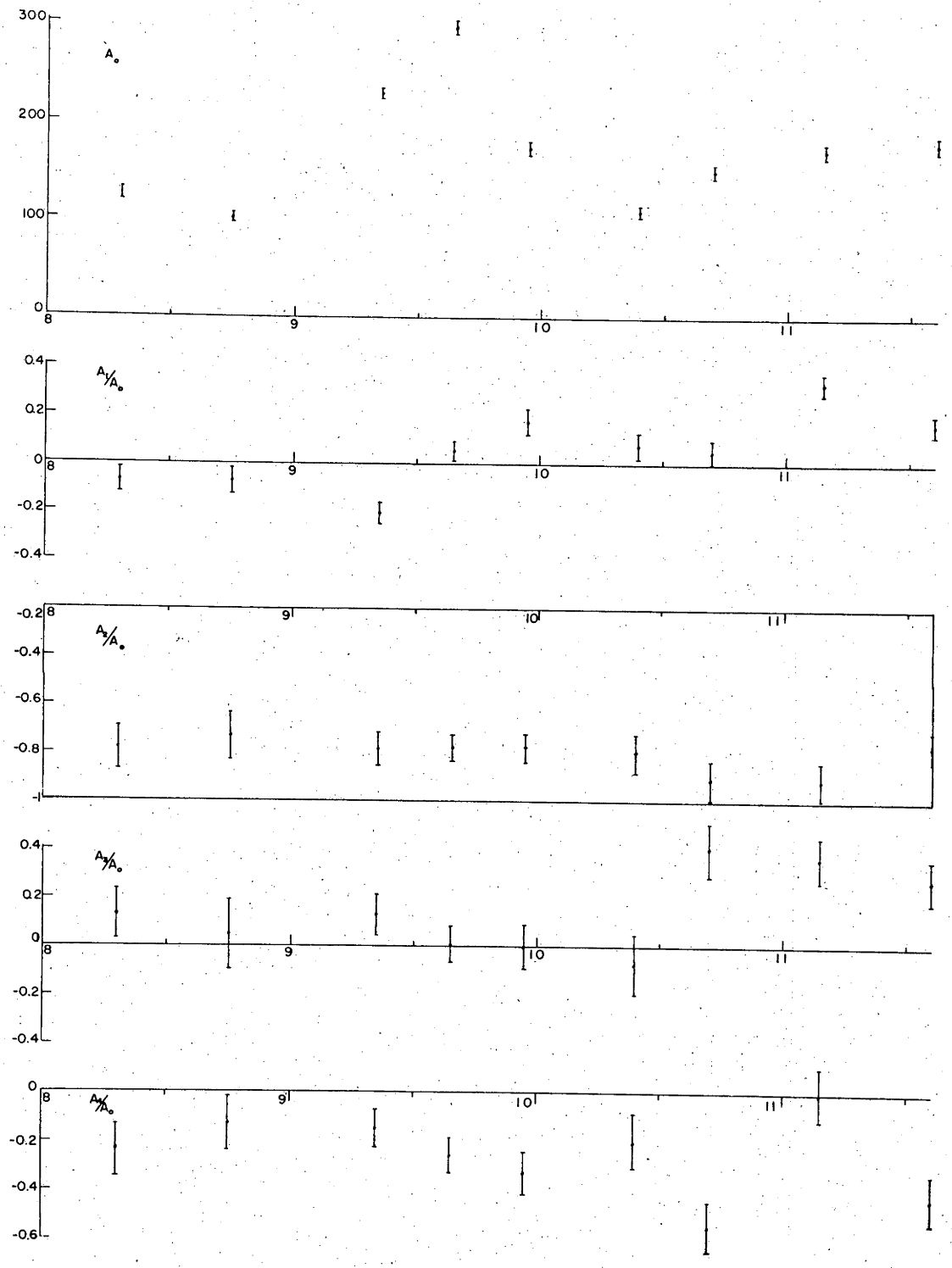

Fig.4.24. ^{54}Fe γ_0

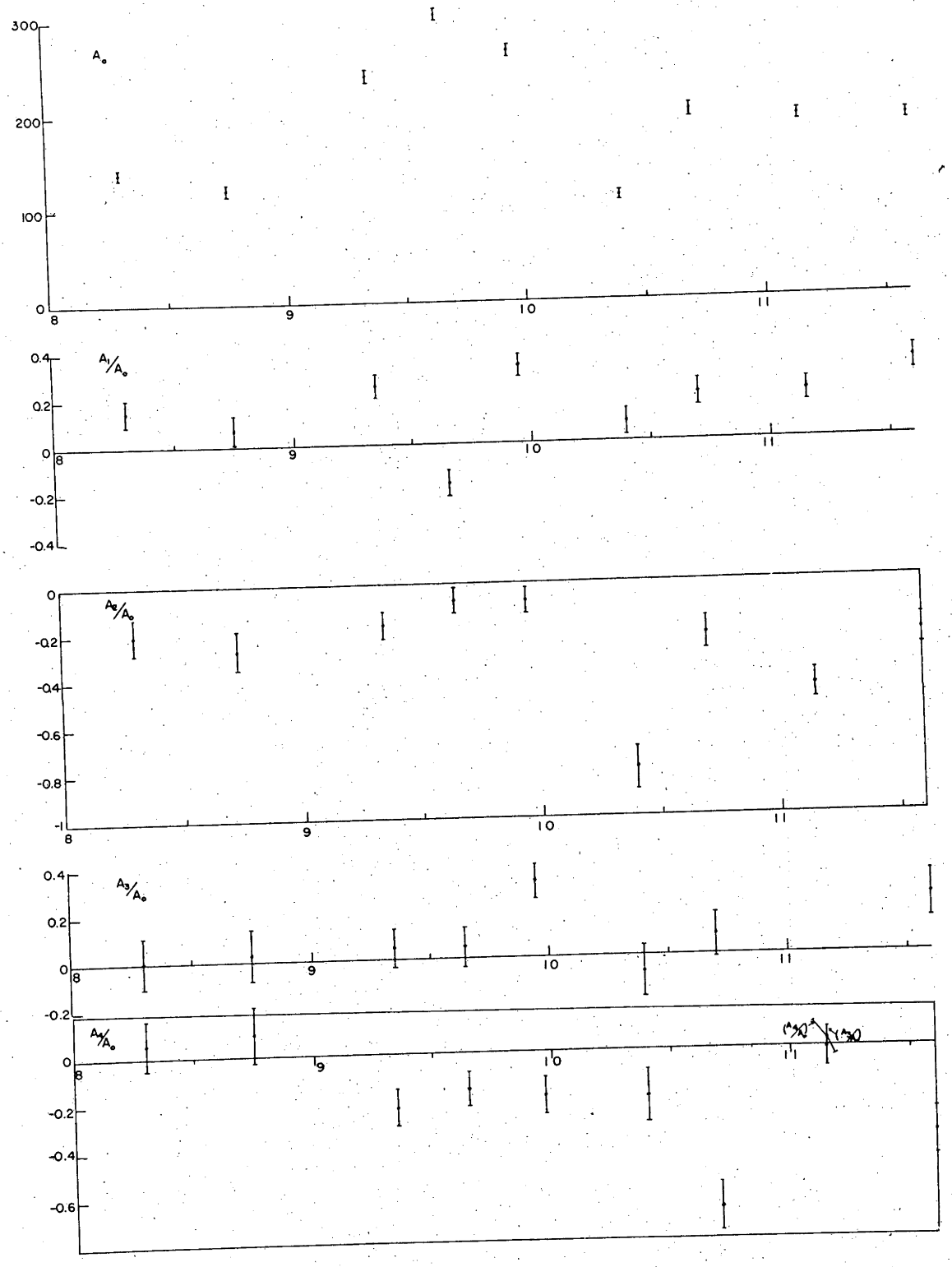

Fig. 4.25. ^{54}Fe γ_1

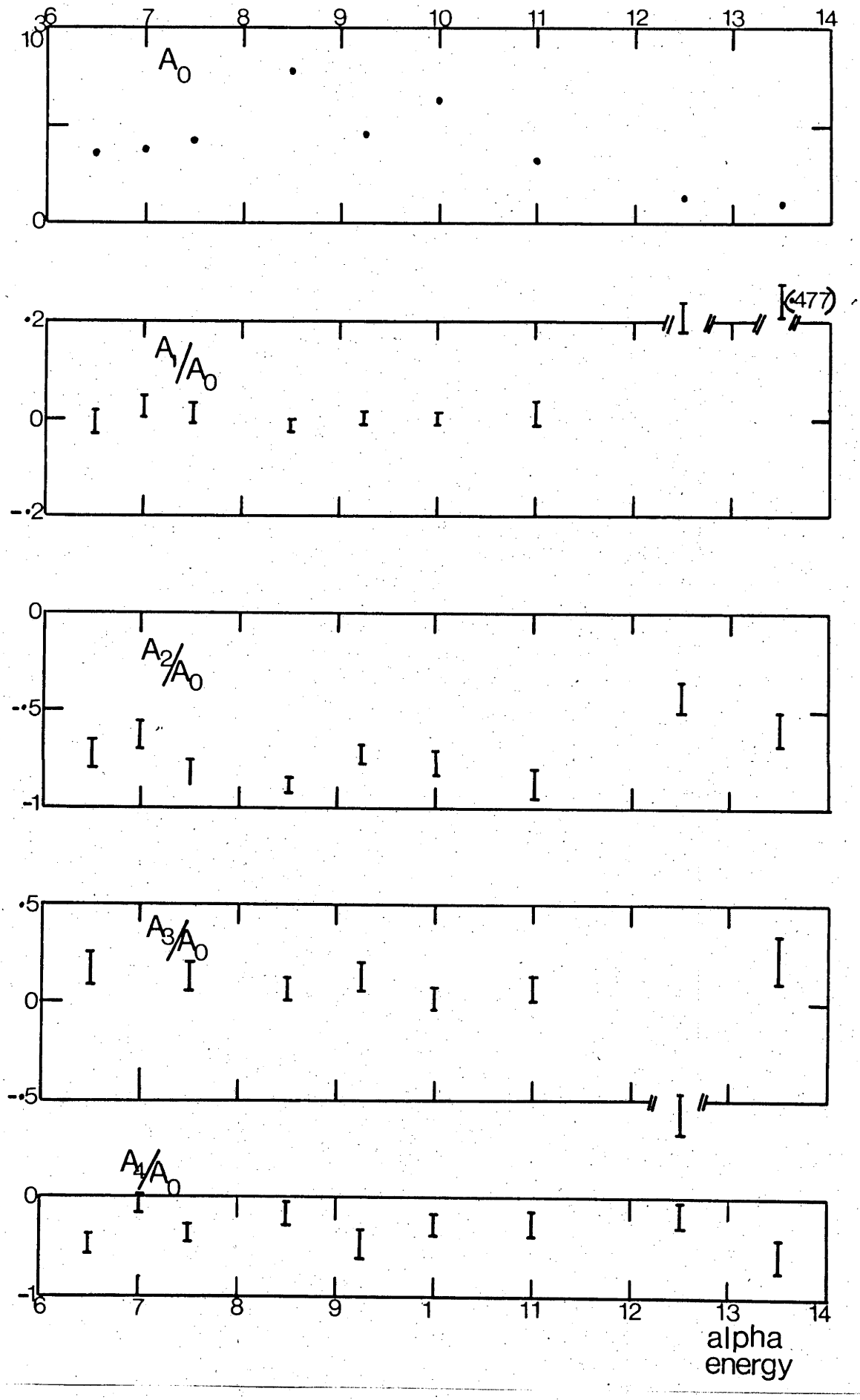

Fig.4.26. ^{60}Ni γ_0

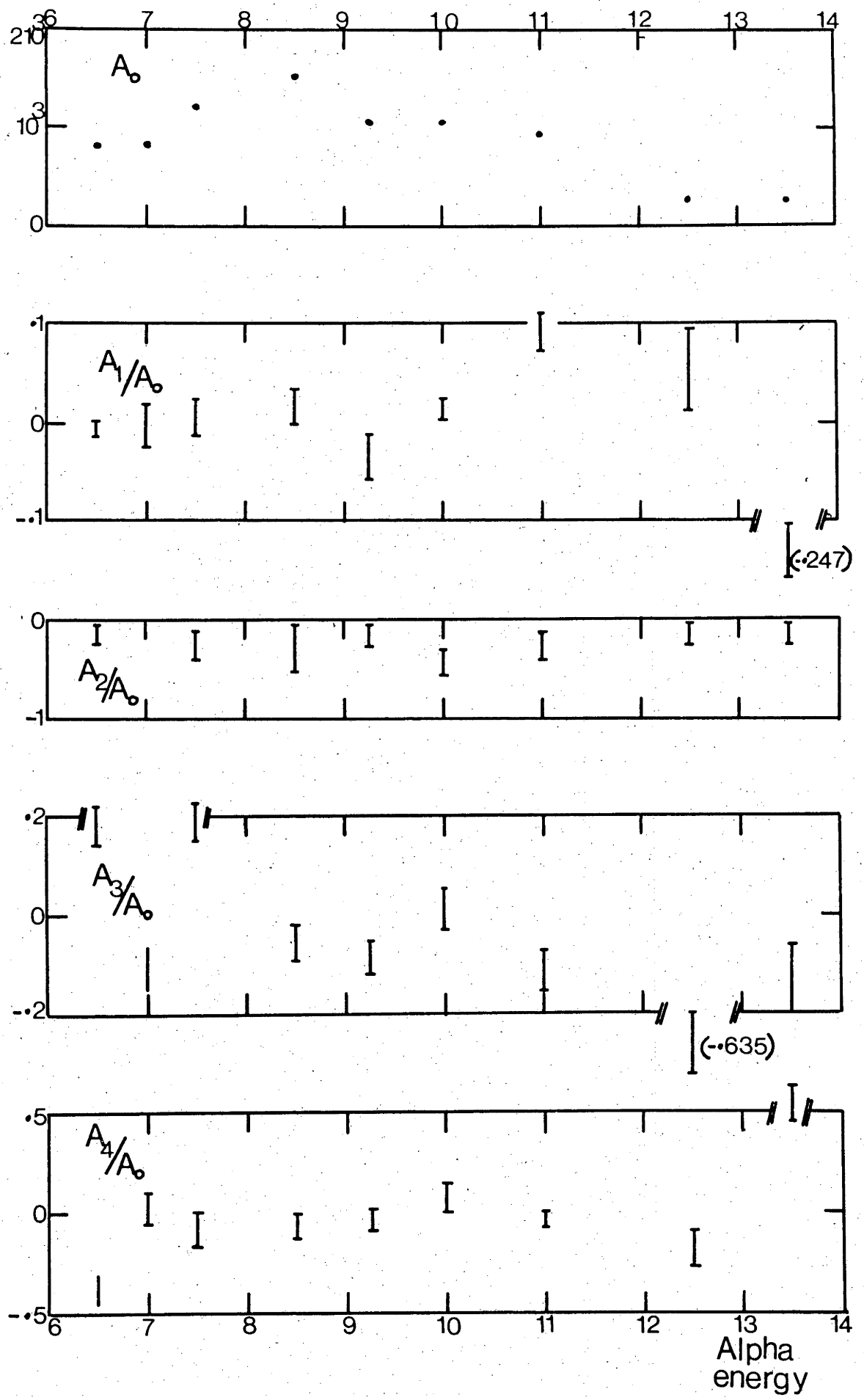

Fig.4.27. ^{60}Ni γ_1

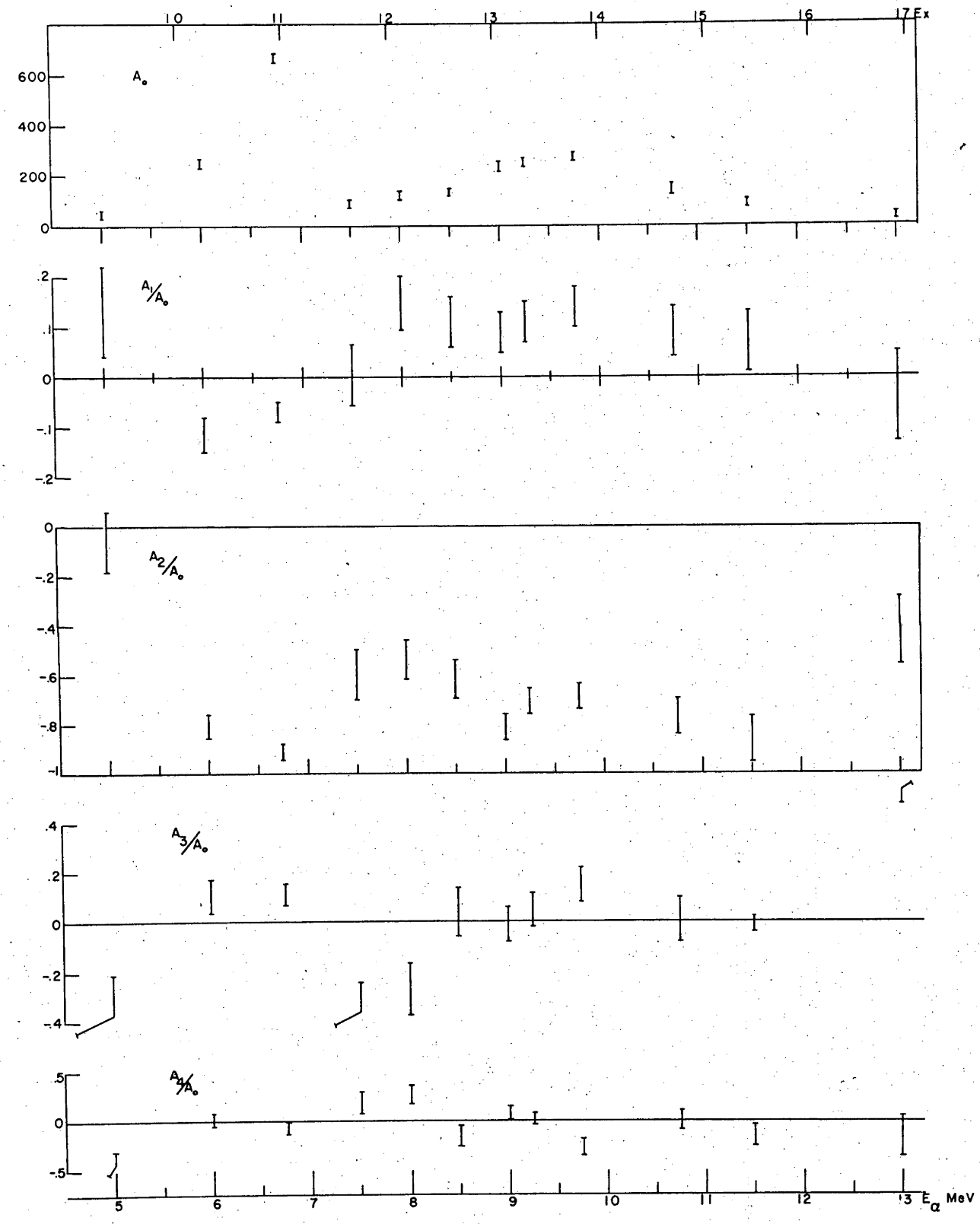

Fig. 4.28. ^{62}Ni γ_0

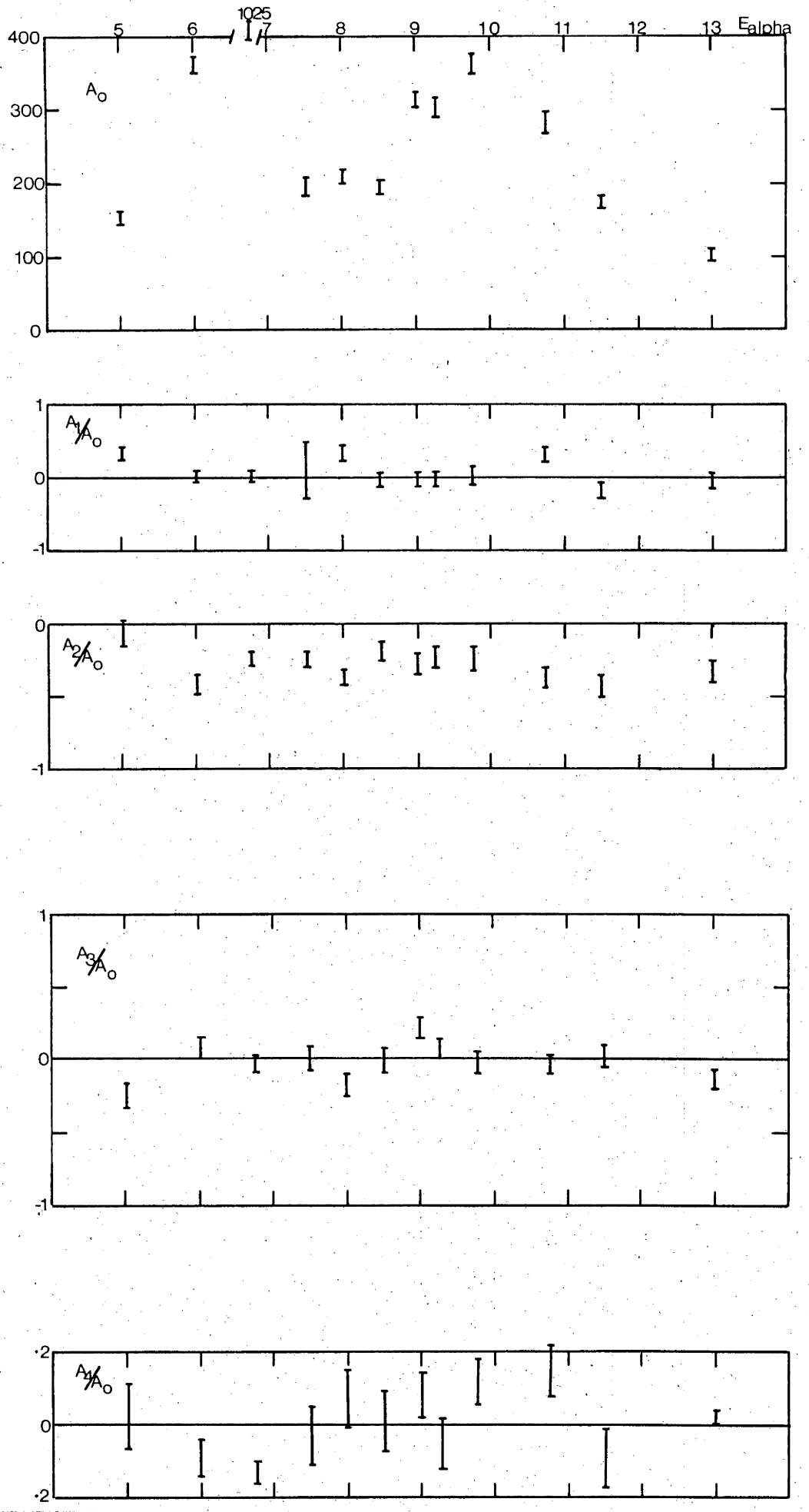

Fig.4.29. ^{62}Ni γ_1

In table 4.2, the values of the Legendre Polynomial coefficients for the transition averaged over all the angular distributions are shown. Also shown are the average ratios of the E2/E1 cross sections obtained by fitting $|f(\theta)|^2$ (eq.4.16) to the γ_0 angular distributions. In table 4.4, values of the phase angle θ_{12} are listed together with their average values. In table 4.3, the Legendre polynomial coefficients for the γ_1 transition averaged over all the angular distributions are shown.

TABLE 4.2.

Average values of $A_j/A_0(j=1,4)$ for the γ_0 transitions. Also listed are the ratios $\sigma(2^+)/\sigma(1^-)$.

Reaction	$\sigma(2^+)/\sigma(1^-)$%	$\langle A_1/A_0\rangle$	$\langle A_2/A_0\rangle$	$\langle A_3/A_0\rangle$	$\langle A_4/A_0\rangle$
$^{40}Ca(\alpha,\gamma_0)^{44}Ti$	14	-0.0293 ±0.0159	-0.796 ±0.025	0.0951 ±0.0330	-0.0657 ±0.0323
$^{54}Fe(\alpha,\gamma_0)^{58}Ni$	18	0.0499 ±0.0144	-0.750 ±0.0223	0.0123 ±0.0299	-0.262 ±0.030
$^{60}Ni(\alpha,\gamma_0)^{64}Zn$	15	0.0244 ±0.0096	-0.771 ±0.0152	0.0894 ±0.0197	-0.183 ±0.0196
$^{62}Ni(\alpha,\gamma_0)^{66}Zn$	16	0.0603 ±0.0115	-0.743 ±0.0182	0.0324 ±0.0231	-0.076 ±0.0232

TABLE 4.3.

Average values of $A_j/A_0(j=1,4)$ for the γ_1 transitions.

Reaction	$\langle A_1/A_0\rangle$	$\langle A_2/A_0\rangle$	$\langle A_3/A_0\rangle$	$\langle A_4/A_0\rangle$
$^{40}Ca(\alpha,\gamma_1)^{44}Ti$	-0.009 ±0.036	-0.426 ±0.048	0.0338 ±0.0722	-0.0660 ±0.0702
$^{54}Fe(\alpha,\gamma_1)^{58}Ni$	0.0568 ±0.0472	-0.0789 ±0.0596	-0.0644 ±0.0857	-0.204 ±0.0836
$^{60}Ni(\alpha,\gamma_1)^{64}Zn$	-0.0195 ±0.0217	-0.232 ±0.0295	-0.0149 ±0.0396	-0.0354 ±0.0407
$^{62}Ni(\alpha,\gamma_1)^{66}Zn$	0.0579 ±0.0359	-0.261 ±0.0484	0.0009 ±0.0642	-0.0386 ±0.0687

TABLE 4.4.

^{44}Ti		^{58}Ni		^{64}Zn		^{66}Zn	
E_x	$\theta_{12}°$	E_x	$\theta_{12}°$	E_x	$\theta_{12}°$	E_x	$\theta_{12}°$
13.69	82± 3.3	14.13	85± 3.1	10.09	88± 4.1	10.0	99± 2.1
13.78	96± 4.4	14.55	86± 3.9	10.56	96± 1.4	10.94	82± 1.6
14.42	80± 1.6	15.11	77± 1.1	11.03	91± 8.9	11.64	83± 1.5
14.55	93± 1.3	15.38	93± 2.9	11.97	85± 1.9	12.35	95± 3.4
14.83	91± 1	15.66	99± 1.4	12.67	89± 9.8	12.82	101± 1.4
15.15	79± 1.4	16.08	95± 3.3	13.38	91± 3.4	13.28	95± 2.5
15.78	85± 4.2	16.36	90± 5.1	14.31	92± 5.1	13.75	98± 1.9
16.51	92± 8.3	16.78	130± 2.2	15.72	105± 0.9	13.99	97± 1.7
17.15	99± 1.7	17.2	94± 3.03	16.66	112± 0.8	14.46	96± 1.5
17.33	68± 1.9	/	/	/	/	15.40	96± 2.7
/	/	/	/	/	/	16.10	95± 4.2
/	/	/	/	/	/	17.51	82± 2.9
*	$<\theta_{12}>$= 88±2.6		$<\theta_{12}>$= 93±1.3		$<\theta_{12}>$= 91.5±1.82		$<\theta_{12}>$= 94±0.8

* The average values of θ_{12} were obtained by averaging the data at seven angles and fitting this average angular distribution.

4.1.10. Calculations of the Cross Sections

An outline of the theory as developed by Shikazono and Terasawa was given in Section 2.3.1. of Chapter 2. Unlike previous theories it includes isospin mixing in the compound nucleus and this leads to a modification of the usual Hauser-Fesbach branching ratio, $T_{\alpha o}/\sum_d Td$. An isospin mixing parameter ε^2 appears explicitly, in the case of E1 radiative capture, it is the mixing ratio of 1^- $T^<$ states with 1^- $T^>$ states. This is especially important in self conjugate nuclei where only $\Delta T=1$ isovector radiation is permitted by isospin selection rules. In eq.2.60, the parameter ε'^2 appears which is related to ε^2 by $\varepsilon'^2 = \varepsilon^2 <D_<>/<D_>>$ where the $<D_{<,>}>$ are average level spacings of the $T^<$ and $T^>$ states. At low excitation energies where known discrete levels have been measured, the experimental data were used to calculate the level densities. Where discrete levels were not known, the level density formula of Gilbert and Cameron was used. This gives the level density as

$$\rho(E,J) = \frac{\exp 2\sqrt{aU}}{12\sqrt{2}\sigma a^{1/4} U^{5/4}} f(J) \qquad --- \qquad 4.19.$$

for $E \gtrsim E_x$, where

$$f(J) = \frac{2J+1}{2\sigma^2} \exp\{-(J+1/2)^2/2\sigma^2\} \qquad --- \qquad 4.20.$$

and

$$\rho(E,J) = \frac{1}{T} \exp\{(E-E_o)/T\} f(J) \qquad --- \qquad 4.21.$$

for $E < E_x$.

$\rho(E,J)$ is the level density of states with spin J, either parity at energy E, the units are MeV^{-1}. The energy U is given by

$$U = E - P(N) - P(Z),$$

where P(N) and P(Z) are pairing energies given by

$$P(N) = 1.374 - 0.00516N$$
$$P(Z) = 1.654 - 0.00958Z$$

E_x is an energy at which the two formulae eq.4.19 and 4.21 join smoothly to each other. σ is a spin cut off parameter given by

$$\sigma^2 = 0.0888(aU)^{1/2} A^{2/3} \qquad ---- \qquad 4.22.$$

The method for obtaining a is described in Gi 65a. The density of $T^>$ levels (T=1 in self conjugate nuclei) is obtained using the parameters for the adjacent $T_3 = 1$ isobaric nucleus, the $T^>$ levels starting at the lowest observed energy of a $T^>$ state in the $T_3 = 0$ nucleus. The level density of

$T^>$ states is then given by

$$\rho_{T^>} = \rho(E-E^>_{min})$$

where $E^>_{min}$ is the energy of the lowest T=1 state in the self conjugate nucleus.

The transmission coefficients were calculated within the framework of the optical model, as before

$$T_c = 1 - \exp(-2Im\delta_c) \qquad --- \qquad 4.23.$$

where δ_c is the phase shift for channel c. In the case of particle decay to discrete levels of daughter nuclei, the sum over transmission coefficients may be performed using experimental level schemes. When $\Gamma/D>1$ or where discrete levels have not been measured, the level density formulae, eqs.4.19 to 4.21 were used. The sum over T_c is then written as

$$\sum_{kj\ell} T^k_{j\ell} = \sum'_{kj\ell} T^k_{j\ell} + \sum_{j\ell I} \int_{\varepsilon_1}^{\varepsilon_m} T_{j\ell}(E)\omega_I(E)dE \qquad --- \qquad 4.24.$$

where the primed sum is over transmission coefficients to the first few discrete levels of the residual nuclei and the integration starts at energy ε, which is the energy where the level density formulae are employed. I is the spin of the residual nucleus after emission of a particle from the compound nucleus with spin J, so $\underline{I} = \underline{J} - \underline{j}$ where j is the outgoing channel spin.

The transmission coefficients were calculated from published optical model analyses. The scattering of alpha particles has been studied for all the targets used in these experiments, and the parameters of the potentials obtained by fitting the data were used.

Parameters for neutron and protons on the appropriate residual nuclei were as in table 4.6.

E1 cross section

If the total gamma absorption cross section can be fitted with a Lorentz line shape, then a radiative width may be derived which exhausts 100% of the classical dipole sum rule

$$\sigma_{\gamma G} = 2\pi\lambda^2_G \frac{(2I'+1)}{(2I+1)} \frac{\Gamma_\gamma}{\Gamma_G} \frac{(E\Gamma_G)^2}{(E_G{}^2-E^2)^2 + (E\Gamma_G)^2} \qquad --- \qquad 4.25.$$

and the integral of this is

$$\int \sigma_{\gamma G} dE = \pi \lambda_G^2 \frac{2I'+1}{2I+1} \Gamma_\gamma \qquad \text{---} \qquad 4.26.$$

If the G.D.R. exhausts the dipole sum rule, then equating eq.4.26 to 60 NZ/A MeV. mb. gives

$$\Gamma_\gamma^{S.R.} = 0.0073 \frac{NZ}{A} E_G^2 \text{ keV} \qquad \text{----} \qquad 4.27.$$

with E_G in MeV.

Thus, the procedure for the E1 radiative capture data is to calculate $\sigma_{\gamma G}$, using eq.2.57. The B_α in this equation is calculated assuming a certain value of ε^2. If $\sigma_{\gamma G}$ has a Lorentzian shape, then a Lorentz line is fitted to it using Γ_γ as a parameter. The ratio $\Gamma_\gamma/\Gamma_\gamma^{S.R.}$ is then a measure of the fraction of the dipole sum rule which is exhausted by the data. Clearly ε^2 and $\Gamma_\gamma/\Gamma_\gamma^{S.R.}$ are not independent parameters. Changing the value of ε will change the value of $\Gamma_\gamma/\Gamma_\gamma^{S.R.}$ required to fit the data. Consequently, the product, $\varepsilon^2\Gamma_\gamma/\Gamma_\gamma^{S.R.}$ is the important number in this context. In the case of self conjugate nuclei, then eq.2.60 has to be used. For nuclei where $N \neq Z$, some simplification occurs, viz.

$$B_\alpha = \frac{T_{\alpha_o}}{\Sigma T_\alpha + \Sigma T_n + \frac{1}{2T^< + 2}\{2T^< + 1 + \varepsilon^2\}\Sigma T_p} \qquad \text{---} \qquad 4.28.$$

The total photoabsorption cross section is written as a linear combination of absorption terms into the $T^<$ and $T^>$ states

$$\sigma_{\gamma G} = \sigma_{\gamma G}^< + \varepsilon^2 \sigma_{\gamma G}^> \qquad \text{---} \qquad 4.29.$$

The $T^<$ and $T^>$ absorption cross sections may not have the same shape, for example it will be seen later that for the ^{54}Fe data, $\sigma_{\gamma G}^<$ = const. and $\sigma_{\gamma G}^>$ = Lorentzian are consistant with the data.

So far, the discussion has been directed to the E1 radiative capture compound process.

E2 cross section

The E2 compound process is treated in a similar way. If the E2 capture takes place by a $\Delta T=0$ transition, then the branching ratio has quite a simple form:

$$B_{\alpha_o} = \frac{T_{\alpha_o}}{\frac{1}{2}\Sigma(T_p+T_n) + \Sigma T_\alpha} \qquad \text{---} \qquad 4.30.$$

Again, a radiative width which exhausts the L.E.W.S.R. ($\lambda=2$) (eq.2.10) can be calculated. The E2 L.E.W.S.R. can be written as

$$121Z^2/A^{1/3} \quad MeV^2.fm^5 \qquad --- \qquad 4.31$$

where the mean square radius, $\langle r^2 \rangle$ has been taken as

$$\langle r^2 \rangle = \tfrac{3}{5} r_o^2 A^{2/3}$$

with $r_o = 1.3$ fm.

In the long wave length limit (which is applicable in this case), the radiative width can be written as

$$\Gamma_\gamma(L) = \frac{8\pi(L+1)}{L[(2L+1)!!]^2} k^{2L+1} \downarrow B(L) \qquad --- \qquad 4.32.$$

which for L=2 gives

$$\Gamma_\gamma(2) = \frac{4\pi}{25.3} \left(E_\gamma/\hbar c\right)^5 \downarrow B(E2) \qquad --- \qquad 4.33.$$

$\downarrow B(E2)$ is the reduced matrix element for the emission, and is related to the absorption reduced matrix element

$$\downarrow B(E2) = \frac{2I_o + 1}{2I' + 1} \uparrow B(E2)$$

$$= \frac{1}{5} \uparrow B(E2) \qquad --- \qquad 4.34.$$

Combining eqs.4.30-4.33 together leads to the radiative width which exhausts the L.E.W.S.R.

$$\Gamma_\gamma^{S.R}(E2) = 1.33 \times 10^{-5} E_\gamma^4 \frac{Z^2}{A} \langle r^2 \rangle \text{ eV}$$

$$= 1.35.10^{-5} E_\gamma^4 Z^2/A^{1/3} \text{ eV}. \qquad --- \qquad 4.35.$$

The same treatment for the E2 data as for the E1 is made, $\sigma_{\gamma G}(E2)$ is calculated, and a fit is made using $\Gamma_\gamma/\Gamma_\gamma^{S.R.}(E2)$ as a parameter.

As will be seen shortly, the compound process appears to be the dominant mechanism for radiative E1 capture. However, E2 capture is not so clear cut and direct and semi direct mechanisms may play a large part.

Direct processes

Direct radiative capture involves the transition of an alpha particle from a scattering state to a bound state in the final nucleus. The angular momentum change is carried off by an E1 or E2 gamma ray. To calculate the transition matrix element, the wave function of the target nucleus plus alpha particle in a continuum state and the wave function of the alpha particle in a bound state must be known. The scattering state wave function can be generated using the optical model potentials. To calculate the bound state wave function, a correspondence is made between four nucleons bound in a simple shell model potential, and an alpha cluster moving in the optical potential. This is shown in Fig.4.30 where the levels of an harmonic oscillator potential and a Woods-Saxon well are shown.

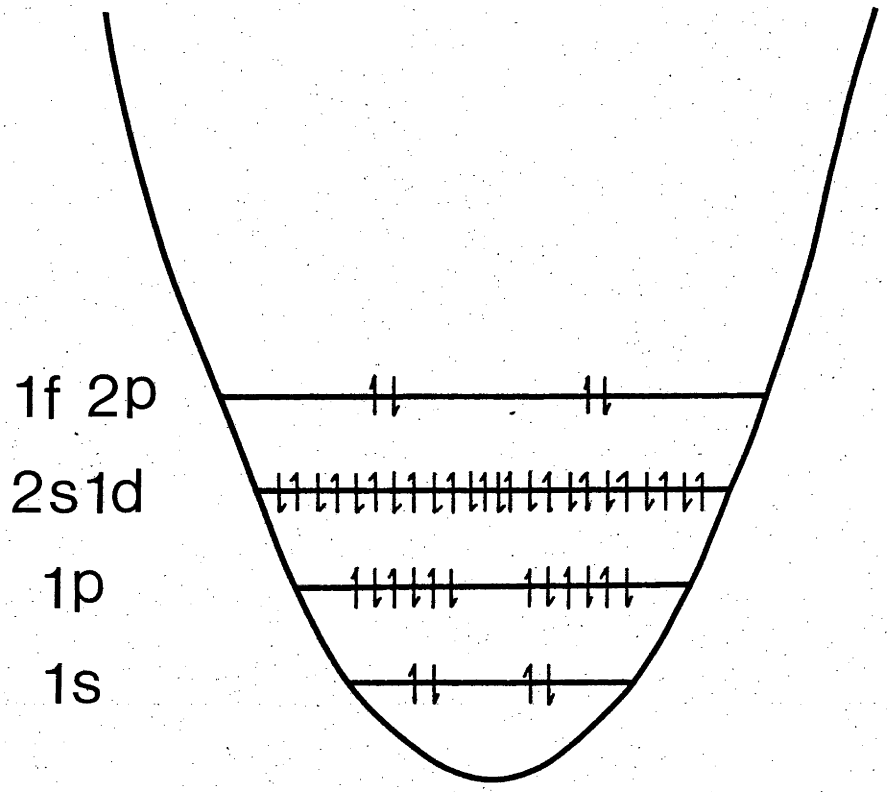

Neutrons and Protons occupying S.H.O. orbits in ^{44}Ti.

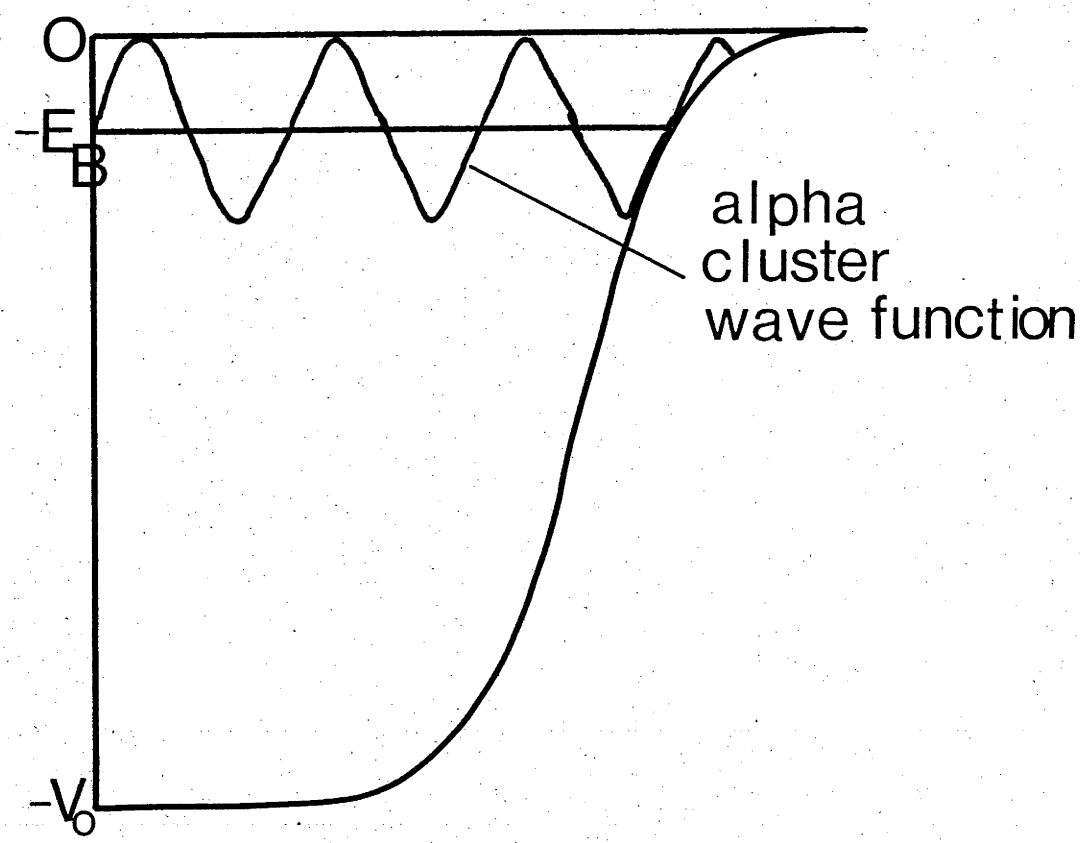

Alpha cluster state in ^{44}Ti. Woods-Saxon potential well. (Real Part).

Fig.4.30.

The energy of the i^{th} particle in the S.H.O. potential is given by

$$E_i = (2n_i+\ell_i-\tfrac{1}{2})\hbar\omega \qquad \text{---} \qquad 4.36.$$

It has been shown that

$$\sum_{i=1}^{4}{}'\{2(n_i-1) + \ell_i\} = 2(N-1) + L \qquad \text{---} \qquad 4.37.$$

where n_i is the number of nodes in the radial wave function and ℓ_i the angular momentum of the i^{th} particle. N and L are similar quantum numbers for the alpha cluster state. For example, in ^{44}Ti, the L.H. side of eq.4.37 gives 12. For L=0, N=7. This immediately imposes a constraint, the alpha cluster state wave function must have 7 nodes (excluding the one at infinity). A second constraint is that the energy of the cluster should equal the alpha particle separation energy. These two constraints are sufficient to calculate the wave function. The potential well depth of the real part of the Woods-Saxon well is treated as a parameter, and adjusted to produce a wave function satisfying the above conditions. Using this wave function and the ℓ=1 (E1) scattering state or ℓ=2 (E2) scattering state, direct transition matrix elements may be calculated. They may be written as

$$T(\ell) = \langle \Psi_{\ell m} | \frac{e}{2} \sum_i (1-\tau_{3i}) r_i^{\ell} Y_{\ell m}(\Omega_i) | \Psi_{\ell o} \rangle \qquad \text{---} \qquad 4.38.$$

Semi direct processes

As stated before, semi direct capture mechanisms are also considered for both E1 and E2 radiations. These involve excitation of the core G.D.R. or G.Q.R. by an interaction with the alpha particle. In E1 capture, this process might be important for self conjugate nuclei where the nuclear potential between the core and alpha particle cannot excite a T=1 oscillation. However, a Coulomb interaction can, and one of the possible semi direct processes (process I) involves a Coulomb matrix element between the incident alpha particle and target. The alpha particle makes a radiationless transition, this time the angular momentum change is conserved by exciting a 1^- T=1 oscillation. The system then decays by dipole emission. The second process (process II) relies upon the existence of little known 1^- T=0 excitations which have appreciable Coulomb matrix elements with 1^- T=1 states. This is therefore a two step process, a nuclear interaction exciting the 1^- T=0 state followed by Coulomb mixing of 1^- T=0 and 1^- T=1 states. The nuclear potential is taken to be a zero range potential. In self conjugate nuclei the direct E1 capture cross section should vanish because $|\Delta T|$=1 is required for dipole radiation. There are small effects which violate this

such as the mass difference between neutron and proton, but the effect produces a negligible cross section in comparison to compound or S.D. processes.

Thus for N=Z nuclei, there are two possible modes of semi-direct capture. The first involves a Coulomb excitation of the G.D.R. of the core, with the alpha particle making a radiationless transition to a bound state in the residual nucleus. This system then decays by dipole emission. The second process involves a nuclear interaction between the core (target) and the alpha particle. The existence of 1^- T=0 states which have non-zero Coulomb matrix elements with 1^- T=1 states is postulated. This is a two step process. A form factor for processes I and II is written

$$F(r) = F_I(r) + \{\frac{\delta^2(1-\delta^2)E_G^3}{4\pi e^2\Gamma_{G\gamma}(\hbar c)^3}\}^{1/2} \int <\phi_{1m}^{T=0}|H'_{II}|\phi_{oo}> Y_{1m}(\Omega)\,d\Omega \qquad 4.39.$$

$F_I(r)$ is a form factor for the Coulomb excitation of the target G.D.R. The matrix element in the second term of eq.4.39 is given by

$$<\phi_{1-m}^{T=0}|H'_{II}|\phi_{oo}> = V_o \int \rho_{tr}(r)\rho_\alpha(r_\alpha - r)\,dr \qquad --- \qquad 4.40.$$

where $\rho_{tr}(r)$ is a transition density for a 1^- T=0 oscillation. It is given by *

$$\rho_{tr}(r) = \frac{Ze}{i}\left(\frac{\hbar k}{2V_s m}\right)^{1/2} \rho_o^{1/2} \frac{\psi_{k1}(r)}{r} Y_\ell^m(\underline{r}) - \frac{\lambda}{k^2}\frac{d\rho_o}{dr} Y_1^m(\hat{r}) \qquad 4.41.$$

where V_s is the velocity of sound in the nucleus. It represents the velocity of the compressional wave. The functions ψ_{k1} satisfy a wave equation

$$\psi''_{k1} - [2/r^2 + B(r) - k^2]\psi_{k1} = \lambda\rho_o^{1/2}\frac{d\rho_o}{dr} r \qquad --- \qquad 4.42.$$

where

$$B(r) = \rho_o^{-1/2} r^{-1} \frac{d^2}{dr^2}(\rho_o^{1/2} r) \qquad ---- \qquad 4.43.$$

λ is a Lagrange multiplier introduced to keep the total number of nucleons constant.

In the case of E2 semi direct capture, excitation of the target G.Q.R. can take place by a nuclear interaction between alpha particle and core. The particle vibration coupling is given by

$$H' = R_o \frac{\partial V_\alpha}{\partial R_o} \sum_m Y_{2m}\alpha^*_{2m} \qquad --- \qquad 4.44.$$

V_α is the alpha particle optical potential, R_o the nuclear radius and α^*_{2m}.

---

* ρ_0 is the time independent equilibrium density.

is an operator which creates the collective E2 state. (See eq.2.70).

These results will now be used to calculate cross sections for the alpha capture reactions investigated.

^{44}Ti

Elastic scattering of alpha particles from ^{40}Ca has been studied at $E_\alpha \sim 10$ MeV (Ro 68) and optical model potentials have been extracted. Using a real Woods-Saxon type nuclear potential and a surface absorption term (proportional to the derivative of the real potential with respect to radius) it was found that three equivalent sets of parameters existed. The surface absorption term had an energy dependence given by

$$W_D = W_o + AE_{cm} \qquad \text{---} \qquad 4.45.$$

where W_D is the potential well depth. The three parameter sets are in Table 4.5.

Table 4.5.

Opt.Set.	V_o	A	W_o
(I)	25	0.506	-0.644
(II)	105	2.607	-10.665
(III)	132	3.047	-12.188

The real and imaginary radii and diffuseness parameters were the same for all three sets:

$$R_r = 5.2 \text{ fm.} \qquad R_i = 5.0 \text{ fm.}$$
$$a_R = 0.588 \text{ fm.} \qquad a_i = 0.3 \text{ fm.}$$

The Coulomb potential was taken to be that of a uniformly charged sphere inside the nuclear radius, and as 1/r outside the nucleus.

In self conjugate nuclei, isospin mixing is used to account for the observed radiative cross section through the compound mechanism. In this case, eq.2.60 is used to calculate the branching ratio of the compound state. Transmission coefficients for neutrons and protons are obtained by calculating phase shifts for p and n on the appropriate residual nucleus. Optical model parameters were taken from Pe 63 and Wi 64, these are listed in table 4.6. These were used for all the calculations done. In Fig.4.31, the $B_{\alpha o}$ for ^{44}Ti are shown for both E1 and E2 capture. Optical model parameter sets (I) and (III) have been used, and three values of ε^2 were used (10%, 20%, 40%). Using the value of 10%, the total gamma ray absorption cross section

(actually $\sigma_{\gamma G}\Gamma_G\downarrow/\Gamma_G$) is calculated. This is shown in Fig.4.32. The continuous line is a fit to $\sigma_{\gamma G}$ with a Lorentzian with E_r = 18 MeV, Γ_G = 4 MeV, $\Gamma_{G\gamma}$ = 19.6 keV which exhausts 80% of the dipole sum rule. An alternative way of showing this is in Fig.4.33. Here, the (α,γ) cross section is calculated from eq.2.51, and the parameter product $\varepsilon^2\Gamma_\gamma/\Gamma^{S.R.}$ = 0.08 used. In this reaction, the direct reaction mechanism is isospin forbidden. There are small isospin violating components such as the neutron-proton mass difference, but these have been shown to give a negligible contribution (Sh 75). Lines a to e in Fig.4.33 are calculations of semi direct processes I and II using different optical model parameter sets.

E2 radiative capture can take place by compound or direct-semi direct processes. In Fig.4.34, calculations of compound and S.D. mechanisms are shown. It can be seen that the D.-S.D. mechanism using parameter set I is larger than the compound process, and it is difficult to decide which mechanism is dominant. The two D.-S.D. calculations have been made assuming that $\Gamma_\gamma/\Gamma_\gamma^{S.R.}$ = 60%, S_α = 0.1, and it is the different optical parameter sets which cause the differences in the calculations.

^{58}Ni

For N≠Z nuclei, the modified branching ratio which includes isospin mixing is given by

$$B_\alpha = \frac{T_{\alpha_o}}{\Sigma T_\alpha + \Sigma T_n + \frac{1}{2T^<+2}\{(2T^<+1) + \varepsilon^2\}\Sigma T_p}$$

These are isospin allowed reactions for exciting the G.D.R. The total absorption cross section for the ^{58}Ni data was calculated using the above expression and the relationship between $\sigma(\alpha,\gamma)$ and $\sigma_{\gamma G}$ eq.2.57*. The result is quite insensitive to the isospin mixing parameter ε^2, and is shown in Fig.4.35. $\sigma_{\gamma G}$ is quite constant in the expected position of the $T^<$ G.D.R., but increases in the region of a possible $T^>$ G.D.R. Only 20% of the L.E.W.S.R. is exhausted over the G.D.R. region as located from (γ,n) reactions. Consequently, a rectangular shape was assumed for the $T^<$ resonance centred at the G.D.R. exhausting 20% of the sum rule. A sharp upper resonance was assumed with E_R = 19.5 MeV, Γ = 1 MeV. In Fig.4.37, it can be seen that the data are quite well fitted with these assumptions, namely $\sigma_{\gamma G} = \sigma_{\gamma G}^< + \varepsilon^2\sigma_{\gamma G}^>$ where the superscripts refer to $T^<$ and $T^>$ resonances. The parameter product $\varepsilon^2\Gamma_\gamma/\Gamma^{S.R.}$ ≐ 16%. The upper resonance is taken to be located at 19.5 MeV with Γ = 1 MeV. Also shown in Fig.4.37 are calculations of the direct and semi direct cross sections. In both cases S_α = 1. The S.D. calculation is for

* Together with eq.2.51.

process I (Coulomb excitation only).

In Table 4.2, it can be seen that $\langle A_4/A_0 \rangle = -0.262 \pm 0.030$ has the largest value of all the reactions studied. In Fig.4.38, the E2 data extracted from angular distributions are shown together with calculations of compound, direct and semi direct processes. The data can be quite well fitted with a compound calculation with $\Gamma_\gamma/\Gamma_\gamma^{S.R.} = 60\%$. However, the G.Q.R. of ^{58}Ni has been measured by Chang et.al. (Ch 75) and found to exhaust 45% of the sum rule. If this is correct, the data can still be fitted with $\Gamma_\gamma/\Gamma_\gamma^{S.R.} = 45\%$ plus the direct-semi direct contributions, $S_\alpha = 0.1$.

For the remaining two reactions, exactly the same procedure has been carried out. For both ^{64}Zn and ^{66}Zn*, the general trend of the data are reproduced qualitatively by the compound cross section calculation (E1). The E2 data cannot be fitted by any or all of the mechanisms, the maximum cross section is about an order of magnitude larger than the calculation. Again in the case of ^{66}Zn, the qualitative features of the E1 cross section are well reproduced, especially the sudden fall when the neutron exit channel becomes available. This feature persists in the E2 calculations where the minimum of the dip is about two orders of magnitude smaller than the data. There is a failure of the theory for the E2 strength in the case of the two zinc isotopes.

In Table 4.6., the optical model parameters for calculating neutron and proton transmission coefficients are shown.

TABLE 4.6.

	Neutron	Proton
V	$47.01-0.267E$ $-0.0018E^2$	$53.3-0.55E$ $+27(N-Z)/A-0.4ZA^{-1/3}$
W	0	0
W_D	9.52-0.053E	13.5
V_{so}	0	7.5
a_r	0.66	0.65
a_i	0.48	0.47
a_{so}	-	0.65
r_r	$1.322-7.6A.10^{-4}$ $+4A^2.10^{-6}$	1.25
r_i	$1.266-3.7A.10^{-4}$	1.25
r_i	-	1.25
r_{so}	-	1.25

The parameters for the protons were taken from Pe 63, and those for the neutron from Wi 63.

* See Figs.4.39 to 4.46.

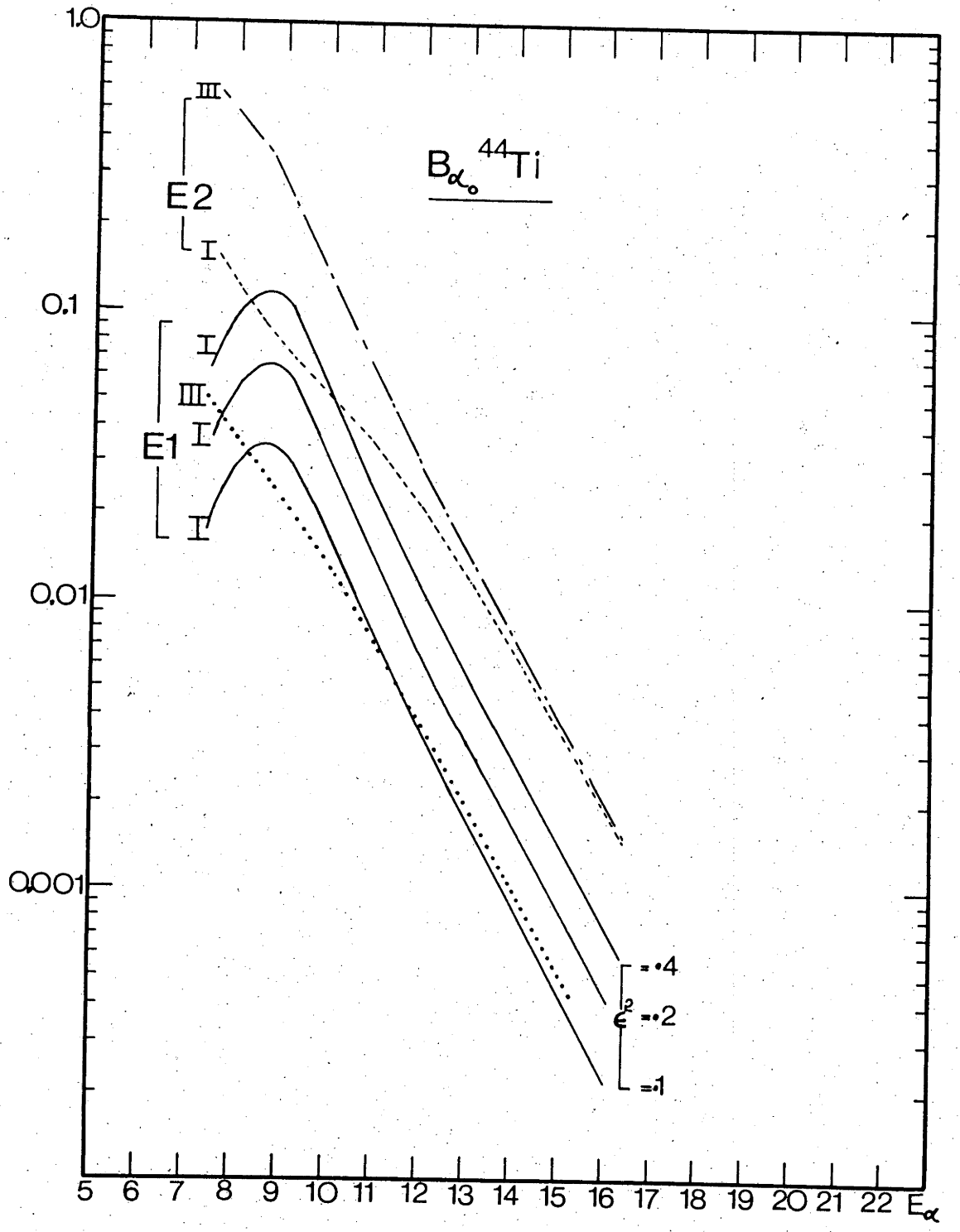

Fig.4.31. Calculations of the branching ratio. B_α for optical model parameter sets (I) and (III) ((II) and (III) gave almost identical answers). Values of the isospin mixing coefficient ϵ^2 were 10, 20 and 40%.

Fig.4.32. Calculation of $\sigma_{\gamma G}$ from the measured (α,γ) cross section using the B_α from Fig.4.31. It can be seen that parameter sets I and III give similar results. The resulting data are fitted with a Lorentz curve with $\Gamma_{G_\gamma}/\Gamma_{G_\gamma}^{S.R.} = 80\%$ and $\varepsilon^2\Gamma_{G_\gamma}/\Gamma_{G_\gamma}^{S.R.} = 0.08$.

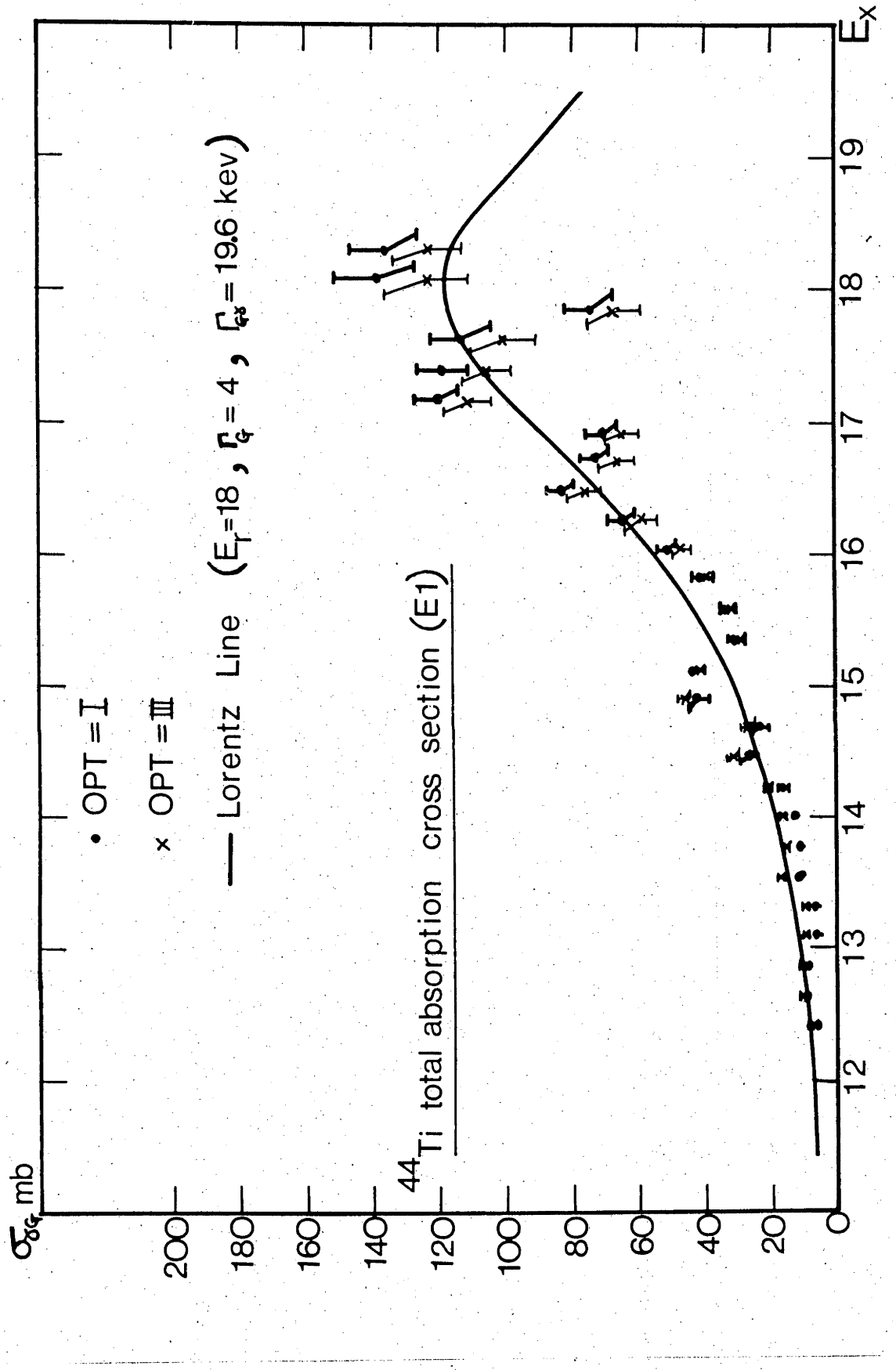
$\sigma_{\alpha\gamma}$ mb
200
180
160
140
120
100
80
60
40
20
0
12
13
14
15
16
17
18
19
E_x
• OPT = I
× OPT = III
— Lorentz Line (E_r=18 , Γ_G = 4 , Γ_{α} = 19.6 kev)
^{44}Ti total absorption cross section (E1)

Fig.4.32.

Fig.4.33. (Refer to p.146)

Calculations of compound and S.D. reaction cross sections. The two solid lines are compound cross sections calculated with optical model parameter sets I and III (Table 4.5). The parameters of the Lorentzian shape of $\sigma_{\gamma G}$ were taken as E_R = 18 MeV, Γ_G = 4 MeV, $\Gamma_G^{\downarrow}/\Gamma_G$ = 1 and $\varepsilon^2\Gamma_\gamma/\Gamma^{S.R.}$ = 0.08. Curves a to e were calculated using the parameters listed below:

Curve	S.D.process	Opt.Set.	S_α	δ
a	II	(III)	0.1	0.2
b	II	(II)	0.1	0.2
c	I	(I)	1	-
d	I	(II)	1	-
e	II	(I)	1	0.2
Not shown (off scale)	I	(III)	1	0.2

For definition of parameter sets, see Table 4.5. Note that parameter set numbers are in brackets; semi-direct processes I and II are without brackets.

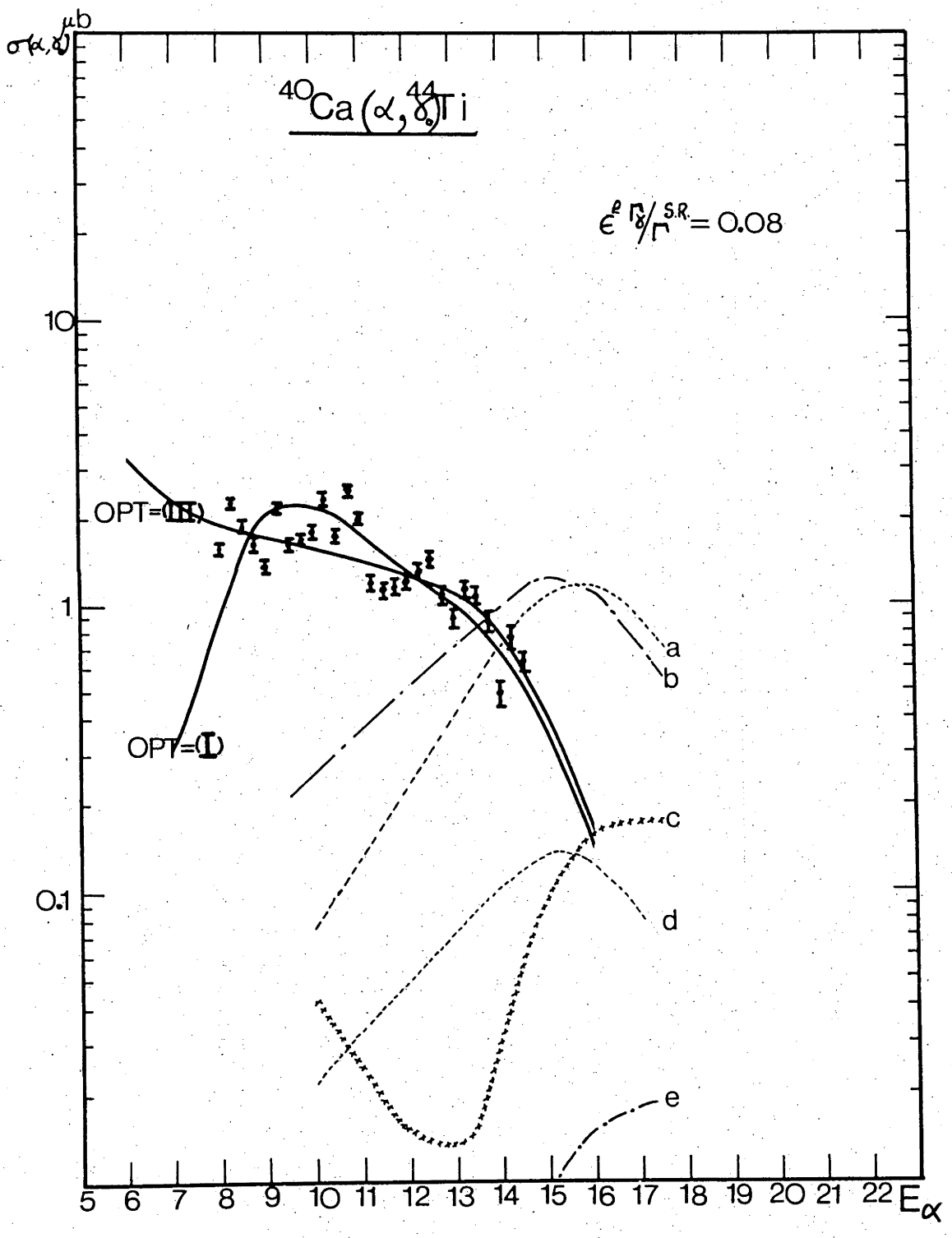
σ(α,δ) μb
40Ca(α,δ)44Ti
ε^e Γδ/Γ^S.R. = 0.08
10
1
0.1
OPT=(IF)
OPT=(I)
a
b
c
d
e
5 6 7 8 9 10 11 12 13 14 15 16 17 18 19 20 21 22 Eα

Fig.4.33.

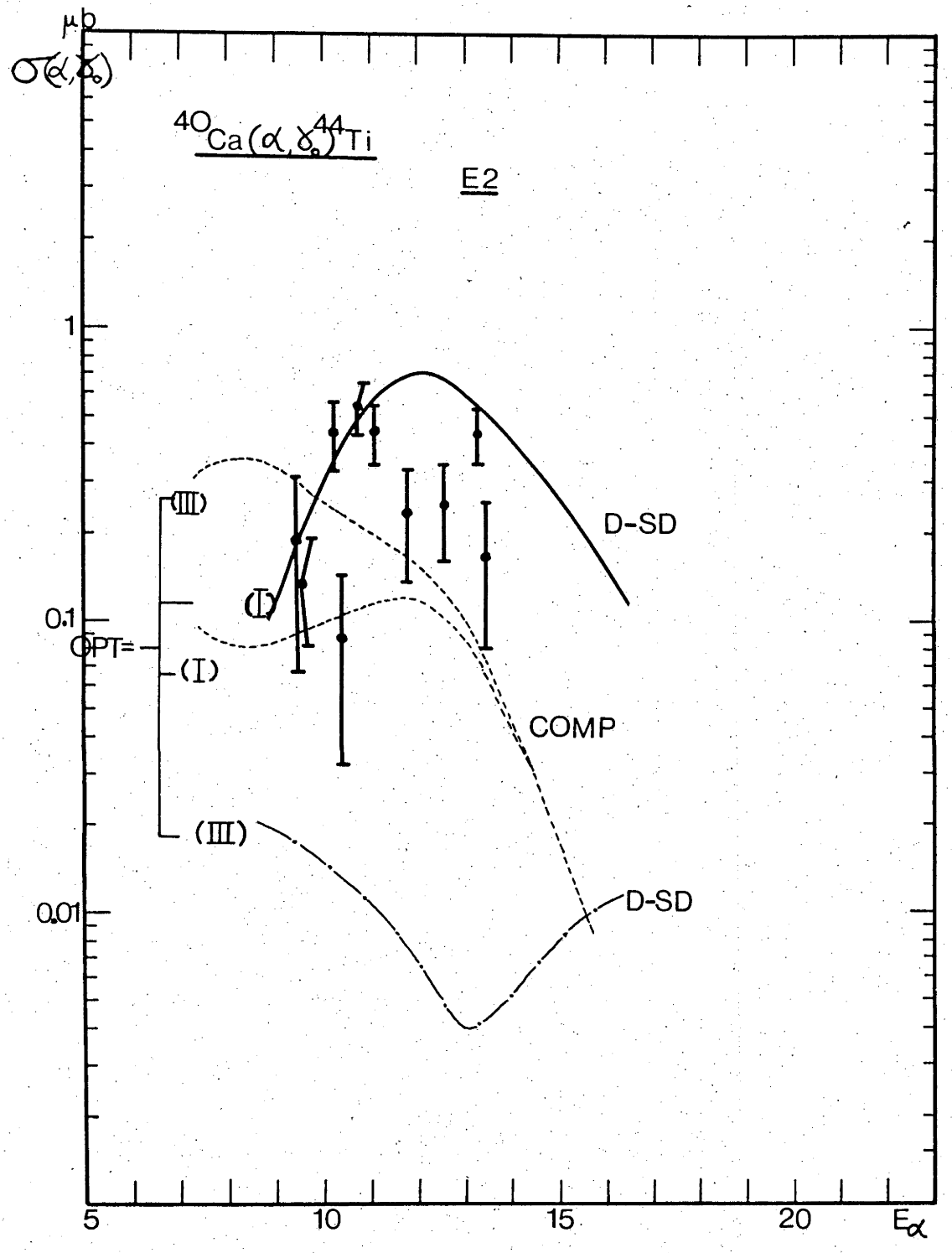

Fig.4.34. Calculations of the E2 radiative capture cross section. The compound cross section has been calculated using the B_α from Fig.4.31. ($\Gamma_{G\downarrow}/\Gamma_G$ is taken to be unity.) The D.-S.D. calculations assume that $\Gamma_\gamma/\Gamma_\gamma^{S.R.} = 60\%$, $S_\alpha = 0.1$. The parameters of the G.Q.R. are $E_R = 17$ MeV, $\Gamma = 4$ MeV.

Fig.4.35. The total gamma absorption cross section calculated using the B_α shown in Fig.4.36. It is seen that in the expected region of the $T^<$ G.D.R., the cross section is fairly constant. For comparison, a Lorentz line shape is shown which exhausts 100% of the dipole sum rule. The experimental cross section exhausts about 21%.

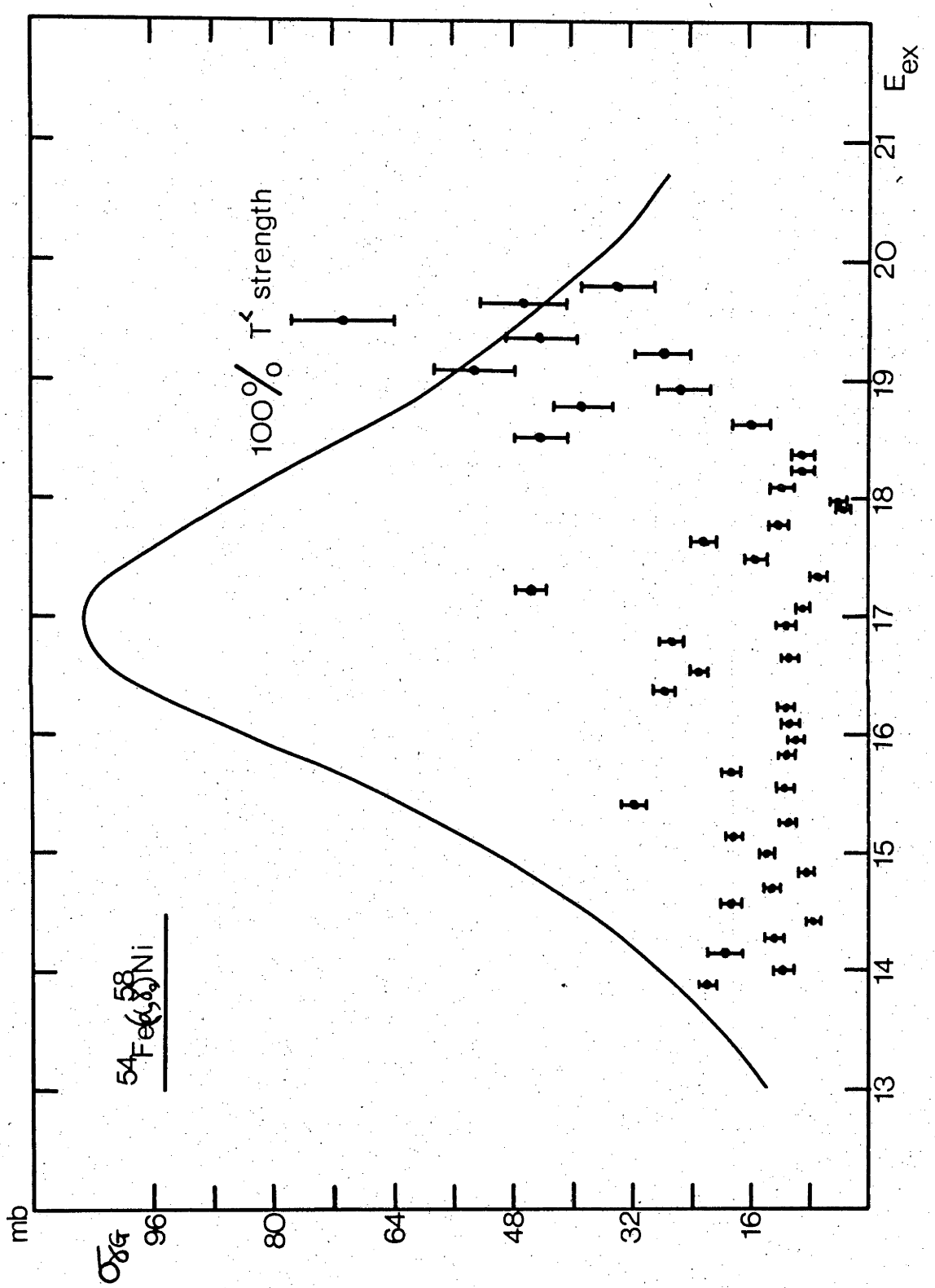
mb
$\sigma_{\gamma G}$
96
80
64
48
32
16
13
14
15
16
17
18
19
20
21
E_{ex}
100% T< strength
$^{54}Fe(\gamma,\delta)^{58}Ni$

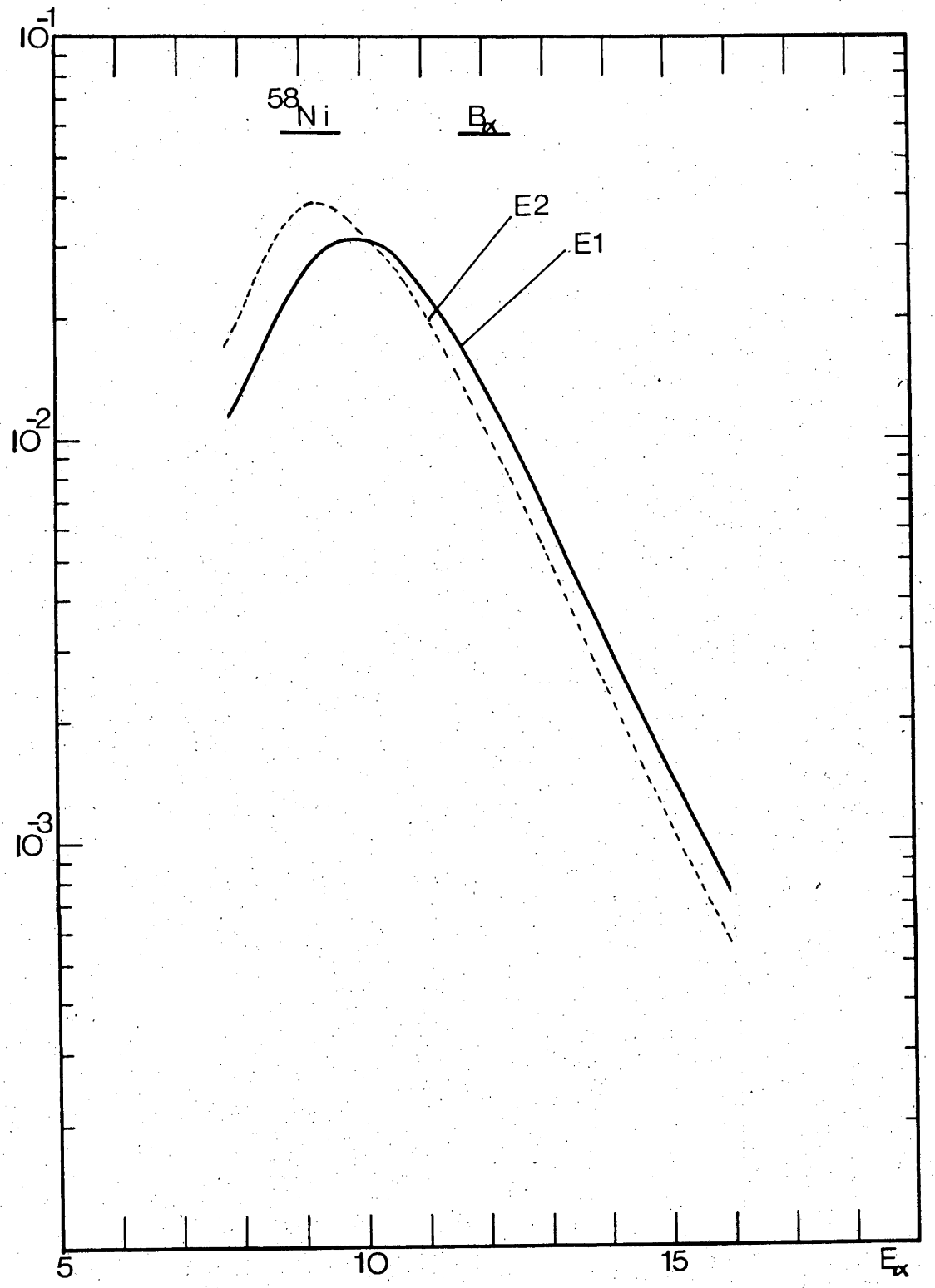

Fig.4.36. Calculations of E1 and E2 B_α for ^{58}Ni. The optical model parameter set was taken from Ya 73. The nuclear potential was parameterised with a Woods-Saxon potential with an imaginary term similar to the real part (Volume absorption)

$V_o = 42.5$	$W_o = -5.5$
$R_r = 5.65$	$R_i = 6.1$
$a_r = 0.57$	$a_i = 0.57$

The imaginary well depth had an energy dependence given by

$$W = W_o + AE_{cm}$$

with A = 1.094

(units are MeV, fm.)

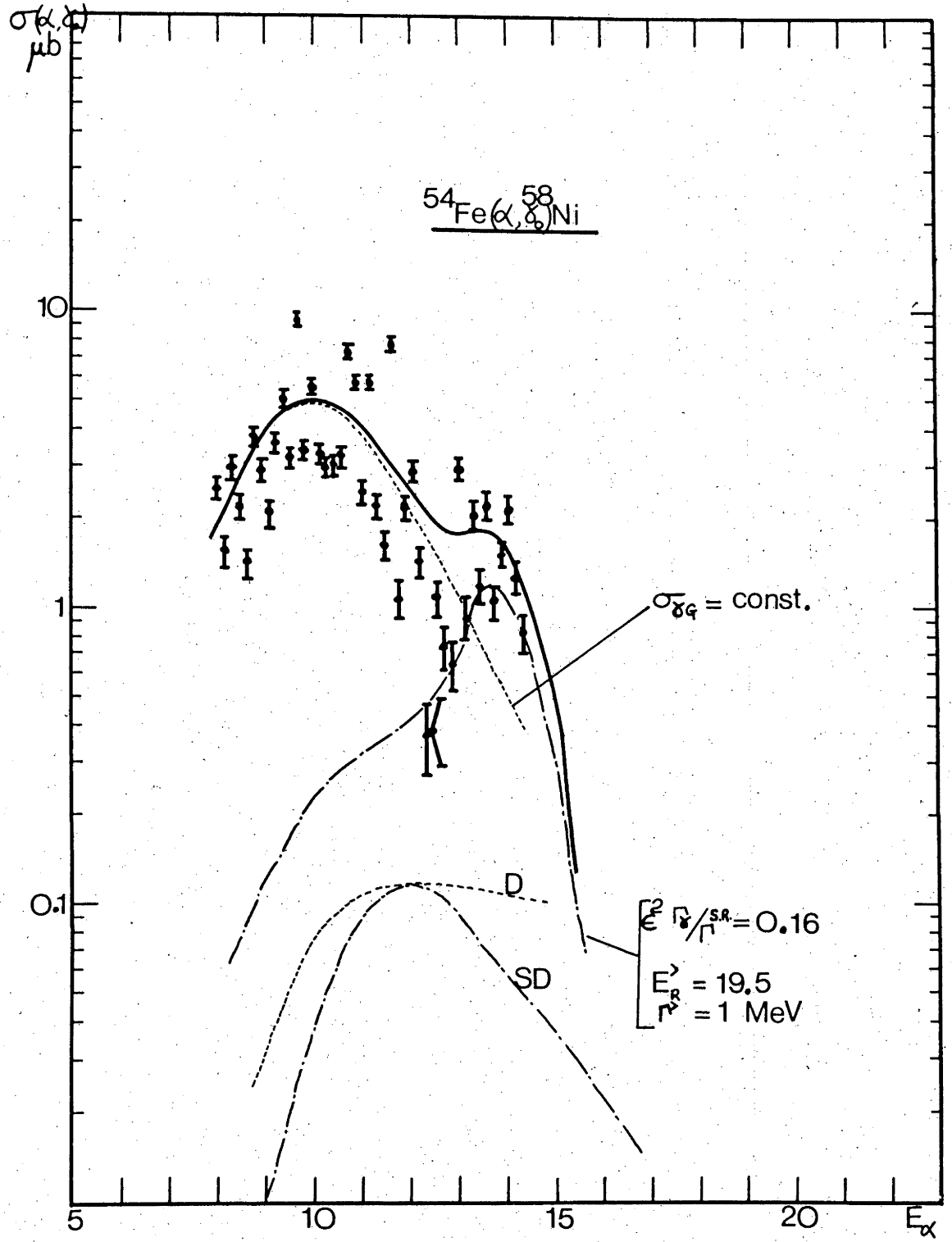

Fig.4.37. Calculations of compound, direct and semi direct cross sections for E1 radiative capture. The S.D. calculation is for process I only. The compound calculation is made assuming a constant value for the $T^<$ resonance, and a Lorentz shape for the $T^>$ with $E_R^> = 19.5$ MeV, $\Gamma^> = 1$ MeV, $\varepsilon^2\Gamma_\gamma/\Gamma^{SR} = 16\%$.

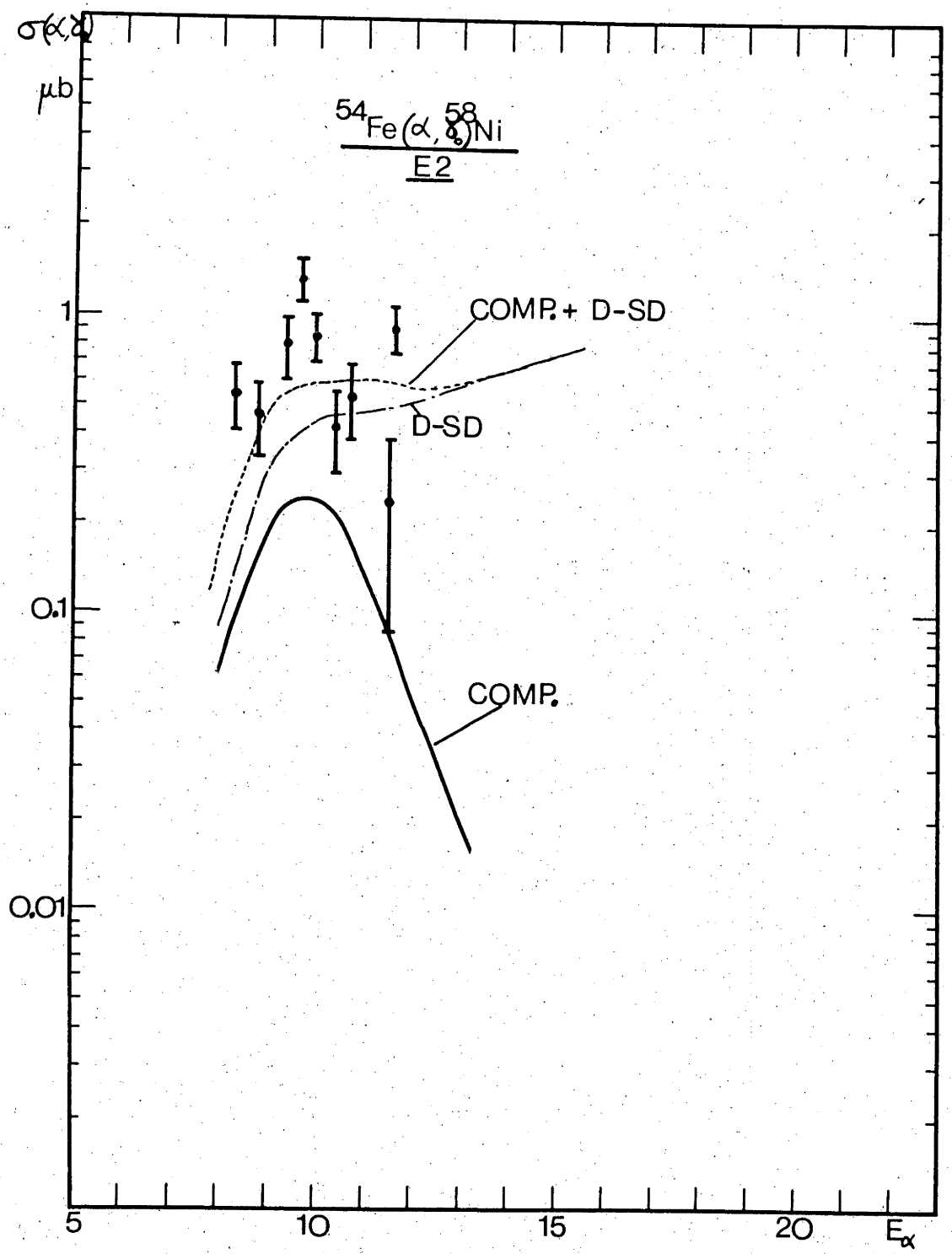

Fig.4.38. Calculations of compound, direct and semi direct cross sections for E2 radiative capture. The data indicate that direct and semi direct mechanisms contribute to the cross section. This is with $S_\alpha = 0.1$ and $\Gamma_\gamma/\Gamma_\gamma^{S.R.} = 45\%$. However, the fit is also good if the compound cross section is calculated with $\Gamma_\gamma/\Gamma_\gamma^{S.R.} = 60\%$. It is not possible to decide from the data between the two possibilities.

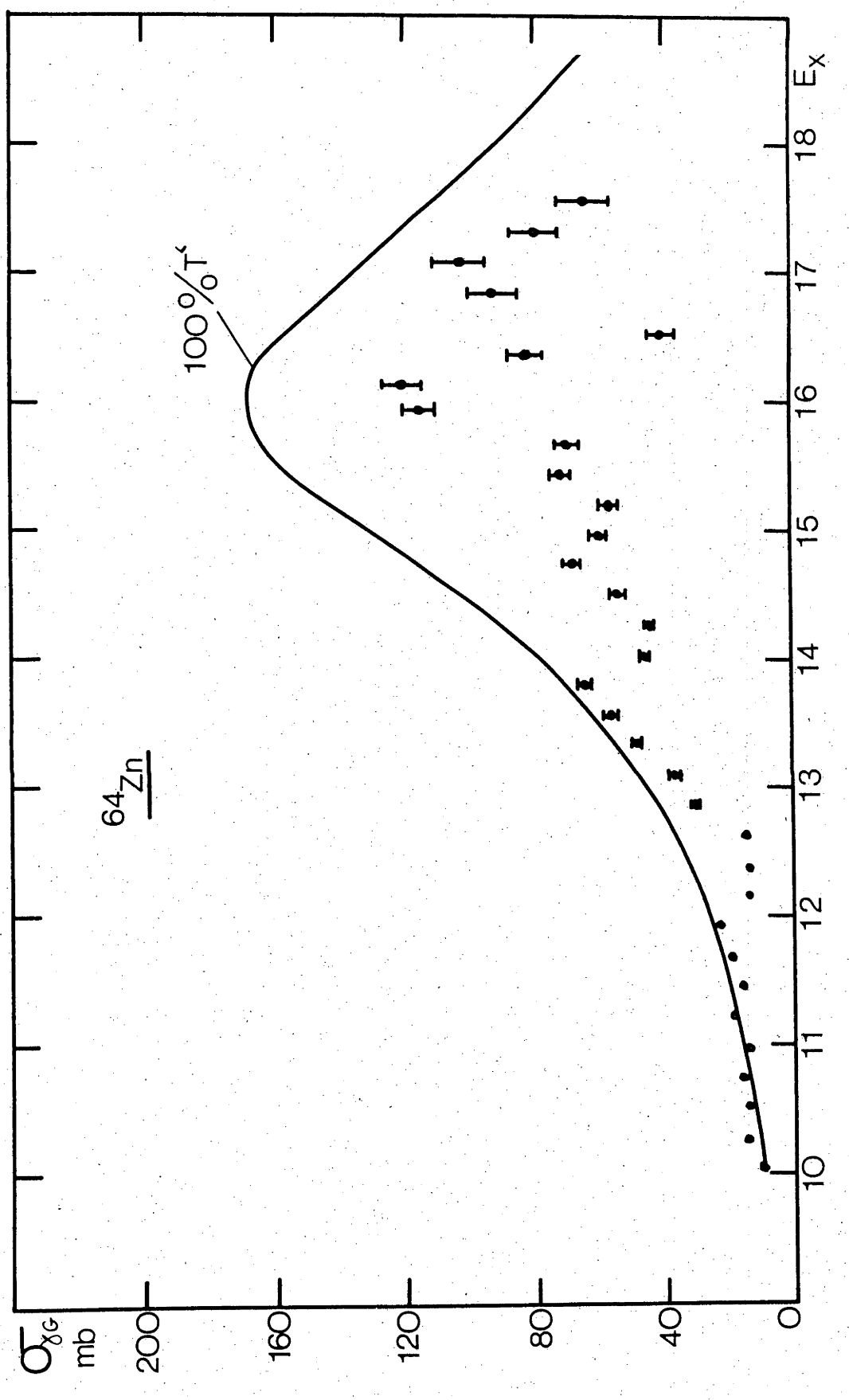

Fig.4.39. The total gamma absorption cross section for ^{64}Zn. The curve marked 100% T↙ is a Lorentz line exhausting 100% of the dipole sum rule. Its parameters are E_R = 16 MeV, Γ = 4 MeV. The same optical model parameters were used as for the ^{54}Fe data. ε^2=0.

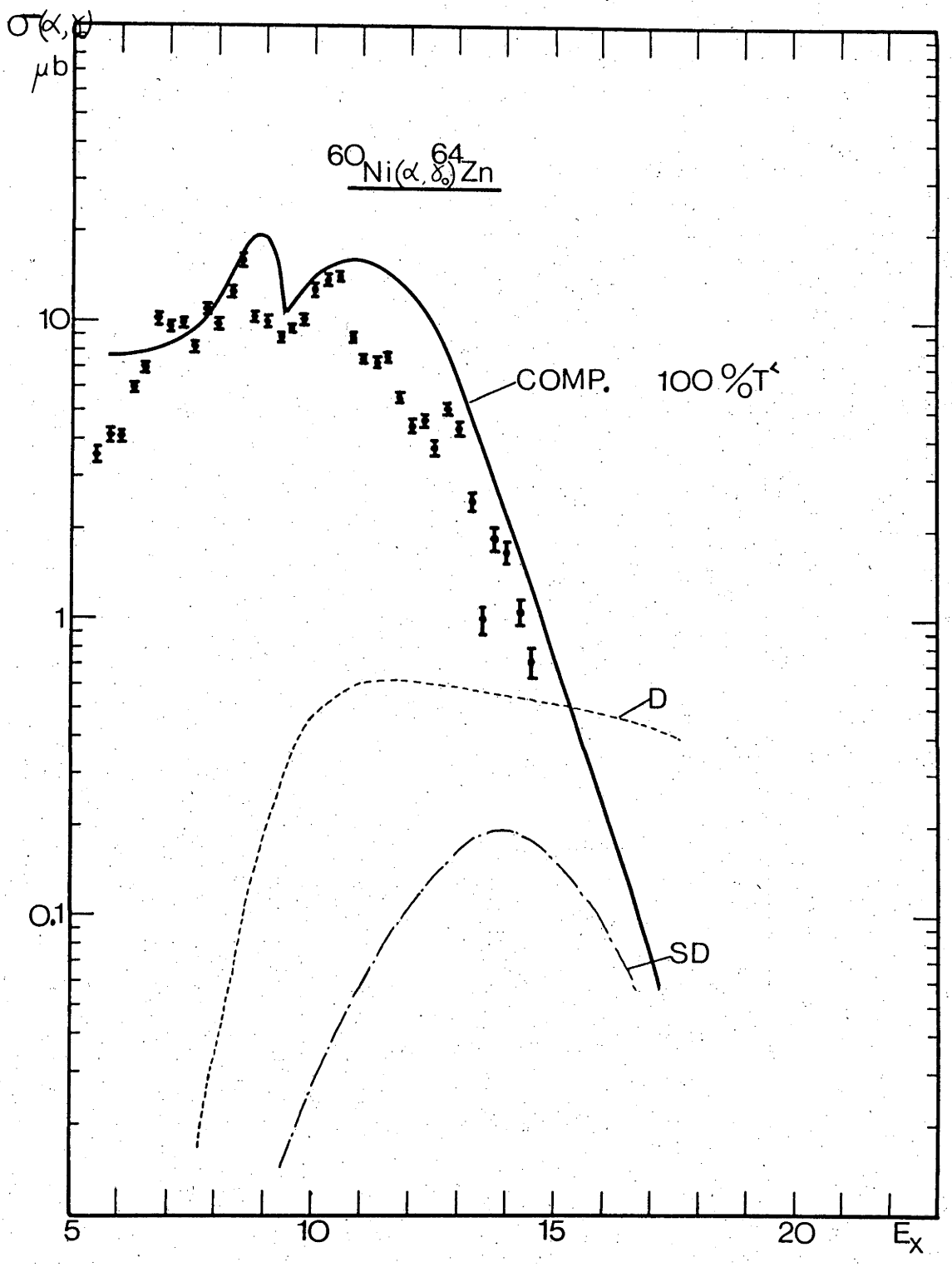

Fig.4.40. The measured $\sigma(\alpha,\gamma_0)$ cross section with a fit obtained assuming 100% exhaustion of the dipole sum rule (solid line). Direct and semi-direct calculations are also shown for comparison.

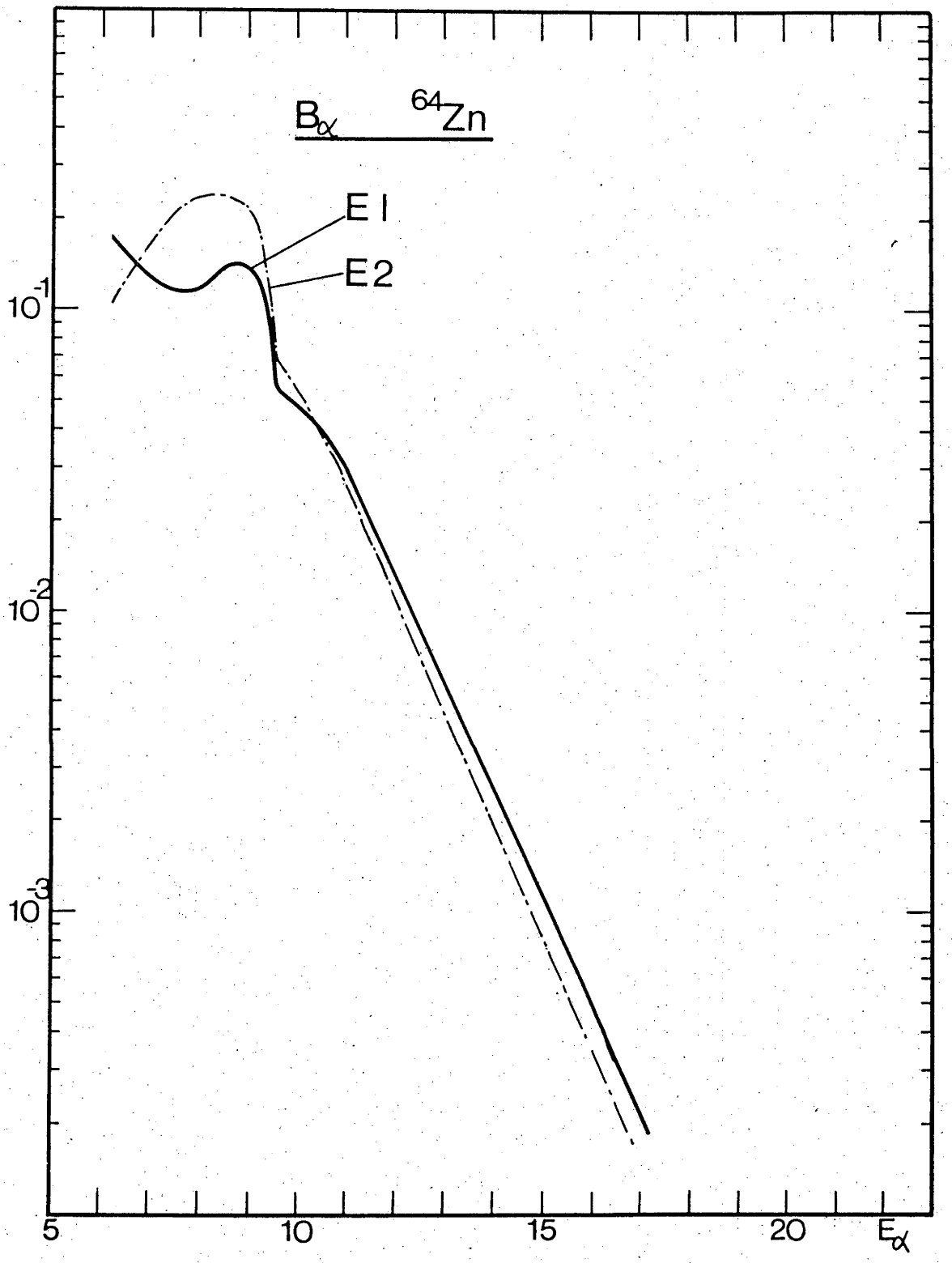

Fig.4.41. The E1 and E2 branching ratios B_α. These were calculated using optical model parameters for the scattering of alpha particles from ^{54}Fe.

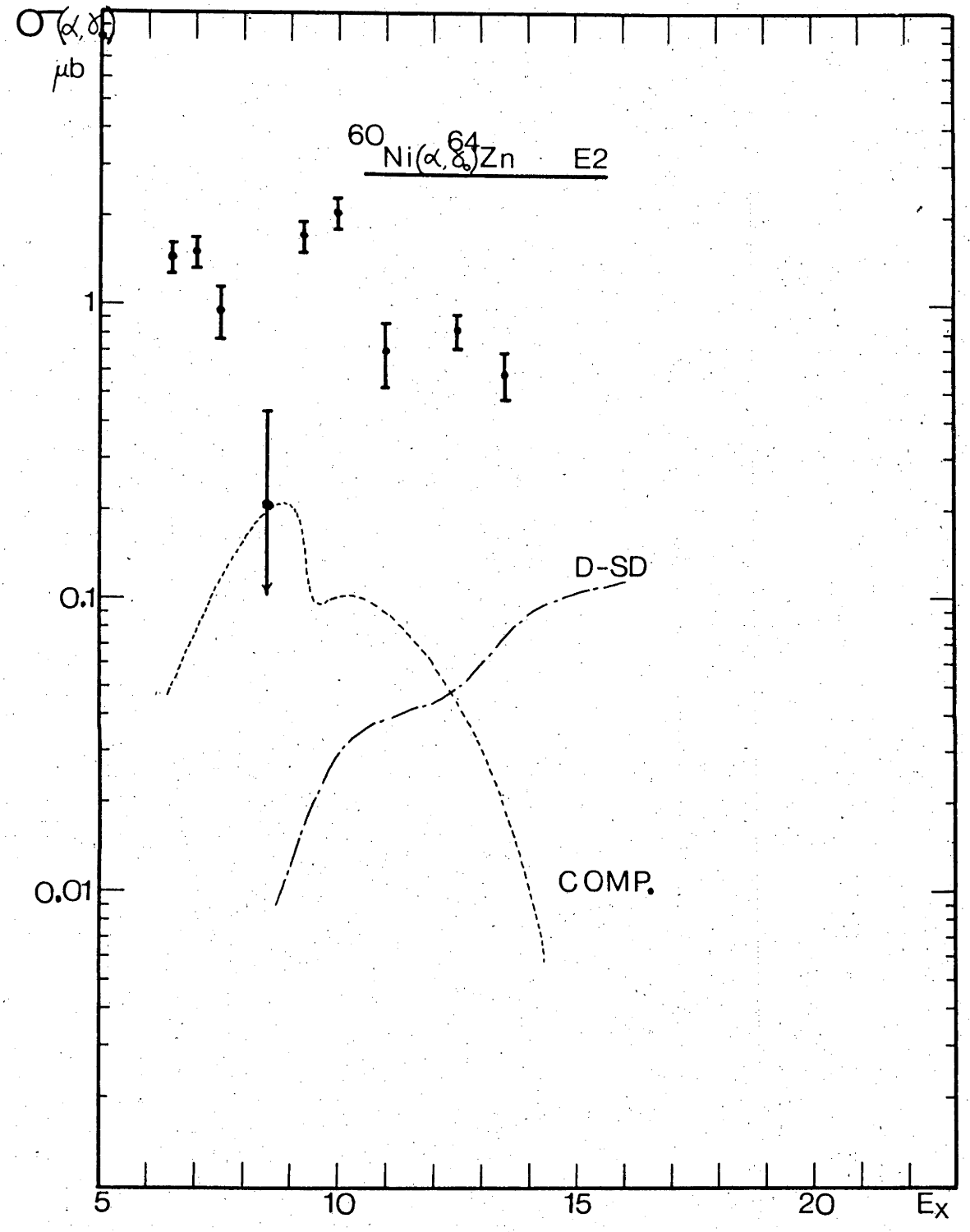

Fig.4.42. The $\sigma(\alpha,\gamma_0)$ cross section for E2 radiation. The compound calculation assumed that $\Gamma_\gamma/\Gamma_\gamma^{S.R.} = 45\%$, $E_R = 16$ MeV, $\Gamma = 4$ MeV. The D.-S.D. calculation was made with $S_\alpha = 0.1$, $\Gamma_\gamma/\Gamma_\gamma^{S.R.} = 45\%$.

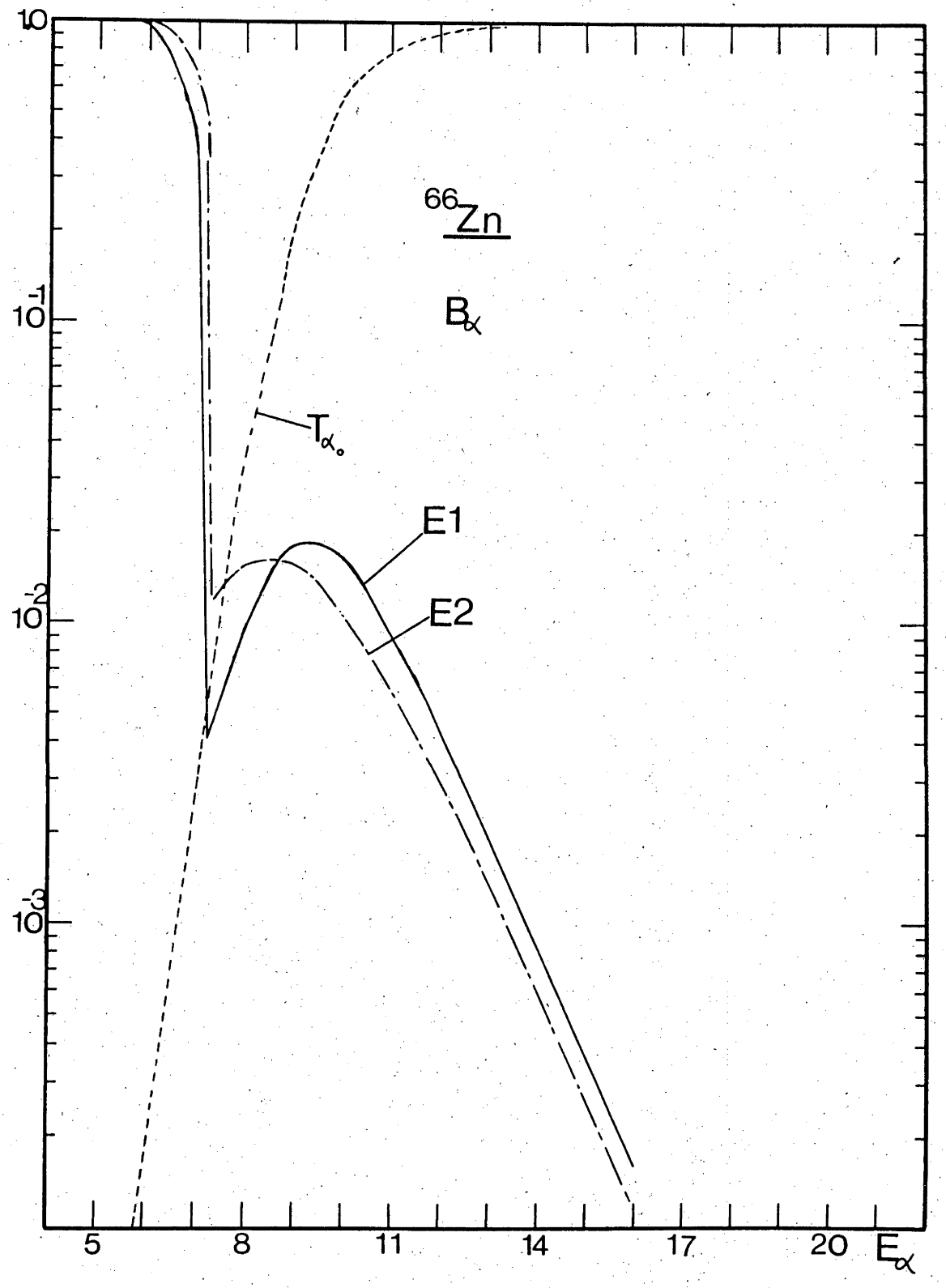

Fig.4.43. The E1 and E2 branching ratios for ^{66}Zn. These were calculated with the same optical model parameters as for ^{54}Fe. Also shown is the α_o transmission coefficient, T_{α_o}.

Fig.4.43.

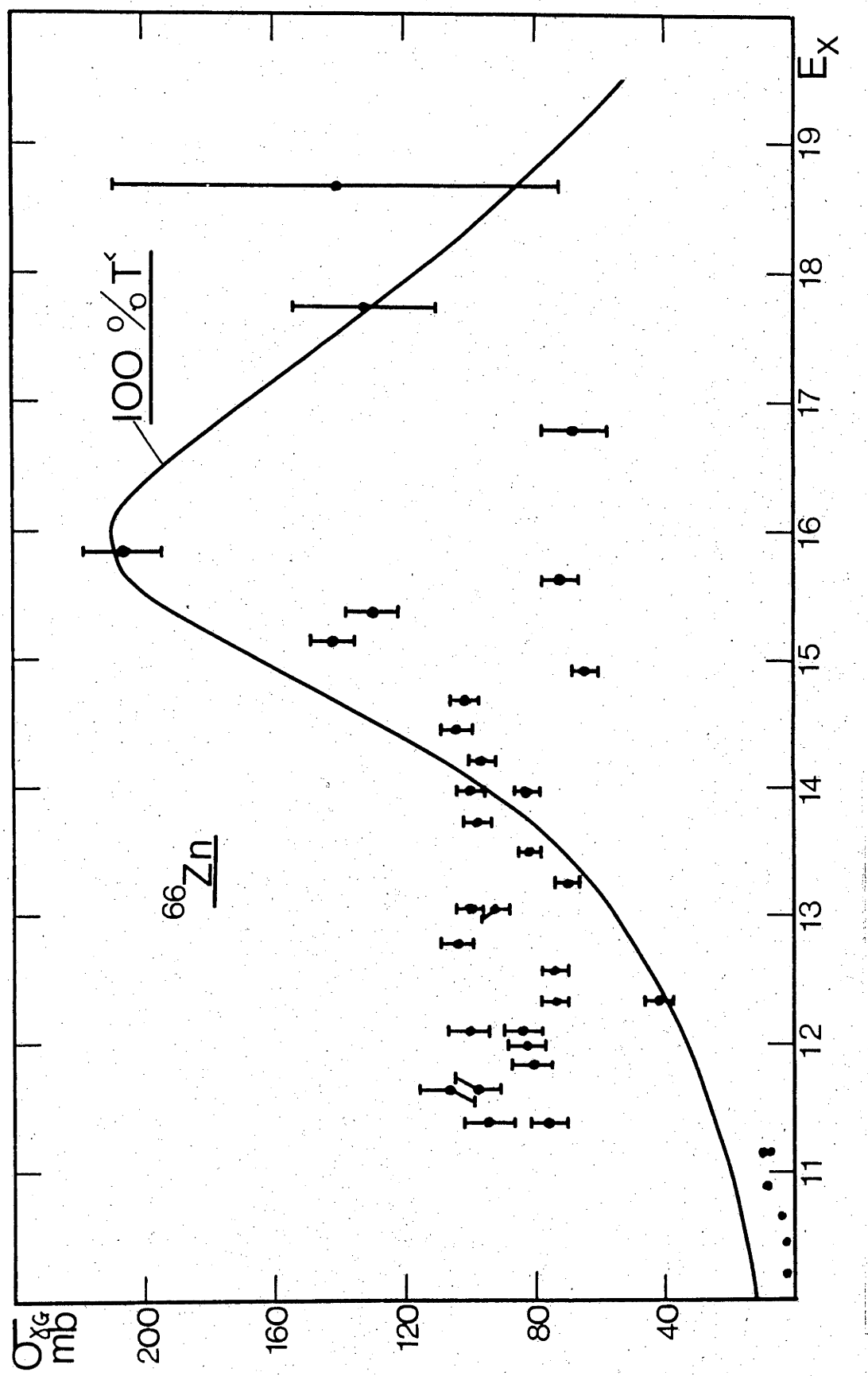

Fig.4.44. The total gamma absorption cross section for ^{66}Zn. The solid line is a Lorentzian exhausting 100% of the dipole sum rule.

Fig.4.44.

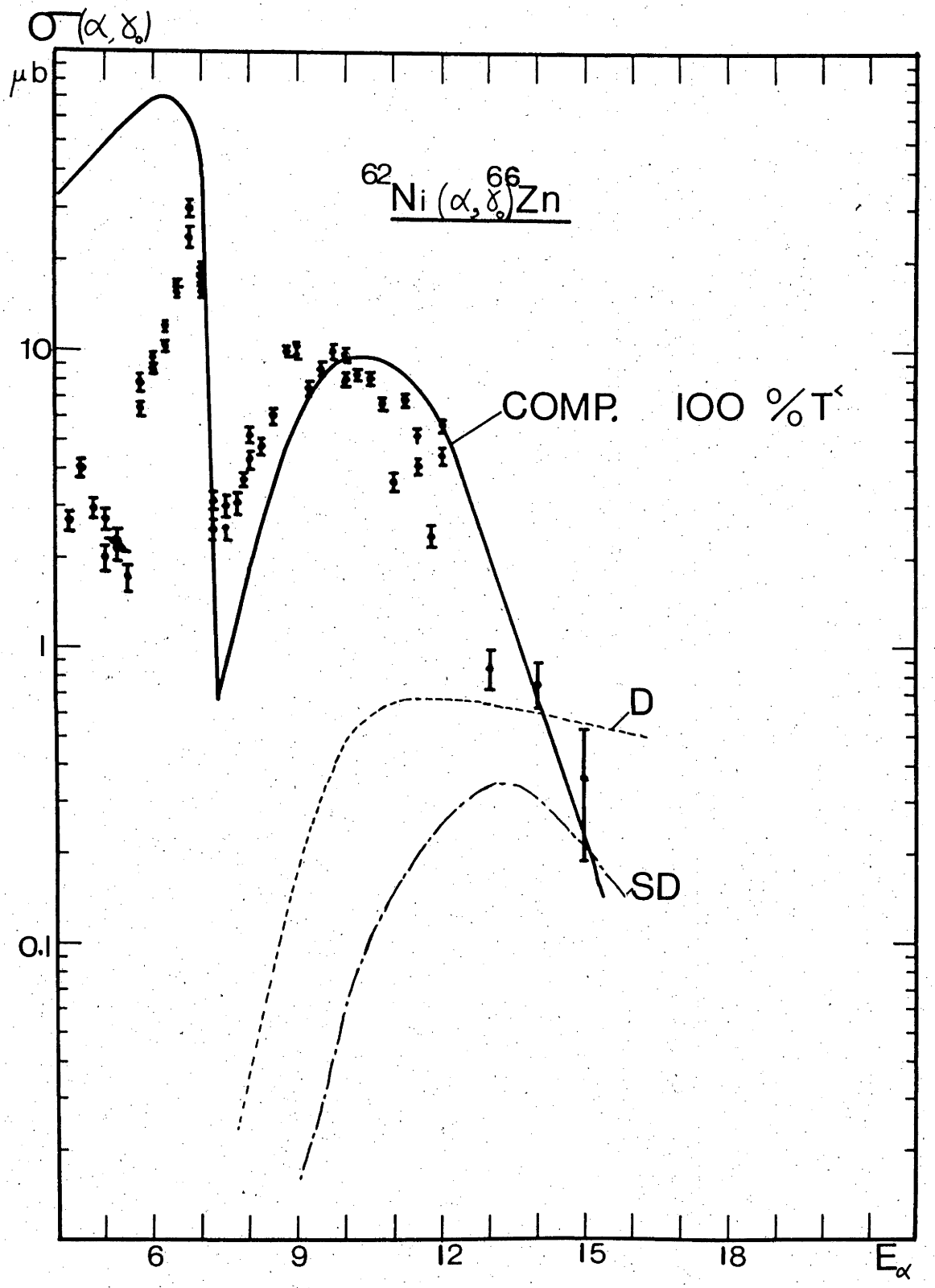

Fig.4.45. The (α,γ_0) cross section. The compound calculation is made assuming the $T^<$ cross section exhausts 100% of the dipole sum rule. Direct and semi direct calculations are also shown, these were done with $S_\alpha = 1$, $E_R = 17$ MeV, $\Gamma = 4$ MeV.

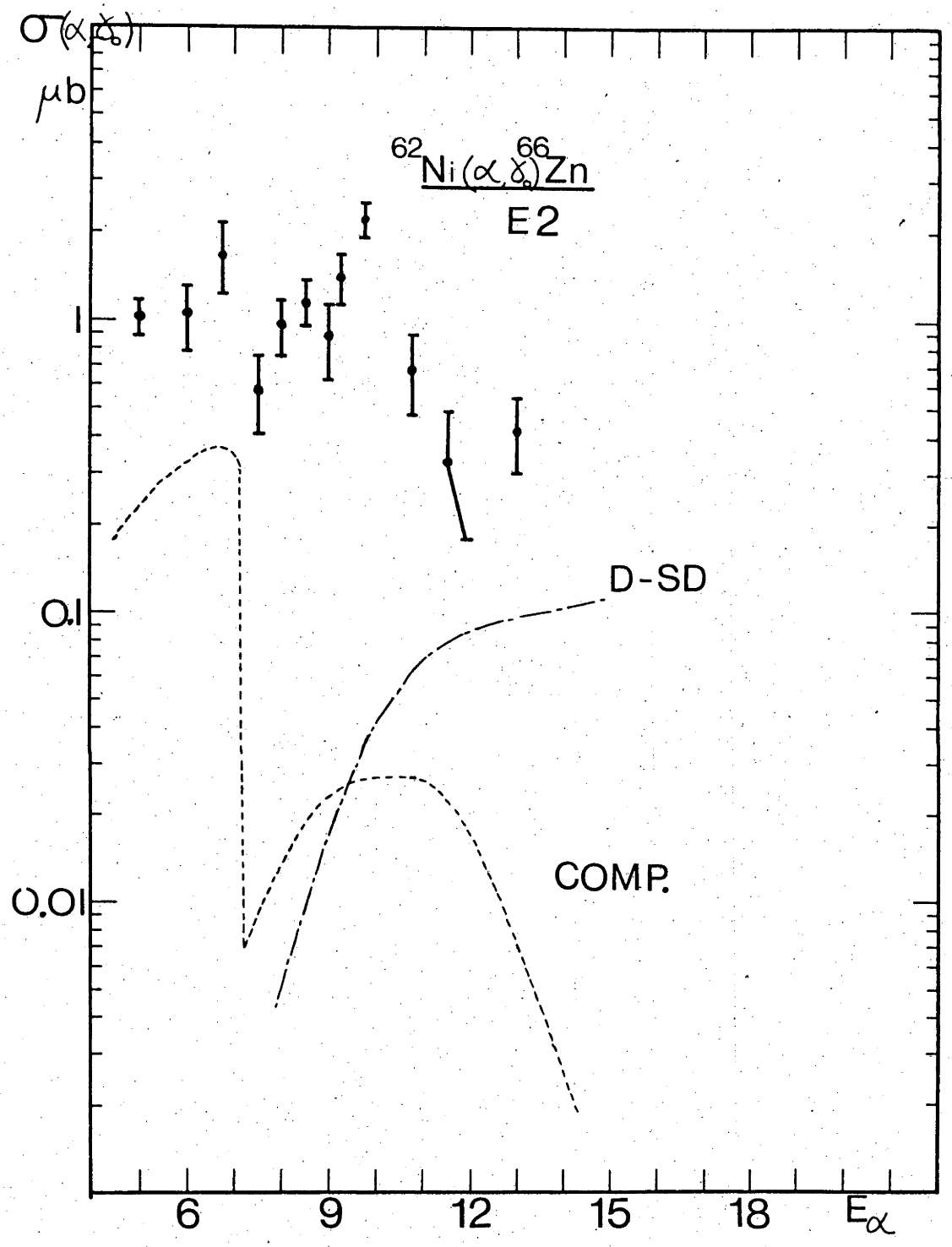

Fig.4.46. The (α,γ_0) E2 cross section. The compound calculation is made with $\Gamma_\gamma/\Gamma_\gamma^{S.R.} = 45\%$, $E_R = 16$ MeV, $\Gamma = 4$ MeV. The D.-S.D. calculation is made with $S_\alpha = 0.1$.

CHAPTER 5

5.1.1. Introduction

This chapter will collect together results of the analyses made in Chapter 4. Interpretation of the data will be made which indicate properties of highly excited states in the nuclei studied; that is, in ^{44}Ti, ^{58}Ni, ^{64}Zn and ^{66}Zn at around 15 MeV excitation energy.

The first part will summarise the values of $\langle\Gamma\rangle$ which were determined from analysis of the excitation functions. The following section will elaborate on the results of angular distribution analysis. Finally, the methods used in calculating the E1 and E2 radiative capture cross sections shown in Figs.4.31 to 4.46 will be discussed.

5.1.2. Excitation Functions and Mean Level Widths

All of the excitation functions show varying degrees of structure (Figs.4.2 to 4.4, pp.88-91). This is characteristic of the random fluctuation structure seen in excitation functions where gamma ray or particle emission takes place from a compound nucleus in a region of excitation where $\Gamma/D>>1$.

In the case of ^{44}Ti, there were a sufficient number of data to calculate the cross section probability distribution $P(\sigma/\langle\sigma\rangle)$. If the number of data is small, then the statistical error on each value of $P(\sigma/\langle\sigma\rangle)$ is large, and a meaningful histogram such as shown in Fig.4.11 (p.101) cannot be constructed. It was shown in Fig.4.9 (p.99) that when $\rho>>\langle\Gamma\rangle$ (experimental resolution >> mean level width) $P(\sigma/\langle\sigma\rangle)$ has a more or less symmetrical distribution about $\sigma/\langle\sigma\rangle = 1$. This analysis was made on an artificially generated excitation function with N=1 which is the situation in the γ_0 decay channel. As can be seen in Fig.4.11 (p.101), the $^{40}Ca(\alpha,\gamma_0)^{44}Ti$ and $^{40}Ca(\alpha,\gamma_1)^{44}Ti$ excitation functions had distributions of $\sigma/\langle\sigma\rangle$ which resembled those of Fig.4.9 (p.99) for $\rho>>\Gamma$ ($\rho = 10\Gamma$). This suggests that the structure is caused by overlapping compound nucleus states. The instrinsic fluctuation structure is averaged over by the experimental resolution.

The assumption that this (α,γ) reaction proceeds through a compound mechanism is strengthened by the calculated cross section shown in Fig.4.33 (p.146). Excitation of T=1 states in the compound nucleus is forbidden if T is a good quantum number, but on the assumption that there is overlap between $T^>$ and $T^<$ states in the continuum, the strength of the γ_0 transition can be accounted for.

The one contradictory piece of evidence against a compound mechanism is the small but significant cross correlation between γ_0 and γ_1 channels (Fig.4.10, p.101). This is probably caused by the resolution damping of the fluctuation structure in the two excitation functions.

Analyses of the three remaining reactions were made on the assumption that structure in the excitation functions resulted from damped Ericson fluctuations.

Below the Coulomb barrier, the (α,γ_0) cross section is small due to a small alpha particle penetrability. Once they are sufficiently energetic to penetrate the target nucleus, the (α,γ) cross section rises but then falls due to favoured emission of neutrons and protons over gamma rays.

The $^{62}Ni(\alpha,\gamma)^{66}Zn$ excitation functions (Fig.4.4, p.91) are good examples of gamma emission before there is sufficient energy available for neutron emission. Between 6 and 7 MeV. LAB energy, the γ_0 cross section increases by a factor of 4, while above the neutron threshold energy it rapidly falls. The further increase above about 7 MeV alpha energy is due to the increased alpha particle penetrability. The cross section falls at higher energies as the denominator of the branching ratio, $T_{\alpha_o}/\sum_c T_c$, increases. This is shown by the calculation of B_{α_o} in Fig.4.43.

All the excitation functions were analysed by the methods described in Sect.4.1.3. p.94. It was found that the auto-correlation technique gave a value of $\langle\Gamma\rangle$ which was of the order of the experimental resolution ρ. Two other methods were also tried. The method of counting maxima in the excitation function (e.g. El 66) is only suitable when $\rho<<<\Gamma>$. Similarly, the technique of Fourier analysis (He 68) is only suitable when $\rho<<<\Gamma>$. In the present cases, $\langle\Gamma\rangle$ turned out to be similar to ρ.

When the effects of experimental resolution are taken into account, (Sect.4.1.5, p.96), mean level widths can be determined when $\rho>><\Gamma>$. These agreed quite well with the systematics of $\langle\Gamma\rangle$ in this mass region. A few examples are shown in Table 5.1 together with values from the present experiments.

5.1.3. Angular Distributions

The angular distributions all showed assymetry about 90° in the γ_0 channel. This is consistent with radiation from overlapping 1^- and 2^+ levels in the compound nucleus. The absolute cross sections for the 1^- and 2^+ components were extracted by fitting the distributions with eq.4.16 (p.107).

TABLE 5.1.

Nucleus	E_x(MeV)	<Γ> keV
^{40}Ca*	18.8	10 ±5.0
^{44}Ti†	12.5-18.5	3.4±0.5
^{46}Ti*	19.1	7.4±0.5
^{54}Fe*	9.5-9.9	5 ±1.0
^{58}Ni†	14.0-19.5	7.3±1.1
^{64}Zn†	10.0-18.5	5.2±2.0
^{66}Zn†	8.0-18.0	3.3±1.4
^{76}Se*	17.0	0.7±0.1

The nuclei marked with a * are from the tabulation of Braga-Marcazzan and Milazzo-Colli (B-M 68). † are from the present experiments.

The average ratio of $\sigma(2^+)/\sigma(1^-)$ varied from about 14% in ^{44}Ti to 18% in ^{54}Fe (Table 4.2.) and the average value of the interference angle θ_{12} lay within a few degrees of 90°. (Table 4.4, p.133). This value of θ_{12} has been obtained from most alpha capture work on SD shell nuclei. It may be understood on the basis that there are many 1^- and 2^+ states contained within the resolution ρ. Various amounts of interference will occur over this energy interval ($\theta_{12}<90°$ and $\theta_{12}>90°$) but the average effect will be no interference ($\theta_{12}=90°$).

γ_1 Transitions

The γ_1 transition to the first excited state are from highly excited collective states to low energy collective states. The first excited states in the residual nuclei all have $J^\pi = 2^+$ at about 1 MeV above the ground state. These decay by E2 transitions which are enhanced over the extreme single particle Weisskopf estimate by a factor of roughly twenty, and have energies which are well accounted for by the collective model.

It is convenient to think of the inverse process of the γ_1 decay. This means that gamma ray absorption occurs exciting the residual nucleus from its 2^+ initial state to the final particle unbound state. This process is compared with the γ_0 absorption in Fig.5.1.

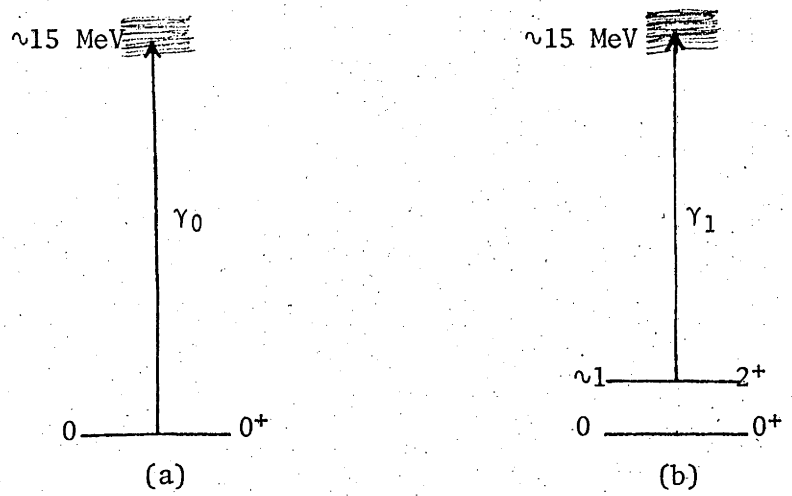

Fig.5.1.

In (a) absorption of radiation excites the nucleus from the ground state to the continuum state; in (b) absorption occurs from the first 2^+ state to the continuum.

As discussed in Chapter 2, the absorption of E1 radiation from the ground state approximately exhausts the E1 sum rule. The strength of the γ_1 absorption is usually of the same order as the γ_0 strength, and consequently a G.D.R. is said to be built on the first excited state. Coupling of the E1 angular momentum to the 2^+ state can lead to final states with $J^\pi = 3^-$, 2^- or 1^-. However, in the alpha capture reaction, only states of natural parity can be excited and these will have $J^\pi = 3^-$ or 1^-.

The absorption of M1 radiation leads to positive parity states, but again the only type of concern in alpha capture reactions are those with $J^\pi = 2^+$.

States with $J^\pi = 4^+$, 3^+, 2^+, 1^+ and 0^+ can be excited by the absorption of E2 radiation. The levels participating in the γ_1 E2 decay will be 4^+, 2^+ and 0^+ only.

To summarise, states with $J^\pi = 4^+$, 3^-, 2^+, 1^- and 0^+ may be excited in the alpha capture reaction, and E1, E2 and M1/E2 admixtures can be present in decay to the 2^+ first excited state.

It is assumed that electric dipole absorption to 1^- and 3^- states will have a much larger strength than E2 and M1/E2 absorption. This is because

a) an appreciable fraction of the total E2 and M1 strength is exhausted in transitions between discrete levels ($\sim$50% of the appropriate sum rule); and

b) the ratios of E2 and M1 radiative widths to the E1 width are expected to be small. Even if both transitions exhaust the appropriate sum rules, then $\Gamma_\gamma(E2)/\Gamma_\gamma(E1)\sim 0.5\%$. (Eq.4.27 and 4.35).

As long as the m component of angular momentum is conserved during the γ_1 decay, the radiation can have an (ℓ,m) angular distribution where m is not necessarily zero. However, the initially aligned state of the excited nucleus makes analysis of the angular distributions possible. The observed cross section is divided into component cross sections due to excitation of particular states. The fraction of each in the total cross section is denoted by $F^{J^\pi}(\Lambda L)$ where ΛL is the type of radiation from a particular state J^π. They are normalised such that

$$\sum_{J^\pi,\Lambda L} F^{J^\pi}(\Lambda L) = A_0 \qquad \text{---} \qquad 5.1.$$

where A_0 is the first coefficient in the expansion:

$$W(\theta) = \sum_{n=0}^{4} A_n Q_n P_n(\cos\theta) \qquad \text{---} \qquad 5.2.$$

where the Q_n's (n = 0,4) are attenuation coefficients as in eq.4.17, Chapter 4.

The angular distribution can be written as

$$\begin{aligned} W(\theta) = [&F^{3^-}(E1)\{1+a_2^{3^-}P_2(\cos\theta)\} + F^{1^-}(E1)\{1+a_2^{1^-}P_2(\cos\theta)\} \\ &+ F^{0^+}(E2)\{1+a_2^{0^+}P_2(\cos\theta)+a_4^{0^+}P_4(\cos\theta)\} \\ &+ F^{2^+}(M1/E2)\{1+a_2^{2^+}P_2(\cos\theta)+a_4^{2^+}P_4(\cos\theta)\}\ ] \times A_0 \\ &+ (\text{Interference terms involving } P_1 \text{ and } P_3) \qquad \text{---} \qquad 5.3. \end{aligned}$$

where the $a_j^{J^\pi}$ (j = 2,4) coefficients are listed in Table 5.3.

Interference effects are present because $\Gamma/D \gg 1$, and all the states can be excited coherently. If the coefficients of eq.5.2 are equated to those of eq.5.3, a set of equations results.

There are four unknown $F^{J^\pi}(\Lambda L)$ in three equations, and so a unique solution is not possible.

TABLE 5.3.

Type	$a_2^{J^\pi}$	$a_4^{J^\pi}$	Levels Involved
E1	-0.4	0	$3^-\rightarrow 2^+$
E1	-0.1	0	$1^-\rightarrow 2^+$
M1	0.5	0	$2^+\rightarrow 2^+$
E2	-0.15306	-0.48980	$2^+\rightarrow 2^+$
E2	0	0	$0^+\rightarrow 2^+$

Legendre polynomial coefficients for eq.5.3. It is implicit in eq.5.3. that each $a_j^{J^\pi}$ is multiplied by Q_j $(j = 2,4)$.

$$\left.\begin{aligned} &F^{3^-}(E1) + F^{1^-}(E1) + F^{0^+}(E2) + F^{2^+}(M1/E2) = 1 \\ &a_2^{3^-}F^{3^-}(E1) + a_2^{1^-}F^{1^-}(E1) + a_2^{0^+}F^{0^+}(E2) + a_2^{2^+}F^{2^+}(M1/E2) = A_2/A_0 \\ &a_4^{0^+}F^{0^+}(E2) + a_4^{2^+}F^{2^+}(M1/E2) = A_4/A_0 \end{aligned}\right\} \text{--- 5.4.}$$

However, in the event that A_4/A_0 is close to zero, the $2^+\rightarrow 2^+$ (M1/E2) transition strength will be negligible. This does not exclude the possibility of a pure E2 $0^+\rightarrow 2^+$ transition though which will contribute an isotropic background to the distribution. For reasons given earlier, it is probable that this E2 component is quite small. In the γ_0 transition it was found to be about 15% of the E1 strength. If F^{2^+} (M1/E2) and F^{0^+} (E2) $\simeq 0$, then eqs.5.4 simplify and the solutions

$$\left.\begin{aligned} F^{3^-}(E1) &= -(0.1+A_2/A_0)/0.3 \\ F^{1^-}(E1) &= (0.4+A_2/A_0)/0.3 \end{aligned}\right\} \text{---} \qquad 5.5.$$

are obtained. These fractions were computed for the γ_1 transitions and are shown in Tables 5.4 to 5.8. They are only for distributions where A_4/A_0 was close to zero.

In the $^{40}Ca(\alpha,\gamma_1)^{44}Ti$ reaction, from the three data available in Table 5.4, there appears to be an increasing contribution from 1^- states as the excitation energy increases. However, it is difficult to affirm these trends with any certainty on the basis of only three points. The average values give about equal contributions from 1^- and 3^- states.

TABLE 5.4.

$^{40}Ca(\alpha,\gamma_1)^{44}Ti$

Excitation Energy (MeV)	$F^{3-}(E1)$	$F^{1-}(E1)$	Error
14.59	0.827	0.173	0.129
14.83	0.683	0.317	0.123
15.15	0.163	0.837	0.173
14.86	< >=0.558	< >=0.442	0.083

TABLE 5.5.

$^{54}Fe(\alpha,\gamma_1)^{58}Ni$

Excitation Energy (MeV)	$F^{3-}(E1)$	$F^{1-}(E1)$	Error
14.13	0.337	0.663	0.245
14.55	0.577	0.423	0.266
16.78	1.177	-0.177	0.210
15.15	< >=0.697	< >=0.303	0.139

For the $^{54}Fe(\alpha,\gamma_1)^{58}Ni$ reaction, again there are only three angular distributions where $A_4/A_0 \simeq 0$. There appears to be a decreasing contribution from 1^- states from E_x = 14.13 to 16.78, and on the average the $3^-\rightarrow 2^+$ E1 cross section is twice as large as the $1^-\rightarrow 2^+$ E1 cross section.

In Tables 5.6 and 5.7, the $F^{3-}(E1)$ and $F^{1-}(E1)$ values are shown for the $^{60}Ni(\alpha,\gamma_1)^{64}Zn$ and $^{62}Ni(\alpha,\gamma_1)^{66}Zn$ reactions. There is no systematic trend in these values, and the average F^{3-}&F^{1-} ratios are 44&59 and 66&40 for the two reactions respectively.

In all the reactions except $^{60}Ni(\alpha,\gamma_1)^{64}Zn$, there was on average a slightly larger contribution to the cross section from $3^-\rightarrow 2^+$ transitions than $1^-\rightarrow 2^+$. In order of the Tables 5.4 to 5.7, the ratios of $3^-\rightarrow 2^+$&$1^-\rightarrow 2^+$ strengths were 56&44, 70&30, 44&59 and 60&40.

TABLE 5.6.

$^{60}Ni(\alpha,\gamma_1)^{64}Zn$

Excitation Energy (MeV)	$F^{3-}(E1)$	$F^{1-}(E1)$	Error
10.56	0.019	0.980	0.101
11.03	0.533	0.467	0.083
11.97	0.533	0.467	0.073
12.67	0.219	0.780	0.087
13.38	1.003	-0.003	0.086
14.31	0.510	0.490	0.093
15.72	0.059	0.940	0.164
12.81	< >=0.410	< >=0.589	0.039

TABLE 5.7.

$^{62}Ni(\alpha,\gamma_1)^{66}Zn$

Excitation Energy (MeV)	$F^{3-}(E1)$	$F^{1-}(E1)$	Error
9.30	-0.155	1.155	0.220
10.24	1.027	-0.027	0.147
10.94	0.480	0.520	0.087
11.65	0.660	0.340	0.200
12.12	0.873	0.127	0.187
12.58	0.310	0.690	0.206
13.05	0.557	0.443	0.160
13.29	0.430	0.570	0.163
13.76	0.440	0.560	0.147
14.70	0.880	0.120	0.163
15.40	1.077	-0.077	0.217
12.46	< >=0.598	< >=0.402	0.053

The $^{40}Ca(\alpha,\gamma_1)^{44}Ti$ and $^{54}Fe(\alpha,\gamma_1)^{58}Ni$ data indicated that there was M1/E2 radiation from $2^+ \rightarrow 2^+$ transitions over most of the energy range. ($A_4/A_0 = 0$). The other two reactions showed little M1/E2 admixture in the γ_1 channel, $\langle A_4/A_0 \rangle = -0.014$ for $^{60}Ni(\alpha,\gamma_1)^{64}Zn$ and $\langle A_4/A_0 \rangle = -0.022$ for $^{62}Ni(\alpha,\gamma_1)^{66}Zn$.

It may be concluded that the G.D.R. built on the first excited state was excited by the alpha capture reaction. Evidence of a G.Q.R. can only be obtained if 2^+ states are excited predominantly. No information can be obtained from E2 radiation from $0^+ \rightarrow 2^+$ transitions since this contributes an isotropic background to the angular distribution. The G.Q.R. built on the first excited state is thus very difficult to observe because a) it can have a J^π of 4^+, 2^+ or 0^+ populated by the alpha capture reaction, and b) the gamma ray intensity is expected to be small compared with particle emission because $\Gamma_\gamma^{G.Q.R.}/\sum_i \Gamma_i \ll 1$. (Note that $\Gamma_\gamma^{G.Q.R.}$(built on 2^+ state)/ $\Gamma_\gamma^{G.Q.R.}$(built on 0^+ state) $\sim [(E_x - 1\ \text{MeV})/E_x]^5 \sim 70\%$).

5.1.4. Calculations of E1 and E2 Cross Sections

In all the reactions studied, the E1 cross section has been satisfactorily explained by assuming a compound nucleus type mechanism. The total photonuclear absorption cross section ($\sigma_{\gamma G}$) was calculated by dividing the (α,γ_0) cross section by essentially B_{α_0}, the alpha particle branching ratio from the highly excited compound nucleus state. In the case of self conjugate nuclei, it is necessary to include an isospin mixing parameter in B_{α_0} because excitation of $T^>$ states ($T_{gs}+1$) by alpha capture is forbidden by elementary isospin coupling rules.

Similarly, in $N \neq Z$ nuclei, only $T^<$ states are excited, and if there is evidence of $T^>$ states contributing to the cross section, it is necessary to include isospin mixing.

$^{40}Ca(\alpha,\gamma_0)^{44}Ti$ E1 cross section

The total photoabsorption cross section is shown in Fig.4.32, p.144. The G.D.R. appears to be localised in a Lorentz-shaped peak centered at 18 MeV excitation energy. Unfortunately, the (α,γ_0) cross section above about 18½ MeV excitation energy became too small to reliably measure and so the full line shape cannot be obtained from the data.

Three sets of optical model parameters were available (Sets (I), (II) and (III)) from analysis of alpha particle scattering on ^{40}Ca. Over the range of data, they gave quite similar values of $\sigma_{\gamma G}$. A value of $\varepsilon^2 = 0.1$

was used in the calculation, and this produced a Lorentz-shaped line with E_R = 18 MeV, $\Gamma_\gamma/\Gamma_\gamma^{S.R.}$ = 80% and Γ_G = 4 MeV. It should be noted that only the product of ε^2 and $\Gamma_\gamma/\Gamma_\gamma^{S.R.}$ is meaningful, different values of ε^2 lead to different values of $\Gamma_\gamma/\Gamma_\gamma^{S.R.}$ so that $\varepsilon^2\Gamma_\gamma/\Gamma_\gamma^{S.R.}$ is always constant with a value of 0.08. All the strength of the G.D.R. should lie in this single resonance, and a value of $\Gamma_\gamma/\Gamma_\gamma^{S.R.}$ = 80% is reasonable. In Fig.4.33, p.145, the same data are shown in the form of the (α,γ_0) cross section. As mentioned above, the different optical model parameter sets gave similar fits over the range E_α = 8 to 16 MeV (E_x=12.4-19.6), but below E_α = 8 MeV, for sets (I) and (III) the calculations diverge. It is probable that the cross section also falls below this energy since the Coulomb barrier is at roughly 8.8 MeV. This tends to favour parameter set (I).

The conclusion is that the G.D.R. of ^{44}Ti built on the ground state is excited by alpha particle capture. A reasonable overlap between $T^>$ and $T^<$ states (~10%) can adequately account for this.

^{54}Fe$(\alpha,\gamma_0)^{58}$Ni E1 cross section

^{58}Ni has been studied at excitation energy in the continuum by several different reactions. Cross sections for (γ,n), (γ,p), (γ,xn) and (e,e') have been measured. Many of the experiments before 1960 were done with ^{nat}Ni targets (67.8% ^{58}Ni) and activation analysis was used. (That is, the decay of ^{57}Ni in the (γ,n) reactions). These data tend to have quite smooth excitation functions with a peak energy around 19 MeV and a F.W.H.M. of about 5 MeV. The integrated (γ,n) cross sections vary from $\int_{th}^{24}$ = 0.18 to $\int_{th}^{24}$ = 0.33 MeV.b.* It was found that proton emission was more favoured than neutron emission from ^{58}Ni with $\int_{th}^{32}\sigma(\gamma,p)/\int_{th}^{32}\sigma(\gamma,n)$ = 2.35±0.2. As pointed out, these data were obtained with ^{nat}Ni targets, and the method of analysis gives the cross section for decay to all possible states of ^{57}Ni.

Later experiments used enriched ^{58}Ni (≥99%) and detected the neutrons directly. These data favoured a peak at around 17 MeV with Γ = 4.5 MeV and $\int_{th}^{25}$ = 0.185. This agreed quite well with the (e,e') result of E_R = 17.3 MeV, Γ = 4.5 MeV and $\int_{th}^{30}\sigma_{TOT}$ = 0.87. It should be mentioned that the (e,e') data took no account of the different multipolarities being excited. (See Table 5.4. for reference).

More refined (γ,n) measurements showed that the excitation function had several peaks and $\int_{th}^{30}$ = 0.310. In Table 5.4, some of the data from (γ,n) (activation analysis, ^{nat}Ni) (γ,n) (neutron detection, enriched ^{58}Ni) and (e,e') experiments are shown.

* The notation $\int_a^b$ is used for $\int_a^b\sigma dE$, with th for threshold.

TABLE 5.4.

Cross Section	E_o	Γ	$\int_a^b$ MeV.b.	% S.R.	Ref.
$(\gamma,n)^{\dagger}$	18.5	4.6	$\int_0^{24} = 0.33$	38	Ka 51
$(\gamma,n)^{\dagger}$	18.5	5.6	$\int_0^{24} = 0.18$	21	Ka 51a
$(\gamma,n)^{\dagger}$	19.0	4.4	$\int_0^{32} = 0.22$	25	Ti 58
$(\gamma,n)^{\dagger}$	19.5	4.8	$\int_0^{32} = 0.32$ $\frac{\int_0^{32} \sigma(\gamma,p)}{\int_0^{32} \sigma(\gamma,n)} = 2.35\pm0.2$	37	Ca 59
$(\gamma,n)^{*}$	17.0	4.5	$\int_0^{25} = 0.185$	21	Mi 68
$(\gamma,n)^{*}$	Fragmented		$\int_0^{30} = 0.310$	36	Go 70
$(e,e')^{-}$	17.3	6.4	$\int_0^{30} = 0.87$ (TOT)	100	Gu 69

† ^{nat}Ni, activation analysis.

* enriched ^{58}Ni, neutron detection.

- enriched ^{58}Ni, all multipolarities included.

The differences between pre 1960 and post 1960 data are probably due to the differences in technique.

In Fig.4.35, p.148, the data from the present experiment show that $\sigma_{\gamma G}$ is quite constant over the region 14-18 MeV excitation energy, but increases at about 19 MeV. There is no evidence of the shape found in (γ,n) and (γ,p) experiments. It is assumed that the G.D.R. is split into $T^<$ and $T^>$ resonances and that both are excited in the alpha capture reaction. The total photoabsorption cross section is then written as

$$\sigma_{\gamma G} = \sigma_{\gamma G}^{<} + \varepsilon^2 \sigma_{\gamma G}^{>}$$

$\sigma_{\gamma G}^{<}$ is taken to be constant, and $\sigma_{\gamma G}^{>}$ a Lorentzian with E_R = 19.5 MeV and Γ = 1 MeV. It was found that $\sigma_{\gamma G}$ was quite insensitive to the value of ε in the calculation. The data exhausted about 20% of the E1 sum rule and a fit was made with $\varepsilon^2 \Gamma_\gamma / \Gamma_\gamma^{S.R.} = 0.16$.

Because the lower resonance is quite constant, it is difficult to estimate the separation of $T^<$ and $T^>$ centroids. From the (γ,n) work in Table 4.5, the $T^<$ resonance energy may lie at about 17 MeV. In this case, the energy splitting of the resonances is about 2.5 MeV. This gives a value for the symmetry energy U (eq.2.34, p.44) of 1.25 MeV, or $\tilde{V}$ = 73 MeV (Table 2.2, p.53). This value appears to fit in quite well with those in Table 2.2. However, the shape of the upper resonance is not certain because the (α,γ_0) cross section became too small to measure above $E_x \simeq 20$ MeV. It is probable that considerable strength lies above the limit of the present data since $\int_{14}^{20} \sigma_{\gamma G} / \frac{60NZ}{A} \sim 20\%$. This makes the parameters assigned to the $T^>$ resonance rather uncertain and consequently the value of $\tilde{V}$ unreliable.

<u>^{60}Ni$(\alpha,\gamma_0)^{64}$Zn E1 cross section</u>

Most of the previous measurements on ^{64}Zn have been made by activation analysis. (1 to 5 in Table 5.5.) Paul et.al. (Pa 71) have measured the ^{63}Cu$(p,\gamma)^{64}$Zn reaction and deduced a splitting of the G.D.R. into $T^>$ and $T^<$ components. (See Fig.4.14, p.105).

In the (α,γ) reaction, the cross section falls rapidly in the region of 16 MeV where the $T^<$ resonance might lie (Fig.4.14 and 4.40). In Fig.4.39, $\sigma_{\gamma G}$ has been calculated from the (α,γ) cross section. It is quite constant in the region of 16 MeV on average. It is difficult to say whether $\sigma_{\gamma G}$ is falling above E_x = 17 MeV as would be the case if the $T^<$ resonance lay at about 16 MeV and the $T^>$ at about 19 MeV. The compound calculation in Fig.4.40 has been made with $\varepsilon^2 = 0$ and $\Gamma_\gamma / \Gamma_\gamma^{S.R.} = 100\%$. From Fig.4.39, it appears that

Cross Section	E_o	Γ	$\int_a^b dE$	% S.R.	Ref.
(γ,n)	18.5	7.1	$\int_0^{24}$ 0.83	87	Pr 50
(γ,n)	18.7	7.9	$\int_0^{24}$ 0.99	103	Ka 51
(γ,n)	16.3	6.3	$\int_0^{27}$ 0.66	69	Ga 56
(γ,n)	17.2	7.0	$\int_0^{23}$ 0.33	34	Ro 60
(γ,n)	16.0 17.5 19.5	8	$\int_0^{23}$ 0.36	38	Ow 68
(p,γ)	15.8 18.9	4 2	-	-	Pa 71

TABLE 5.5.

The G.D.R. of ^{64}Zn seems to be split into at least two peaks and possibly three (Ow 68).

the $T^<$ resonance is excited consistent with that identified by Paul et.al. (Pa 71) from (p,γ) measurements. As in the previous cases, the (α,γ) cross section becomes too small to measure in the region of the proposed upper G.D.R.

$^{62}Ni(\alpha,\gamma_0)^{66}Zn$ E1 cross section

The (α,γ_0) cross section for this reaction was converted to $\sigma_{\gamma G}$ as in the previous cases. It is quite constant over the region 11.5 to 15 MeV. There is some evidence of a peak at about 16 MeV, and it was assumed that the $T^<$ resonance lay at 16 MeV with Γ = 4 MeV.

The qualitative features of the (α,γ) cross section are reproduced by the compound calculation in Fig.4.45. Below E_α = 7 MeV though, the cross section falls off much more rapidly than the calculation.

Summary of the E1 data

The (α,γ_0) E1 cross sections have been quite well fitted by compound nucleus calculations. In the case of ^{44}Ti, roughly 10% overlap of $T^>$ and $T^<$

states in the region of the G.D.R. could explain the strength of the isospin forbidden E1 decay. The G.D.R. of ^{58}Ni appears to be split into upper and lower components. Excitation of the upper resonance is due to the isospin mixing of $T^{>}$ and $T^{<}$ states. The G.D.R. of ^{64}Zn and ^{66}Zn consisted of a single $T^{<}$ component over the region of excitation energy studied.

Direct and semi direct contributions to the cross sections were found to be negligible compared with the compound nucleus contribution.

E2 transitions

The E2 radiative capture cross section has much larger statistical uncertainties than the E1 cross section. For example, if the fraction of E2 strength in the cross section is 10%, then the statistical error in 200 counts would be about 7% in the E1 cross section and 22% in the E2 cross section. It is therefore difficult to accurately obtain the E2 cross section in alpha capture reaction data.

In the S.D. shell nuclei, whenever the data are more or less completely known up to the expected position of the G.Q.R., the integrated gamma ray strength is found to exhaust approximately 50% of the isoscaler Gell-Mann-Telegdi sum rule, $\int(\sigma_\gamma/E^2)dE$. The remaining strength lies in the isoscaler G.Q.R. (See Table 2.3, p.56).

^{40}Ca(α,γ)^{44}Ti E2 cross section

The data and fit for this reaction are shown in Fig.4.34. It is difficult to decide whether the direct-semi direct or the compound calculation gives a better fit. The equivalent optical model parameter sets give very large differences in the D-S.D. calculations and appreciable differences in the low energy part of the compound calculation. It was found that the direct and semi direct capture processes for E2 capture in the ^{28}Si(α,γ_0)^{32}S and ^{36}Ar(α,γ_0)^{40}Ca were dominant (Sh 75). It is plausible that this will also be the case in ^{44}Ti where the target nucleus (^{40}Ca) acts as an inert core with its doubly closed neutron and proton shells.

^{54}Fe(α,γ_0)^{58}Ni E2 cross section

The direct-semi direct and compound calculations are of the same order of magnitude (Fig.4.38). The G.Q.R. in ^{58}Ni has been investigated by Chang et.al. (Ch 75) and found to exhaust 45% of the L.E.W.S.R. If $\Gamma_\gamma/\Gamma_\gamma^{S.R.}$ = 45%, the E2 cross section in the present experiment can be fitted with the sum of direct-semi direct and compound calculations. However, the compound cross section calculation can also fit the data if $\Gamma_\gamma/\Gamma_\gamma^{S.R.}$ = 60%. Since there is a

10% error on the number given by Chang et.al., it is not possible to decide unambiguously the mixture of D-SD and compound contributions.

$^{60}Ni(\alpha,\gamma_0)^{64}Zn$ and $^{62}Ni(\alpha,\gamma_0)^{66}Zn$ E2 cross sections

The E2 cross section calculations for these two reactions failed completely to reproduce the magnitude or shape of the E2 cross section. There is roughly a factor of ten difference between the data and the calculated cross section.

General conclusions on E2 cross sections

The E2 capture cross section calculations show that direct and semi direct processes are much more important than in the E1 case.

In the nuclei studied, the E2 strength was spread out over the interval of excitation energy with no evidence of a compact giant quadrupole resonance.

As mentioned on p.173, the E2 capture cross section is difficult to measure accurately, basically because of the very small cross sections involved. A small background contribution to the spectrum does not increase the error on the extracted E1 intensity very much, but it can greatly affect the extracted E2 intensity. Reverting to the example on p.173, suppose that in 200 counts, 20 of them are due to the E2 cross section. If there is a background of 10 counts say, then the statistical errors will be

E1	(180-10) ± 14	Fractional error ∿7%
E2	(20-10) ± 6	Fractional error ∿60%

APPENDIX A A(I)

In this appendix, the exchange energy J(R) will be derived.

The basic ideas involved are seen if the neutron is considered to be in a pure nℓj orbit and the cores are taken as point particles. Since the spin of the cores is zero, there is no coupling of the valence neutron to the core involved, but the initial formalism ignores the spectroscopic factor of the $p_{1/2}$ state in ^{13}C.

With this in mind, the exchange energy is given by:

$$J(R) = \int \phi_a(\underline{r}) V_{cn}(r) \phi_b(\underline{r}-\underline{R}) d^3r \quad \text{---} \quad A(1)$$

where V_{cn} is spherically symmetric. The integral can be evaluated analytically if the assymptotic forms of the neutron eigenfunctions are used. This is justified post priori by comparison of the answer with one obtained by numerical integration of equation A(1). In the analytic approach

$$\left.\begin{aligned} \phi_a(\underline{r}) &= N_1 h^{(1)}_{\ell_1}(i\alpha r) Y^{m_1}_{\ell_1}(\hat{\underline{r}}) \\ \phi_b(\underline{r}-\underline{R}) &= N_2 h^{(1)}_{\ell_2}(i\alpha|\underline{r}-\underline{R}|) Y^{m_2}_{\ell_2}(\underline{r}-\underline{R}) \end{aligned}\right\} \quad \text{---} \quad A(2)$$

where N_1 and N_2 are normalisation constant which are the ratio between the real assymptotic wave function and the spherical hankel function. This is subject to some variation depending on how the real wave function is calculated. Ambiguities in the optical model parameters make it impossible to assign a universal value to N. In this respect, the parameter used to fit the data is a product of N and S (S is the spectroscopic amplitude). A useful comparison of S^2 between different experiments can only be made when a constant value of N is used. In this experiment, N was the same as that used by W. von Oertzen et.al. (von Oe 75) so that direct comparison of S^2 obtained by him and the present work was possible.

The first step in the analytic evaluation of eq.A(1) is to use an addition theorem derived by Buttle and Goldfarb (Bu 66) inter alia. $\phi_b(\underline{r}-\underline{R})$ (eq.A(2)) is written

$$\phi_b(\underline{r}-\underline{R}) = N_2\sqrt{4\pi}\sum_{\ell\ell' mm'}(-1)^{1/2(\ell_2+\ell-\ell')}\frac{\hat{\ell}_2\hat{\ell}}{\hat{\ell}'} \times$$

$$(\ell m \ell_2 m_2|\ell' m')(\ell 0 \ell_2 0|\ell' 0) \times h^{(1)}_{\ell}(i\alpha R) Y^*_{\ell m}(\underline{R}) j_{\ell'}(i\alpha r) Y_{\ell' m'}(\hat{\underline{r}}) \quad \text{---} \quad A(3)$$

Where the symbol â appears, it stands for $(2a+1)^{1/2}$. Spherical harmonics are denoted by Y^m_ℓ as well as $Y_{\ell m}$. If $\phi_a(\underline{r})$ (eq.A(2)) and $\phi_b(\underline{r}-\underline{R})$ (eq.A(3)) are inserted in eq.A(1), then the first thing to notice is that an integration

over the angular coordinates of $\underline{r}$, (θ,ϕ), results of the form

$$\int\int Y^*_{\ell',m'}(\hat{\underline{r}})Y_{\ell_1 m_1}(\hat{\underline{r}})\sin\theta d\theta d\phi = \delta_{\ell',\ell_1} \qquad \text{---} \qquad \text{A(4)}$$

because this is the orthonormality condition for spherical harmonics.

In the transfer of a $p_{1/2}$ neutron from an initial state to an identical state in ^{13}C, $\ell_1=\ell_2=1$. This simplifies eq.A(3) somewhat:

$$\phi_b(\underline{r}-\underline{R}) = N_2\sqrt{4\pi}\sum_{\ell\ell',mm'}(-1)^{1/2\ell}\hat{\ell}(\ell m\ell_1 m_1|\ell_1 m_1)$$

$$\times(\ell 0\ell_1 0|\ell_1 0)h^{(1)}_{\ell}(i\alpha R)Y^*_{\ell m}(\hat{\underline{R}}) \times j_{\ell_1}(i\alpha r)Y_{\ell_1 m_1}(\hat{\underline{r}}) \qquad \text{A(5)}$$

where the result of eq.A(4) has been used also.

The remaining cordinate of eq.A(1) is r, and an integral of the type

$$I = \int_0^\infty j^*_{\ell_1}(i\alpha r)V_{cn}(r)h^{(1)}_{\ell_1}(i\alpha r)r^2dr \qquad \text{---} \qquad \text{A(6)}$$

remains.

Buttle and Goldfarb (Bu 66) show that this can be evaluated independently of the functional form of $V_{cn}(r)$ as

$$I = (-1)^{\ell}E_B/\alpha^3 \qquad \text{---} \qquad \text{A(7)}$$

where E_B is the neutron separation energy from ^{13}C, and α is given by

$$\alpha^2 = 2m_n E_B/\hbar^2 \qquad \text{---} \qquad \text{A(8)}$$

m_n is the reduced neutron mass. (Reduced with respect to a ^{12}C core).

From eq.A(5), it can be seen that $0\leq\ell\leq2$. This is the obvious result that the transferred angular momentum in going from a $p_{1/2}$ state to a $p_{1/2}$ state can be 0, 1 or 2 units of angular momentum. If $\ell>0$, J(R) becomes a tensor interaction by virtue of the $Y^*_{\ell m}(\underline{R})$. However, in a proper treatment which also includes the spins of the two nuclei, a coupling coefficient of the type

$$(j_1 m_1 \ell m|j_2 m_2) \qquad \text{---} \qquad \text{A(9)}$$

results.

Since $j_1=j_2=1/2$, ℓ is further restricted to 0 or 1. There is a further final restriction on ℓ which is due to parity conservation. It is necessary for

$$P_i(-1)^{\ell} = P_f \qquad \text{---} \qquad A(10)$$

where P_i and P_f are the parities of the initial and final states respectively. Since $0 \leq \ell \leq 1$, the only value allowed for the transferred angular momentum is zero. Collecting the results of the previous equations together gives

$$J(R) = \frac{N^2 E_B}{\alpha^3} \frac{e^{-\alpha R}}{\alpha R} \qquad \text{---} \qquad A(11)$$

The equation which includes the spectroscopic amplitudes of the $p_{1/2}$ state in ^{13}C merely replaces N^2 with $(SN)^2$. Hence eq.A(11) becomes

$$J(R) = \frac{(SN)^2 E_B}{\alpha^3} \frac{e^{-\alpha R}}{\alpha R} \qquad \text{---} \qquad (A12)$$

which is eq.5.5.

APPENDIX B

In this appendix, a list of typical instrument settings used when detecting gamma rays in the range 10-20 MeV. These may be useful to people who use the instrument in future.

Fluke H.V. supply. (For 60 A.V.P.) - 2160V on dials.

Fluke H.V. supply. (For XP1030) - 2250V on dials.

Ortec 453 C.F.T.D.

LLD = 700 (Arbitrary)

Fraction = 0

Walk adjust = Fully anticlockwise (most important).

Terminate bridging input and external delay with 3 50Ω terminators.

First 1455 A Logic shaper and delay.

Input = Positive

Amplitude = 9

Width = 2.5

Width switch = X0.1

Delay = 1μs.

Second 1455 A

Input = positive

Amplitude = 7.5

Width = 1.5

Width Switch = X1

Delay = 2.41μs.

1446 Coincidence

Coincidence events = 1

A = Coincidence

B = Anti coincidence

1443 TAC

Range = 500ns.

Gate mode = Anti coincidence

Output timing = start

S.C.A.

Time = 10

ΔTime = 990

1437 S.C.A.

Window = 920

Baseline = 14

Delay = 6

Mode. S.C.A. L.E.

Output = positive

---

434 T.F.A.

Coarse gain = 5

Fine gain = 8

Time constant: Out, out. (Int., Diff)

Input = neg.

---

436 100 MHz Discrimination

Level = 70.0

Reset = Prompt.

1454 Gate

Output 10V Pos.

Gate = Coincidence

Input Rate = Hi.

---

408 Bias amp.

Level = 0

Gain = 1

---

410 Linear Amplifier

Input = Positive

Attenuation = 10

Course gain = 1

Fine gain = 2.5

$\int\tau$ = ·1μs.

$\tau_{Diff.}$ = DL, DL (1st, 2nd)

REFERENCES

Al 64 R.G. Allas, S.S. Hanna, Luise Meyer-Schützmeister and R.E. Segel. Nucl.Phys. 58 (1964) 122.

Al 64a R.G. Allas, S.S. Hanna, L. Meyer-Schützmeister, R.E. Segel, P.P. Singh and Z. Vager. Phys.Rev.Letters 13 (1964) 628.

Al 65 B.W. Allardyce, P.J. Dallimore, I. Hall, N.W. Tanner, A. Richter, P. von Brentano and T. Mayer-Kuckuk. Max-Planck-Institut Für Kemphysik, 1965/V/8. (See Da 66).

Al 72 K. Alder, R. Morf, M. Pauli and D. Trautmann. Nucl.Phys. A191 (1972) 399.

An 61 J.D. Anderson and C. Wong. Phys.Rev.Letters 7 (1961) 250.

Ba 75 J. Barrette, P. Braun-Munzinger and C.K. Gelbke. N.I.M. 126 (1975) 181.

Be 68 R.C. Bearse, L. Meyer-Schützmeister and R.E. Segel. Nucl.Phys. A116 (1968) 682.

Be 69 B.L. Berman, M.A. Kelly, R.L. Bramblett, J.T. Caldwell, H.S. Davis and S.C. Fultz. Phys.Rev. 185 (1969) 1576.

Be 72 H-D. Betz. Rev.of Mod.Phys. 44 (1972) 465.

Be 74 F. Becker, S. Joffily, C. Beccaria and G. Baron. Nucl.Phys. A221 (1974) 475.

Be 75 G.F. Bertsch. Nucl.Phys. A249 (1975) 253.

Bevington P.R. Bevington. Data Reduction and Error analysis for the Physical Sciences, McGraw-Hill Book Co. 1969.

Bl 66 A.E. Blaugrund. Nucl.Phys. 88 (1966) 501.

Bl 71 J.L. Black, W.J. Caelli and R.B. Watson. Report - ANU-P/540, 1971. Unpublished.

B-M 68 B.M. Braga-Marcazzan and L. Milazzo-Colli. Energia Nucleare 15 (1968) 186.

Bo 15 N. Bohr. Phil.Mag. 30 (1915) 581.

Bo 56 T.W. Bonner, A.A. Kraus, J.B. Marion and J.P. Schiffer.
Phys.Rev. 102 (1956) 1348.

Bo 71 H.G. Bohlen and W. von Oertzen.
Phys.Letters 37B (1971) 451.

Br 59 G.E. Brown and M. Bolsterli.
Phys.Rev.Letters 3 (1959) 472.

Br 71 G.E. Brown. Unified theory of Nuclear Models and Forces, p.258.
North Holland Pub.Co. 1971.

Bu 66 P.J.A. Buttle and L.J.B. Goldfarb.
Nucl.Phys. 78 (1966) 409.

Bu 67 G.G. Bunatyan. Sov.J.Nucl.Phys. 4 (1967) 659.

Bu 73 P.J.A. Buttle. Private communication.

Ca 59 J.H. Carver and W. Turchinetz.
Proc.Phys.Soc. London. 73 (1959) 585.

Ca 74 A.J. Campillo, R.C. Hyer and S.L. Shapiro.
N.I.M. 120 (1974) 533.

Ch 34 J. Chadwick and M. Goldhaber.
Nature 134 (1934) 237.

Ch 75 C.C. Chang, F.E. Bertrand and D.C. Kocher.
Phys.Rev.Letters 34 (1975) 221. (See also Ko 73).

Co 66 M. Corti, M.G. Marcazzan, L. Milazzo-Colli and M. Milazzo.
Energia Nucleare 13 (1966) 312.

Co 67 S. Cohen and D. Kurath.
Nucl.Phys. A101 (1967) 1.

Da 58 M. Danos. Nucl.Phys. 5 (1958) 23.

Da 65 M. Danos and E.G. Fuller.
Ann.Rev.of Nucl.Science 15 (1965) 29.

Da 66 P.J. Dallimore and I. Hall.
Nucl.Phys. 88 (1966) 193.

Da 68 J.P. Davidson. Collective models of the nucleus, p.141.
Academic Press. 1968.

Da 71 H. Dahmen, F. Dreyer, J. Staude and H.H. Thies.
Nucl.Phys. A164 (1971) 140.

Di 73 E.M. Diener, J.F. Amann and P. Paul.
Phys.Rev. C7 (1973) 695.

Dr 72 F. Dreyer, H. Dahmen, J. Staude and H.H. Thies.
Nucl.Phys. A192 (1972) 433.

Ei 70 J.M. Eisenberg and W. Greiner.
Nuclear Models, Vol.1. North Holland Pub.Co. 1970.

El 66 R.V. Elliott and R.H. Spear.
Nucl.Phys. 84 (1966) 209.

El 68 R.V. Elliott. Thesis - A.N.U. Canberra (1968). Unpublished.

En 73 P.M. Endt and C. Van der Leun.
Nucl.Phys. A214 (1973) 1.

Er 63 T. Ericson. Annals of Physics 23 (1963) 390.

Ev 55 R.D. Evans. The Atomic Nucleus.
McGraw-Hill Book Co.Inc.

Ev 67 A.E. Evans. Phys.Rev. 155 (1967) 1047.

Fa 65 S. Fallieros, B. Goulard and R.H. Venter.
Phys.Letters 19 (1965) 398.

Fe 65 P. Fessenden, W.R. Gibbs and R.B. Leachman.
Phys.Rev.Letters 15 (1965) 796.

Fo 74 G.S. Foote. Thesis - A.N.U. Canberra (1974).

Fu 58 E.G. Fuller and M.S. Weiss.
Phys.Rev. 112 (1958) 560.

Fu 72 S. Fukuda and Y. Torizuka.
Phys.Rev.Letters 29 (1972) 1109.

Ga 56 G.I. Gavrilov and L.A. Lazareva.
Zhur.Eksptl. i Teoret. Fiz. 30(5) (1956) 855.

Ga 65 E. Gadioli. Phys.Letters 16 (1965) 288.

Ge-Ma 53 M. Gell-Mann and V. Telegdi.
Phys.Rev. 91 (1953) 169.

Ge-Ma 54 M. Gell-Mann, M.L. Goldberger and W.E. Thirring.
Phys.Rev. 95 (1954) 1612.

Ge 73 G.K. Gelbke, R. Bock, P. Braun-Munzinger, D. Fick, K.D. Hildenbrand, W. Weiss, S. Wermeis and G. Baur.
Phys.Letters 43B (1973) 284.

Gi 64 V. Gillet and N. Vinh-Mau.
Nucl.Phys. 54 (1964) 321.

Gi 65 W.R. Gibbs. Phys.Rev. B139 (1965) 1185.

Gi 65a A. Gilbert and A.G.W. Cameron.
Can.J.Phys. 43 (1965) 1446.

Go 70 B.I. Goryachev, B.S. Ishknavov, I.M. Kapitonov, I.M. Piskarev, V.G. Shevchenko and O.P. Shevchenko.
Soviet Journal of Nucl.Phys. 11 (1970) 141.

Gu 69 I.S. Gul'karov, N.G. Afanas'ev, V.M. Khvastunov, N.G. Shevchenko, V.D. Afanas'ev, G.A. Savitskii and A.A. Khomich.
Soviet Journal of Nucl.Phys. 9 (1969) 274.

Ha 75 S.S. Hanna, H.F. Glavish, J.R. Calarco, R. LaCanna, E. Kuhlmann and D.G. Mavis.
Int.Symp. on Highly Excited States in Nuclei. Jülich. Sept.1975. Unpublished.

Ha 75a S.S. Hanna. Amsterdam Conference, 1975. Unpublished.

He 68 J. Hellström and P.J. Dallimore.
Nucl.Phys. A125 (1968) 684.

Hi 72 K.D. Hildenbrand, R. Bock, H.G. Bohlen, P. Braun-Munzinger, D. Fick, C.K. Gelbke, W. von Oertzen and W. Weiss.
Phys.Letters 42B (1972) 425.

Ho 71 P.E. Hodgson. Nuclear Reactions and Nuclear Structure.
Clarendon Press. Oxford. 1971.

Ho 74 B.W. Hooton, J.W. Freeman and P.P. Kane.
A.E.R.E. R7779. Nucl.Phys.Division, Harwell, 1974.
Published in N.I.M. 124 (1975) 29.

Im 74 B. Imanishi, H. Onishi and O. Tanimura.
Int.Conf. on Reactions between complex nuclei. June 10-14, 1974.
Ed. R.L. Robinson, F.K. McGowan, J.B. Ball and J.H. Hamilton.
North Holland Pub.Co. American Elsevier Pub.Co.Inc.

Ja 62 J.D. Jackson. Classical Electrodynamics.
John Wiley and Sons Inc. 1962.

Jackson J.D. Jackson. Classical Electrodynamics.
John Wiley and Sons Inc. 1962.

Ka 51 L. Katz and A.G.W. Cameron.
Can.J.Phys. 29 (1951) 518.

Ka 51a L. Katz, H.E. Johns, R.G. Barker, R.N.H. Haslam and R.A. Douglas.
Phys.Rev. 82 (1951) 271.

Kn 75 H. Breuer, K.T. Knöpfle, C. Mayer-Böricke, M. Rogge and G.J. Wagner.
Int.Symp. on Highly Excited States in Nuclei. Julich. Sept.1975.

Ko 73 D.C. Kocher, F.E. Bertrand, E.E. Gross, R.S. Lord and E. Newman.
Phys.Rev.Letters 31 (1973) 1070.

Ku 75 E. Kuhlmann, E. Ventura and S.S. Hanna.
Phys.Rev. C11 (1975) 1525.

Le 50 J.S. Levinger and H.A. Bethe.
Phys.Rev. 78 (1950) 115.

Le 59 I.A.D. Lewis and F.H. Wells.
Millimocrosecond Pulse Techniques. Permagon Press, 1959.

Le 67 C.M. Lederer, J.M. Hollander and I. Perlman.
Table of Isotopes.
John Wiley and Sons, Inc. 1967.

Le 72 M.B. Lewis and F.E. Bertrand.
Nucl.Phys. A196 (1972) 337.

Le 72a M.B. Lewis. Phys.Rev.Letters 29 (1972) 1257.

Li 61 J. Lindhard and M. Scharff.
Phys.Rev.124 (1961) 128.

Li 63 J. Lindhard, M. Scharff and H.E. Schiott.
Kgl. Danske Videnskab Selskab.
Mat.Fys.Medd. 33 (1963) 14.

Ma 55 W.M. Macdonald. Phys.Rev. 100 (1955) 51.

Ma 56 W.M. Macdonald. Phys.Rev. 101 (1956) 271.

Ma 58 W.M. Macdonald. Phys.Rev. 110 (1958) 1420.

Ma 68 J.B. Marion and F.C. Young.
Nuclear Reaction Analysis.
North Holland Pub.Co. 1968.

Ma 71 J.R. Macdonald and F.W. Martin.
Phys.Rev. A4 (1971) 1965.

Me 67 L. Meyer-Schützmeister, Z. Vager, R.E. Segel and P.P. Singh.
Nucl.Phys. A108 (1968) 180.

Me 71 L. Meyer. Phys.Stat.Sol.(B) 44 (1971) 253.

Me 71a M.C. Mermaz, C.A. Whitten, J.W. Champlin, A.J. Howard and D.A. Bromley.
Phys.Rev. C4 (1971) 1778.

Mi 68 K. Min and T.A. White.
Phys.Rev.Letters 21 (1968) 1200.

Mi 72 T.G. Miller, F.P. Gibson, R. Hagland, W. Morrison and G. Westley.
Nucl.Phys. A191 (1972) 1.

NBS 380 Photonuclear Reaction Data.
U.S. Dept.of Commerce. Nat.Bureau of Standards. 1973.

Ne 75 C.S. Newton. Thesis - A.N.U. Canberra, 1975.

No 70 L.C. Northcliffe and R.F. Schilling.
Nucl.data tables A7 (1970) 233.

On 70 D.S. Onley. Nucl.Phys. A149 (1970) 197.

Op 64 T.R. Ophel and I.V. Mitchell.
Nucl.Phys. 58 (1964) 529.

Op 75 Ophel et.al. Preprint.

Ow 70 D.G. Owen, E.G. Muirhead and B.M. Spicer.
Nucl.Phys. A140 (1970) 523.

Pa 71 P. Paul, J.F. Amann and K.A. Snover.
Phys.Rev.Letters 27 (1971) 1013.

Pa 74 D.M. Parkinson. Thesis - A.N.U. Canberra, 1974.

Pa 75 P. Paul, J.W. Noé, K.A. Snover, M. Suffert, E.K. Warburton, H.M. Kuan.
Int.Symp.on Highly Excited States in Nuclei, Vol.1. Jülich, 1975.

Pe 63 F.G. Perey. Phys.Rev. 131 (1963) 745.

Pe 64 J.D. Pearson and R.H. Spear.
Nucl.Phys. 54 (1964) 434.

Pe 74 R.E. Peschel, J.M. Long, H.D. Shay and D.A. Bromley.
Nucl.Phys. A232 (1974) 269.

Pr 50 G.A. Price and D.W. Kerst.
Phys.Rev. 77 (1950) 499.

Pr 62 M.A. Preston. Physics of the Nucleus. Addison-Wesley Pub.Co.Inc. 1962.

Ro 60 J.P. Roalsvig, R.N.H. Haslam and J.L. Bergsteinsson. Can.J.Phys. 38 (1960) 321.

Ro 68 C.P. Robinson, J.P. Aldridge, J. John and R.H. Davis. Phys.Rev. 171 (1968) 1241.

Sa 72 G.R. Satchler. Nucl.Phys. A195 (1972) 1.

Se 60 Experimental Nuclear Physics, Vol.I. Ed. E. Segre. John Wiley and Sons Inc. 1960.

Sh 67 Scintillation Spectroscopy of Gamma Radiation, Vol.I. Ed. S.M. Shafroth. Gordon and Breach Publishers, 1967.

Shafroth Scintillation Spectroscopy of Gamma Radiation, Vol.I. Ed. S.M. Shafroth. Gordon and Breach Publishers, 1967.

Sh 75 N. Shikazono and T. Terasawa. Nucl.Phys. A250 (1975) 260.

Sn 74 K.A. Snover, E.G. Adelburger and D.R. Brown. Phys.Rev.Letters 32 (1974) 1061.

So 69 See Wi 69.

Sp 69 B.M. Spicer. Advances in Nuclear Physics 2 (1969) 1.

St 53 K. Strauch. Ann.Rev.of Nucl.Science 2 (1953) 105.

Su 67 M. Suffert and W. Feldman. Phys.Letters 24B (1967) 579.

Su 68 M. Suffert, W. Feldman, J. Mahieux and S.S. Hanna. N.I.M. 63 (1968) 1.

Su 73 T. Suzuki. Nucl.Phys. A217 (1973) 182. (See also Sa 72)

Sz 34 L. Szilard and T.A. Chalmers. Nature 134 (1934) 494.

Ti 58 Conference on Photonuclear Reactions. Washington, D.C. Paper A1. 1958. E.W. Titterton.

Ve 70 A. Veyssiere, H. Beil, R. Bergere, P. Carlos and A. Lepretre. Nucl.Phys. A159 (1970) 561.

Vo 69 U.C. Voos, W. von Oertzen and R. Bock. Nucl.Phys. A135 (1969) 207.

von Oe 70 W. von Oertzen, Nucl.Phys. A148 (1970) 529.

von Oe 71 W. von Oertzen, G. Bohlen, B. Gebauer, E.E. Habib and N. Marquardt.
Phys.Letters 34B (1971) 51.

von Oe 73 W. von Oertzen and W. Norenberg.
Nucl.Phys. A207 (1973) 113.

von Oe 75 W. von Oertzen and H.G. Bohlen.
Physics Reports 19C (1975) No.1.

Wa 57 R.B. Walton, J.D. Clement and F. Boreli.
Phys.Rev. 107 (1957) 1065.

Wa 72 R.B. Watson, D. Branford, J.L. Black and W.J. Caelli.
Nucl.Phys. A203 (1973) 209.

Wa 73 Proc.of the Int.Conf.on Nucl.Phys. Vol.2, p.509. 1973.
Ed. J. de Boer and H.J. Mang.
North Holland/American Elsevier.

Wi 64 D. Wilmore and P.E. Hodgson.
Nucl.Phys. 55 (1964) 673.

Wi 66 C.F. Williamson, J.P. Boujot and J. Picard.
Centre D'etudes Nucleaires De Saclay.
CEA R 3042, 1966.

Wi 69 Isospin in Nuclear Reactions.
Ed. Wilkinson. North Holland Pub.Co. Amsterdam, 1969.

Ya 66 T. Yamazaki. Lawrence Rad.Lab.Report. UCRL 17086 (1966).

Ya 73 B. Yaramis, D.D. Tolbert and R.H. Davis.
Nucl.Phys. A215 (1973) 197.